

UNCLASSIFIED

AD NUMBER

AD325237

CLASSIFICATION CHANGES

TO: unclassified

FROM: confidential

LIMITATION CHANGES

TO:
Approved for public release, distribution
unlimited

FROM:
Controlling DoD
Organization...Aeronautical Systems
Division, Eglin AFB, FL. NOFORN.

AUTHORITY

28 Feb 1973, per document marking, DoDD
5200.10; WL/DOOS' [AFSC]ltr, 24 Feb 1992

THIS PAGE IS UNCLASSIFIED

UNCLASSIFIED

AD NUMBER
AD325237
CLASSIFICATION CHANGES
TO
confidential
FROM
secret
AUTHORITY
28 Feb 1964, per document marking, DoDD 5200.10

THIS PAGE IS UNCLASSIFIED

UNCLASSIFIED

SECRET

AD 325 237

*Reproduced
by the*

ARMED SERVICES TECHNICAL INFORMATION AGENCY
ARLINGTON HALL STATION
ARLINGTON 12, VIRGINIA



UNCLASSIFIED

NOTICE: When government or other drawings, specifications or other data are used for any purpose other than in connection with a definitely related government procurement operation, the U. S. Government thereby incurs no responsibility, nor any obligation whatsoever; and the fact that the Government may have formulated, furnished, or in any way supplied the said drawings, specifications, or other data is not to be regarded by implication or otherwise as in any manner licensing the holder or any other person or corporation, or conveying any rights or permission to manufacture, use or sell any patented invention that may in any way be related thereto.

ASD-TR-61-34 (II)

ASTIA
DOCUMENT

JULY 1961

CR 341 377 001

AFSC Project 3811

Contract AF 08(635)-1168

Copy Nr. 011 of 118 Copies

XEROX

PYE WACKET Feasibility Test Vehicle Study (Aerodynamics)

(TITLE UNCLASSIFIED)

VOLUME II

Prepared by

Convair/Pomona
General Dynamics Corporation
Pomona, California

for

AIR PROving GROUND CENTER

EGLIN AIR FORCE BASE, FLORIDA

SPECIAL HANDLING REQUIRED
NOT RELEASABLE TO FOREIGN NATIONALS
The information contained in this document will not be
disclosed to Foreign Nationals or their representatives.

DOWNGRADED AT 3 YEAR INTERVALS;
DECLASSIFIED AFTER 12 YEARS.

DOD DIR 5200.10

Reproduced From
Best Available Copy

UNCLASSIFIED

June 1961

UNCLASSIFIED

PYE WACKET
Feasibility Test Vehicle Study
(Aerodynamics)

CR 341 377 001
AFSC Project 3811
Contract AF 08(635)-1168

15 February 1961

Convair/Pomona
Convair Division of General Dynamics Corporation
Pomona, California

Prepared for

Detachment 4
HEADQUARTERS, AERONAUTICAL SYSTEMS DIVISION
Air Force Systems Command
United States Air Force
Eglin Air Force Base, Florida

Copies of this report were printed at Eglin AFB by photo-offset process from the reproducible furnished by the contractor.

UNCLASSIFIED

FOREWORD

This report was prepared under Air Force Contract Number AF 08(635)-1168, Project 3811, (U) "Lenticular Rockets." The work was administered initially under the direction of the Directorate of Development, AFGC, and completed under the guidance of Detachment 4, Hq Aeronautical Systems Division at Eglin Air Force Base, Florida.

This document, except the title, is classified SECRET in accordance with AFR 205-1, paragraph 10b, because of the nature and potential military application of the research work and data described herein, and NOT RELEASABLE TO FOREIGN NATIONALS in accordance with AFDCMI 56.

UNCLASSIFIED

ABSTRACT

Feasibility studies were conducted of a circular planform, modified lenticular cross section vehicle. The results of these studies form the basis for the ultimate fabrication and flight test of vehicles to prove the omnidirectional launch, stability and control, and maneuver capability of the basic concept.

Wind tunnel tests were conducted over the Mach number range of 0.6 to 5 and for yaw angles from 0 to 180 degrees. Force and moment data were obtained as well as pressure distributions (including the effects of reaction control jets).

The complete task is reported in three volumes: Volume I--Summary, Volume II--Aerodynamics, and Volume III--Configuration and Autopilot/Control.

THIS ABSTRACT IS CLASSIFIED SECRET
Catalog cards with an unclassified abstract
may be found at the back of this publication.

UNCLASSIFIED

CONTENTS

SYMBOLS AND DEFINITIONS

PAGE

SECTION

1.	INTRODUCTION	
1.1	History	1.1
1.2	Objective	1.2
2.	DISCUSSION AND RESULTS	
2.1	Configuration Geometry	2.1
2.2	Basic Studies	2.1
2.2.1	Theoretical Aerodynamics	2.1
2.2.2	Yaw Moment Origin	2.12
2.3	Experimental Program	2.13
2.3.1	Models and Test Conditions	2.13
2.3.2	Evaluation of Data	2.25
2.4	Aerodynamic Characteristics	2.31
2.4.1	Axis System	2.31
2.4.2	Applicability of Aerodynamic Coefficients	2.34
2.4.3	Power-Off Data Presentation	2.34
2.4.3.1	Normal Force Coefficient	2.38
2.4.3.2	Pitching Moment Coefficient	2.60
2.4.3.3	Side Force Coefficient	2.81
2.4.3.4	Yawing Moment Coefficient	2.87
2.4.3.5	Rolling Moment Coefficient	2.96
2.4.3.6	Center of Pressure Location	2.96
2.4.3.7	Axial Drag Coefficient	2.106
2.4.4	Wind Tunnel Photographs - Jets Off	2.119
2.4.5	Power-On Aerodynamic Characteristics	2.131
2.4.5.1	Axial Drag Coefficient	2.131
2.4.5.2	Side Force and Yawing Moment Coefficients	2.141
2.4.6	Pressure Distributions	2.144
2.4.6.1	Control Jets Off	2.144
2.4.6.2	Control Jets On	2.154
2.4.7	Wind Tunnel Photographs - Jets On	2.167
2.5	Performance	2.181
2.6	Launch Studies	2.188
2.6.1	Sled Configuration	2.188
2.6.2	Support Structure	2.189
2.6.3	Estimated Composite Sled Characteristics	2.189
2.6.4	Estimated Sled Performance	2.189
2.6.5	Interference Effects	2.190

SECRET

2.6.6	Vibration Effects	2.198
2.7	Problem Areas	2.198
2.7.1	Rear Launch, Power-On	2.198
2.7.2	Dynamic Considerations	2.199
2.7.3	Damping Derivatives	2.202
2.8	Prototype Considerations	2.202
3.	CONCLUSIONS	3.1
4.	RECOMMENDATIONS	4.1
5.	BIBLIOGRAPHY	5.1
6.	APPENDIX	6.1
6.1	Surface Pressure Integration Method	6.1
6.2	Equation for Level Flight Trajectories	6.3

FIGURE

PAGE

2.1.1	Phase I Configuration	2.2
2.1.2	FTV Configuration	2.3
2.2.1	Comparison of Experimental and Theoretical Normal Force Coefficients, $M = 3.0$	2.7
2.2.2	Comparison of Experimental and Theoretical Normal Force Coefficients, $M = 4.0$	2.8
2.2.3	Comparison of Experimental and Theoretical Normal Force Coefficients, $M = 5.0$	2.9
2.2.4	Comparison of Experimental and Theoretical Wave Drag Coefficients	2.10
2.2.5	Comparison of Experimental and Theoretical Center of Pressure Locations	2.11
2.3.1	Wind Tunnel Model Configuration	2.14
2.3.2	PWT Model Installation	2.15
2.3.3	Force Model	2.18
2.3.4	Pressure Model	2.20
2.3.5	Pressure Model, Orifice Numbering	2.24
2.3.6	Pitching Moment Comparison of Force and Pressure Data	2.26
2.3.7	Normal Force Comparison of Force and Pressure Data	2.27
2.3.8	Comparison of Longitudinal Pressure Symmetry, $\beta = 0^\circ$	2.28
2.4.1	Axis System, Angle Relationships	2.32
2.4.2	Stability Axis System	2.33
2.4.3	Variation of Normal Force Coefficient with Angle of Attack, Power-Off	2.41
2.4.4	Variation of Normal Force Derivative with Mach Number, Power-Off	2.54
2.4.5	Variation of Normal Force Coefficient with Angle of Sideslip, Power-Off	2.56
2.4.6	Variation of Pitching Moment Coefficient with Angle of Attack, Power-Off	2.62
2.4.7	Variation of Pitching Moment Derivative with Mach Number, Power-Off	2.75
2.4.8	Variation of Pitching Moment Coefficient with Angle of Sideslip, Power-Off	2.77
2.4.9	Variation of Side Force Coefficient with Angle of Sideslip, Power-Off	2.83
2.4.10	Variation of Yawing Moment Coefficient with Angle of Sideslip, Power-Off	2.89
2.4.11	Variation of Rolling Moment Coefficient with Angle of Sideslip, Power-Off	2.97

2.4.12	Variation of Center of Pressure Location with Mach Number for $\beta = 0^\circ$ and $\beta = 90^\circ$, Power-Off	2.104
2.4.13	Variation of Center of Pressure Location with Angle of Sideslip, Power-Off	2.105
2.4.14	Variation of Axial Drag Coefficient with Mach Number, $\beta = 0^\circ, 90^\circ, 180^\circ$, Power-Off	2.110
2.4.15	Variation of the Components of Axial Drag Coefficient with Mach Number, Power-Off, $\beta = 0^\circ$	2.111
2.4.16	Variation of Axial Drag, Coefficient with Angle of Sideslip, Power-Off	2.112
2.4.17	Fluorescent - Oil Film Photographs, Power-Off	2.120
2.4.18	Schlieren Photographs, Power-Off	2.123
2.4.19	Variation of Axial Drag Coefficient with Mach Number, Power-On, $\beta = 0^\circ$	2.133
2.4.20	Comparison of Power-Off and Power-On Base Drag Coefficients, $\beta = 0^\circ$	2.134
2.4.21	Comparison of Base Drag Coefficients for Control Jets On and Off, Main Rocket Motor Off, $\beta = 0^\circ$	2.135
2.4.22	Variation of Wave Plus Afterbody Drag and Skin Friction Drag with Mach Number, $\beta = 0^\circ$	2.136
2.4.23	Variation of Axial Drag Coefficient with Mach Number, Power-On, $\beta = 90^\circ$	2.137
2.4.24	Variation of Axial Drag Coefficient with Mach Number, Angle of Sideslip as a Parameter, Power-On	2.138
2.4.25	Variation of Axial Drag Coefficient with Mach Number, Control Jets On. Main Rocket Off, $\beta = 0^\circ$	2.139
2.4.26	Variation of Axial Drag Coefficient with Mach Number, Angle of Sideslip Parameter, Control Jets On, Main Rocket Off	2.140
2.4.27	Variation of Estimated Side Force Coefficient with Mach Number, Power-On	2.142
2.4.28	Variation of Estimated Yawing Moment Coefficient with Mach Number, Power-On	2.143
2.4.29	Subsonic Longitudinal Pressure Distributions for Various Lateral Chords	2.147
2.4.30	Supersonic Longitudinal Pressure Distributions for Various Lateral Chords	2.148
2.4.31	Effect of Mach Number on Center Line Pressure Distributions	2.149
2.4.32	Effect of Angle of Attack on the Longitudinal Centerline Pressure Distribution, $\beta = 0^\circ$	2.150
2.4.33	Effect of Angle of Attack on the Lateral Centerline Pressure Distribution, $\beta = 90^\circ$	2.151

2.4.34	Variation of Base Pressure Coefficient with Angle of Sideslip, Mach Number 0.8	2.152
2.4.35	Effect of Angle of Attack on the Longitudinal Centerline Pressure Distribution, $\alpha = 180^\circ$. . .	2.153
2.4.36	Comparison of Pressure Coefficients Around Reaction Jets for Jets On and Off, Mach Number 0.6	2.156
2.4.37	Comparison of Pressure Coefficients Around Reaction Jets for Jets On and Off, Mach Number 1.6	2.159
2.4.38	Comparison of Pressure Coefficients Around Reaction Jets for Jets On and Off, Mach Number 3.0	2.162
2.4.39	Comparison of Maximum and Minimum Pressures Adjacent to Reaction Jets	2.165
2.4.40	Schematic Flow Structure of Reaction Jets	2.166
2.4.41	Fluorescent-Oil Film Photographs. Control Jets On .	2.168
2.4.42	Schlieren Photographs, Control Jets On	2.171
2.5.1	Variation of Maneuverability with Mach Number . . .	2.183
2.5.2	Angle of Attack Necessary for Level Flight.	2.184
2.5.3	Maximum Controllable Angle of Attack versus Mach Number, $\alpha = 0^\circ$	2.185
2.5.4	Maximum Controllable Angle of Attack versus Mach Number, $\alpha = 90^\circ$	2.186
2.5.5	Mach Number Time-History	2.187
2.6.1	PYE WACKET FTV and E.A.F.B. High Speed Sled, Forward Launch Position	2.191
2.6.2	PYE WACKET FTV and E.A.F.B. High Speed Sled, Side Launch Position	2.192
2.6.3	Estimated Composite Sled Characteristics	2.193
2.6.4	Estimated Sled Performance	2.194
2.6.5	Ground Effect on Lift Curve Slope	2.195
2.6.6	Longitudinal Angular Flow Field About an Airfoil Section	2.196
2.6.7	Lateral Angular Flow Field in the Vicinity of the FTV	2.197
2.7.1	Mach Number Range for Model Oscillations and Model Bouncing	2.201
2.8.1	Variation of Dynamic Pressure with Mach Number, Mach Number to 18	2.206
2.8.2	Variation of Dynamic Pressure with Mach Number, Mach Number to 8	2.207

TABLE

PAGE

2.4.1	Sled Captive Phase Figure Index (Main Motors Off)	2.35
2.4.2	Power-On Phase Figure Index (Main Motors On	2.36
2.4.3	Coast Phase Figure Index (Main Motors Off)	2.36
2.4.4	Power-Off Aerodynamic Coefficients - Figure Index (Main Motors Off, Reaction Control Jets Off)	2.37

SYMBOLS AND DEFINITIONS

AR	Aspect ratio, d^2/s
A_s	Axial drag force, lb
c	Local chord length, in.
C_{A_s}	Axial drag coefficient, $\frac{A_s}{qS}$
C_D	Drag coefficient, $\frac{D}{qS}$
C_{D_0}	Drag coefficient at zero angle of attack
C_{DB}	Drag coefficient for blunt base only. Computed from wind tunnel pressure measurements
C_{Df}	Skin friction drag coefficient
C_{DW}	Wave drag coefficient
C_{l_s}	Rolling moment coefficient, $\frac{RM_s}{qSd}$
C_L	Lift coefficient, $\frac{L}{qS}$
$C_{L\alpha}$	Lift coefficient derivative, $\frac{\partial C_L}{\partial \alpha}$, per degree angle of attack.
C_{m_s}	Pitching moment coefficient, $\frac{PM}{qSd}$
$C_{m_{\alpha s}}$	Pitching moment derivative, $\frac{\partial C_{m_s}}{\partial \alpha}$, per degree angle of attack.
C_N	Normal force coefficient, $\frac{N}{qS}$
ΔC_N	Incremental change in normal force
$C_{N\alpha}$	Normal force derivative, $\frac{\partial C_N}{\partial \alpha}$, per degree angle of attack.
C_{n_s}	Yawing moment coefficient, $\frac{YM_s}{qSd}$
C_p	Pressure coefficient, $\frac{P-P_\infty}{q}$

C_{Y_s}	Side force coefficient, $\frac{Y_s}{qS}$
C.G.	Center of gravity
C.P.	Center of pressure
d	Diameter of missile, 60.0 inches (FTV)
D	Drag, lb
l	Distance parallel to x-axis from center of gravity to center of reaction jets
M	Mach number, $\frac{V}{a}$
N	Normal force, lb
P	Static pressure, psf
P_j	Chamber pressure of reaction jets, psia
PM	Pitching moment, ft-lb
q	Dynamic pressure, psf
R_N	Reynolds number, $R_N = \frac{\rho V d}{\mu}$
RM	Rolling moment, ft-lb
S	Planform area, 2827.4 in. ² (Full scale)
S_B	Base area, = 369.0 in. ² main rockets off = 225.0 in. ² main rockets on (FULL SCALE)
S_A	Frontal area, = 540.9 in. ² $\theta = 0^\circ$ and 180° = 469.0 in. ² $\theta = 90^\circ$ (FULL SCALE)
T_j	Thrust of control jets (TWO JETS), lb
t	Maximum thickness of missile, 12.6 inches (FULL SCALE)
u	Flow velocity vector along x_B axis

v	Flow velocity vector along y_p axis
V	Total flow velocity vector
W	Weight of missile, lb
$x_{C.P.}$	Distance on x-axis from center of pressure to center of gravity
Δx	Distance on x-axis between any arbitrary center of gravity and the mid chord center of gravity = $30 - x_{C.G.}$ inches
$y_{C.P.}$	Distance on y-axis from center of pressure to center of gravity
$x_b y_b z_b$	Rectangular coordinates of the body axis system
$x_s y_s z_s$	Rectangular coordinates of the stability axis system
α	Angle of attack, deg
β	Angle of sideslip, deg
ϕ	Angle of roll, deg
$\Delta\phi$	Incremental change in angle of roll, deg
δ	Thickness ratio $\frac{t}{c}$; for FTV, $\frac{t}{c}$ maximum = 0.21
Λ	Angle of sweepback, deg
γ	Ratio of specific heats, 1.4
η_α	Normal "G"'s per degree angle of attack
ρ	Density, slugs/ft ³
μ	Viscosity, lb/ft ² /sec

SUPSCRIPTS

b	Body axis system
s	Stability axis system

SECRET

Section 1.0 INTRODUCTION

1.1 HISTORY

The lenticular configuration concept originated with the Technical Planning Group, formerly of the Directorate of Development of the Air Proving Ground Center, now of Detachment 4 of Wright Air Development Division, Target and Armament Development Directorate, Eglin Air Force Base, Florida. This group conducted a preliminary in-house study on the feasibility of lenticular rockets. Parameters for a bi-convex cross-section, circular planform configuration were chosen and feasibility calculations were made. Data obtained from these theoretical analyses, augmented by wind tunnel data obtained in Tunnel E-1 of the Gas Dynamics Facility, Arnold Engineering Development Center, indicated a possibility for advanced missile applications for both offensive and defensive roles. The results of this study indicated that a circular planform configuration can offer an efficient aerodynamic configuration of very high maneuver capability.

As a result of this effort, a request for a proposal was issued by the Directorate of Procurement of the Air Proving Ground Center. This request concerned a study program whose purpose was the evaluation of the technical feasibility of the lenticular configuration as a potentially significant advance in airborne weaponry. Particular emphasis was placed on the determination of those characteristics of the circular planform pertaining to flight characteristics, stability, control and maneuverability. A further objective of the study was to establish the design feasibility of the configuration as a potential airborne weapon.

A contract (AF 08(635)-542) was awarded to Convair-Pomona in June, 1959 whose purpose was the evaluation of the configuration aerodynamically, and the establishment of the design feasibility for airborne weapon applications. As a result of the Phase I study, an improved cross section shape was determined for use with a circular planform. The improved configuration, designated Model III, has the maximum thickness located at the extreme aft end. The major aerodynamic advantage exhibited by Model III over the basic symmetrical lenticular configuration is a rearward shift of center of pressure. This rearward shift of center of pressure greatly simplifies the problem of controlling the missile in flight. Another advantage shown in Phase I was the supersonic drag reduction associated with the blunt trailing edge of Model III. The decreased

*Manuscript Released
29 May 1961*

SECRET

SECRET

drag results in a higher lift-drag ratio, and in turn, an increased range and maximum speed. In short, the Phase I configuration is feasible as a design for airborne weapons.

Analyses, experimentation, and laboratory simulations are useful in the determination of concepts, and are necessary in the establishment of a design that can be fabricated into a vehicle. However, they cannot furnish the final evidence of the practicality of a concept. This can only be firmly established by a flight test program. As a result, recommendations made during Phase I included a flight test program for the practical demonstration of (1) stabilized, controllable flight, and (2) omnidirectional launch capability. It was recommended that off-the-shelf components be utilized in the flight test program in order to minimize the time and funds required to prove the concept.

1.2 OBJECTIVE

At the conclusion of the Phase I study, Convair-Pomona was awarded a Phase II contract, AF 08(63)-1168, for the necessary studies to permit future design and successful flight of vehicles launched from a high-speed rocket-sled. The studies to be conducted were both theoretical and experimental in nature. Eighty hours of wind tunnel time were provided for use in determining the PYE WACKET aerodynamic characteristics between Mach numbers of 0.6 and 5.0. This volume presents the results of the aerodynamic studies conducted during the Phase II PYE WACKET program.

Section 2.0 RESULTS AND DISCUSSION

2.1 CONFIGURATION GEOMETRY

Two feasible-design configurations were described in the PYE WACKET Phase I Feasibility Study, Reference 5.1. These configurations have circular planforms with a blunt trailing edge and circular arc cross-section. Both configurations are 60 inches in diameter with one having a thickness-to-chord ratio of 0.21 and the other 0.14. Figure 2.1.1 is a sketch of the 21 percent thick configuration.

The Feasibility Test Vehicle (FTV) configuration selection, developed in Volume III of this report, is shown in Figure 2.1.2. The overall dimensions are identical to the prototype configuration with a thickness-to-chord ratio of 0.21. However, the base geometry was modified to accommodate the three rocket motors. This modification consisted primarily of a lateral slot across the aft end of the vehicle at the exit plane of the rocket motor nozzles. The two wind tunnel models were fabricated to the same configuration. As the studies progressed and wind tunnel results became available, it was evident that the slot produced certain undesirable effects. The wind tunnel data are reported for the configuration tested; however, later studies showed that the basic vehicle arrangement could be retained even though the slot was deleted. Test vehicle fabrication in a follow-on phase will be based on the configuration most likely to produce successful flights (i.e. no lateral slot).

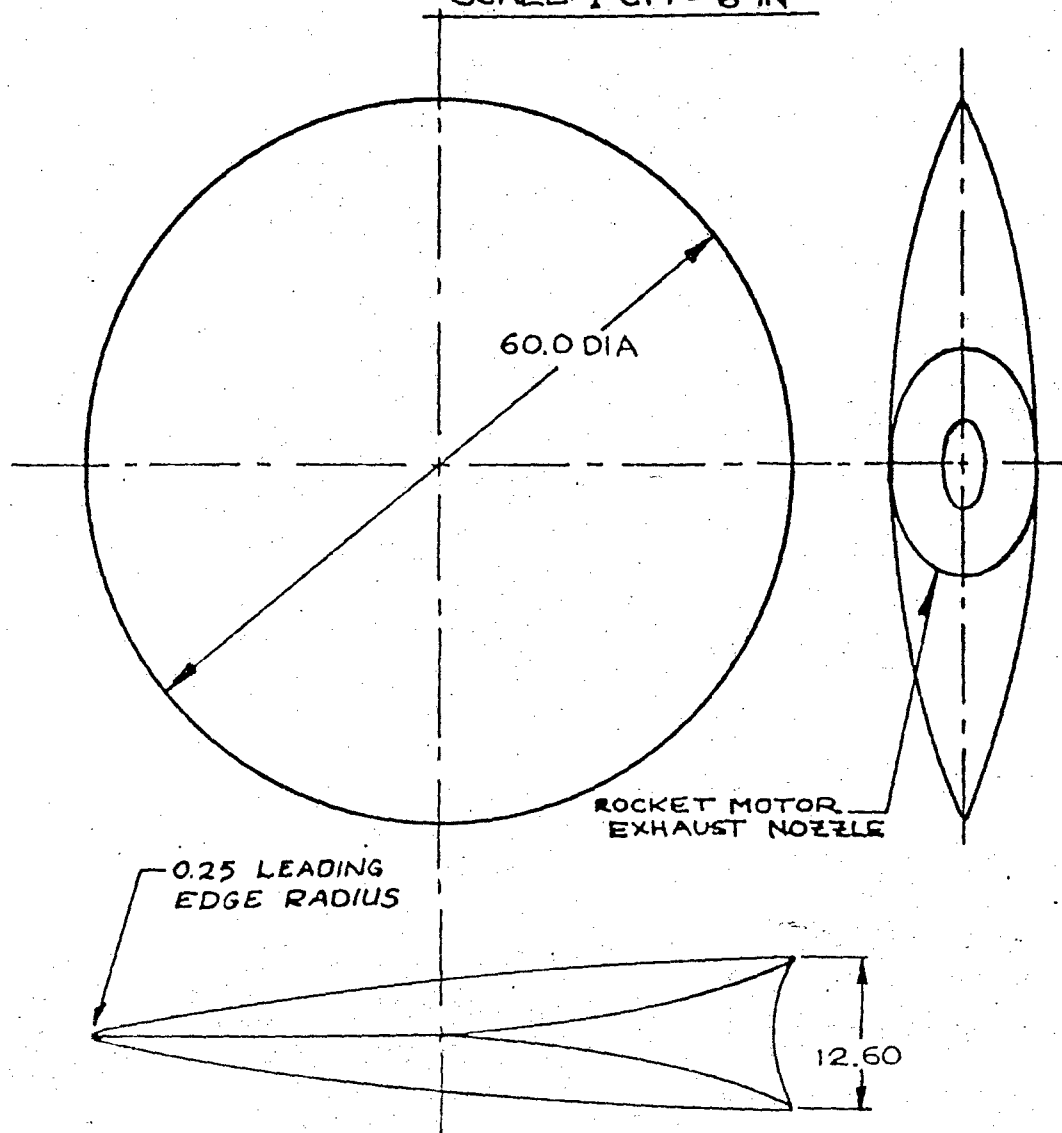
A detailed drawing and a weight and balance statement are presented in Volume III of this report.

2.2 BASIC STUDIES

2.2.1 THEORETICAL AERODYNAMICS From the work of Linnell, Reference 5.2, the characteristics of hypersonic, two-dimensional airfoils were established. These showed the lift and drag characteristics to be a function of airfoil thickness, a hypersonic similarity parameter, and the specific heat ratio. This work was based on shock expansion theory combined with hypersonic similarity relations. Dorrance, Reference 5.3, in his work extended the field by showing that the expressions for expansion and compression are almost identical when the hypersonic similarity parameter, $M\delta$, is less than one. The main contribution was the conclusion that compression, from the Rankine-Hugoniot relation, and expansion, from the Prandtl-Meyer

SECRET

FIGURE 2.1.1
PYE WACKET
PHASE I CONFIGURATION
THICKNESS-TO-CHORD RATIO=0.21
DIMENSIONS IN INCHES
SCALE: 1 CM = 6 IN



2.2

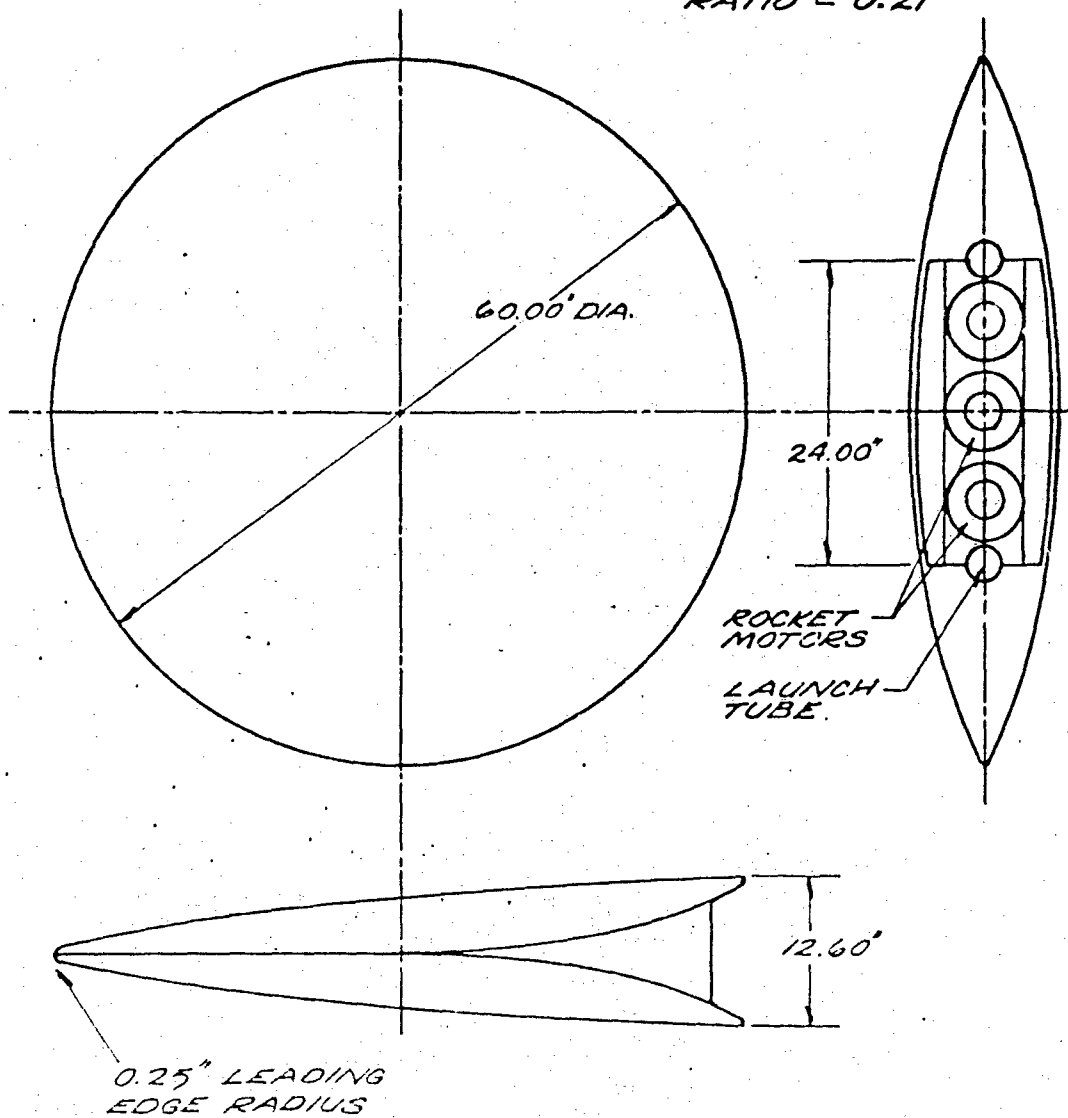
SECRET

FIGURE 2.1.2

PYE WACKET FTV

FEASIBILITY TEST VEHICLE

NOTE: THICKNESS-TO-CHORD
RATIO = 0.21



relation, provided the same three first terms of a power series in M_∞ . This immediately allowed a closed form solution to be obtained for lift, drag and moment coefficients. These solutions apply over hypersonic Mach numbers between 3 and 12. The method was applied to 12 airfoil sections ranging from a flat plate to a combination of parabolic arcs and flat surfaces. The results are two-dimensional and apply only for a value of M_∞ between 0 and 1. The angle of attack, α , is limited to a maximum value based on the hypersonic similarity parameter, M_∞^2 . This is expressed in terms of the free stream Mach number and the local slope of the airfoil surface.

$$\left| \alpha_{MAX} \right| \leq \frac{1}{M_\infty} - \left| \left(\frac{dy}{dx} \right)_{MAX} \right| \quad (2.2.1)$$

The convenience of the closed form made the use of this theoretical method most attractive in this study. Further, the range of applicable Mach numbers and angles of attack is suitable for this application.

In order to make more accurate theoretical estimates, the two-dimensional characteristics predicted by Dorrance were modified to account for planform. This process is essentially a modification of the two dimensional coefficients to account for the average sweep over a section of the circular planform. From Reference 5.4, for small angles of attack, the following relations are derived for swept and unswept wings.

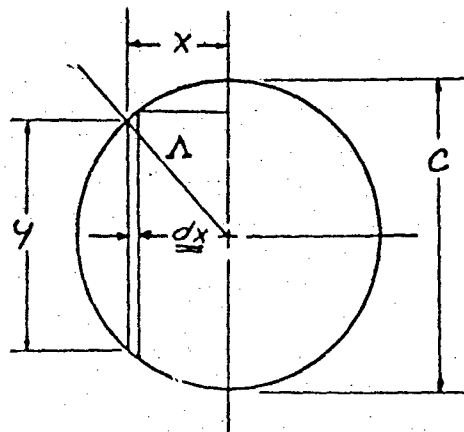
$$C_L \cong C_{L\Lambda=0} \cos^2 \Lambda \quad (2.2.2)$$

$$C_D \cong C_{D\Lambda=0} \cos^3 \Lambda \quad (2.2.3)$$

Expressed more simply, the lift coefficient of a swept wing may be approximated by modifying the lift coefficient of the unswept wing by the cosine squared of the angle of sweep. The drag coefficient may be approximated by multiplying the pressure drag by the cosine cubed of the sweep angle. It is important that friction and base

SECRET

drag be removed from the total drag before performing this modification. In the exact relations, a variation with angle of attack is indicated. For regions in which $\cos \alpha \approx 1$, the above relations yield close agreement. From the above relations, the following corrections to Dorrance's two-dimensional coefficients were derived:



$$C_N \approx C_L$$

$$C_N = C_{N\Lambda=0} \cos^2 \Lambda$$

$$x = \frac{c}{2} \sin \Lambda \quad dx = \frac{c}{2} \cos \Lambda d\Lambda$$

$$y = c \cos \Lambda \quad dA = y dx$$

$$C_N = \frac{1}{S} \int C_{N\Lambda=0} \cos^2 \Lambda dA = \frac{c^2 C_{N\Lambda=0}}{S} \int_0^{\pi/2} \cos^4 \Lambda d\Lambda$$

$$C_N = \frac{3\pi c^2}{16S} C_{N\Lambda=0}$$

$$S = \frac{\pi c^2}{4}$$

$$C_N = 0.750 C_{N\Lambda=0} \quad (2.2.4)$$

This correction enables the values of normal force coefficient obtained from Dorrance's work to be applied to a circular planform. By similar derivation, the values for the wave drag result in the following relation:

$$C_D = \frac{8c^2}{15S} C_{D\Lambda=0} \quad (2.2.5)$$

SECRET

which, for this application, results in the following expression:

$$C_D = 0.68 C_{D\Lambda=0} \quad (2.2.6)$$

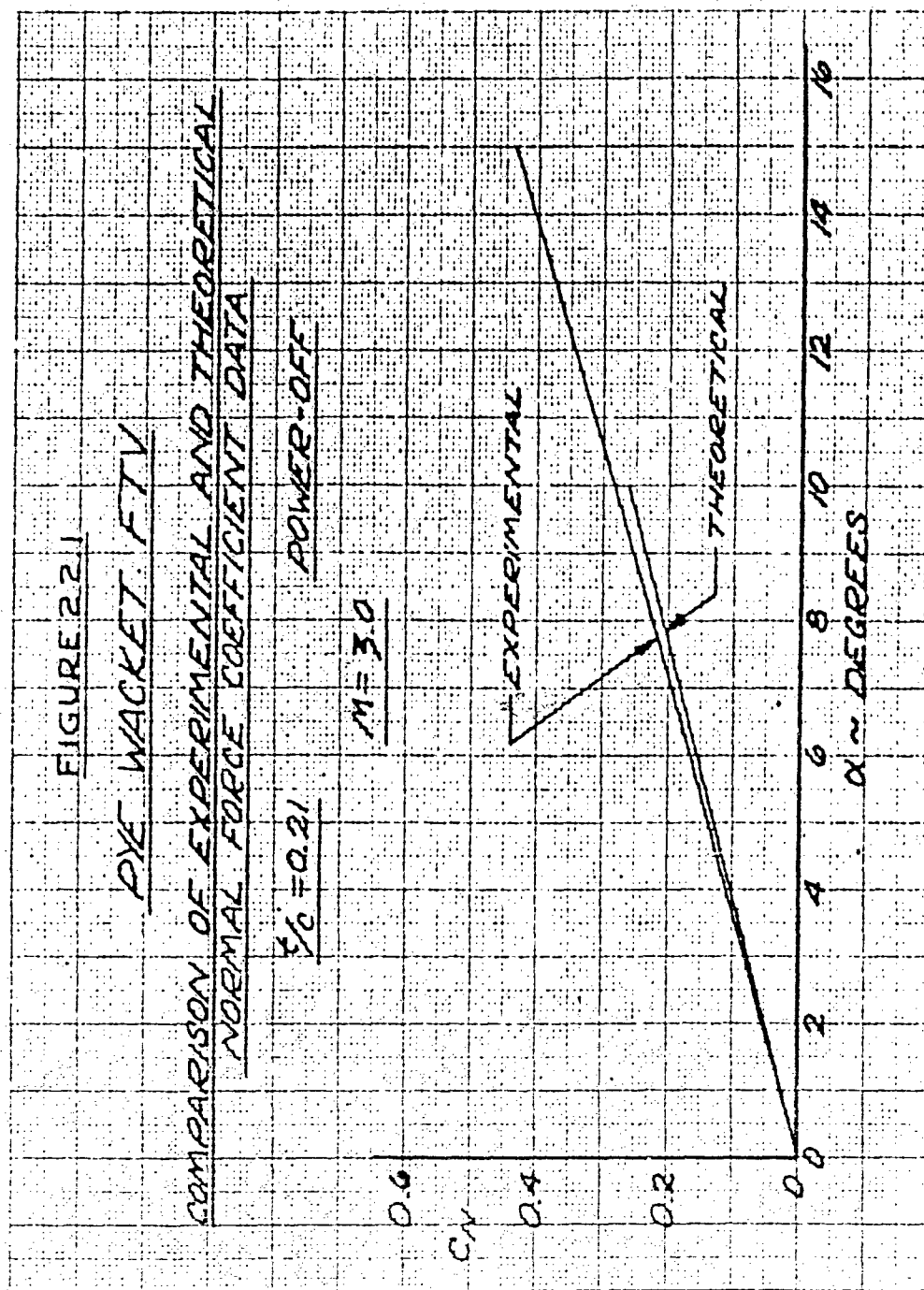
A comparison of theoretical values obtained using Dorrance's work and the above relations is shown in Figures 2.2.1 through 2.2.5. In Figures 2.2.1 to 2.2.3, a comparison is made of normal force coefficients from experimental and theoretical sources. As can be seen, the comparison is excellent. In no case is the difference greater than ten percent. This indicates that Dorrance's data combined with a planform correction does yield excellent results. Figure 2.2.4 compares the wave drag coefficients obtained theoretically and experimentally. The comparison is fair, with the theoretical results approximately 15% lower than the experimental results. It might be well to qualify the values shown in the theoretical curve. These were obtained by modifying Dorrance's wave drag coefficients for planform and adding an increment in drag for the blunted leading edge. This incremental value for leading edge drag amounted to 0.0085 at all the Mach numbers.

Figure 2.2.5 presents a comparison of center of pressure locations between experimental data and values computed using Dorrance's work. As indicated, the values obtained using Dorrance's work are reasonably correct in magnitude, but have a forward movement with increasing Mach number. As a supplement, linear theory is included. The experimental data falls in between the values indicated by linear theory and Dorrance's work.

The results presented in Figures 2.2.1 through 2.2.5 show that theoretical methods can predict reasonable values for normal force, wave drag, and center of pressure. The values for center of pressure show the greatest inaccuracy.

SECRET

SECRET



SECRET

SECRET

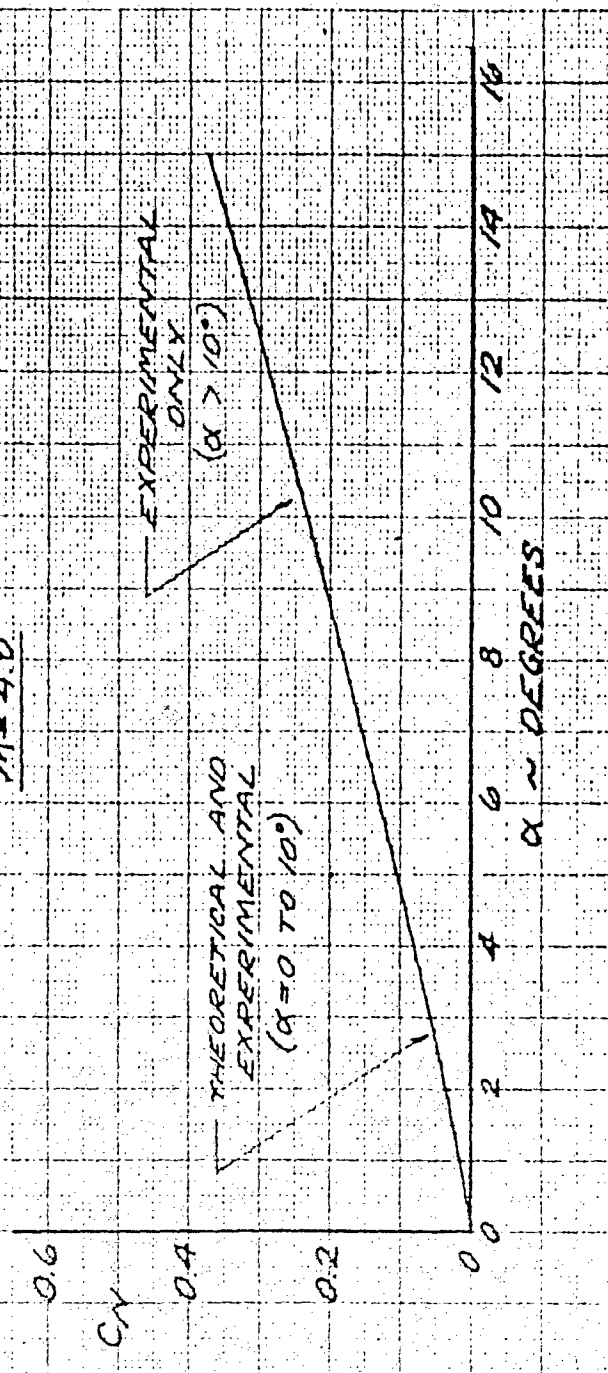
FIGURE 2.2.2

PYE WACKET FTV

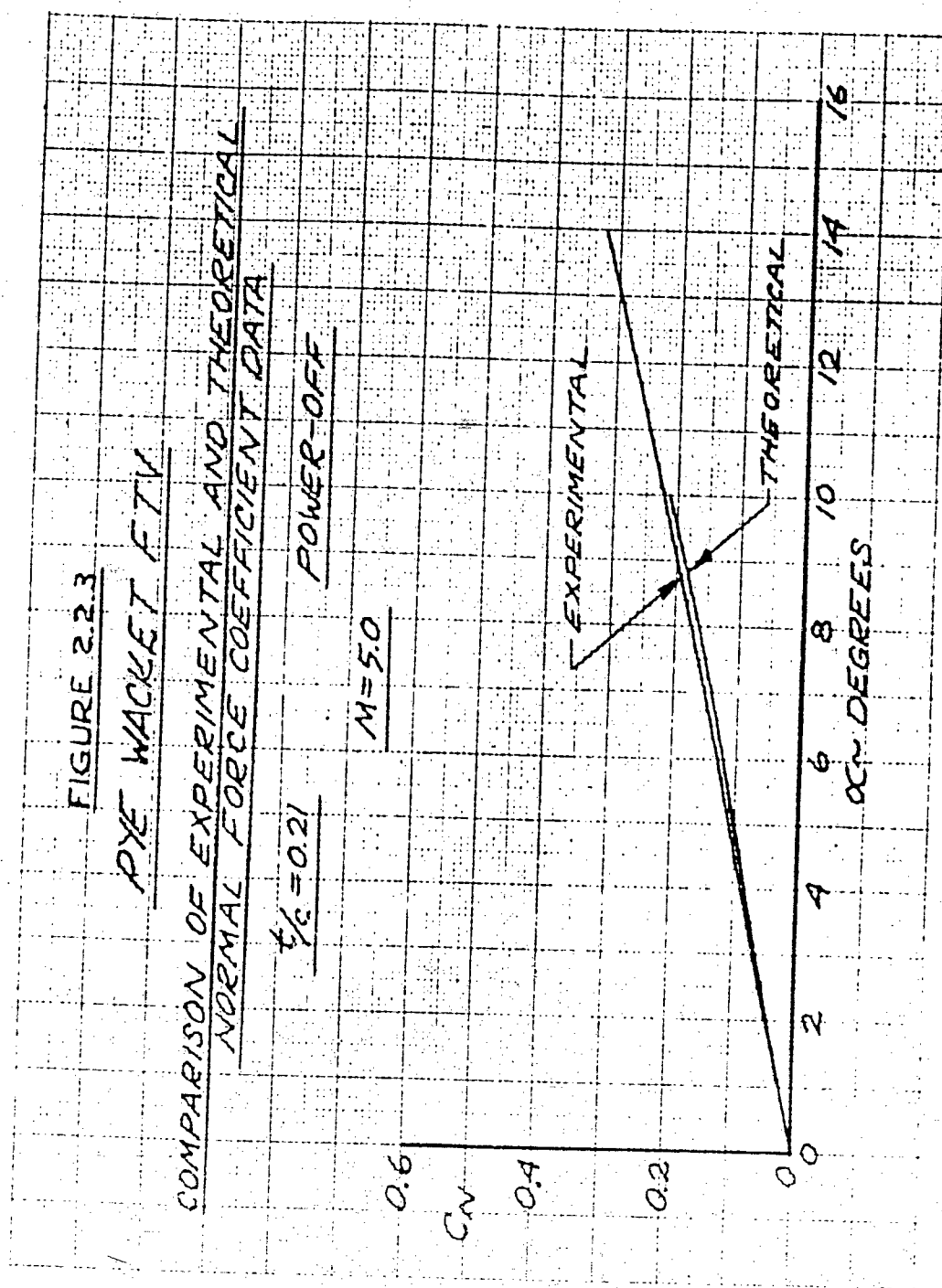
COMPARISON OF EXPERIMENTAL AND THEORETICAL
NORMAL FORCE COEFFICIENT DATA

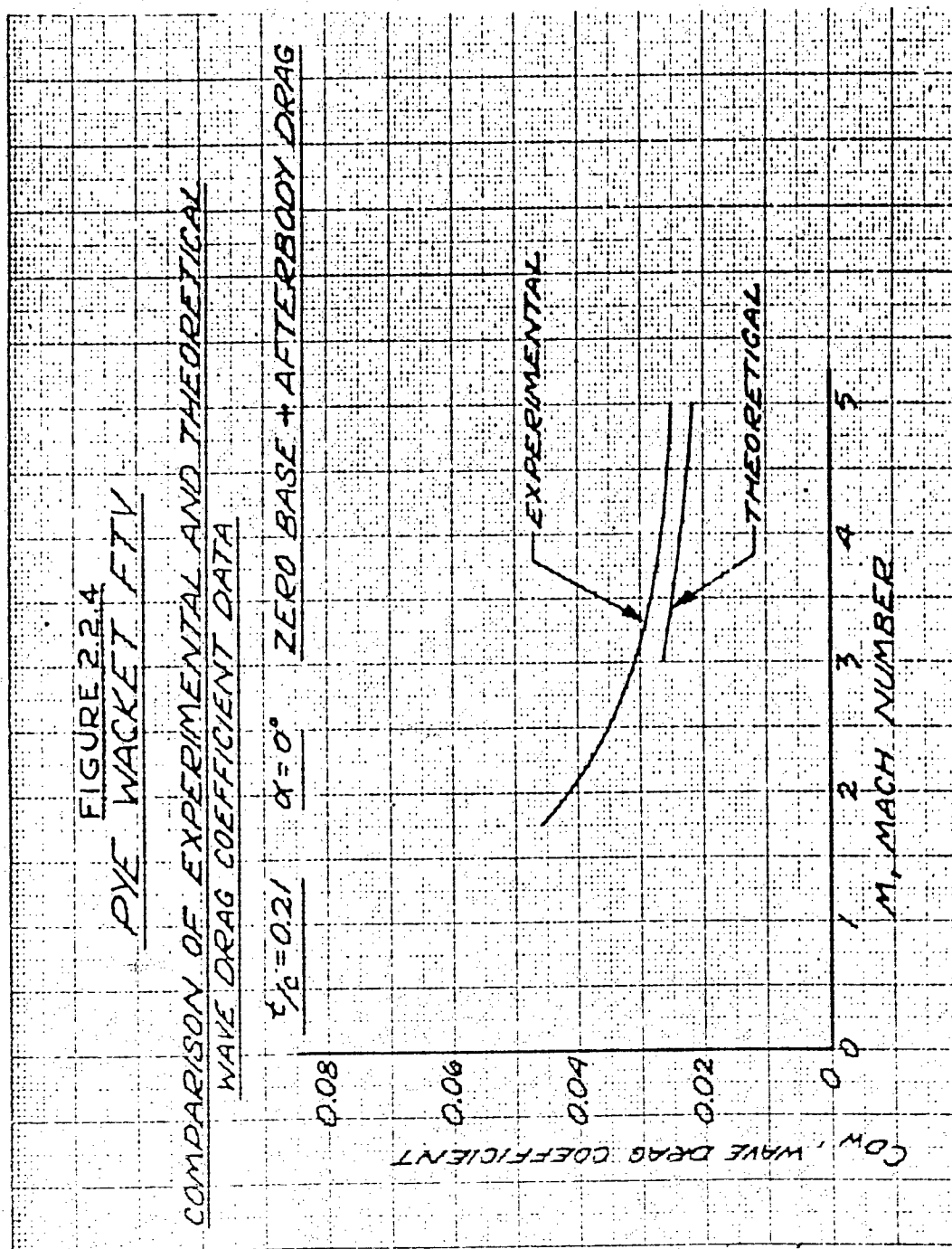
$\frac{1}{2}\rho = 0.21$ POWER-OFF

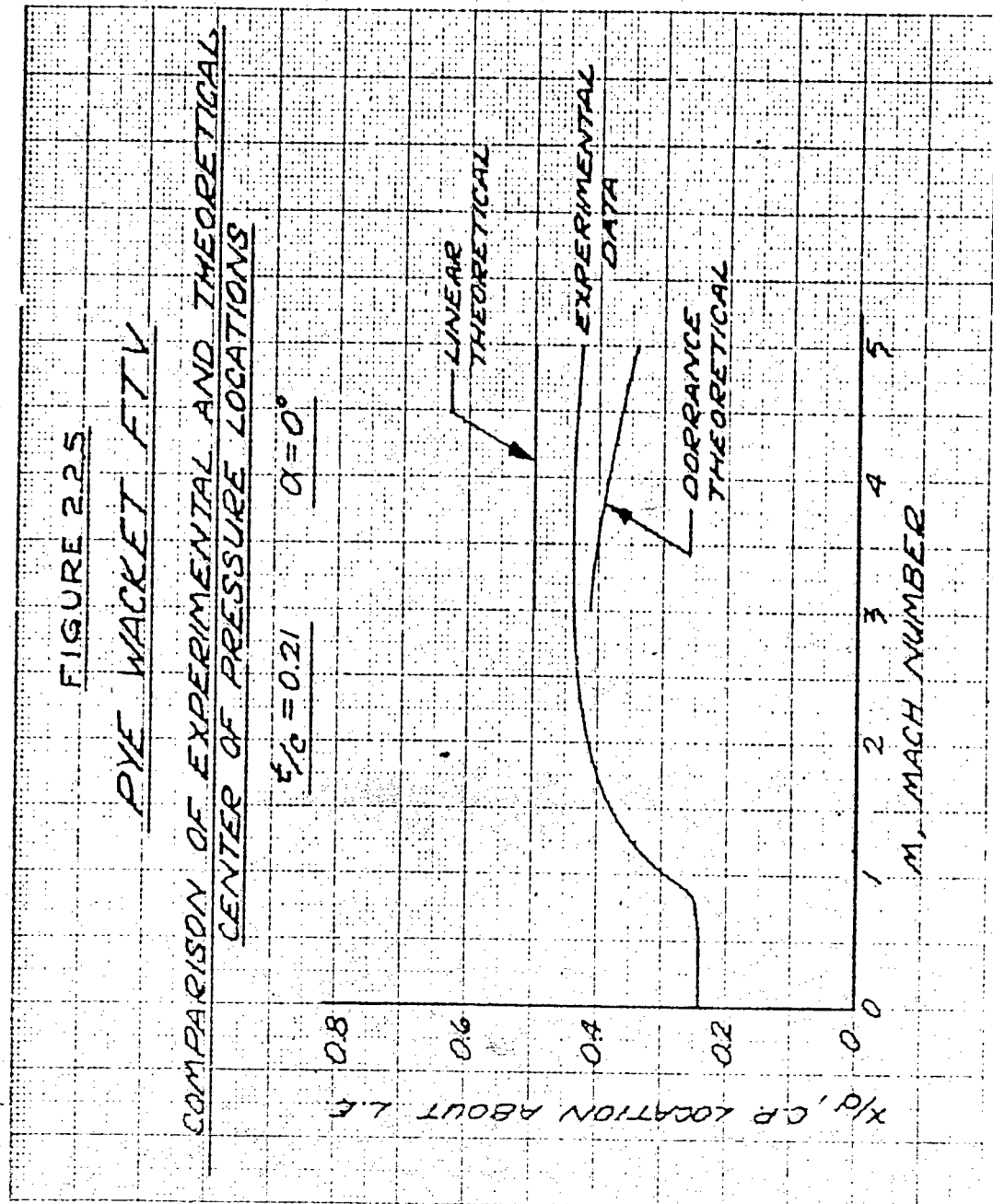
$M = 4.0$



SECRET

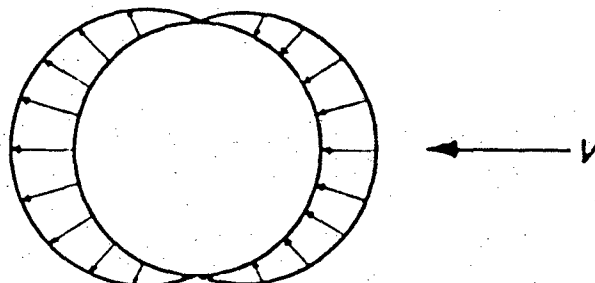






2.2.2 YAW MOMENT ORIGIN One of the major advantages of the PYE WACKET concept is the omnidirectional launch capability. Omnidirectional launch capability is the ability to launch in any direction from the parent aircraft. Launch procedures of this type require that the missile heading remain constant throughout the launch phase. To satisfy the above requirements, reaction jets are used to overcome the aerodynamic yawing moment. In order to reduce hardware and propellant weights, the reaction jets, and hence, the aerodynamic yawing moment, must be as small as possible. In order to reduce the aerodynamic yawing moment, the nature of the airflow producing the yawing moment must be understood.

The blunt base of the proposed PYE WACKET configuration initially appears to destroy the omnidirectional launch capability for which it was designed. However, this is not correct because the high local forces on the base do not produce a yawing moment about the planform center. Only when the center of gravity is moved from the geometric center of the planform does the base contribute to the yawing moment (neglecting the small effects due to base skin friction and reaction jets). This statement must be qualified by defining the base to be solid, and not with a lateral slot as considered for the FTV configuration. The yawing moment about the midchord is due to the pressure acting on the surface of the configuration, and not by any pressure acting around the periphery. Consider a circular planform configuration with a blunted edge such as the PYE WACKET prototype.



PERIPHERAL PRESSURE DISTRIBUTION

From basic physics, it is known that surface pressures act normal to the surface. Since the planform is circular, the normals pass through the geometric center of the planform. Therefore, all pressure forces on the periphery act through the center of the planform and do not produce a yawing moment.

The PYE WACKET yawing moment is primarily produced by surface pressures. Since the upper and lower surfaces are curved, the

yawing moment about the midchord is produced by the summation of lateral components of local forces normal to the surface. This yawing moment produced by surface pressures is called the basic yawing moment. The direction of the moment is stabilizing, i.e., it tends to align the missile with the velocity vector. When the center of gravity is moved forward of the midchord, the pressure forces on the base contribute a yawing moment which increases the stabilizing effect of the basic yawing moment. Conversely, when the center of gravity is moved aft of the midchord, the stabilizing effect is decreased.

Thus, only when the center of gravity is not located at the geometric center of the planform does the blunt base contribute to the yawing moment.

2.3 EXPERIMENTAL PROGRAM

2.3.1 MODELS AND TEST CONDITIONS Two geometrically similar PYE WACKET wind tunnel models were used in the experimental phase of this program, one instrumented for body pressure measurements and the other for force and moment measurements. Figure 2.3.1 is a sketch of the external model geometry showing the basic dimensions. Since test data were desired for yaw angles from 0 to 180 degrees, the models were designed to permit mounting on the wind tunnel sting at the three peripheral positions corresponding to yaw angles of 0, 90, and 180 degrees. The sting holes were filled with flush plugs, discernible in Figure 2.3.1, when not in use. Figures 2.3.2 a, b, and c are photographs of the model mounted in the wind tunnel at yaw angles of 0, 90, and 180 degrees respectively.

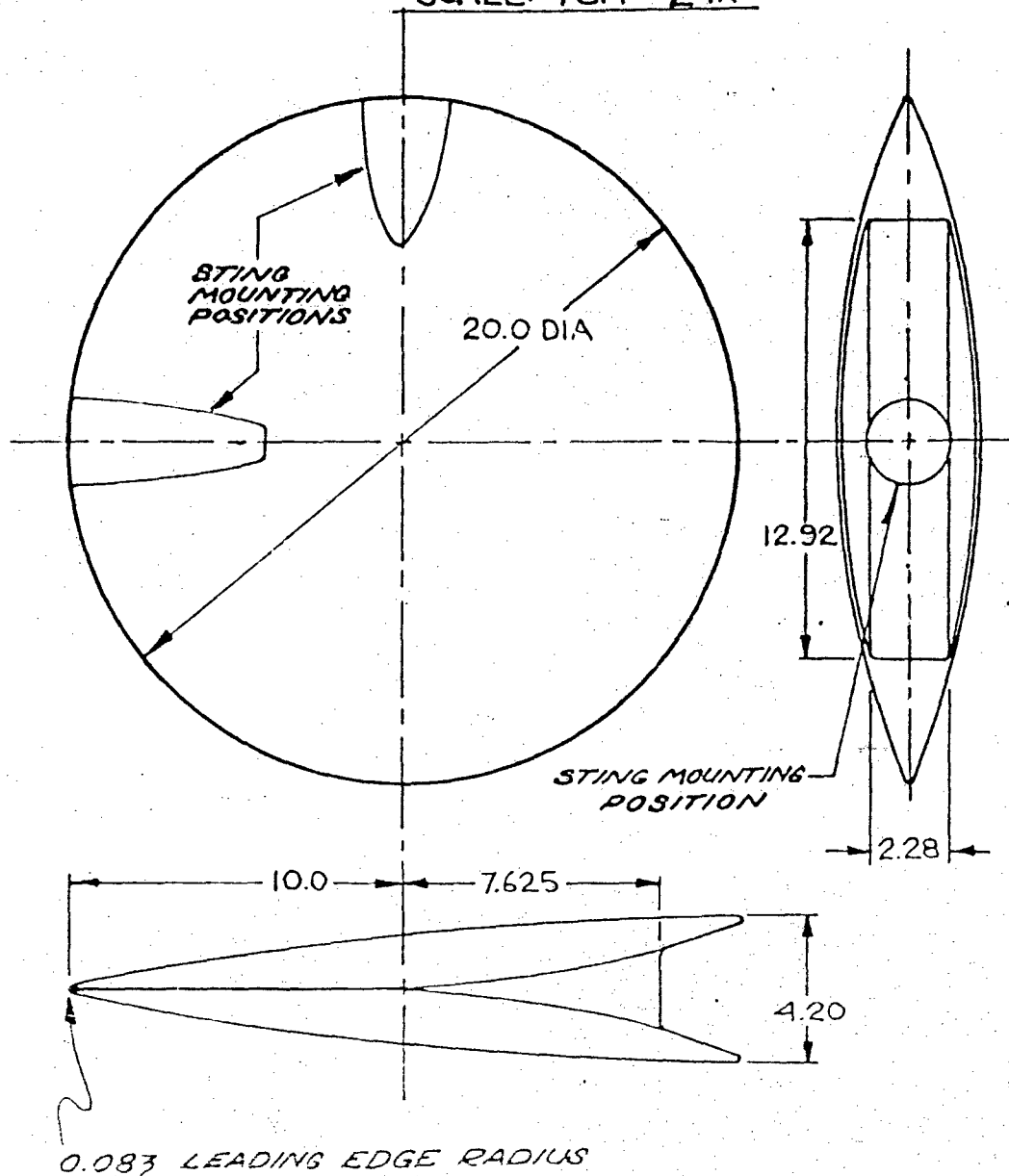
Figures 2.3.3 a, b and c are photographs of the force model. This model was designed to use a 1.6-inch diameter internal strain gage balance.

Figures 2.3.4 a, b, c and d are photographs of the pressure model showing external geometry and internal instrumentation. This model was instrumented for measuring 86 surface pressures, 6 base pressures, and 5 leading edge pressures. The location and numbering system of these pressure taps is shown in Figure 2.3.5. In addition, the pressure model has provisions for simulating the pitch/roll reaction control jets utilizing cold air with chamber pressures ranging from 400 to 1000 psia. Yaw control jets were not included in the test due to the complexity of the model instrumentation.

SECRET

FIGURE 2.3.1
PYE WACKET FTV
WIND TUNNEL MODEL
THICKNESS-TO-CHORD RATIO = 0.21
DIMENSIONS IN INCHES

SCALE: 1 CM = 2 IN



SECRET

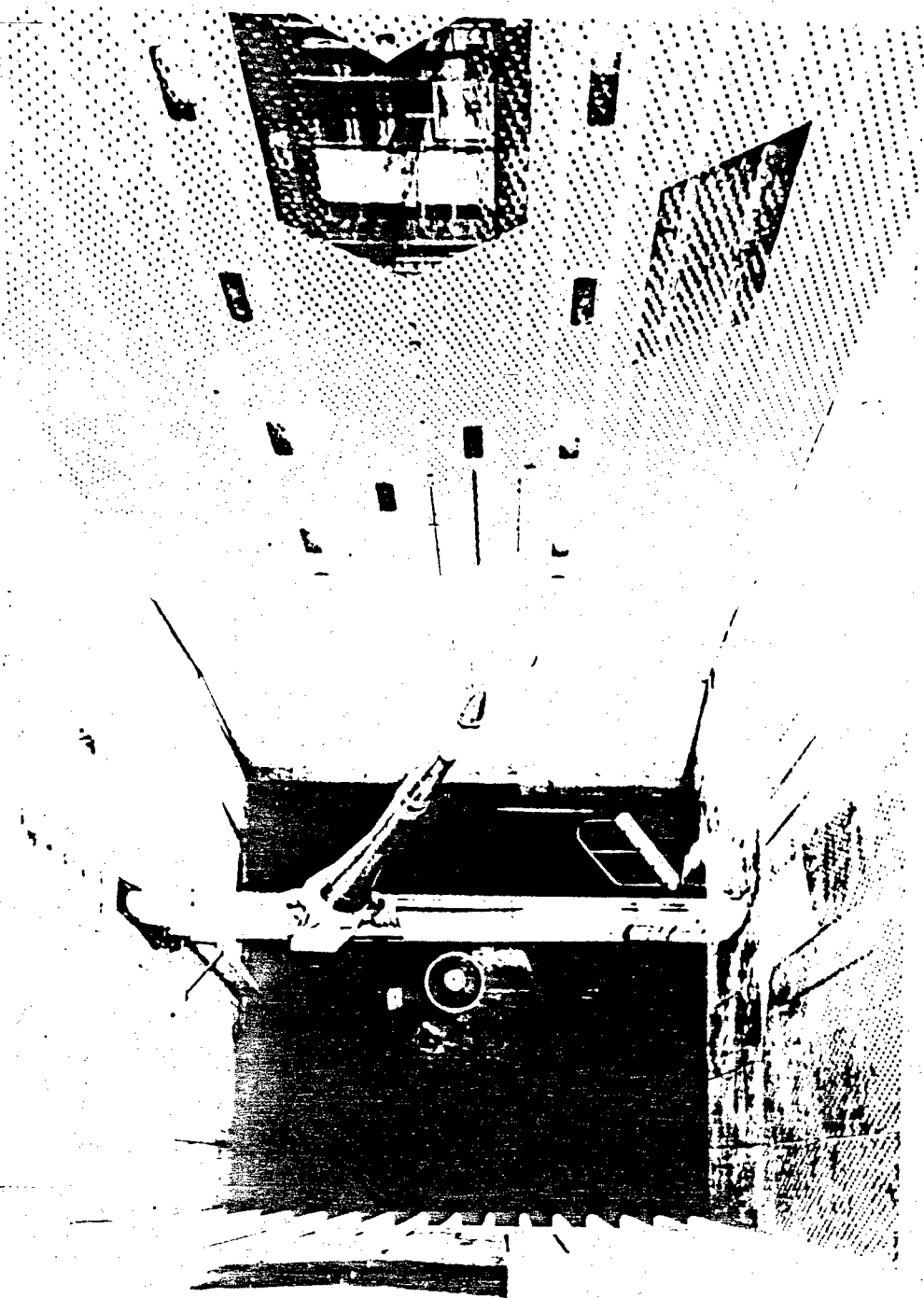


Figure 2.3.2 a PWT Installation, Forward Launch Condition

SECRET

SECRET

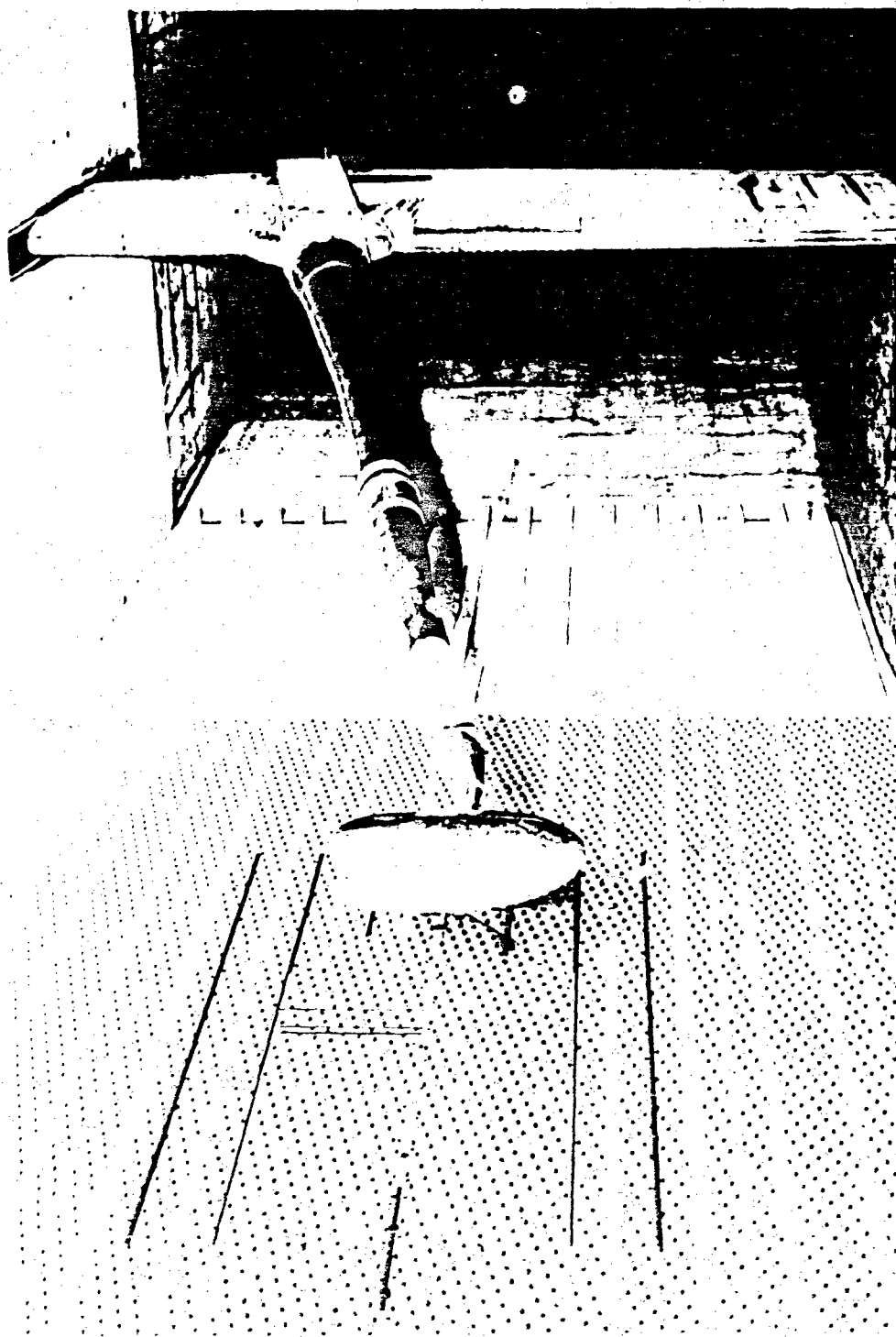


Figure 2.3.2 b PWT Installation, Cross-Wind Launch Condition

SECRET

SECRET

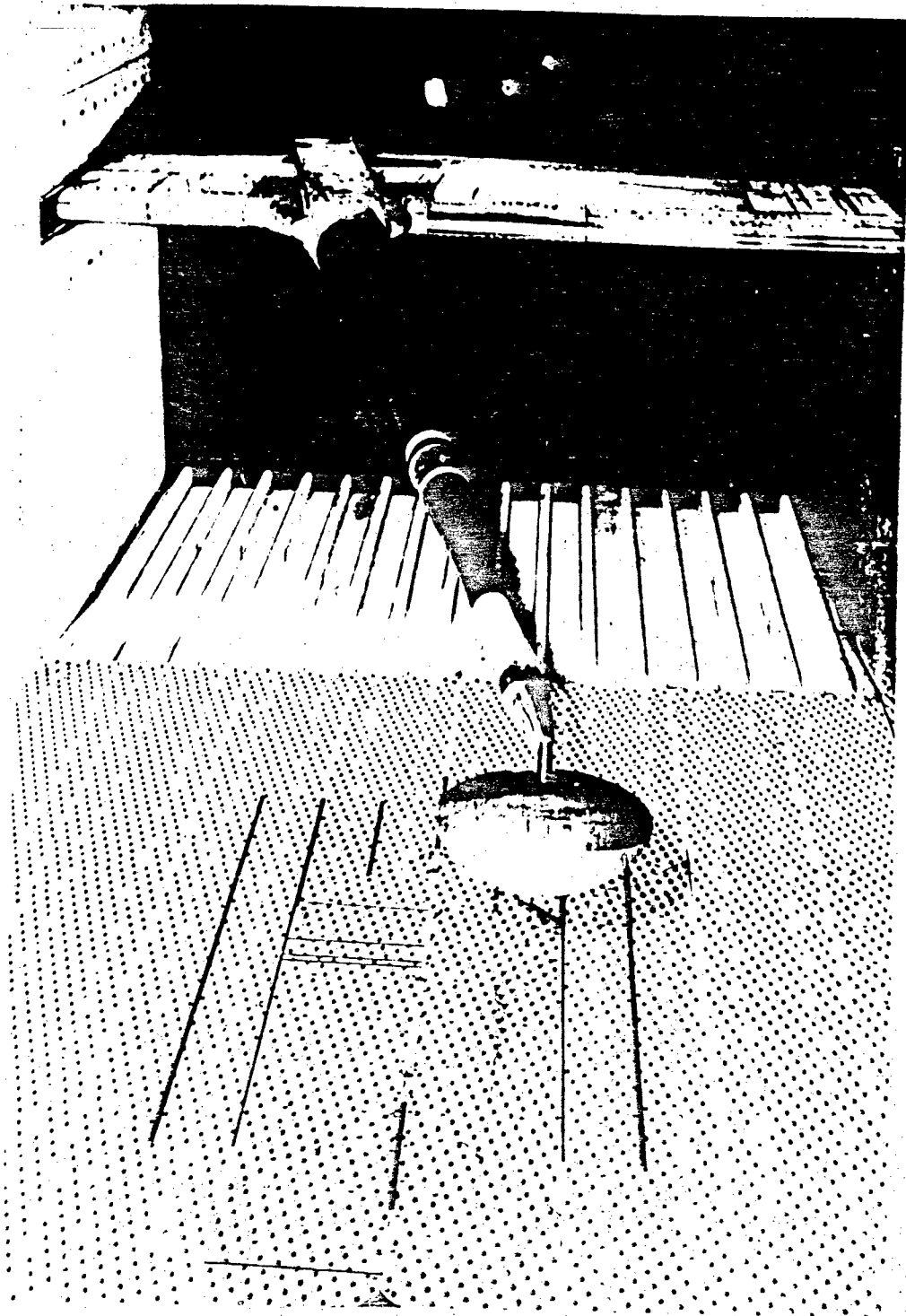


Figure 2.3.2 c PWT Installation, Aft Launch Condition

SECRET

SECRET

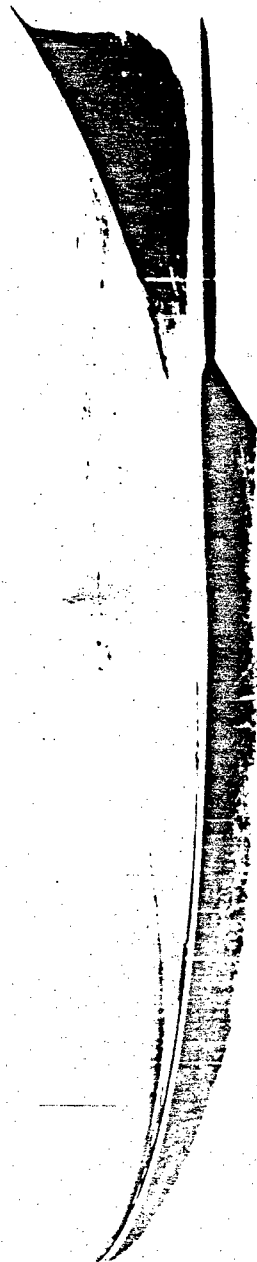


Figure 2.3.3 a Wind Tunnel Force Model

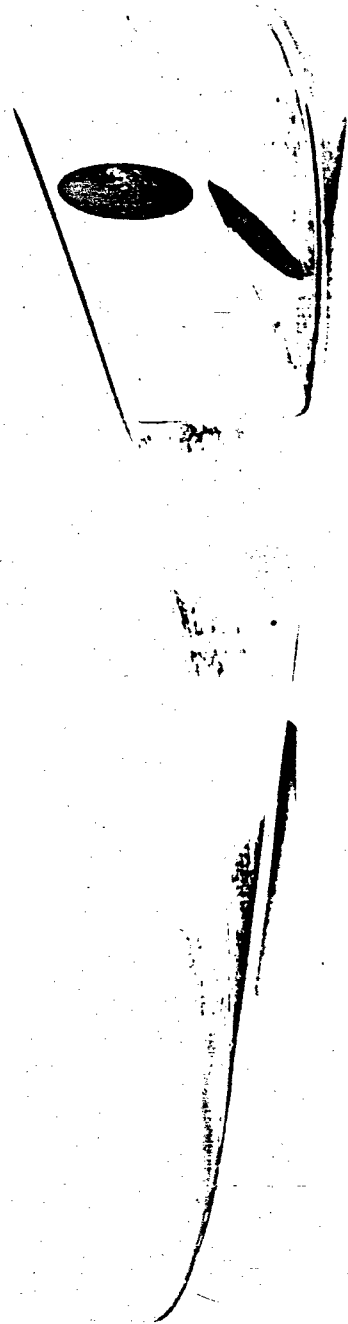


Figure 2.3.3 b Wind Tunnel Force Model

SECRET

SECRET

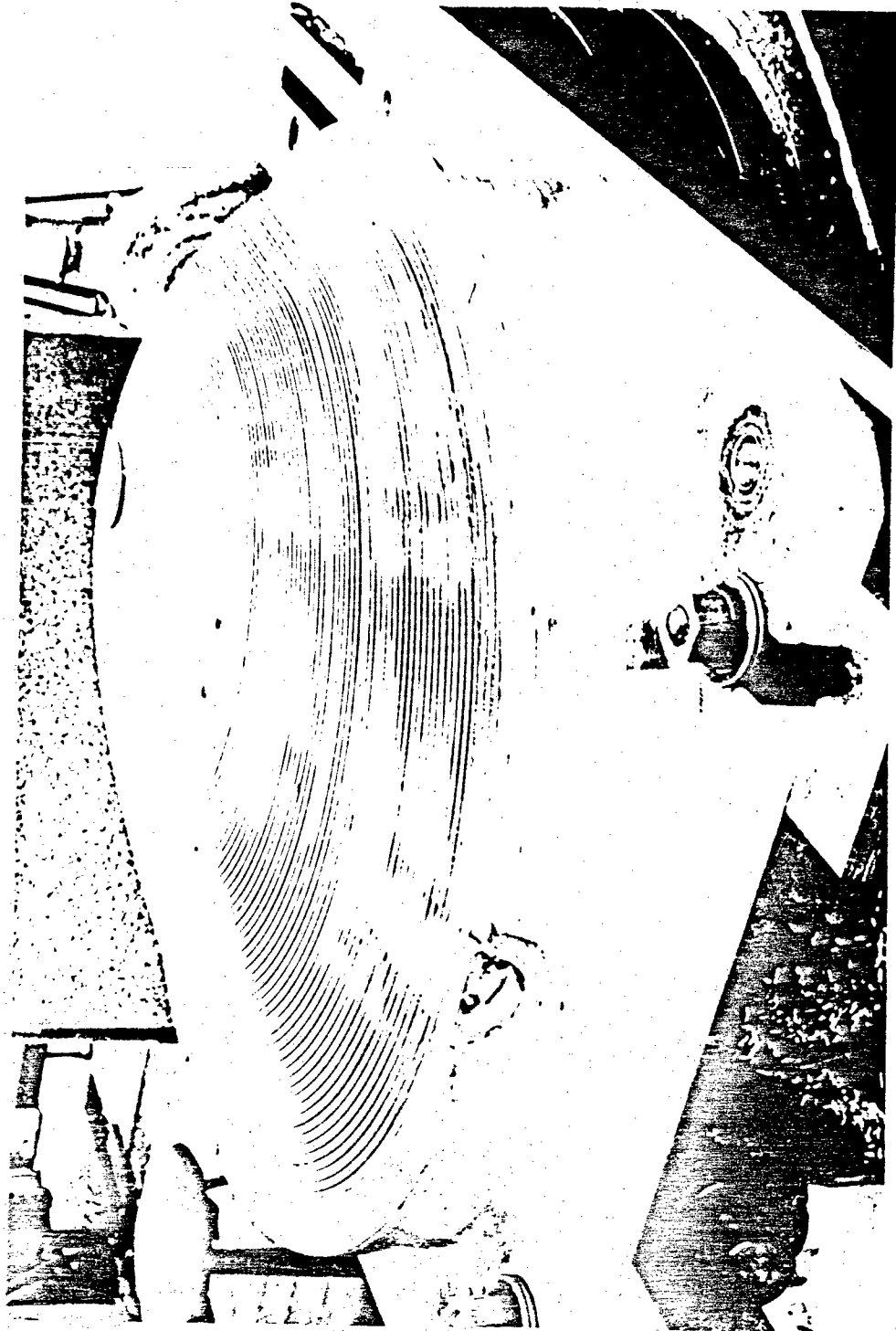


Figure 2.3.3c. Wind Tunnel Force Model,
During Fabrication.

SECRET

SECRET

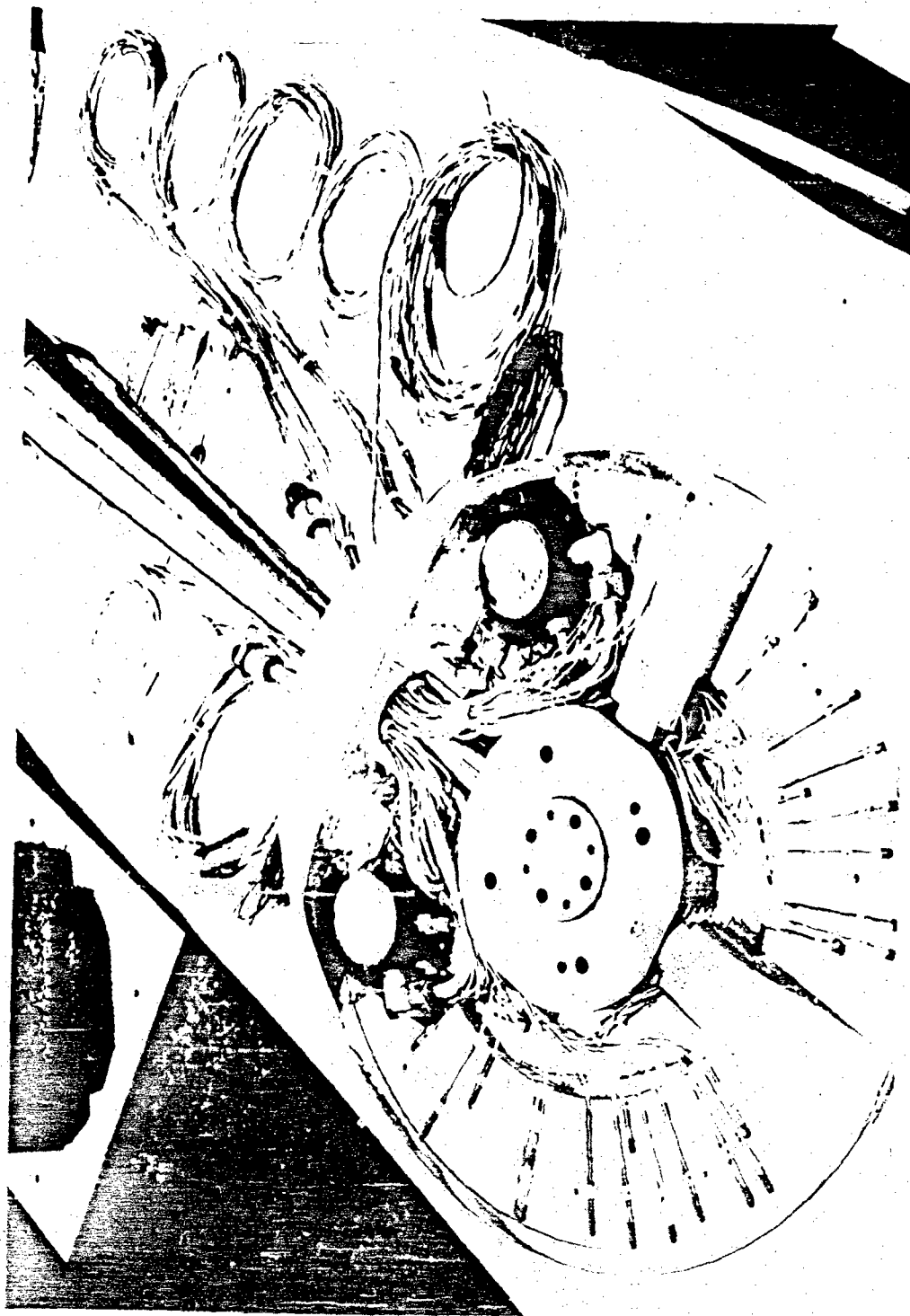


Figure 2.3.4 a Wind Tunnel Pressure Model with Reaction Control Jets

SECRET

SECRET

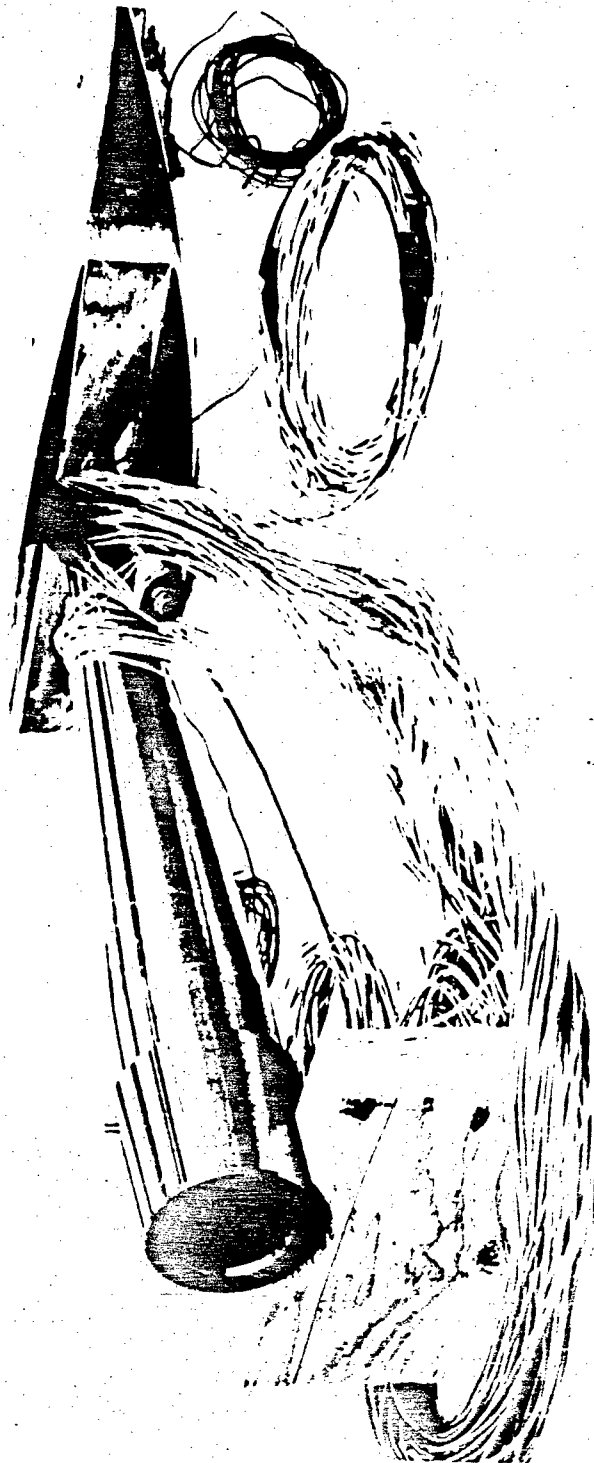


Figure 2.3.4 b Wind Tunnel Pressure Model and Sting

2.21

SECRET

SECRET



Figure 2.3.4 c Wind Tunnel Pressure Model and Sting

SECRET

SECRET

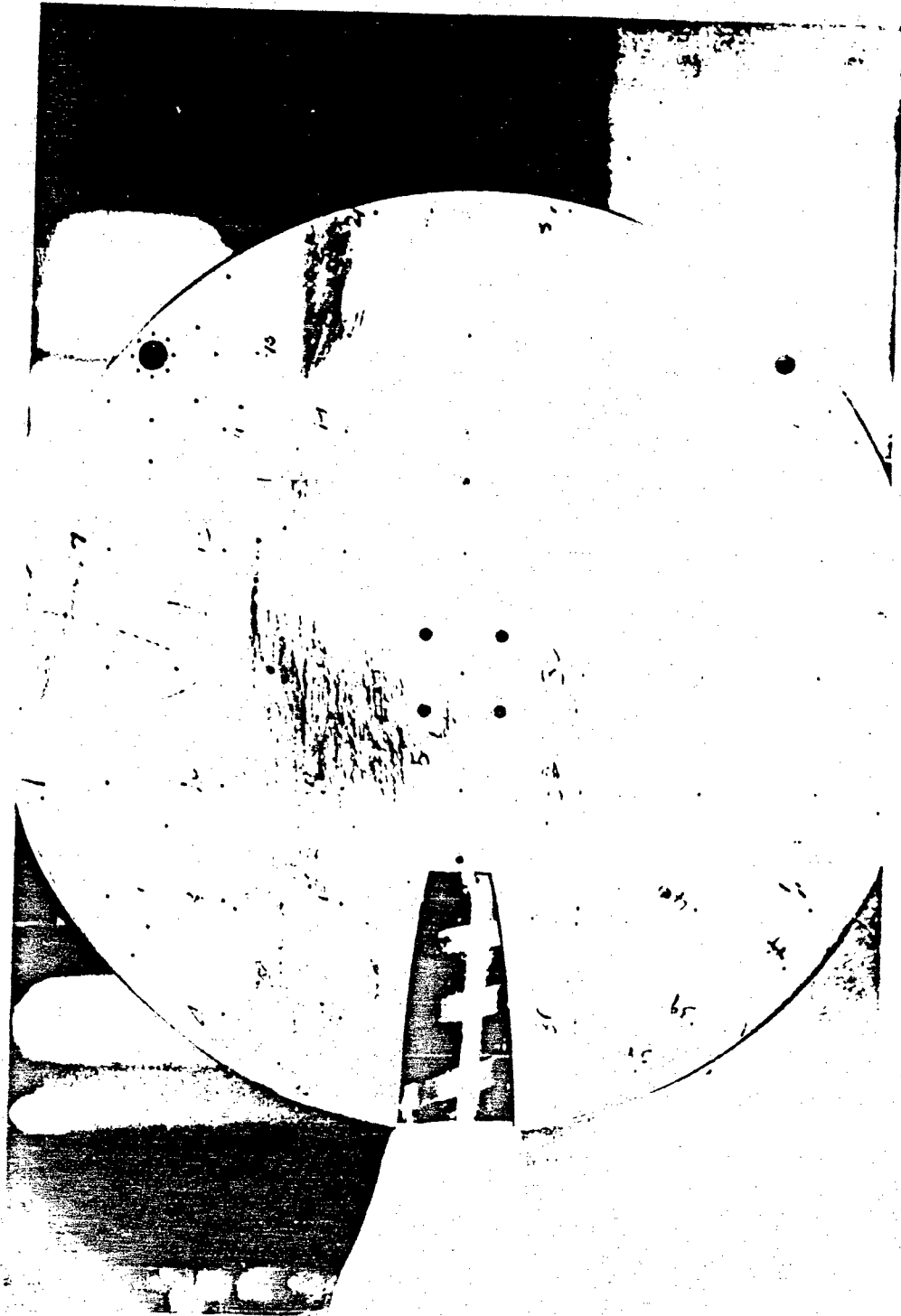


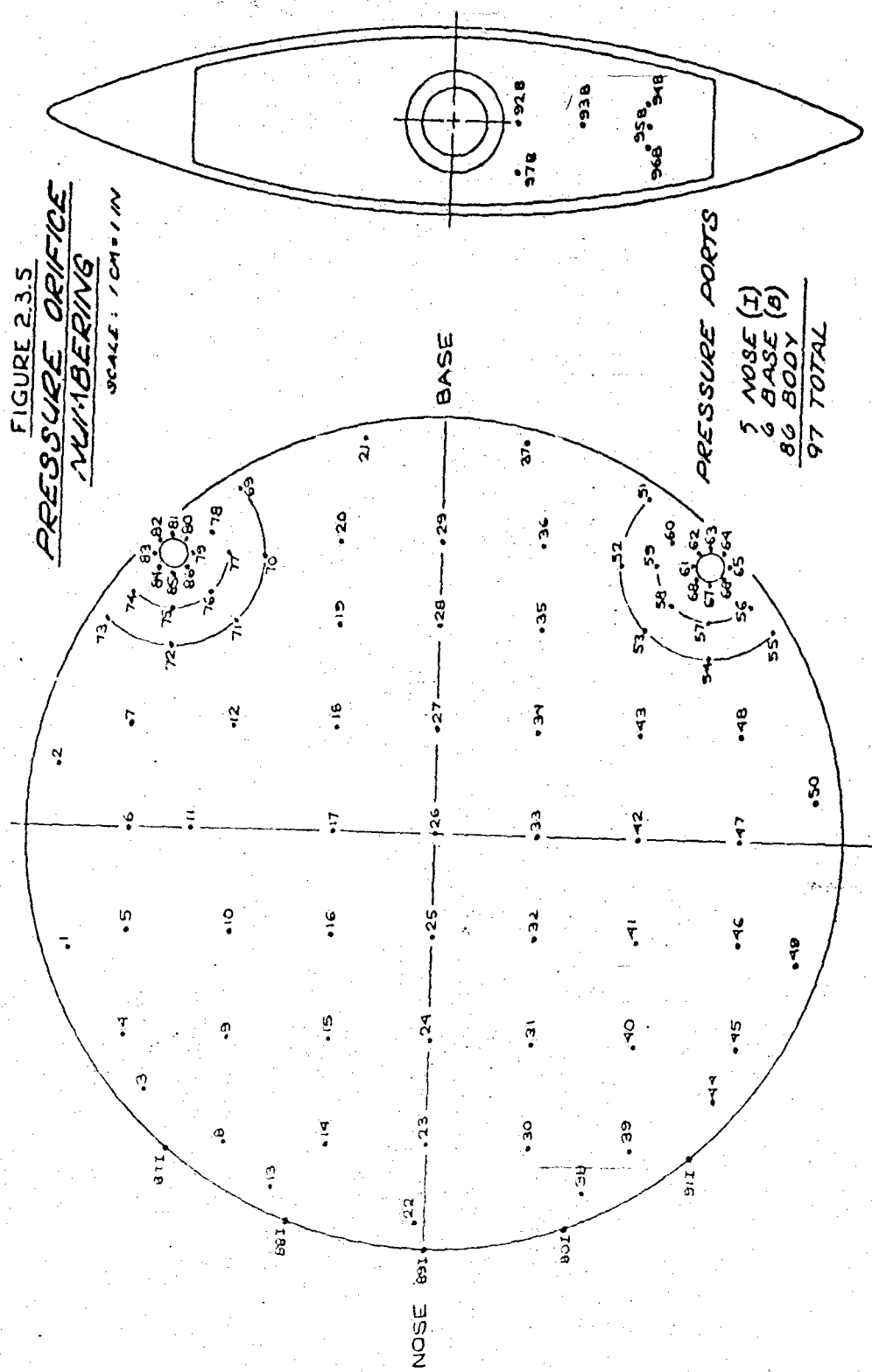
Figure 2.3.4d. Wind Tunnel Pressure Model
Plan View.

2.23

SECRET

SECRET

FIGURE 2.3.5
PRESSURE ORIFICE
NUMBERING
SCALE: 1 CM = 1 IN



SECRET

Tests were conducted in two wind tunnels at the Arnold Engineering Development Center (AEDC), Tullahoma, Tennessee. References 5.5 and 5.6 present the pre-test planning for the test program. Mach numbers from 0.6 to 1.6 were run in the 16-foot test section at the Propulsion Wind Tunnel (PWT). Nominal angles of attack of 0, 3, 6, and 9 degrees were run at angles of yaw including 0 to 20, 70 to 110, and 160 to 180 degrees. Both force and pressure measurements were taken for these conditions. Mach numbers from 1.5 to 5 were run in the Type A wind tunnel of the Von Karman Gas Dynamics Facility. Six-component force data, as well as pressure data, were recorded for angles of attack ranging from 0 to 15 degrees at yaw angles between 0 and 180 degrees.

The Phase II wind tunnel test objective was the determination of: (1) the aerodynamic forces and moments for the free stream conditions and model attitudes expected in the FTV flights, and (2) the effect of the reaction control jets on the pressure field surrounding the models.

2.3.2 EVALUATION OF DATA The force data obtained at AEDC agree quite well with predicted values of Reference 5.7. The only unexpected results discovered in the wind tunnel test occurred at sideslip angles in the vicinity of 90 and 180 degrees. At $\alpha = 90^\circ$, the base cutout altered the lateral stability characteristics to a degree that was not previously calculated. Flow separation at $\alpha = 180^\circ$ also gave results that were not predicted. These two characteristics and their causes are analyzed in a later section.

In order to compare the data obtained at PWT with data obtained at the Type A tunnel, the test program included an overlap of Mach number coverage between the two tunnels. The results obtained in the Mach number overlap agreed very well, providing smooth coefficient curves from $M = 0.6$ to $M = 5$.

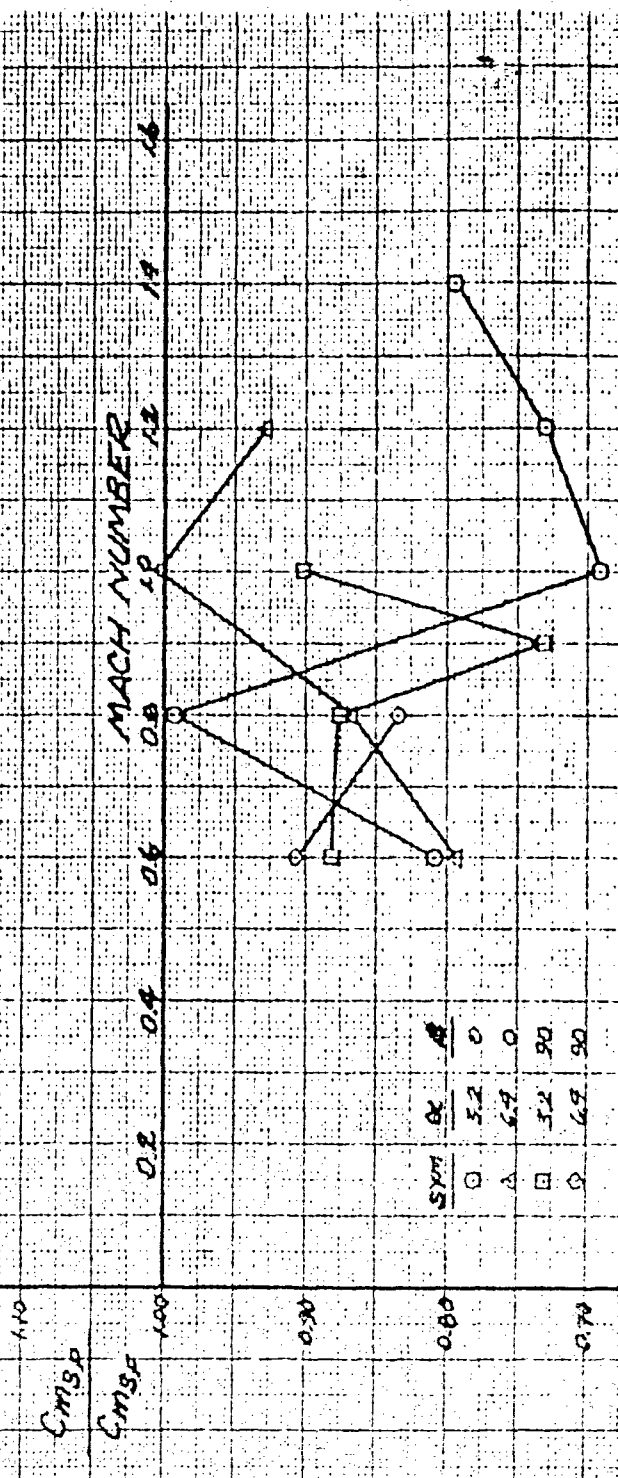
The aerodynamic coefficients obtained by integrating the pressure distribution are not in complete agreement with the data obtained with the internal balance. In general, the pressure results are lower than the force results, as shown in Figures 2.3.6 and 2.3.7.

A comparison of pressure symmetry is made in Figures 2.3.8 a, b, and c. The pressure coefficients along chords equidistant from the centerline are plotted as a function of longitudinal distance. Since the model is at zero sideslip angle, the pressure on these chords should be identical. The plots show that the symmetry is generally good. However, certain pressure measurements are shown to be obviously bad. From past experience with pressure measure-

SECRET

FIGURE 2.36
PYE WACKET FTV
PITCHING MOMENT COMPARISON OF FORCE AND PRESSURE DATA

NOTE: PRESSURE NOT CORRECTED
FOR MODEL MISALIGNMENT



SECRET

SECRET

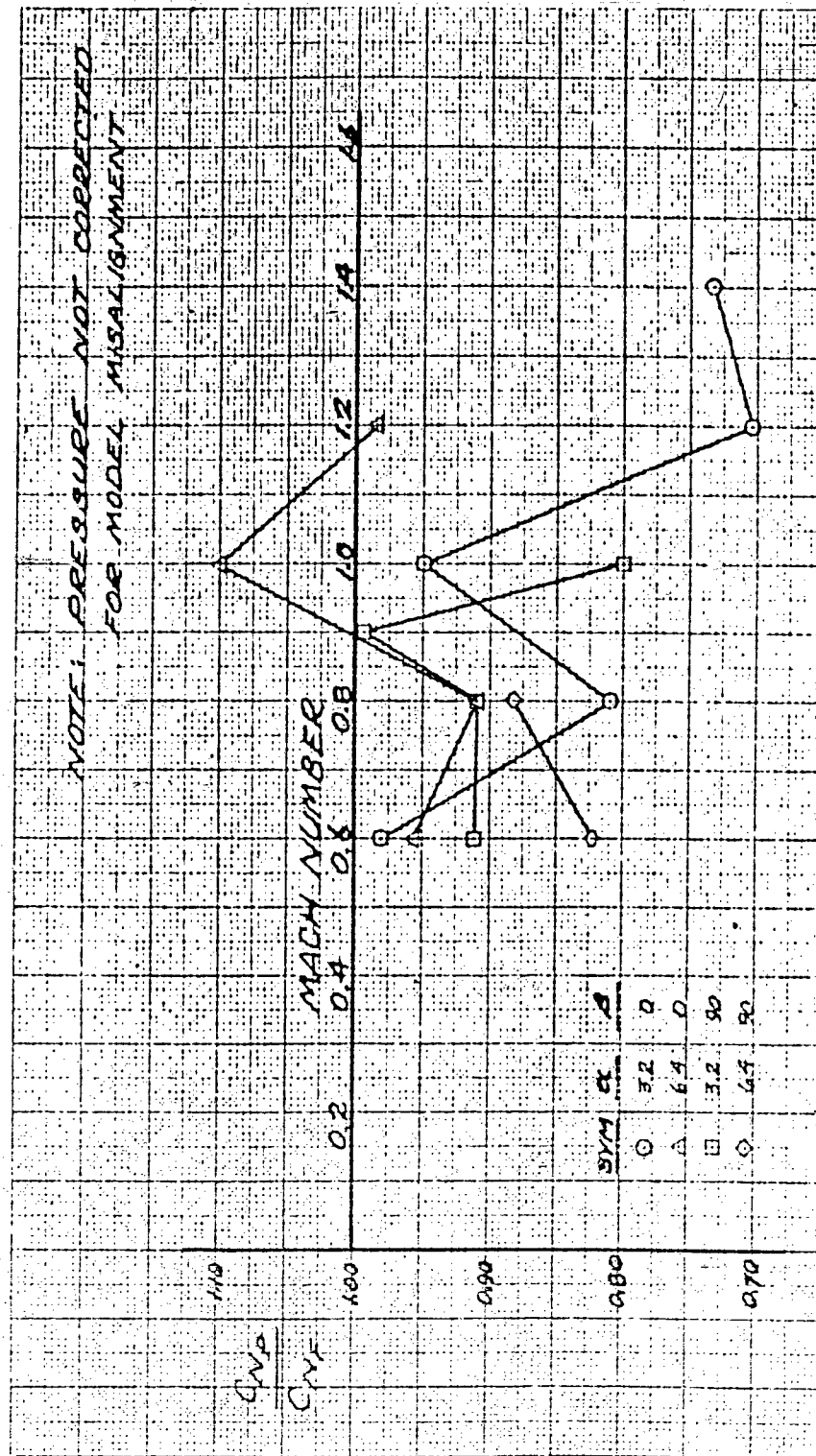
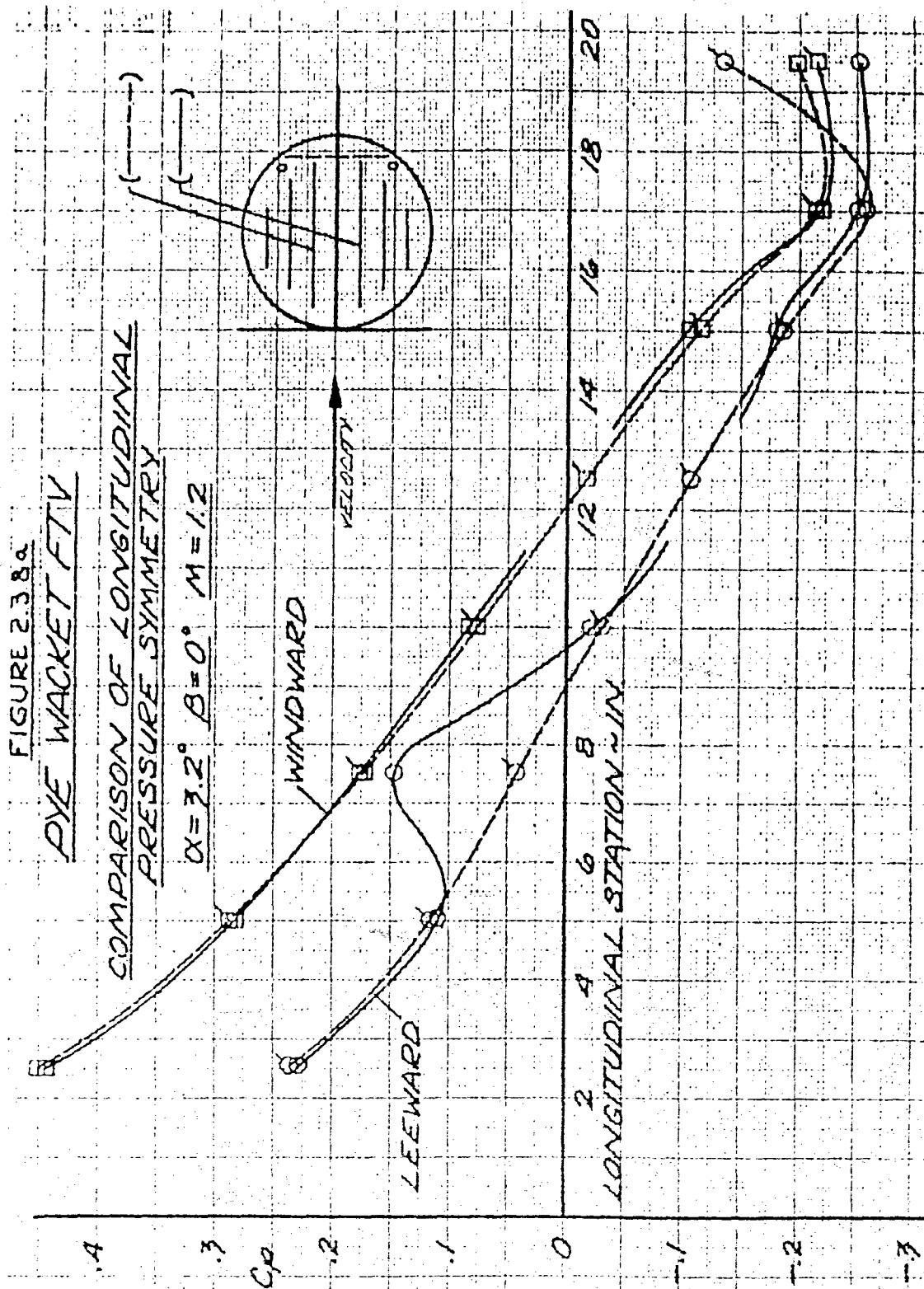


Figure 2.37 PYE WACKET FTV Normal Force Comparison of Force and Pressure Data

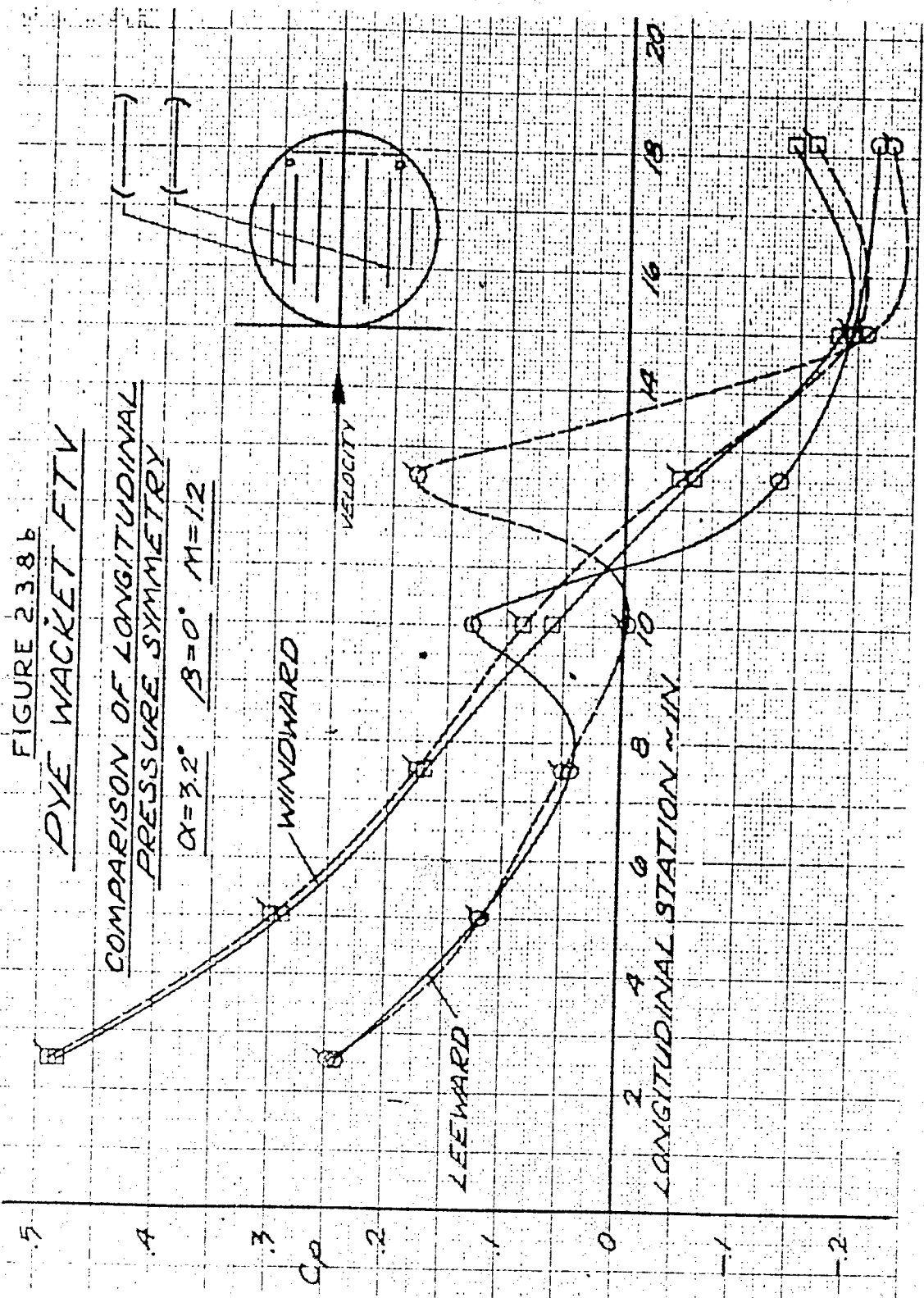
SECRET

SECRET



SECRET

SECRET



SECRET

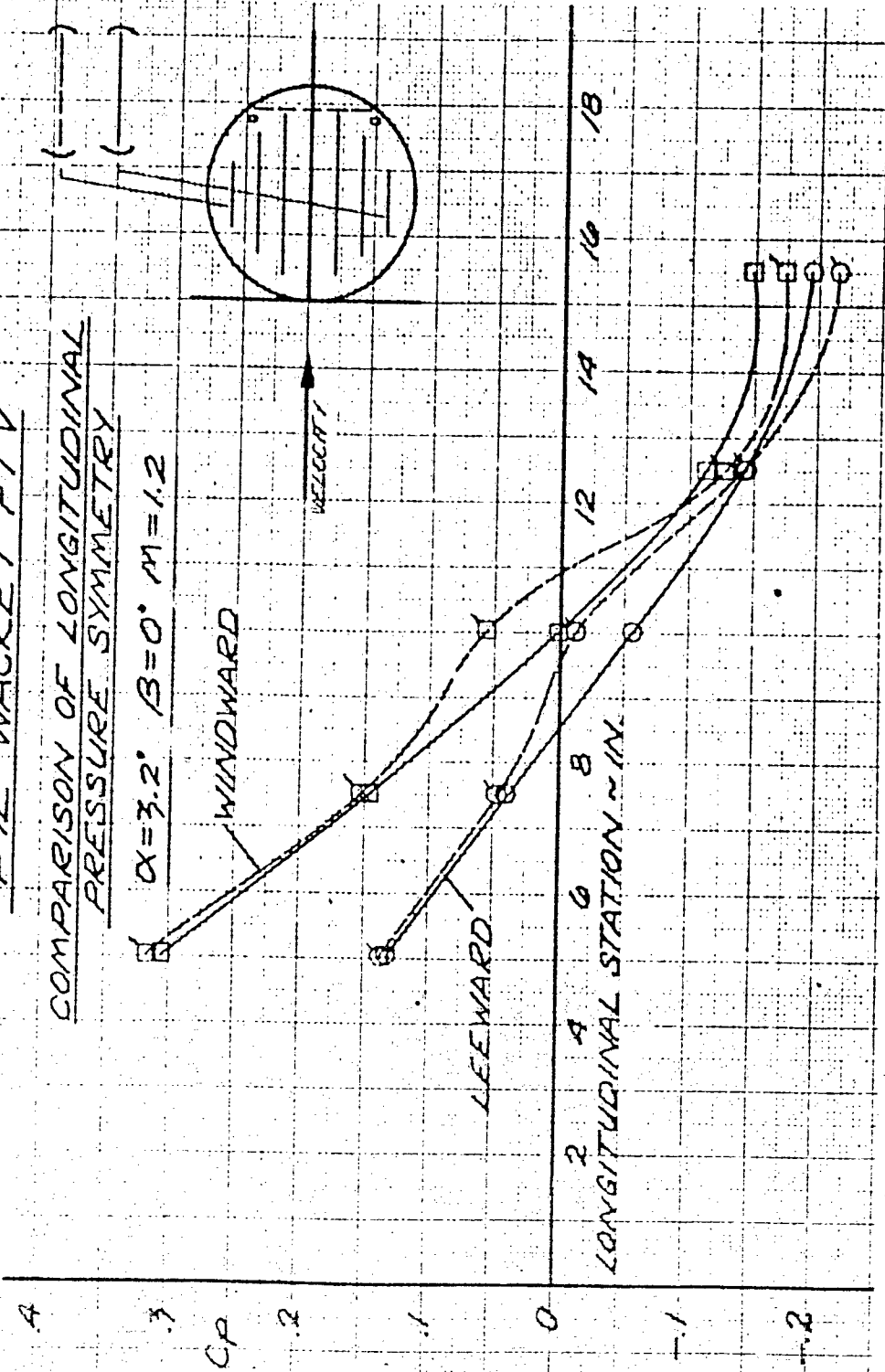
SECRET

FIGURE 2.3.8c

PYE WACKET FTV

COMPARISON OF LONGITUDINAL
PRESSURE SYMMETRY

$\alpha = 3.2^\circ$ $\beta = 0^\circ$ $M = 1.2$



SECRET

ments, these bad readings are to be expected. To obtain reliable pressure integrations, values faired from the adjacent pressure ports must be substituted for the erroneous pressure measurements in the integration procedure. This process is extremely laborious and time consuming. For this reason, the forces and moments obtained by pressure integration could not be completely correlated with the data obtained with the internal balance. However, the reason for the discrepancy is shown. A good correlation between the pressure data and the internal balance data could be obtained in the future if sufficient time were available to correct the erroneous pressure measurements.

2.4 AERODYNAMIC CHARACTERISTICS

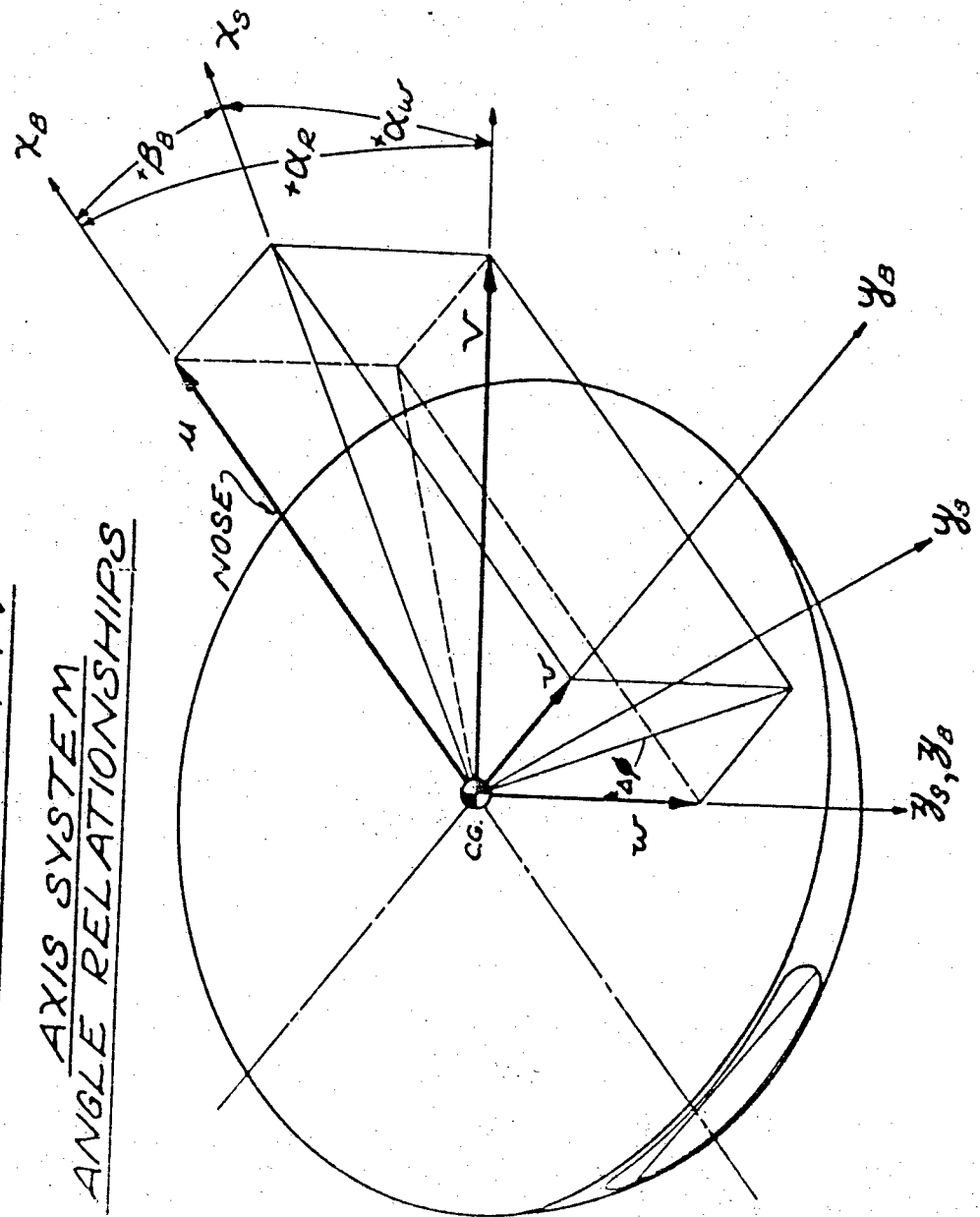
2.4.1 AXIS SYSTEM Two standard axis systems are in current use throughout the missile industry. These systems are "body axes" and "wind axes". Confusion arises, however, when these axis systems are used for large sideslip angles. Since the PYE WACKET inherently utilizes sideslip angles up to 180 degrees, a different axis system is needed to avoid confusion. The system adopted here is called the stability axis system in this report and is distinguished from other axis systems by the subscript "s".

The stability axis system is basically a combination of body and wind axes. It is a right hand orthogonal coordinate system with its origin at the missile center of gravity. The stability axis system is formed by rotating the standard body axes about the z-axis through the sideslip angle β . Thus, the x_s -axis is the intersection of the missile planform and the plane formed by the z-axis and the velocity vector. Note that the z-axes in the body and stability axis systems are identical. The stability axis system is shown in Figures 2.4.1 and 2.4.2.

In stability axes, the angle of attack, α , is defined as the angle between the x_s -axis and the velocity vector. The sideslip angle, β , is defined as the angle between the x_s -axis and missile longitudinal center-line. These angles are illustrated in Figures 2.4.1 and 2.4.2 along with the positive direction of forces and moments for the stability axis system.

SECRET

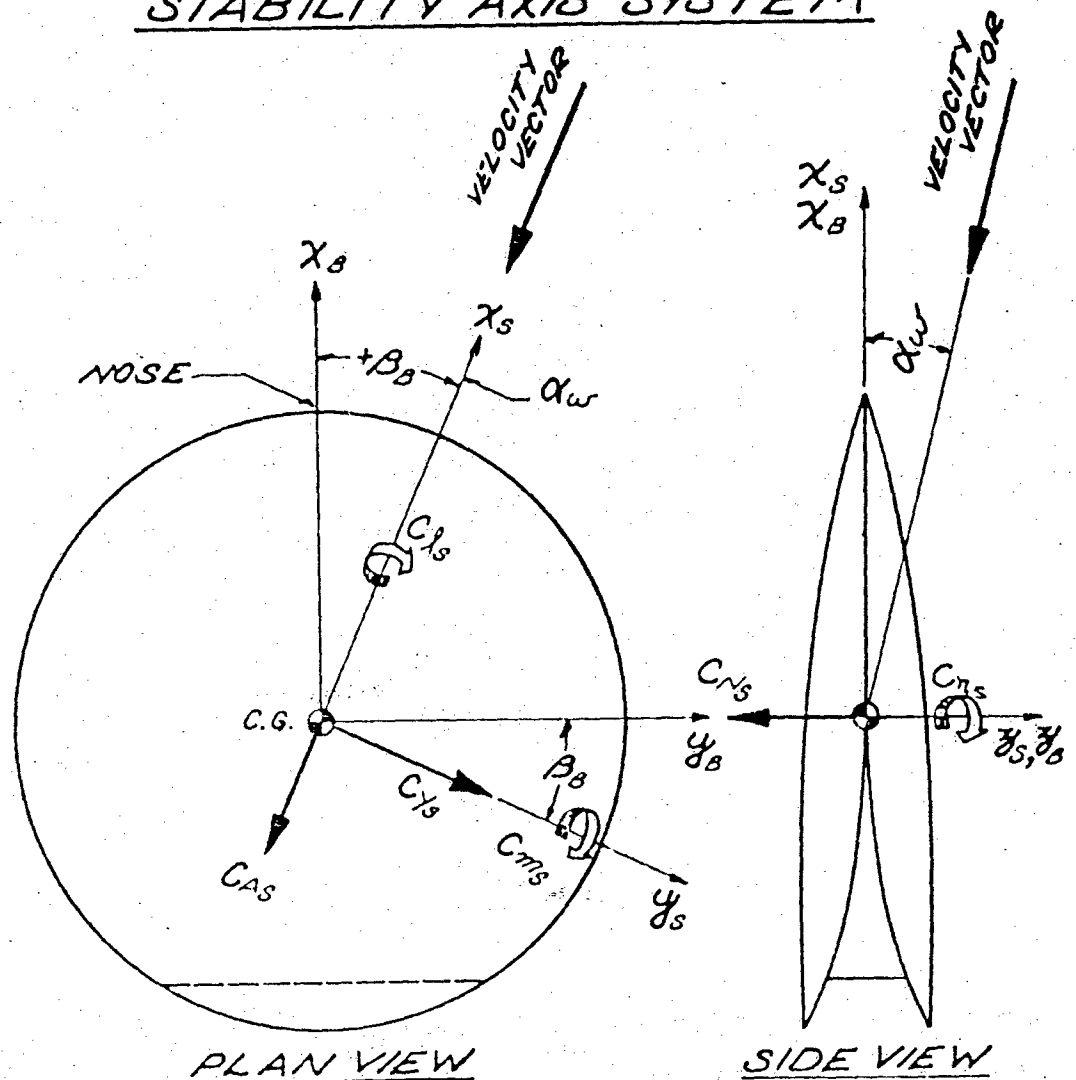
FIGURE 2.4.1
PYE WACKET FTV
AXIS SYSTEM
ANGLE RELATIONSHIPS



SECRET

SECRET

FIGURE 2.4.2
PYE WACKET FTV
STABILITY AXIS SYSTEM



NOTE:

- 1) C_N AND C_η ARE COMMON TO BOTH STABILITY AND BODY AXIS.
- 2) ARROWS INDICATE POSITIVE DIRECTION OF FORCES, MOMENTS, AND ANGLES.

SECRET

SECRET

2.4.2 APPLICABILITY OF AERODYNAMIC COEFFICIENTS This section presents a figure index of the experimental and estimated aerodynamic coefficients as applied to the three phases of PYE WACKET FTV flight. The cross-indexing of the aerodynamic coefficients and figures for the various combinations of main rocket motors and reaction control jets off or on is presented in order to simplify the use of the data for computer simulation studies. A detailed discussion of the individual coefficients may be found in Section 2.4.3 for power-off coefficients (experimental data), and in Section 2.4.5 for power-on coefficients (estimated).

Power-off and power-on aerodynamic coefficients are indexed with the associated figure numbers for the three flight conditions: (1) sled captive phase, (2) power-on phase, and (3) coast phase. The listings corresponding to the three phases of flight are presented in Tables 2.4.1, 2.4.2 and 2.4.3.

2.4.3 POWER-OFF DATA PRESENTATION The basic aerodynamic characteristics for the 21 percent thick PYE WACKET Feasibility Test Vehicle are presented in this section. These data were obtained from a 1/3-scale force model of the PYE WACKET FTV tested in the transonic and supersonic wind tunnels at A.E.D.C., Tullahoma, Tennessee. The coefficients include no effects of the main rocket or the reaction control jets.

A brief listing of the power-off data is presented in Table 2.4.4. The pertinent characteristics of the aerodynamic coefficients will be discussed in detail under the headings of the individual coefficients.

SECRET

SECRET

TABLE 2.4.1

SIED CAPTIVE PHASE FIGURE INDEX
(MAIN MOTORS OFF)

LAUNCH ANGLE, θ	AERODYNAMIC COEFFICIENTS	FIGURE NO'S.	
		REACTION JETS ON	REACTION JETS OFF
0°	C _N	2.4.3	2.4.3
	C _Y	2.4.9	2.4.9
	C _A	2.4.25	2.4.14
	C _m	2.4.6	2.4.6
	C _n	2.4.10	2.4.10
	C _l	2.4.11	2.4.11
90°	C _N	2.4.3	2.4.3
	C _Y	2.4.9	2.4.9
	C _A	2.4.23	2.4.14
	C _m	2.4.6	2.4.6
	C _n	2.4.10	2.4.10
	C _l	2.4.11	2.4.11
180°	C _N	2.4.3	2.4.3
	C _Y	2.4.9	2.4.9
	C _A	2.4.14	2.4.14
	C _m	2.4.6	2.4.6
	C _n	2.4.10	2.4.10
	C _l	2.4.11	2.4.11

SECRET

SECRET

TABLE 2.4.2

POWER-ON PHASE FIGURE INDEX
(MAIN MOTORS ON)

EXPECTED θ RANGE	AERODYNAMIC COEFFICIENTS	FIGURE NO'S.	
		REACTION JETS ON	REACTION JETS OFF
0 to $\pm 90^\circ$	CN	2.4.3	2.4.3
	CY	2.4.27	2.4.27
	CA	2.4.24	2.4.24
	Cm	2.4.6	2.4.6
	Cn	2.4.28	2.4.28
	Cl	2.4.11	2.4.11
180°	CN	DATA NOT AVAILABLE	DATA NOT AVAILABLE
	CY		
	CA		
	Cm		
	Cn		
	Cl		

TABLE 2.4.3

COAST PHASE FIGURE INDEX
(MAIN MOTORS OFF)

EXPECTED θ RANGE	AERODYNAMIC COEFFICIENTS	FIGURE NO'S.	
		REACTION JETS ON	REACTION JETS OFF
0 to $\pm 20^\circ$	CN	2.4.3	2.4.3
	CY	2.4.9	2.4.9
	CA	2.4.25	2.4.14
	Cm	2.4.6	2.4.6
	Cn	2.4.10	2.4.10
	Cl	2.4.11	2.4.11

SECRET

SECRET

TABLE 2.4.4

POWER-OFF AERODYNAMIC COEFFICIENTS

Coefficient	Figure No.	M	β	α	Parameter
C_N vs α	2.4.3	0 to 5.0	$0^\circ, 90^\circ, 180^\circ$	0° to 14°	β
C_{N_x} vs M	2.4.4	0 to 5.0	$0^\circ, 90^\circ, 180^\circ$	0° to 4°	β
C_N vs β	2.4.5	0 to 1.0	0° to 180°	$3^\circ, 6^\circ, 9^\circ$	α
C_m vs α	2.4.6	0 to 5.0	$0^\circ, 90^\circ, 180^\circ$	0° to 14°	β
C_{m_x} vs M	2.4.7	0 to 5.0	$0^\circ, 90^\circ, 180^\circ$	0° to 4°	β
C_m vs β	2.4.8	0 to 1.0	0° to 180°	$3^\circ, 6^\circ, 9^\circ$	α
C_y vs β	2.4.9	0 to 1.0	0° to 180°	$0^\circ, 3^\circ, 6^\circ$	α
C_n vs β	2.4.10	0 to 1.6	0° to 180°	$0^\circ, 3^\circ, 6^\circ$	α
C_z vs β	2.4.11	0 to 1.6	0° to 180°	$3^\circ, 6^\circ$	α
$C.P.$ vs M	2.4.12	0 to 5.0	$0^\circ, 90^\circ$	0°	β
$C.P.$ vs β	2.4.13	0 to 1.6	0° , to 100°	0°	M
C_{A_5} vs M	2.4.14	0 to 5.0	$0^\circ, 90^\circ, 180^\circ$	0°	β
C_{A_5} vs M	2.4.15	0 to 5.0	0°	0°	DRAG COMPONENTS
C_{A_5} vs β	2.4.16	0 to 1.6	0° to 180°	$0^\circ, 3^\circ, 6^\circ$	α

SECRET

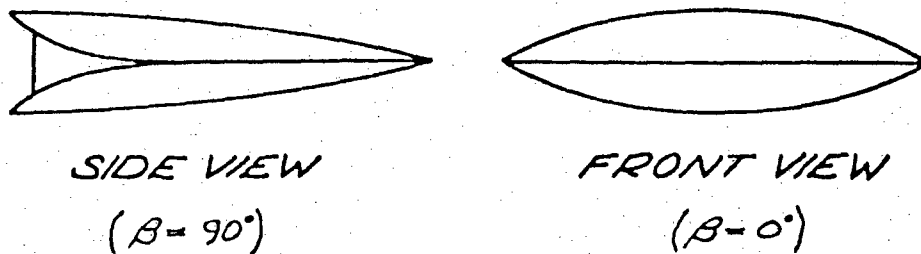
In order to clarify the use of the power-off data presented in this section, a brief description of the method of applying the magnification effects of the control jets is necessary. With the control jets on, two forces are generated in addition to the aerodynamic force already present. These are: (1) the force due to the thrust of the control jet, and (2) the force due to the interaction of the jet exhaust and the aerodynamic flow field. The total normal force (N) on the missile is the sum of the normal force (power-off), the jet reaction component, and the interference.

$$N = C_N q S + F_{JET} + \Delta C_N q S$$

(2.4.1)

The magnification factors resulting from the jet interaction with the body flow field are presented in Volume III, "Configuration and Autopilot/Control". It may be noted that the magnification factors are calculated in relation to the control jet thrust rather than the aerodynamic force. Consequently, the power-off aerodynamic coefficients are readily applicable in computer studies which simulate control jets. The applicability of the power-off aerodynamic coefficients for the flight conditions of the PYE WACKET FTV is presented together with the power-on coefficients in Tables 2.4.1 through 2.4.3 of Section 2.4.2. The coefficients are indexed according to figure number for the three phases of flight: sled captive phase, power-on phase, and coast phase.

2.4.3.1 Normal Force Coefficient The normal force coefficients for the PYE WACKET FTV configuration are presented in Figure 2.4.3. As shown, the normal force coefficient is linear with angle of attack up to approximately 4 degrees for angles of sideslip of 0 and 90 degrees for all Mach numbers presented. For rear launch ($\beta = 180^\circ$), this linearity exists only at supersonic velocities. Examination of Figures 2.4.3a, b, and c reveals slightly higher subsonic and transonic normal force coefficients at $\beta = 90^\circ$ than at $\beta = 0^\circ$. For supersonic Mach numbers the reverse condition exists; i.e., more normal force is generated in the forward launch ($\beta = 0^\circ$) position than for cross-wind launch ($\beta = 90^\circ$). A similar phenomenon, relating subsonic and supersonic pressure distribution on bodies with varying degrees of bluntness, is discussed in Reference 5.8 (bodies without flares). The sketch following emphasizes the geometry of the configuration, for the flow at $\beta = 0^\circ$ and $\beta = 90^\circ$, where the velocity vector is into the page.

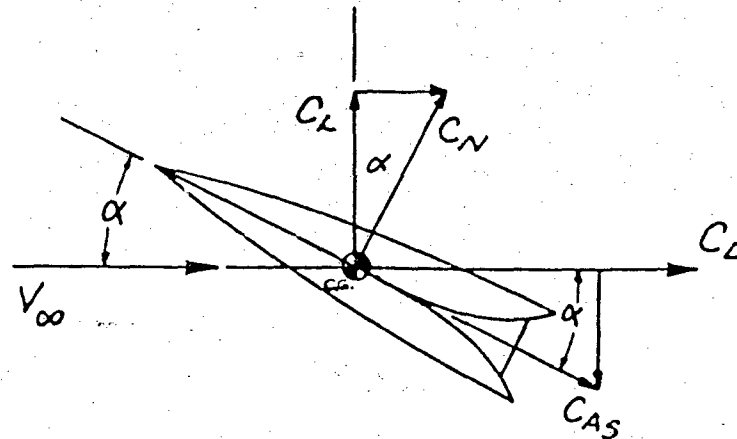


As shown in the sketch, the rearward half of the configuration presents a blunted face to the airstream at $\beta = 90^\circ$. In contrast, the front view presents a symmetrically tapered edge to the airstream at $\beta = 0^\circ$. Subsonically and transonically, for $\beta = 90^\circ$, the small increase in normal force coefficient (see Figures 2.4.3 a, b, and c) is attributed to the increase in effective thickness ratio for the blunted face of the rearward half of the body as compared to the thickness ratio of the symmetrically tapered edge at $\beta = 0^\circ$. An increase in normal force coefficient is characteristic of blunted shapes at subsonic speeds. Examples of the effects of varying degrees of bluntness on subsonic normal force coefficients are given in Reference 5.9. Substantiation of this effect for blunted shapes of varying degrees is given in Reference 5.10.

These small differences in the normal force coefficient for subsonic and supersonic flow at $\beta = 90^\circ$ may be summarized as follows: (1) for subsonic flow, an increase in bluntness results in a higher normal force coefficient which is due to the increased flow velocity over the blunted shape, and (2) for supersonic flow an increase in leading edge bluntness results in a lower normal force coefficient caused by flow separation around the blunt leading edge. Separation occurs in varying degrees over the sharp curvature of the blunted portion of the body, and will occur asymmetrically over the body as angle of attack is increased. As the local flow becomes supercritical over the sharp corners of the blunt leading edge, a system of compression shock waves form. These shocks terminate in a region where the flow is undergoing a significant pressure rise as a result of the basic subsonic pressure distribution. The presence of the shocks tends to increase the adverse pressure gradient and thus causes flow separation. As the flow separates, the large negative pressure gradient collapses, and the lift forces decrease.

For the rear-launch condition ($\beta = 180^\circ$), as seen in Figures 2.4.3 a, b, and c for subsonic and transonic speeds, a negative normal force occurs at positive angles of attack. The maximum negative force occurs between angles of attack of 2 to 3 degrees at a Mach number of 0.9, (Figure 2.4.3 c). This phenomenon is discussed in detail in Section 2.4.6 under PRESSURE DISTRIBUTION and will not be treated in detail here. The accuracy of the data for $\beta = 180^\circ$ is somewhat questionable at Mach numbers of 0.8 and 0.9 due to the lack of normal force coefficients at $\alpha = 0^\circ$. The "zero-shifts" of data at $M = 0.8$ and $M = 0.9$ were interpolated from the $\alpha = 0^\circ$ data at Mach numbers of 0.6, 1.0, 1.2, 1.4, and 1.6.

The slope of the normal force coefficient with respect to angle of attack is presented in Figure 2.4.4 for sideslip angles of 0, 90, and 180 degrees. The normal force derivatives, determined at $\alpha = 0^\circ$, are applicable to either body or stability axes. For reference to wind axes, the lift coefficient may be computed from the following relationship:

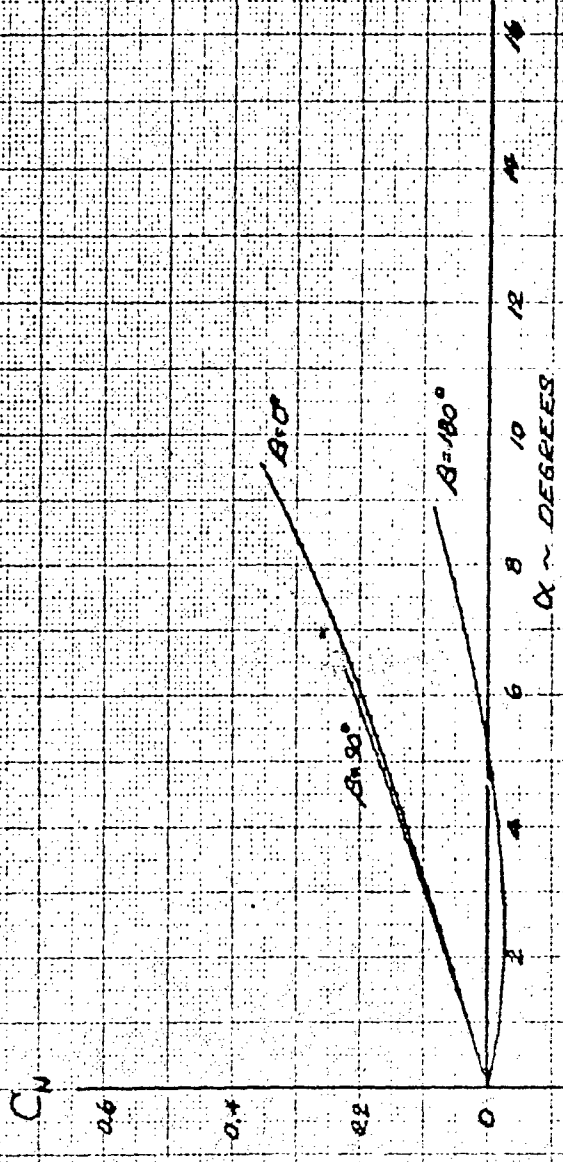


$$C_L = C_N \cos \alpha - C_{A\beta} \sin \alpha \quad 2.4.2$$

SECRET

FIGURE 2.4.3 a

PYE WACKET FTV
 VARIATION OF NORMAL FORCE COEFFICIENT
 WITH ANGLE OF ATTACK
 $\gamma_0 = 0.21$ POWER - OFF
 $M = 0.6$

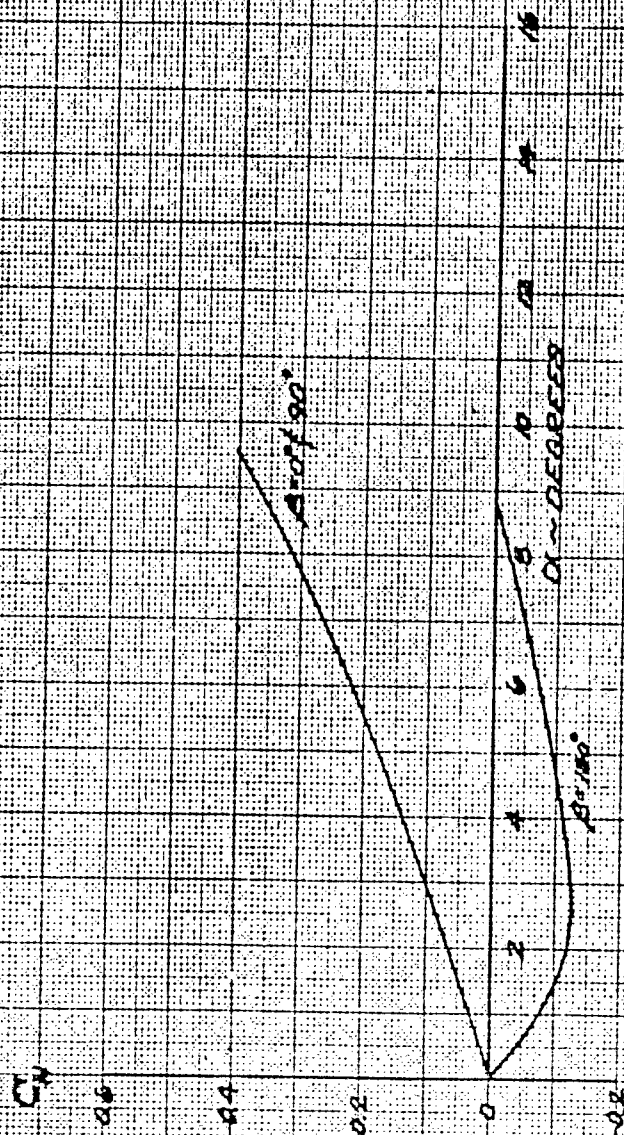


SECRET

SECRET

FIGURE 2-43b

PYE WACKET FTV
 VARIATION OF NORMAL FORCE COEFFICIENT
 WITH ANGLE OF ATTACK
 $\gamma = 0.21$ POWER-OFF
 $M = 0.8$

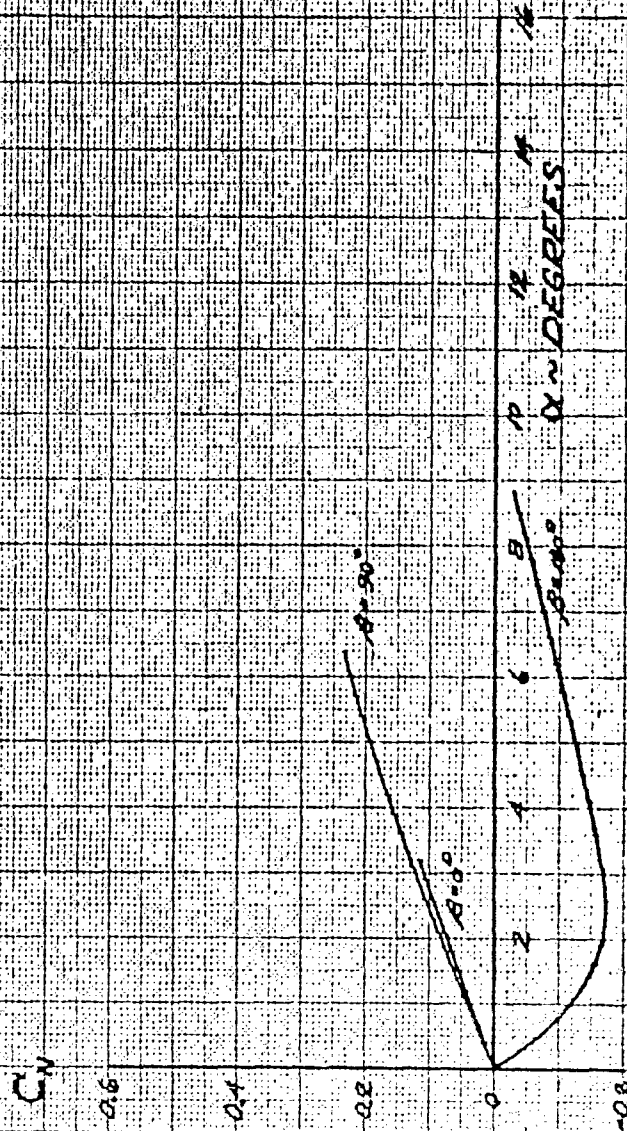


SECRET

SECRET

FIGURE 2-43c

PYE WHACKET FLY
 VARIATION OF NORMAL FORCE COEFFICIENT
 WITH ANGLE OF ATTACK
 $\mu_c = 0.21$ POWER-OFF
 $M = 0.8$

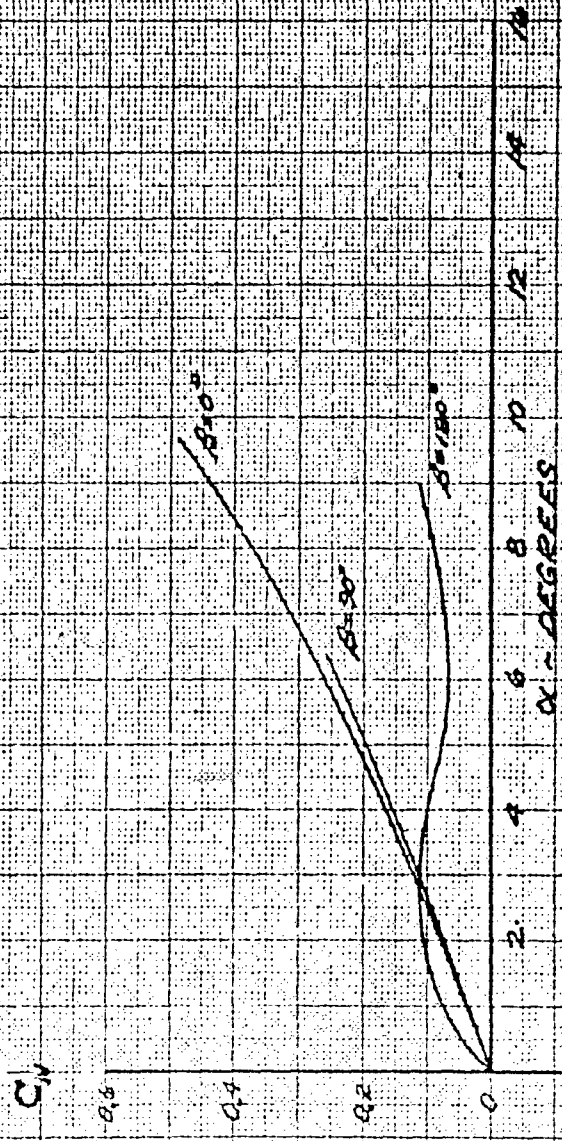


SECRET

SECRET

FIGURE 2.4.3.4

PYE WAGNET FTV
 VARIATION OF NORMAL FORCE COEFFICIENT
 WITH ANGLE OF ATTACK
 $\gamma_0 = 0.21$ POWER-OFF
 $M = 1.0$

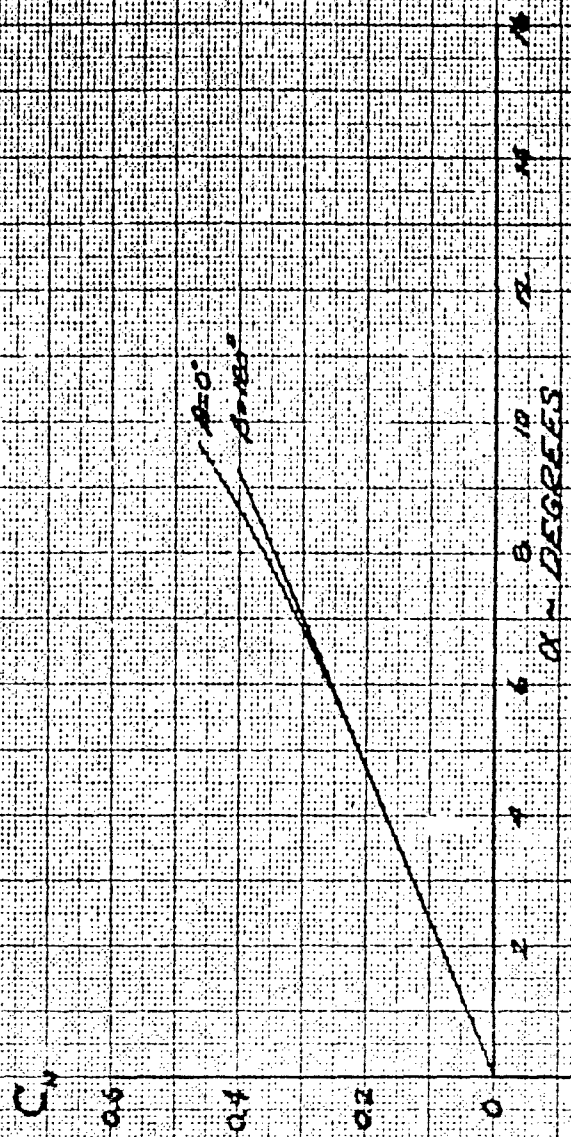


SECRET

SECRET

FIGURE 2-43C

RYE WACKET FTV
VARIATION OF NORMAL FORCE COEFFICIENT
WITH ANGLE OF ATTACK
 $\gamma_c = 0.21$ POWER-OF
 $M = 1.2$



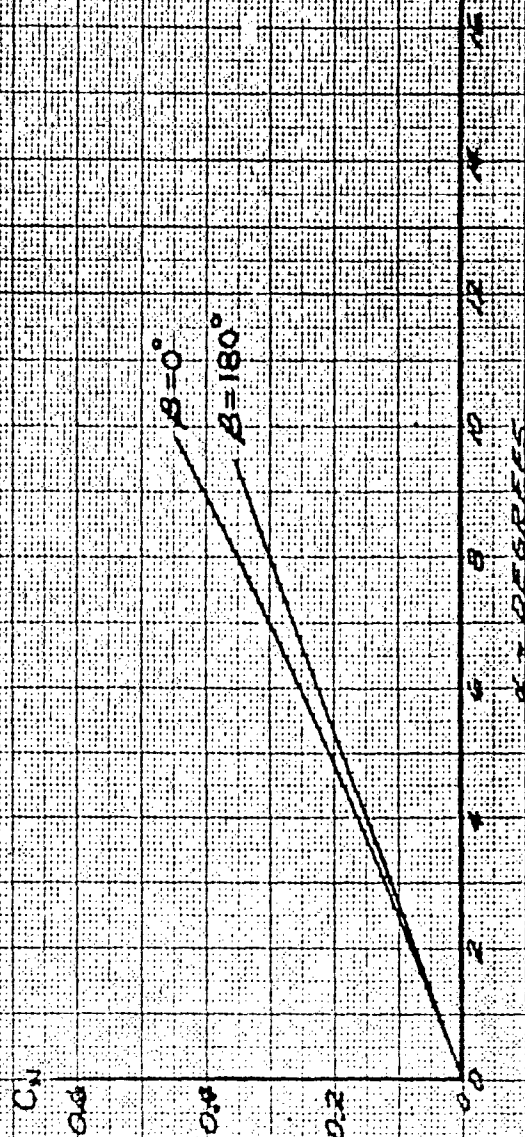
2-15

SECRET

SECRET

FIGURE 2-43f

PVF WACKET FTV
 VARIATION OF NORMAL FORCE COEFFICIENT
 WITH ANGLE OF ATTACK
 $\epsilon_0 = 0.21$ FORMER-055
 $M = 1.8$

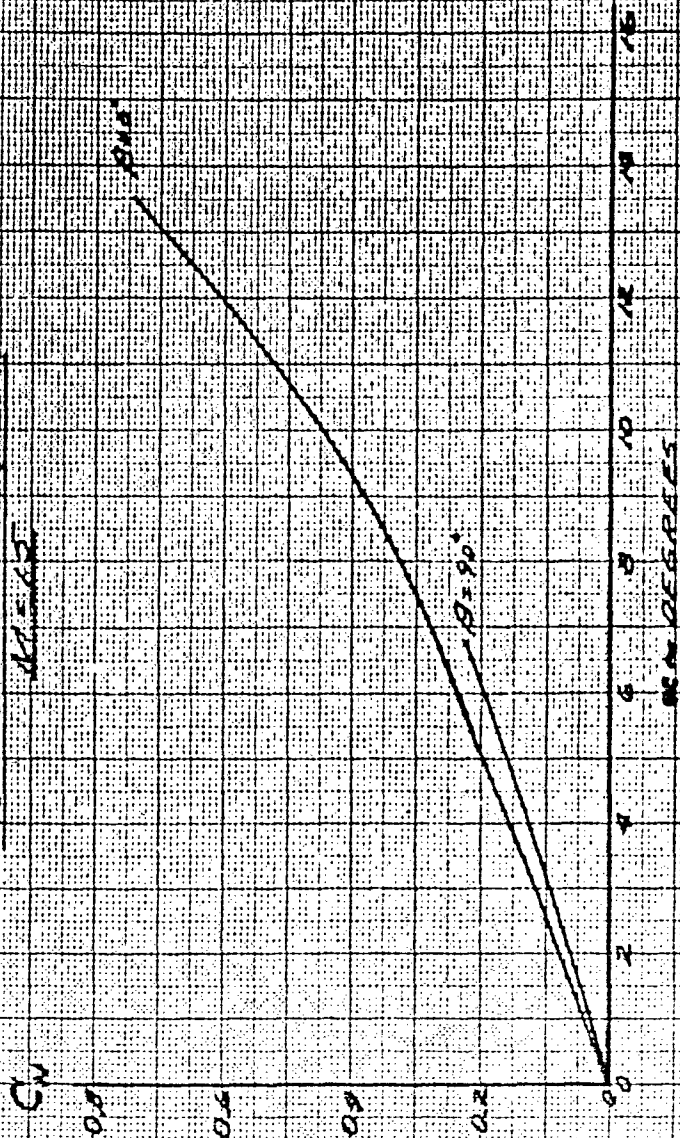


SECRET

SECRET

FIGURE 2-43

CVF WACKET FLY
VARIATION OF NORMAL FORCE COEFFICIENT
WITH ANGLE OF ATTACK
 $\mu_c = 0.21$ POWER OFF
 $M = 0.5$

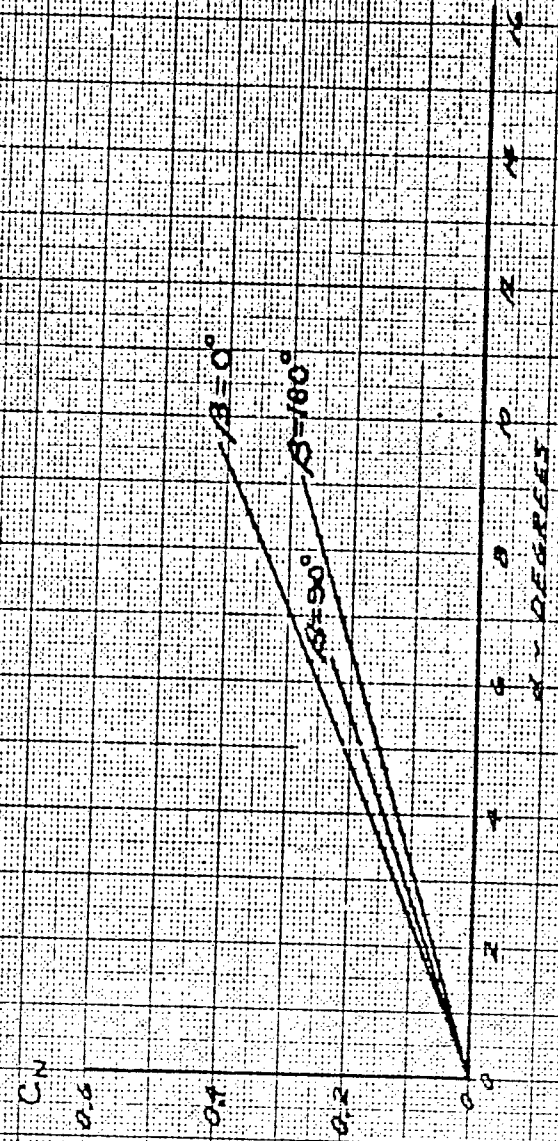


SECRET

SECRET

FIGURE 2.4.3.1

VARIATION OF
PVE WALKER FTV
NORMAL FORCE COEFFICIENT
WITH ANGLE OF ATTACK
 $C_N = 0.21$ POWER-OFF
 $M = 4.6$



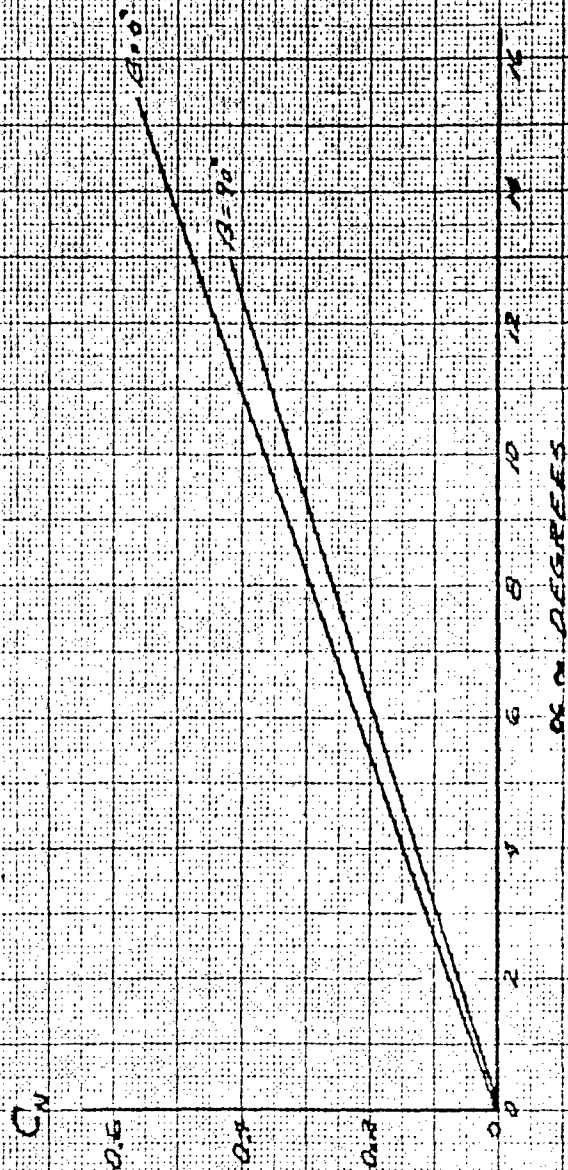
2.4.3

SECRET

SECRET

FIGURE 2.4.31

PYE WACKET FTV
 VARIATION OF NORMAL FORCE COEFFICIENT
 WITH ANGLE OF ATTACK
 $EC=0.21$ POWER-OFF
 $M=2.0$



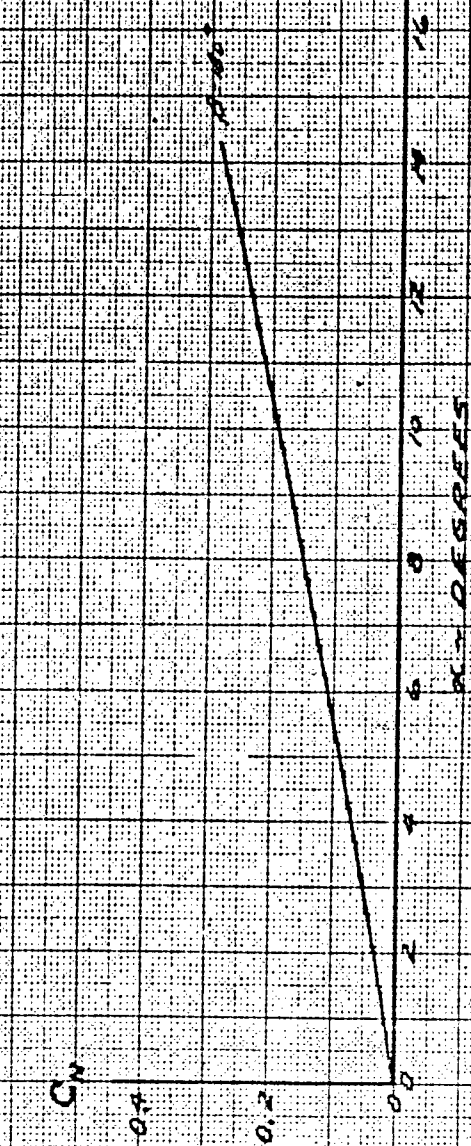
2.43

SECRET

SECRET

FIGURE 24.31

CVF WACHET FTV
VARIATION OF NORMAL FORCE COEFFICIENT
WITH ANGLE OF ATTACK
 $C_L = 0.21$ POWER-OFF
 $M = 2.5$



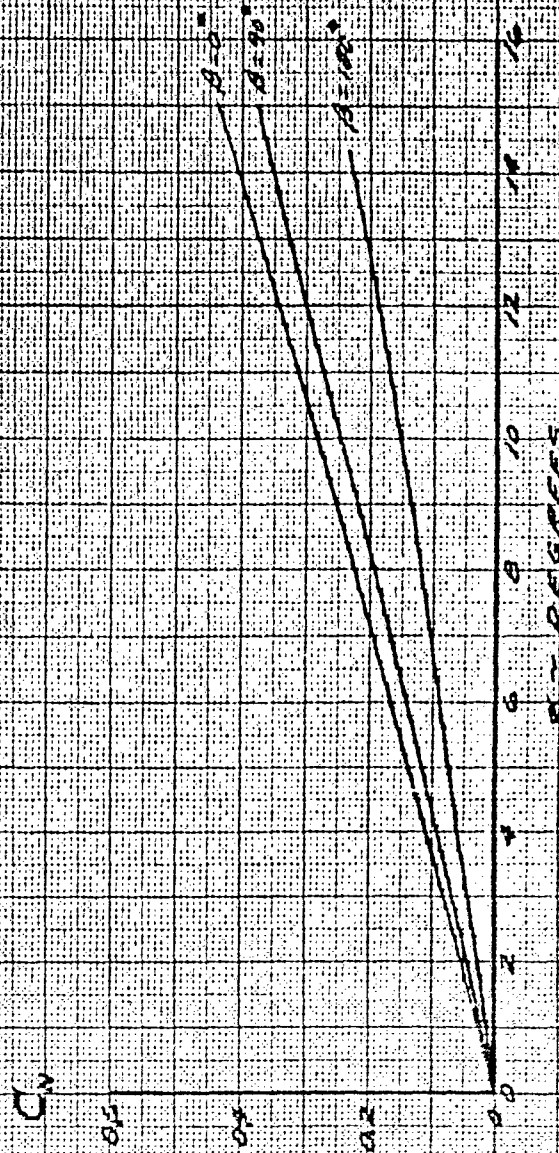
SECRET

SECRET

FIGURE 2.4.3.4

PYE WACKET FTV

VARIATION OF NORMAL FORCE COEFFICIENT
WITH ANGLE OF ATTACK
 $U_0 = 0.21$ POWER OFF
 $M = 3.0$

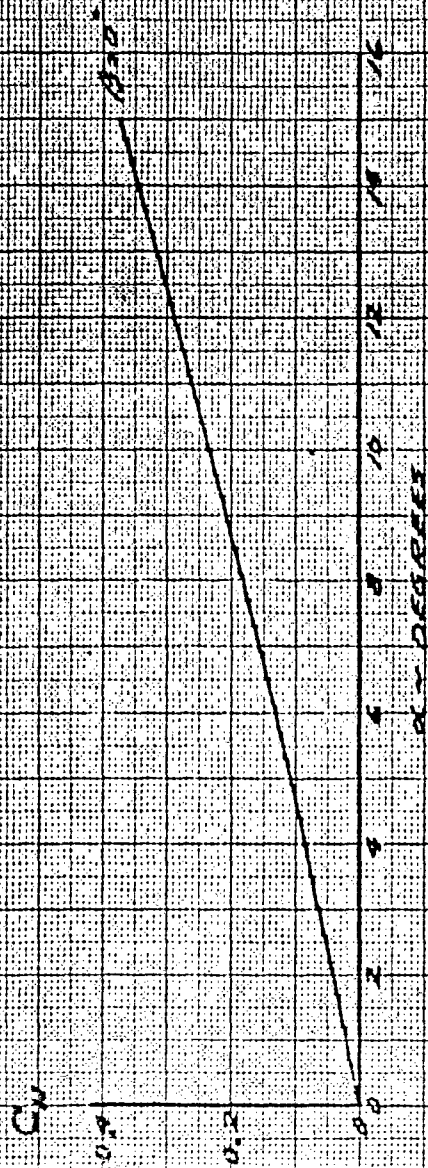


SECRET

SECRET

FIGURE 2.4.3.1

PYE WACKET FTV
 VARIATION OF NORMAL FORCE COEFFICIENT
 WITH ANGLE OF ATTACK
 $\eta_c = 0.21$ POWER LAW
 $M = 10$

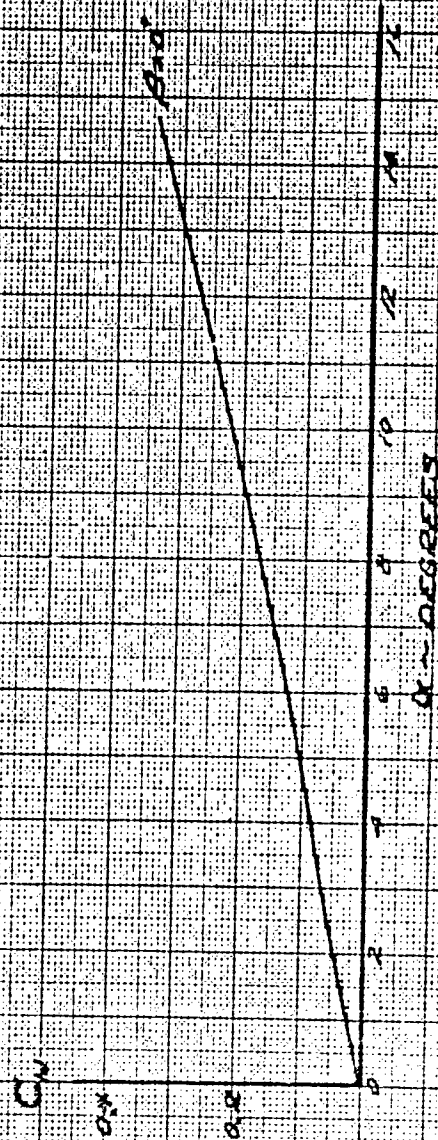


SECRET

SECRET

FIGURE P.4.3 M

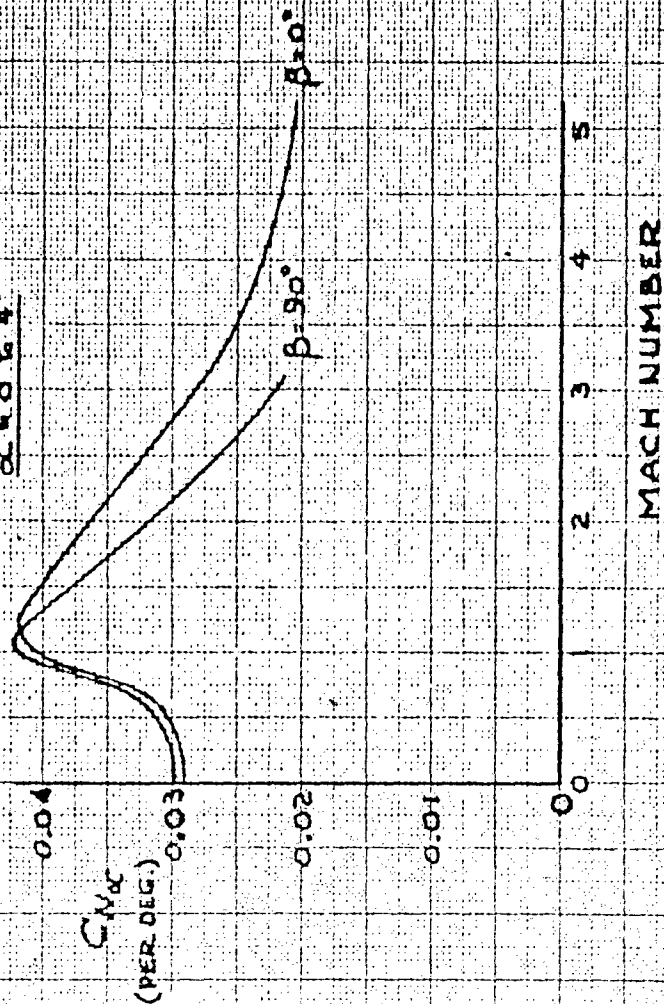
PYE WHISKET FYV
VARIATION OF NORMAL FORCE COEFFICIENT
WITH ANGLE OF ATTACK
 $C_N = 0.21$ POWER-ONE
 $M = 5.0$



SECRET

SECRET

FIGURE 24.4a
 PYE WACKET FTV
 NORMAL FORCE COEFFICIENT PER DEGREE α
 VS. MACH NUMBER
 ALL ROCKETS OFF
 $C_N \approx 0.64$

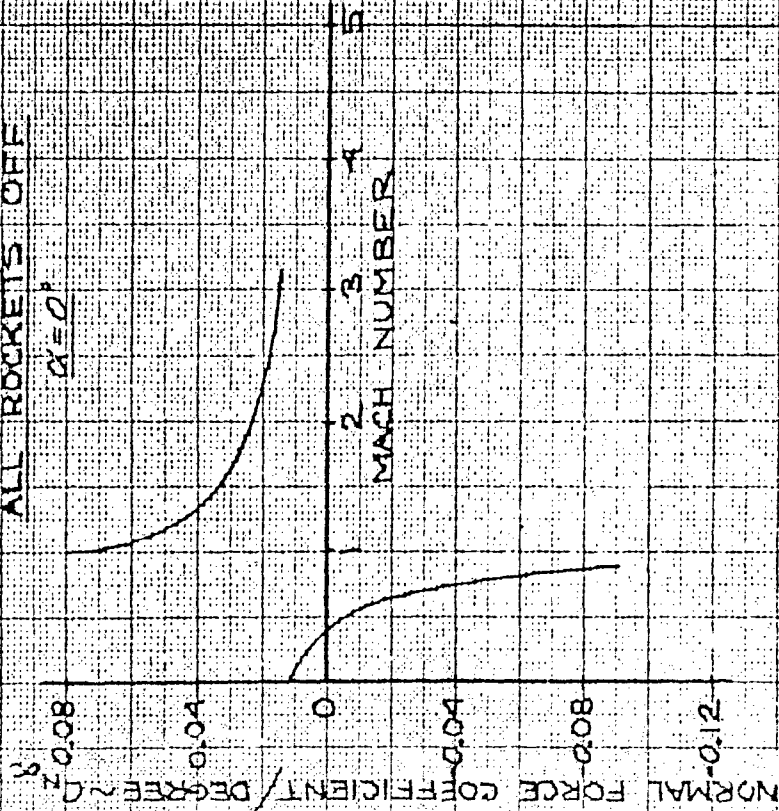


2.54

SECRET

SECRET

FIGURE 2.4.4.b
PYE WACKET FTV
NORMAL FORCE COEFFICIENT PER DEGREE α , β - 180°
VS MACH NUMBER
ALL ROCKETS OFF
 $\alpha = 0^\circ$



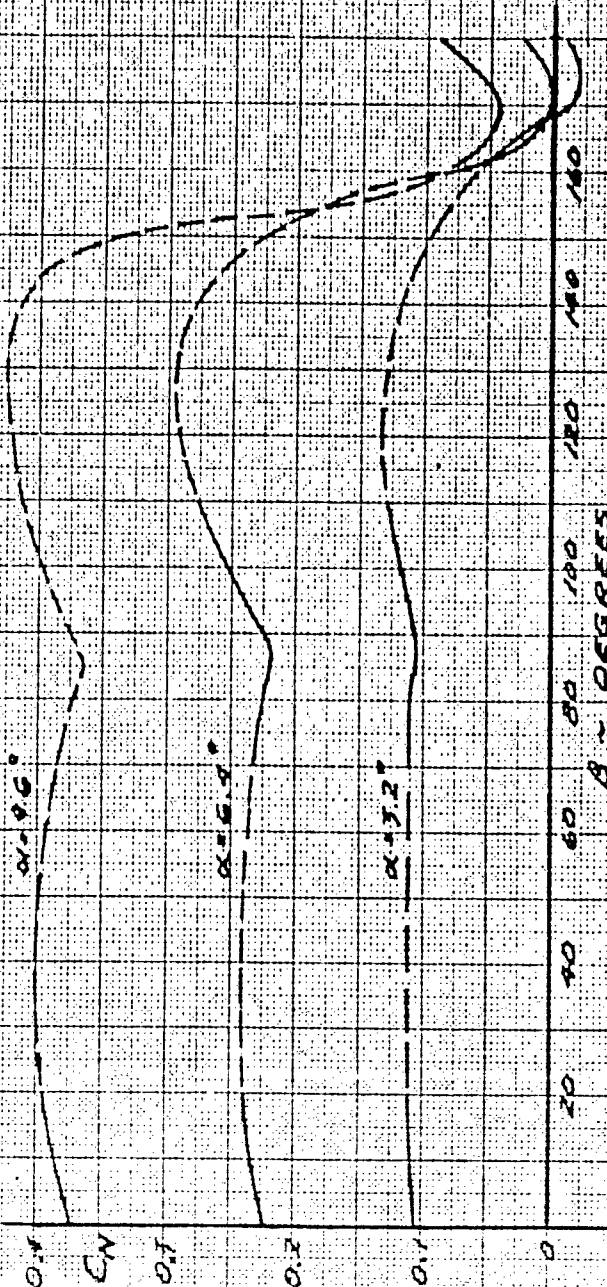
2.55

SECRET

SECRET

FIGURE 2.4.5 a

PYE WACKET FTV
 VARIATION OF NORMAL FORCE COEFFICIENT
 WITH ANGLE OF SLIDE
 $\epsilon/\epsilon = 0.21$ POWER-OFF
 $M = 2.6$



2.50

SECRET

SECRET

FIGURE 2.4.5b
OYE WACKET FTV
VARIATION OF NORMAL FORCE COEFFICIENT
WITH ANGLE OF SIDE SLIP
 $CF = 0.21$ POWER-OFF
 $M = 0.8$



2.57

SECRET

SECRET

FIGURE 2.4.5c

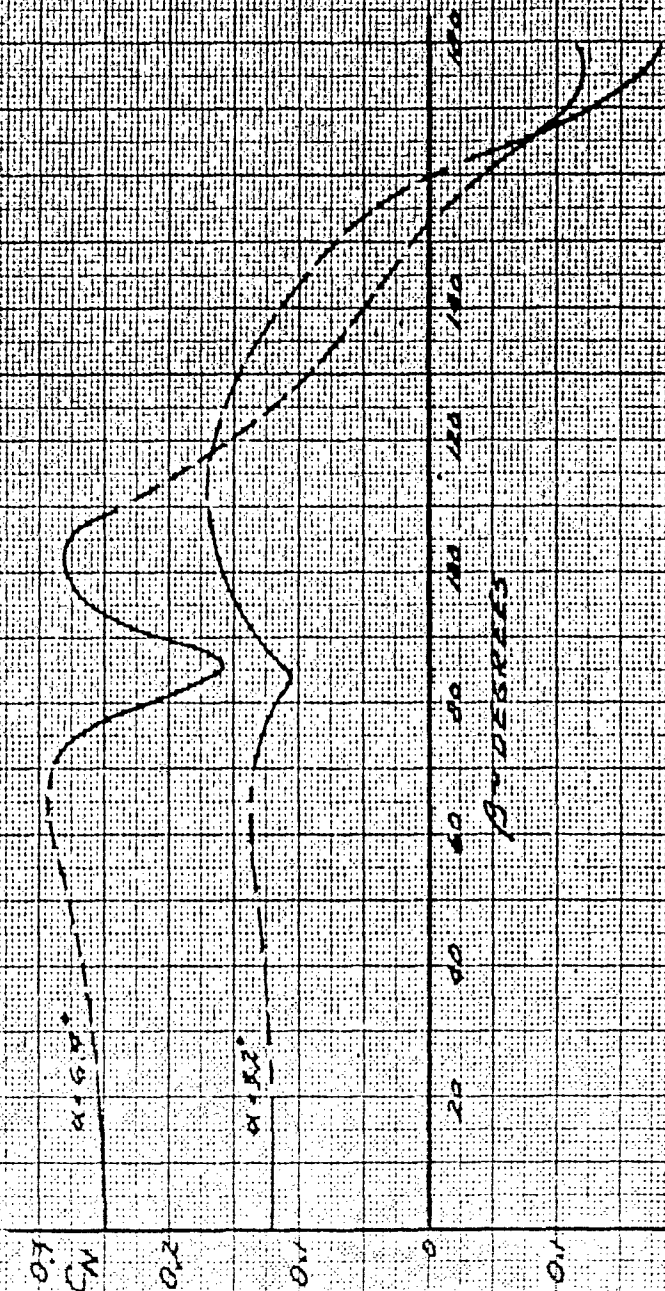
PYE WACKET FTV

VARIATION OF NORMAL FORCE COEFFICIENT

WITH ANGLE OF SIDESLIP

$\gamma_c = 0.21$ POWER-OFF

$M = 0.9$

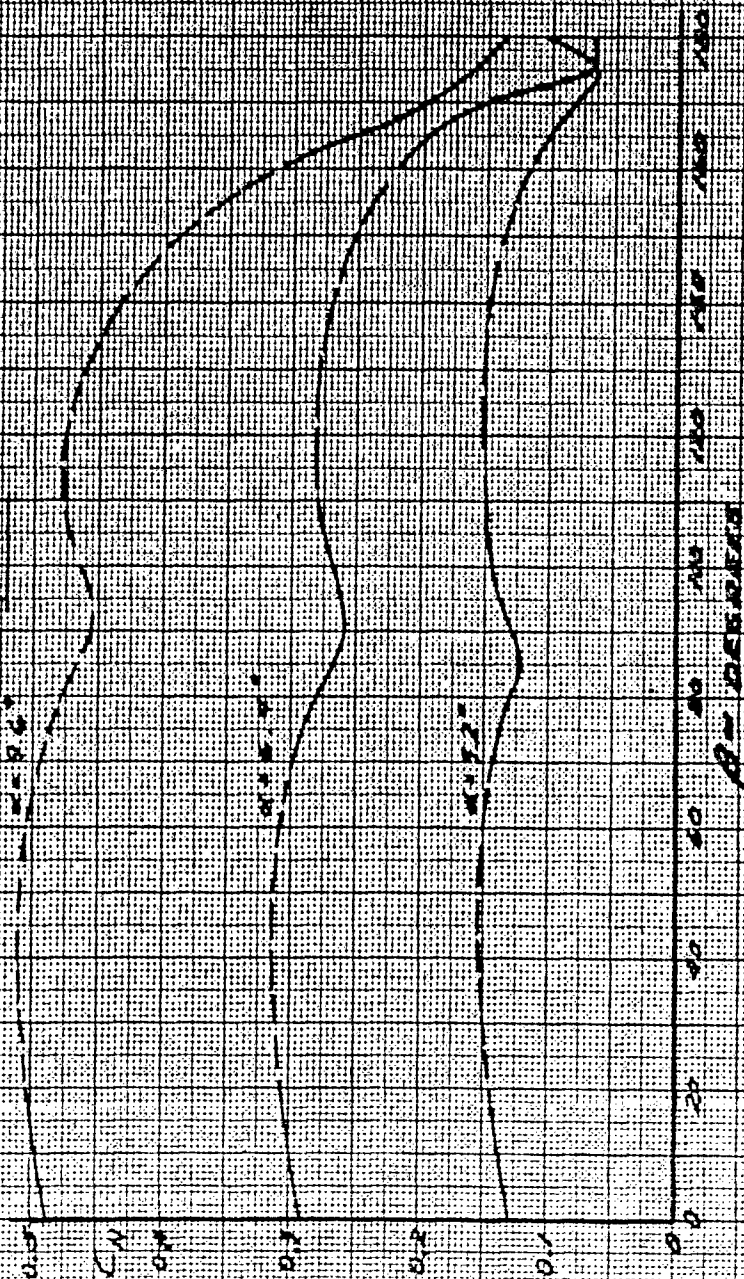


2.5B

SECRET

SECRET

FIGURE 2-43
 FIVE PACKETS 574
 VARIATION OF NORMAL FORCE COEFFICIENT
 WITH ANGLE OF INCIDENCE
 FOR 0.021 SQUARE FEET
 14.18



SECRET

The normal force coefficient as a function of sideslip angle (0° to 180°) is presented in Figure 2.4.5. The coefficients are presented at Mach numbers of 0.6, 0.8, 0.9, and 1.0 with angle of attack as a parameter. For the subsonic and transonic range of flight, the data indicate the peak normal force coefficient to occur generally at an angle of sideslip between 110 and 120 degrees. At a Mach number of 1.0 the maximum normal force coefficient occurs at approximately $\alpha = 45^\circ$. In both cases, the combination of local thickness ratio, angle of attack, and flow separation are major factors in determining the peak normal force as a function of angle of sideslip. It is noted that the solid lines on the graphs indicate experimental data, whereas the dashed lines are interpolated data.

2.4.3.2 Pitching Moment Coefficient The pitching moment coefficients discussed in this section are illustrated in the same manner as the normal force coefficients of the preceding discussion. The listing of the figures with the associated variables and parameters is given in Table 2.4.4. The applicability of the power-off pitching moments is shown in Tables 2.4.1 through 2.4.3 of Section 2.4.2.

The pitching moment coefficients refer to the stability axis system described in Section 2.4.1. The coefficients are based on a center of gravity at 50 percent of the chord, (percent of the body diameter aft of the leading edge). However, the anticipated center of gravity for the PYE WACKET FTV will be located at 43 percent of the chord, and, based on this, the pitching moments would be modified by the following expression:

$$C_{m(0.43C)} = C_{m(0.50C)} - 0.07 C_N \quad 2.4.3$$

or, in a more general expression,

$$C_{mC.G.} = C_{m(0.50C)} - \left(\frac{\Delta x}{c}\right) C_N \quad 2.4.4$$

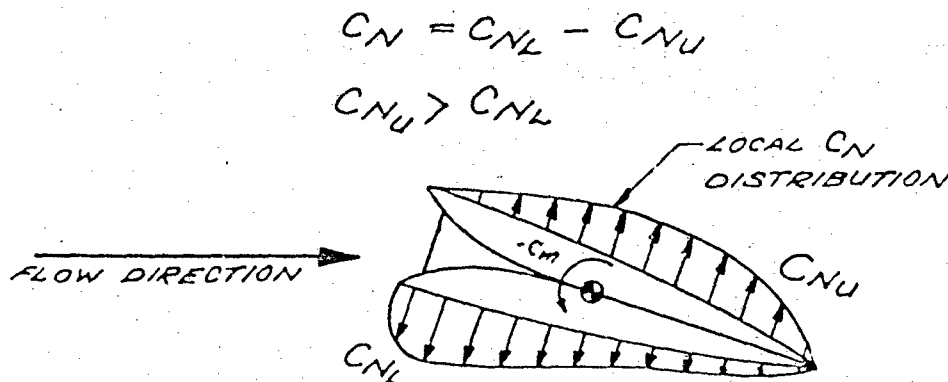
For positive coefficients of normal force, positive pitching moments decrease as the center of gravity is moved forward.

A comparison of the pitching moment coefficients of Figures 2.4.6 a, b, and c with the normal force coefficients of Figures 2.4.3 a, b, and c, $\alpha = 150^\circ$, indicates that the pitching moment coefficient becomes positive at approximately 10 degrees angle of attack for $M = 0.6, 0.8$,

SECRET

and 0.9, whereas, the normal force coefficient becomes positive at angles of attack of 5.0, 8.7, and 9.6 degrees, respectively. For the angle of attack range for both negative pitching moment and normal force coefficients, the center of pressure is located ahead of the center of gravity. With negative pitching moment and positive normal force coefficients, the center of pressure is located behind the center of gravity. Theoretically, the center of pressure may lie off the configuration. However, the more practical view of this situation is to consider two individual center of pressure locations on the top and bottom surfaces (see sketch below).

The phenomenon of pitching moment and normal force both being negative at positive angles of attack for the $\delta = 180^\circ$ power-off condition, subsonically and transonically, is caused by flow separation on the leading edge of the blunt base. Flow separation over the upper surface is more severe than over the lower (windward) surface, resulting in a greater reduction in the absolute value of the pressure coefficient on the upper surface than on the bottom surface. Hence, a negative normal force is produced. For the condition of negative pitching moment in conjunction with a small positive normal force, the forces may be distributed as shown in the sketch below.



As was noted in the discussion of normal force coefficient, the $\delta = 90^\circ$ values of C_q were slightly larger than the $\delta = 0^\circ$ values for subsonic and transonic flow, and for supersonic flow the reverse condition existed. Pitching moment coefficients, however, are greater at $\delta = 90^\circ$ than at $\delta = 0^\circ$ throughout the entire Mach number range (see Figure 2.4.6). Therefore, in order to satisfy the condition of an increase in pitching moment and a decrease in normal force for supersonic flow, a shift in center of pressure toward the leading edge

SECRET

SECRET

FIGURE 3-4-6a
PYE WACKET FTV

VARIAION OF PITCHING MOMENT COEFFICIENT
WITH ANGLE OF ATTACK

$C/G = 0.50$

POWER-OFF

$V/C = 0.21$

$M = 0.6$

$\beta = 0^\circ$

$\beta = 90^\circ$

α - DEGREES

$\beta = 180^\circ$

0.08

0.06

0.04

0.02

0

-0.02

-0.04

C_m

2

4

6

8

10

12

14

16

2.62

SECRET

SECRET

FIGURE 2.4.6b

PYE WACKET FTV

VARIATION OF PITCHING MOMENT COEFFICIENT
WITH ANGLE OF ATTACK

$C.G. = 0.30$
POWER-OFF

$c/c = 0.21$
 $M = 0.8$

0.08

C_m

0.06

0.04

0.02

0

-0.02

-0.04

$\beta = 90^\circ$

$\beta = 0^\circ$

16

14

12

10

8

6

4

2

α - DEGREES

$\beta = 180^\circ$

2.63

SECRET

SECRET

FIGURE 2.4.6.6

DYE WACKET FTV

VARIATION OF PITCHING MOMENT COEFFICIENT
WITH ANGLE OF ATTACK

C.G. = 0.50

POWER-OFF

M = 0.9

$\delta/c = 0.21$

$\beta = 90^\circ$

$\beta = 0^\circ$

$\alpha \sim \text{DEGREES}$

$\beta = 180^\circ$

0.08

0.06

0.04

0.02

0

-0.02

-0.04

Cm_y

16

14

12

10

8

6

4

2

2.64

SECRET

SECRET

FIGURE 2.4.6a

PYE WACKET FTV

VARIAION OF PITCHING MOMENT COEFFICIENT
WITH ANGLE OF ATTACK

$C_G = 0.30$

POWER-OFF

$M = 40$

$\beta = 0^\circ$

$\beta = 90^\circ$

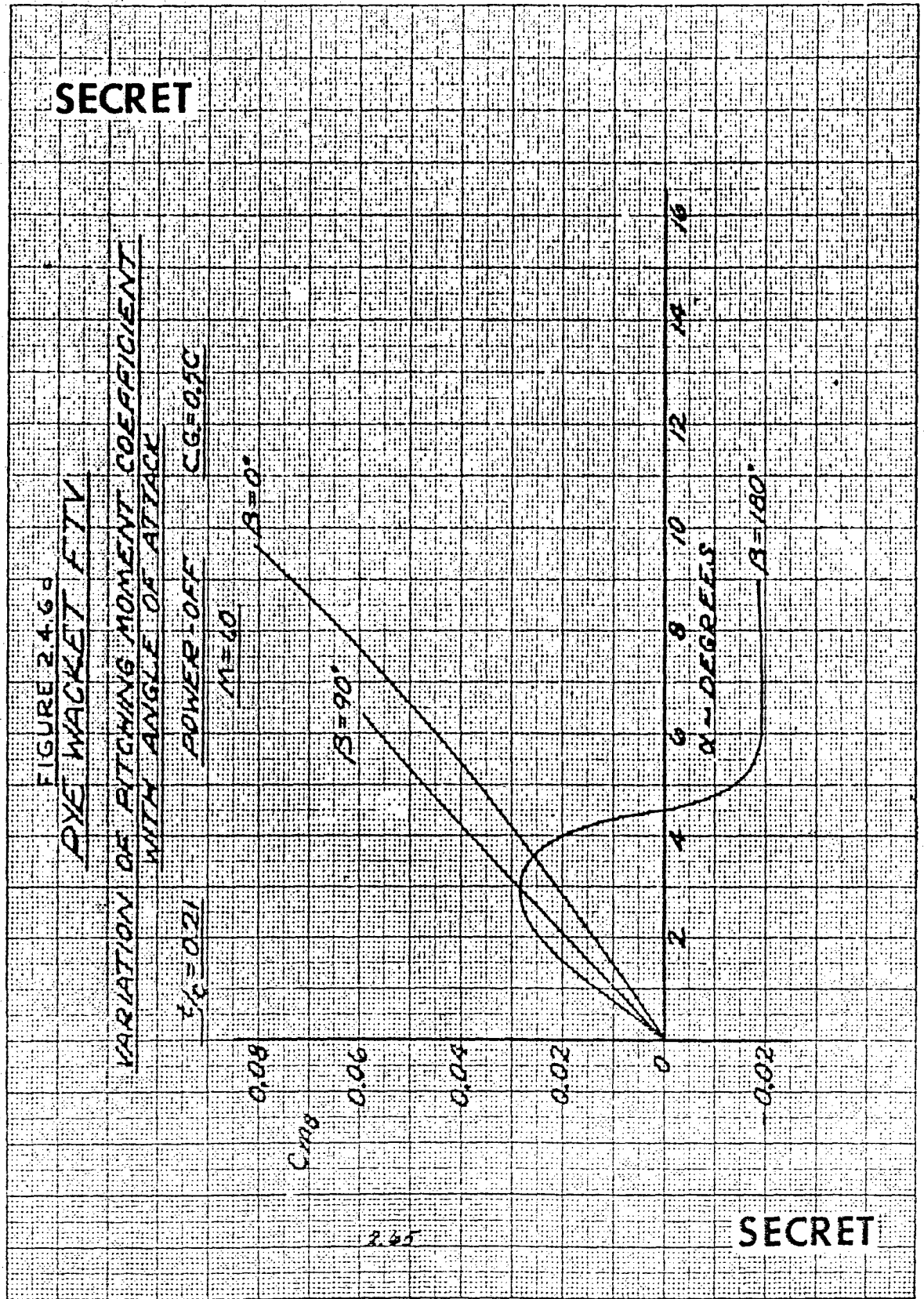
$\beta = 180^\circ$

C_{m0}

α - DEGREES

2.45

SECRET



SECRET

FIGURE 2.4.6c

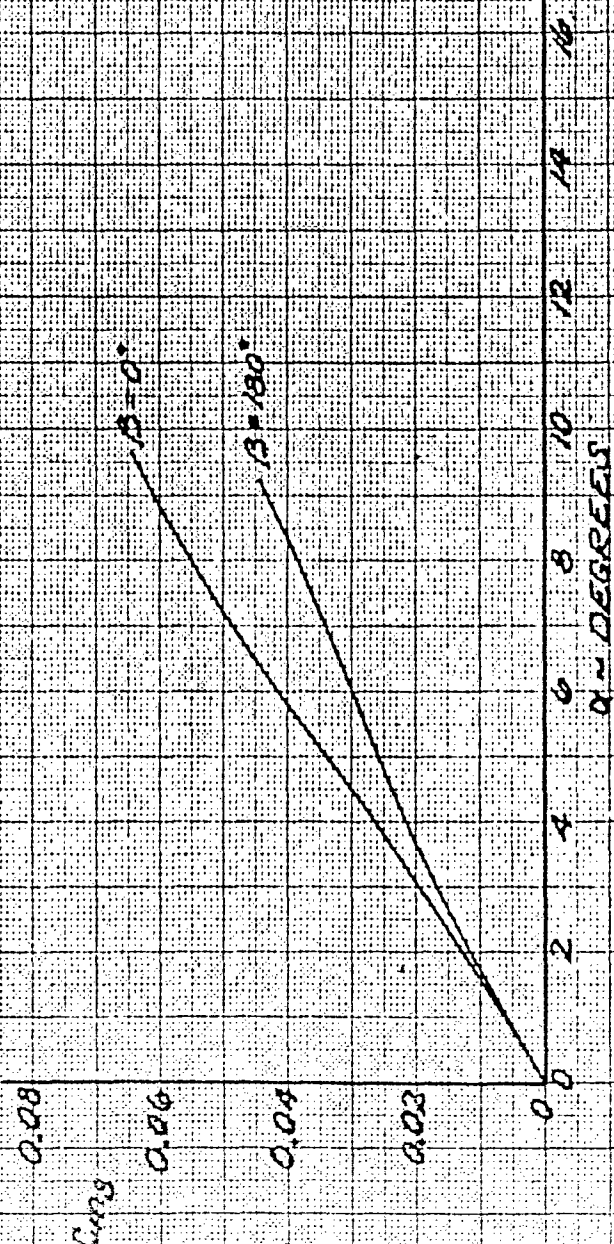
PYE WACKET FTV

VARIATION OF PITCHING MOMENT COEFFICIENT
WITH ANGLE OF ATTACK

$C_{L/C} = 0.21$

POWER-OFF

$M = 1.2$



2.66

SECRET

SECRET

FIGURE 2-165

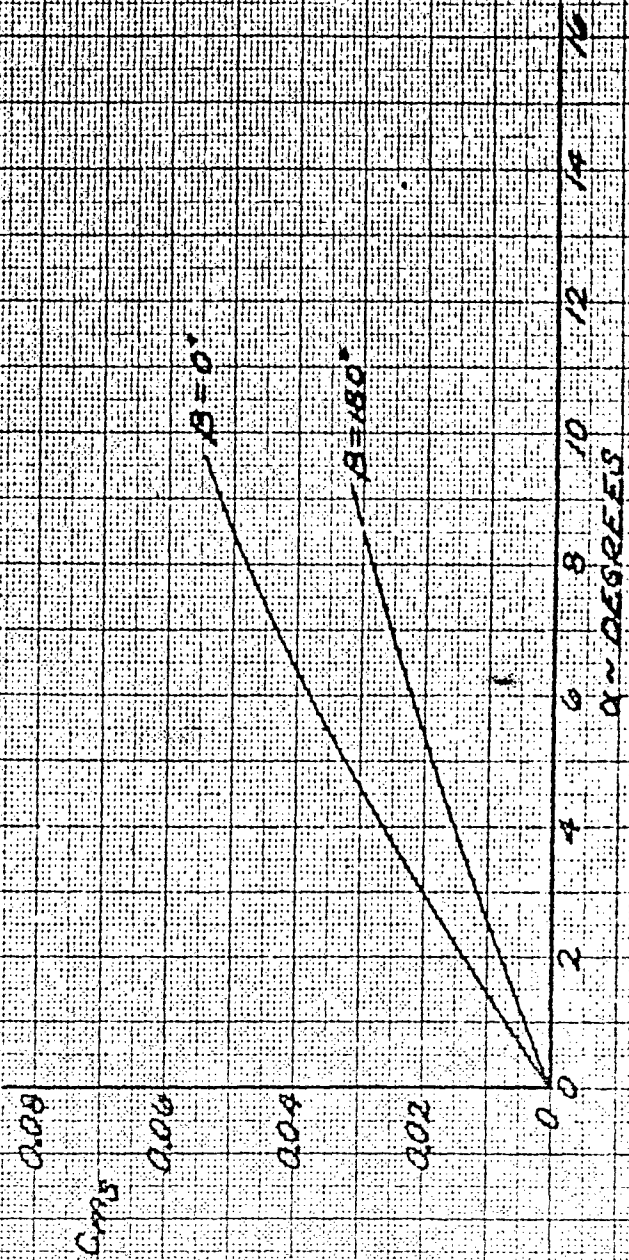
PYE WACKET FTV

VARIAION OF PITCHING MOMENT COEFFICIENT
WITH ANGLE OF ATTACK

$C_G = 0.21$

POWER-OFF

$M = 1.8$



SECRET

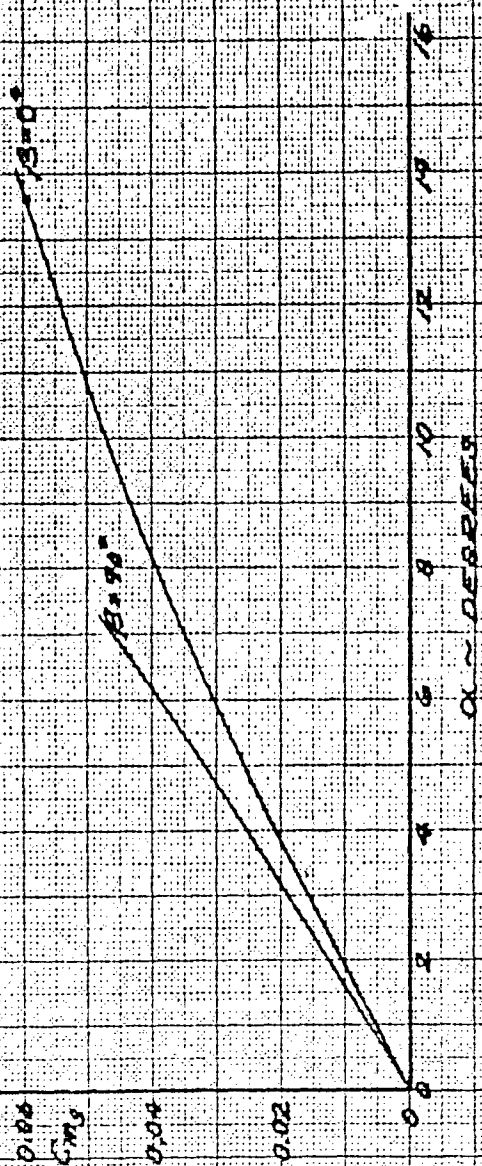
SECRET

FIGURE 2.4.6.9

PYE WACKET FTH
VARIATION OF PITCHING MOMENT COEFFICIENT

WITH ANGLE OF ATTACK
 $\eta_e = 0.21$ POWER OFF

$M = 1.30$
 $C.G. = 0.50$



2.68

SECRET

SECRET

FIGURE 2.4.6 h

PYE WACKET FTV

VARIAION OF PITCHING MOMENT COEFFICIENT
WITH ANGLE OF ATTACK

$$\frac{y}{c} = 0.21$$

POWER-OFF

$$M = 1.6$$

$$C.G. = 0.5C$$

0.08

C_{mg}

0.06

0.04

0.02

0.0

$\beta = 90^\circ$

$\beta = 0^\circ$

$\beta = 180^\circ$

0

2

4

6

8

10

12

14

16

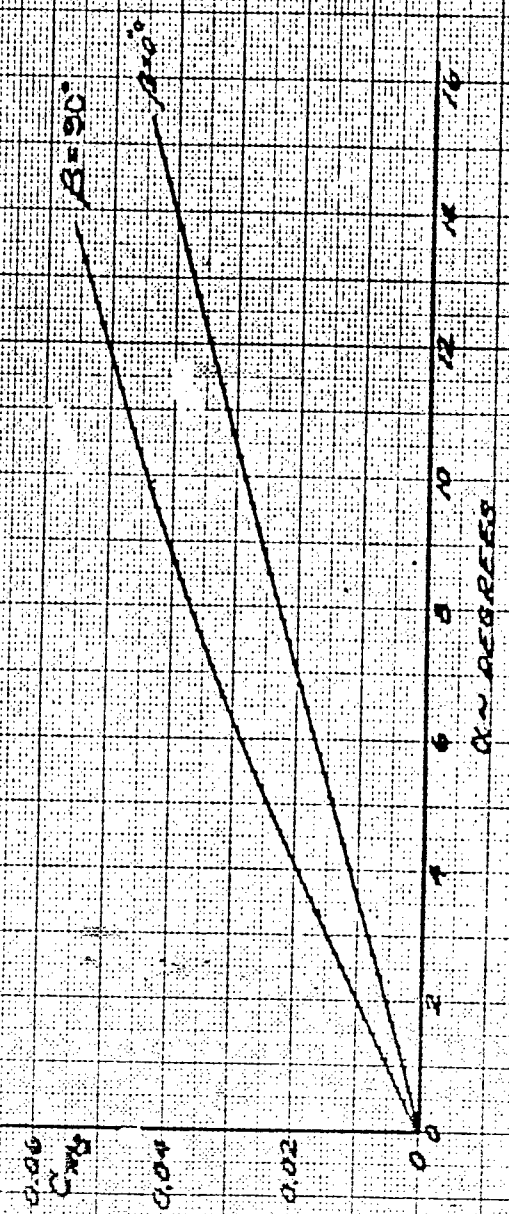
α - DEGREES

269

SECRET

SECRET

FIGURE 2.4.61
PYE WACKET FLY
VARIATION OF PITCHING MOMENT COEFFICIENT
WITH ANGLE OF ATTACK
 $\beta_0 = 0.21$
POWER-OFF CG = 0.50
 $M = 2.0$



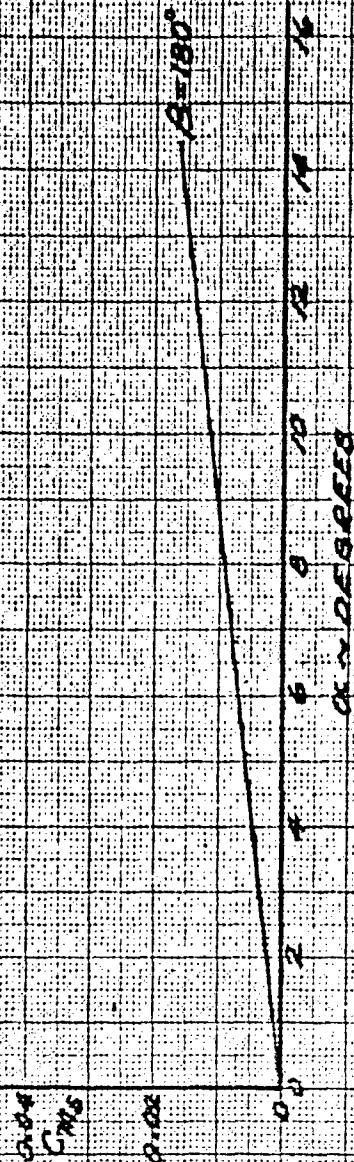
2.70

SECRET

SECRET

FIGURE 2.4.6J

OYE WACKET FLY
VARIATION OF PITCHING MOMENT COEFFICIENT
WITH ANGLE OF ATTACK
 $Y_0 = 0.01$ POWER OFF CG = 0.10
 $M = 2.5$



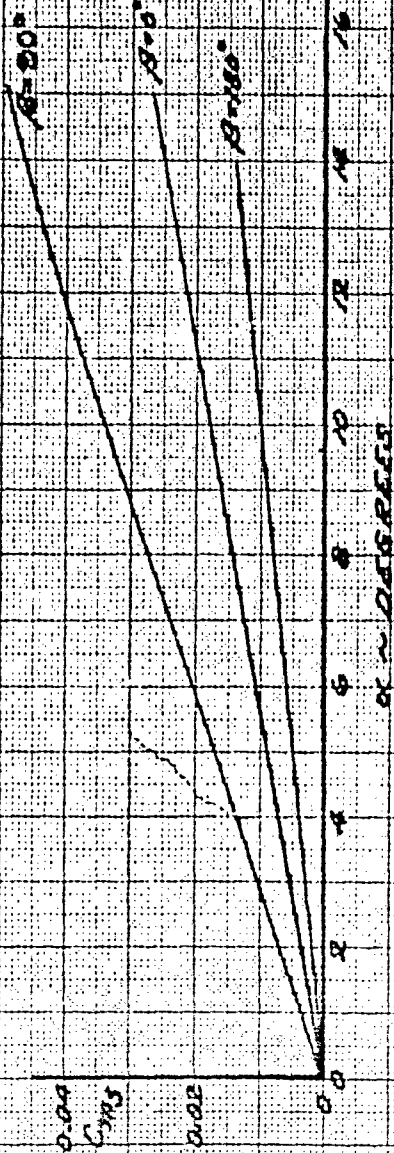
SECRET

SECRET

FIGURE 24.6 R

OYE WACKET FLY
VARIATION OF PITCHING MOMENT COEFFICIENT
WITH ANGLE OF ATTACK

$Y_F = 0.21$ POWER OFF $C_G = 0.50$
 $M = 3.0$

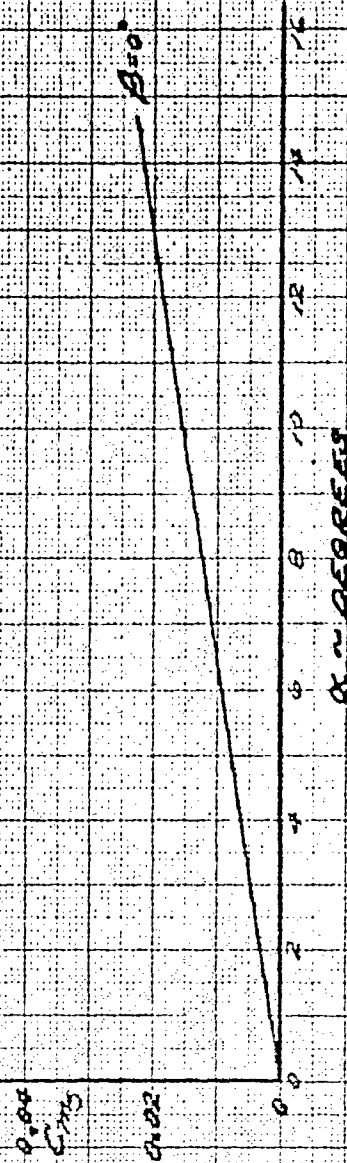


SECRET

SECRET

FIGURE 24.6.1

PYE WACKET FTV
 VARIATION OF PITCHING MOMENT COEFFICIENT
 WITH ANGLE OF ATTACK
 $\beta = 0.21$ POWER-OFF $CO = 0.50$
 $M = 4.0$

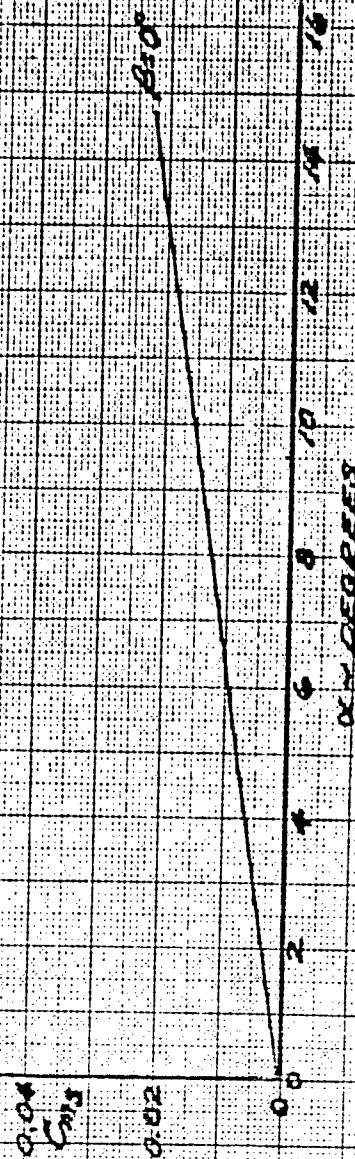


SECRET

SECRET

FIGURE 2.4.6 m

PYE WACKET FIV
VARIATION OF PITCHING MOMENT COEFFICIENT
WITH ANGLE OF ATTACK
 $\beta_0 = 0.21$ POWER-OFF CG = 0.50
 $M = 5.0$



SECRET

SECRET

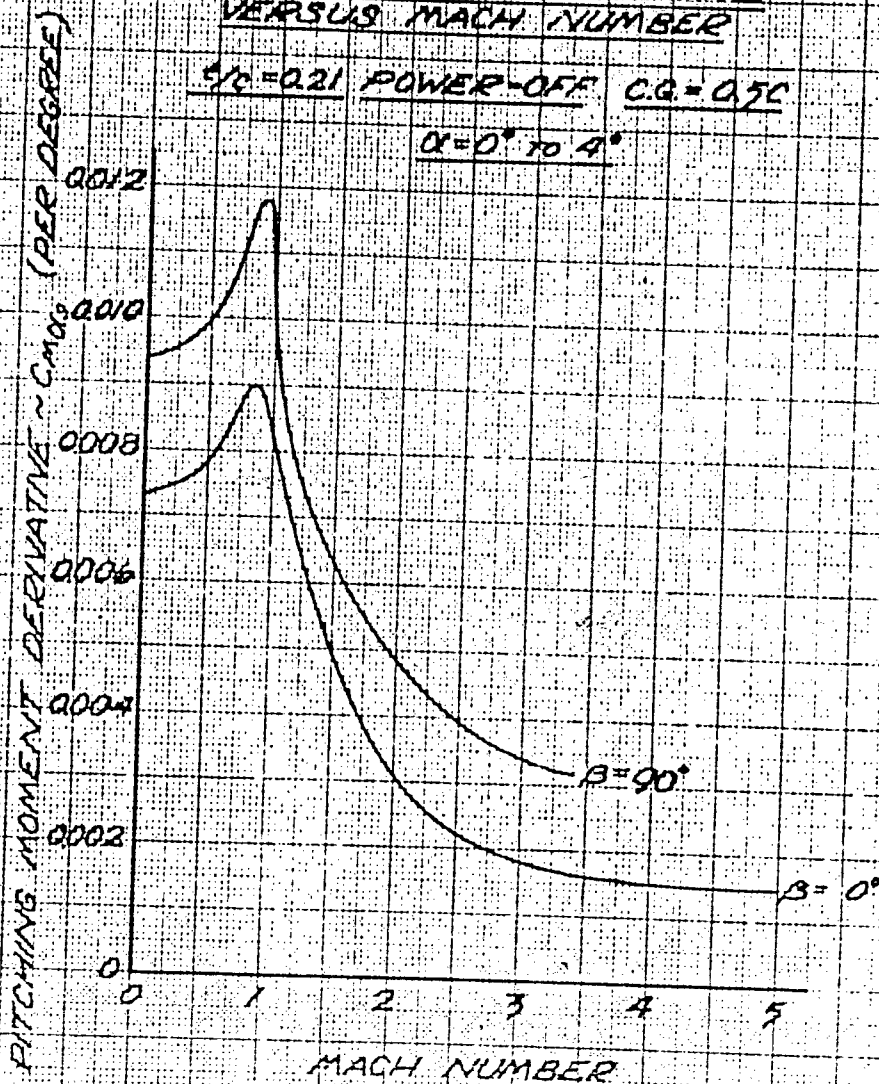
FIGURE 2.4.7a

PYE WACKET FTV

PITCHING MOMENT DERIVATIVE
VERSUS MACH NUMBER

$S/C = 0.21$ POWER-OFF $C.G. = 0.7C$

$\alpha = 0^\circ$ TO 4°



SECRET

SECRET

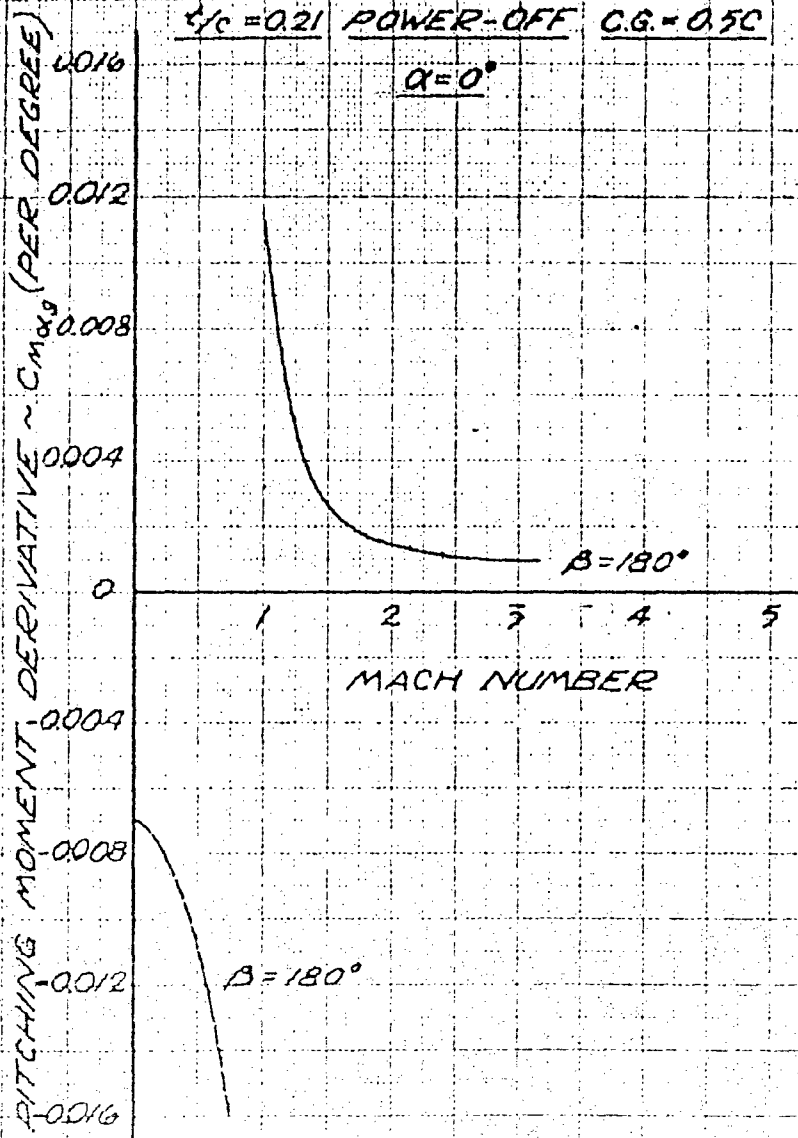
FIGURE 2.4.7.6

PYE WACKET FTV

PITCHING MOMENT DERIVATIVE
VERSUS MACH NUMBER

$x/c = 0.21$ POWER-OFF C.G. = 0.50

$\alpha = 0^\circ$



2.74

SECRET

SECRET

FIGURE 2.4.8 a

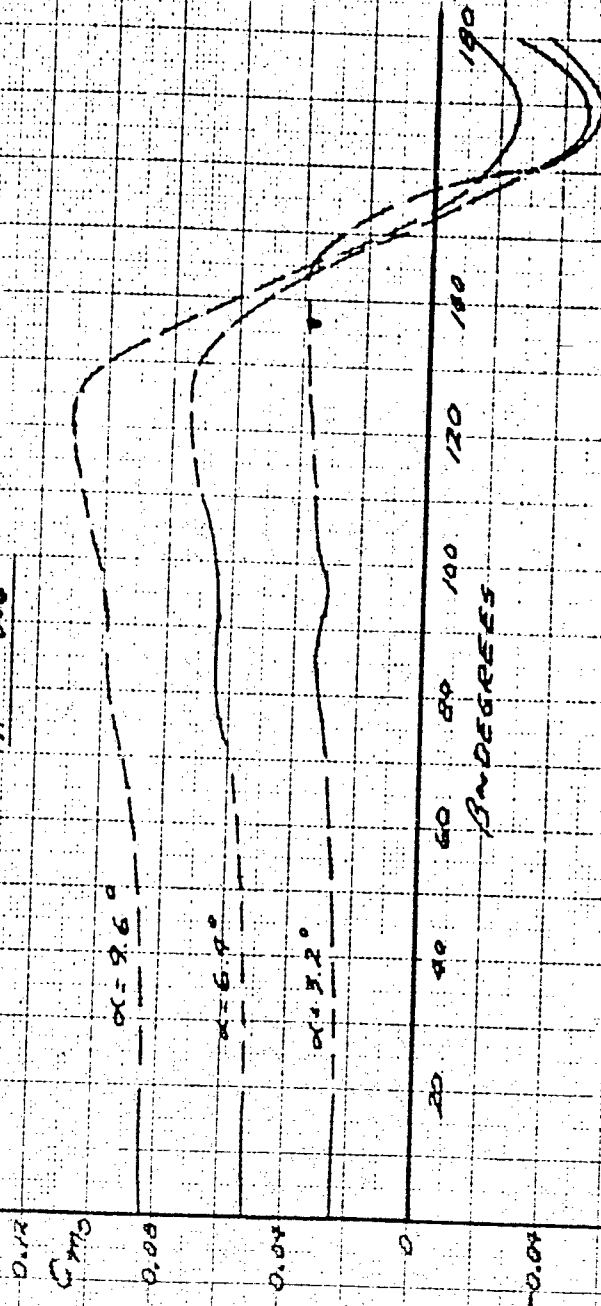
PVF WACKET FIV
VARIATION OF PITCHING MOMENT COEFFICIENT
WITH ANGLE OF SIDESLIP

$$\frac{C_{L_0}}{C_D} = 0.50$$

$$\frac{C_{L_0}}{C_D} = 0.21$$

$$M = 0.6$$

POWER-OFF



2.77

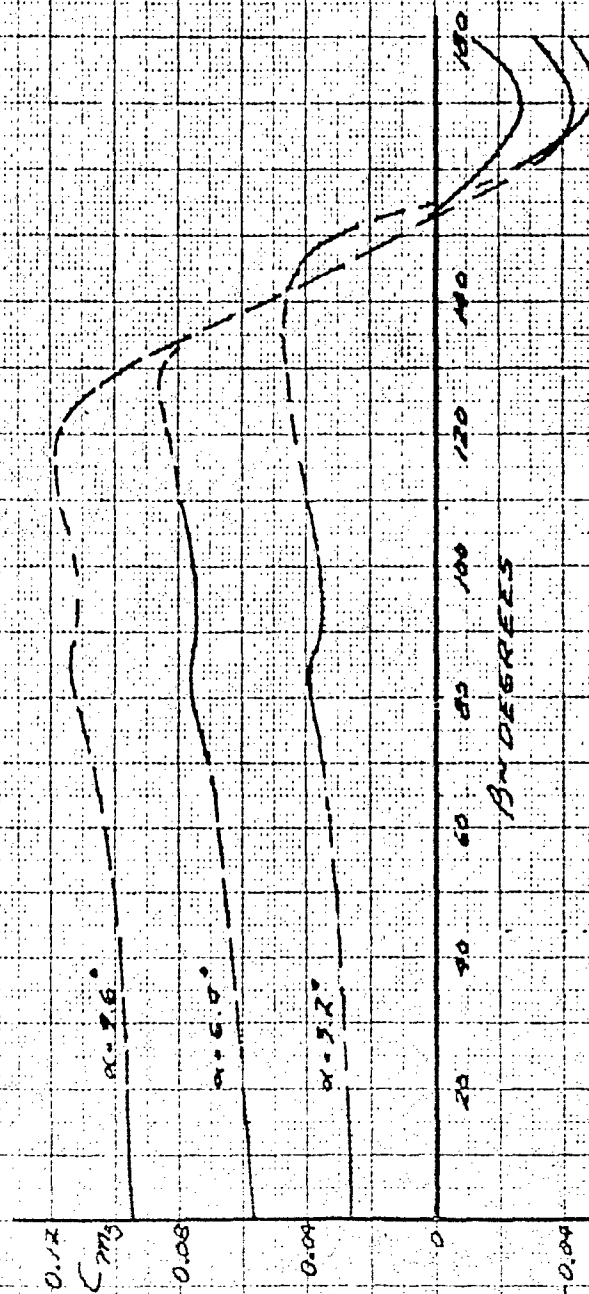
SECRET

SECRET

FIGURE 2.4.3b

PYE WACKET FTV
VARIATION OF PITCHING MOMENT COEFFICIENT
WITH ANGLE OF SIDESLIP

CG = 0.25
CYC = 0.21
M = 0.80
POWER-OFF

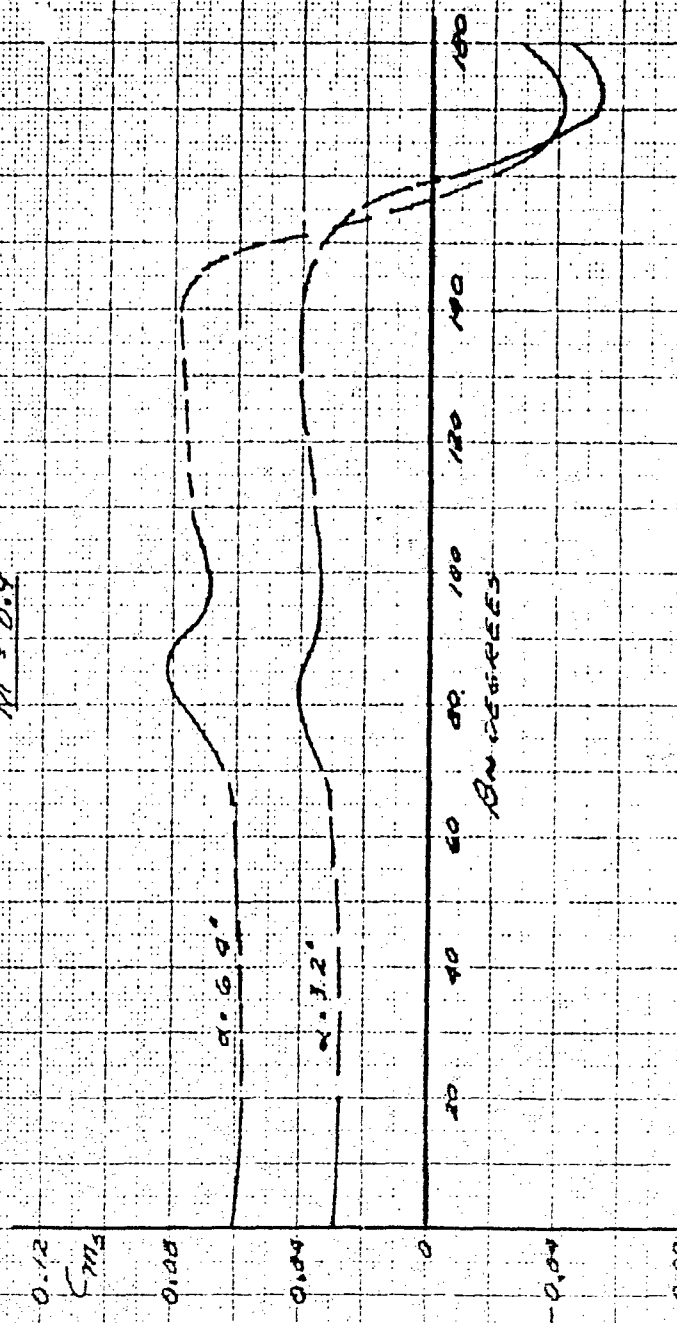


2.70

SECRET

SECRET

FIGURE 2.4.8C
 FYE WACKET FTV
 VARIATION OF PITCHING MOMENT COEFFICIENT
 WITH ANGLE OF Sideslip
 $C.G. = 0.5C$
 $\eta/C = 0.21$
 $M = 0.9$
 POWER OFF

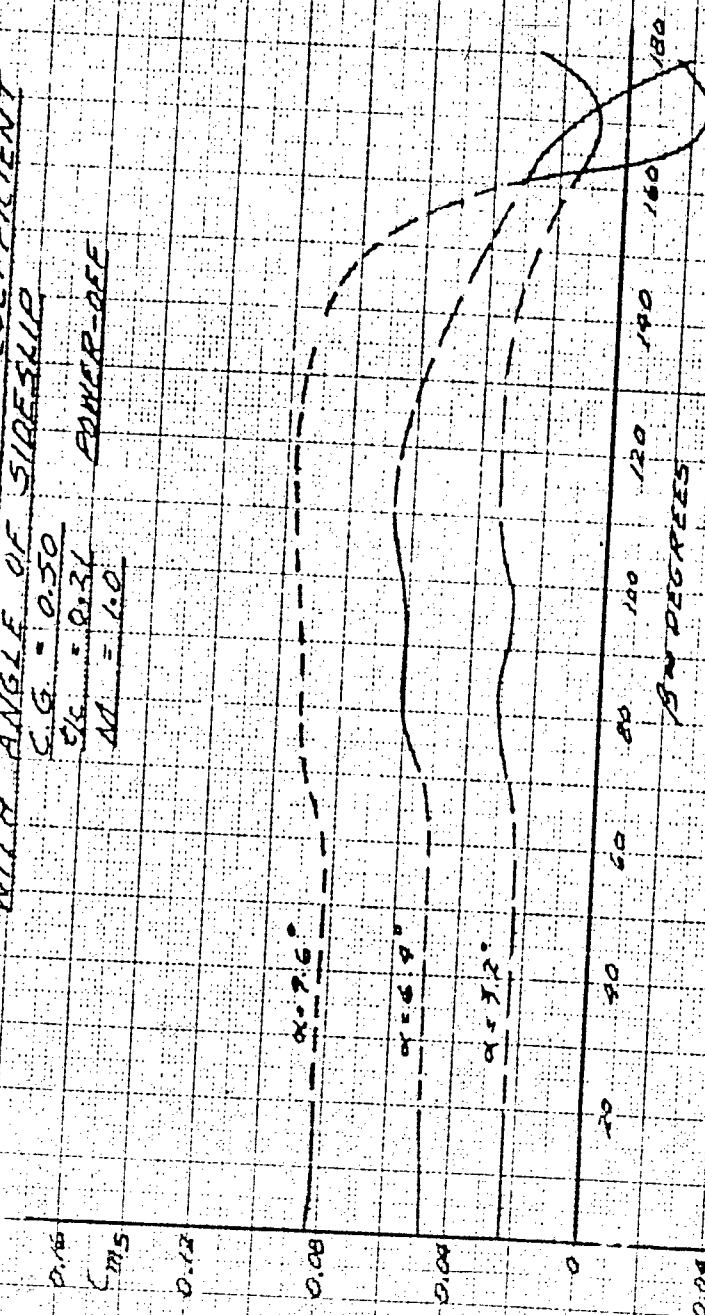


SECRET

SECRET

FIGURE 2.4.8d

PYE WACKET FIV
VARIATION OF PITCHING MOMENT COEFFICIENT
WITH ANGLE OF SIDEWIND
 $C.G. = 0.50$
 $C/L = 0.31$
 $M = 1.0$
POWER-OFF



SECRET

must occur. This condition is illustrated in the center of pressure curves of Figures 2.4.12 and 2.4.13, where the center of pressure for $\beta = 90^\circ$ is closer to the leading edge than the center of pressure at $\beta = 0^\circ$ over the complete Mach number range.

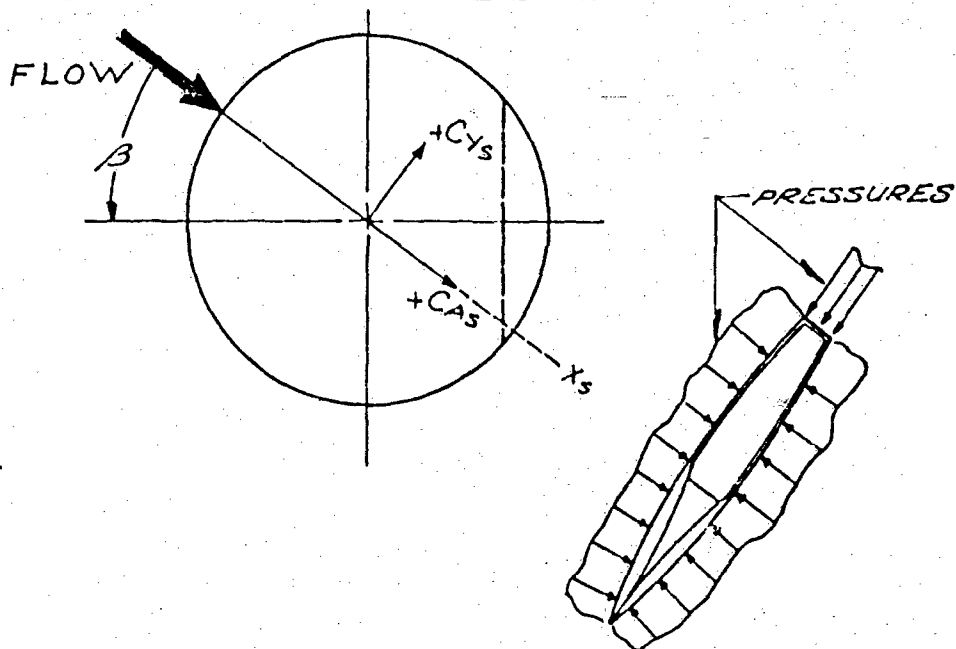
The slope of the pitching moment coefficient with respect to angle of attack, C_{m_α} , is presented in Figure 2.4.7 as a function of Mach number. The pitching moment derivative was obtained by taking the tangent slope of the pitching moment coefficient at an angle of attack of zero degrees. Angle of sideslip is presented as a parameter for $\beta = 0^\circ, 90^\circ$ and 180° . As illustrated in the figure, the configuration has a restoring moment only at $\beta = 180^\circ$ between Mach numbers of zero and approximately 0.9. However, the actual magnitude of the slope of C_{m_α} for this Mach number range should be treated with caution due to the fact that experimental values of pitching moment at $\alpha = 0$ were obtained only at $M = 0.6$ for the subsonic Mach numbers.

The variation of power-off pitching moment coefficient with angle of sideslip from 0° to 180° is shown in Figure 2.4.8. The values as a function of sideslip angle are presented for Mach numbers of 0.6, 0.8, 0.9, and 1.0. As evidenced from the data of Figures 2.4.8 a, b, and c, the configuration has a restoring moment for approximately 25 degrees of sideslip angle about a reference angle of $\beta = 180^\circ$. However, it is emphasized that this condition is realistic only for main rockets off. No estimates have been made of the characteristics of pitching moment with main rockets on.

2.4.3.3 Side Force Coefficient The variation of side force coefficient with sideslip angle, angle of attack as a parameter, is shown for Mach numbers of 0.6, 0.8, 0.9, and 1.0 in Figure 2.4.9. The data shows that C_{Y_β} may be either positive or negative, depending on the sideslip angle.

The side force is the result of lateral components of pressure acting on the periphery and on the top and bottom surfaces of the configuration as shown in the sketch below. If the missile were symmetric about the x_β axis, the pressures and areas on each side of the axis would be equal. As a result there would be no side force. Because of the aft location of the maximum thickness of PYE WACKET, the missile is symmetric only at β of 0° and 180° . Hence, it is apparent that flow over the missile will produce a variation of side force coefficient with sideslip angle.

SECRET



The lateral pressures on the lifting surface, the blunt sides, and the base, all contribute to the side force. At zero angle of attack, and β greater than 90° , the flow impacts directly on one blunt side and the base of the missile. As the impact pressures are large, the side and base contribute the major portion of the side force in the region of β from 90° to 180° . At angles of β from 0 to 90° the pressures are somewhat equal on all the surfaces and it is difficult to predict which surfaces cause the largest side forces.

The data for the Mach numbers of 0.6, 0.8 and 0.9 show that C_{Y_s} is negative up to a sideslip angle of approximately 160° , and remains positive from 160° to 180° . This change in sign is due to the fact that the component of side force resulting from the base approaches zero, while the blunt side is in such a position to contribute a positive side force as shown in the following sketch. From 90° to 160° , the relative position of the blunt side and the base is such to cause a resultant negative side force coefficient.

SECRET

SECRET

FIGURE 24.9a

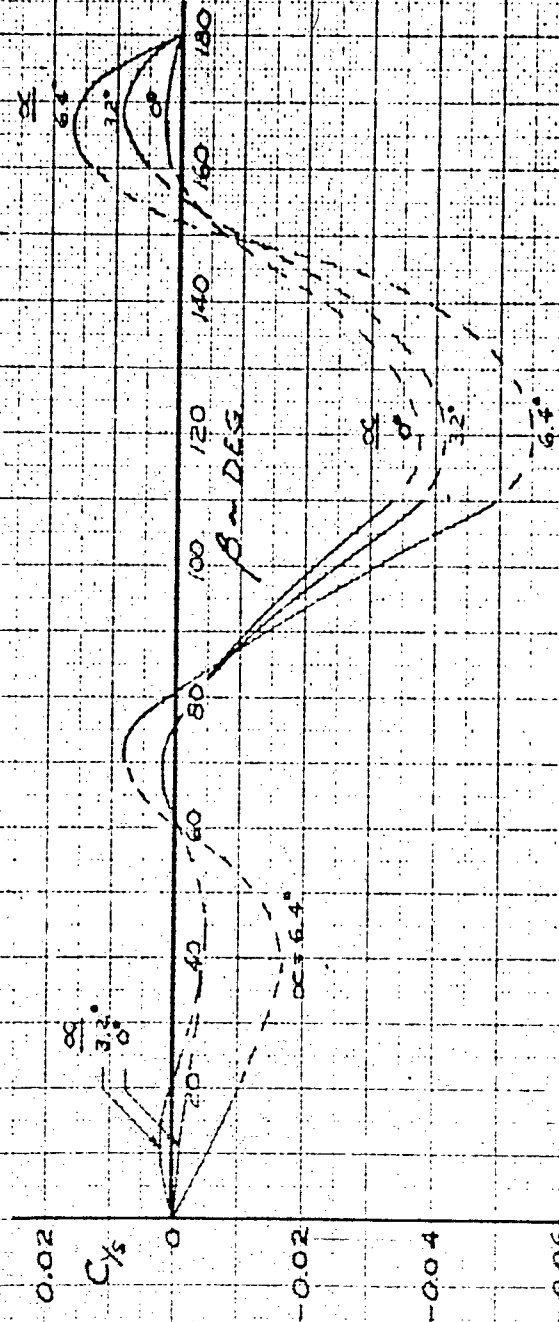
PYE WACKET FTV

VARIATION OF SIDE FORCE COEFFICIENT WITH ANGLE OF SIDESLIP

$C_{Ys} = 0.21$

POWER-OFF

$M = 0.6$



2.83

SECRET

SECRET

FIGURE 2.4.9b

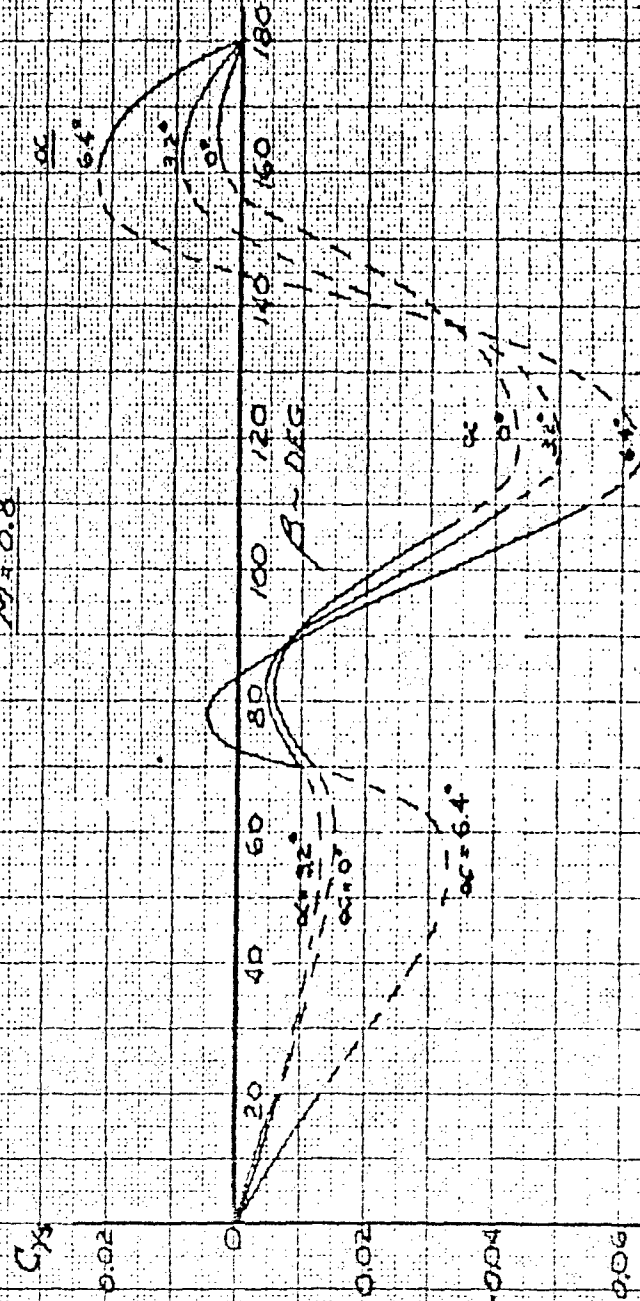
PYE WACKET FIV

VARIAION OF SIDE FORCE COEFFICIENT WITH ANGLE OF SIDESLIP

$SE = 0.21$

POWER-OFF

$MA = 0.8$



SECRET

SECRET

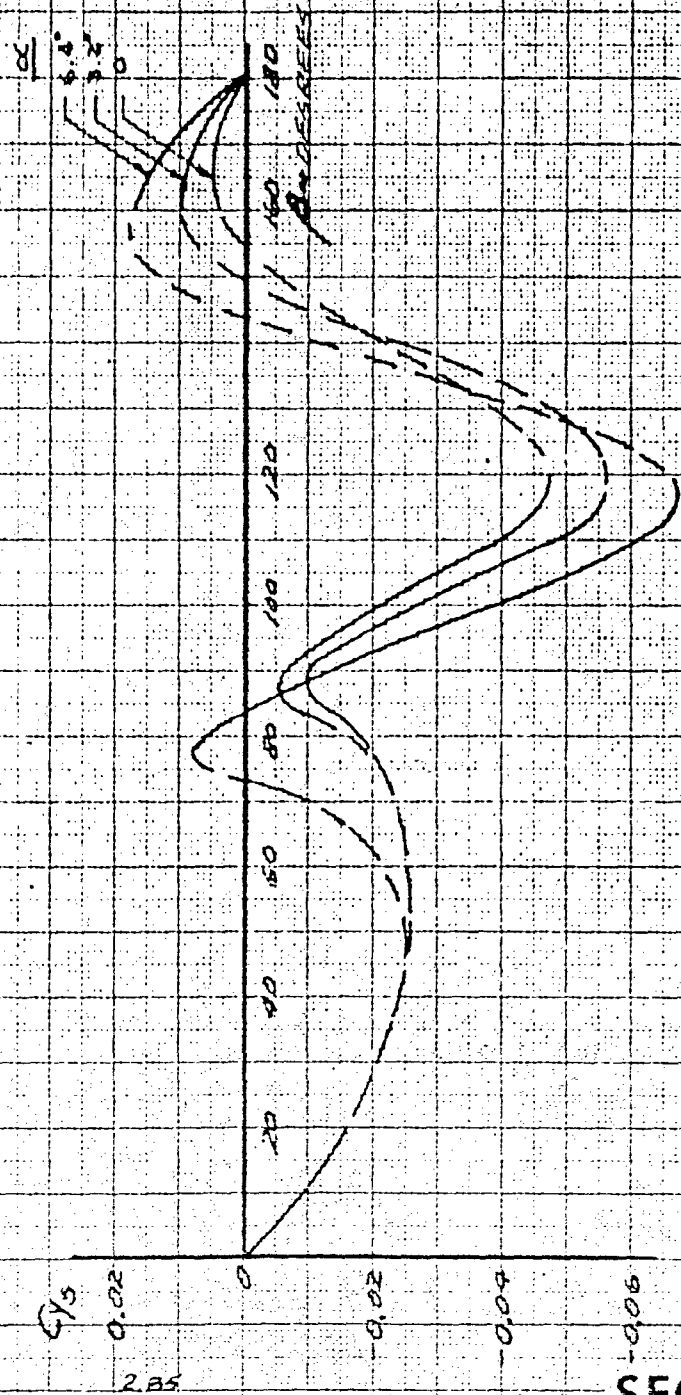
FIGURE 2.4.9c

PYE WACKET FTV

VARIATION OF SIDE FORCE COEFFICIENT WITH ANGLE OF SIDESLIP

$C_{Ys} = 0.21$ POWER-OFF

$M = 0.9$

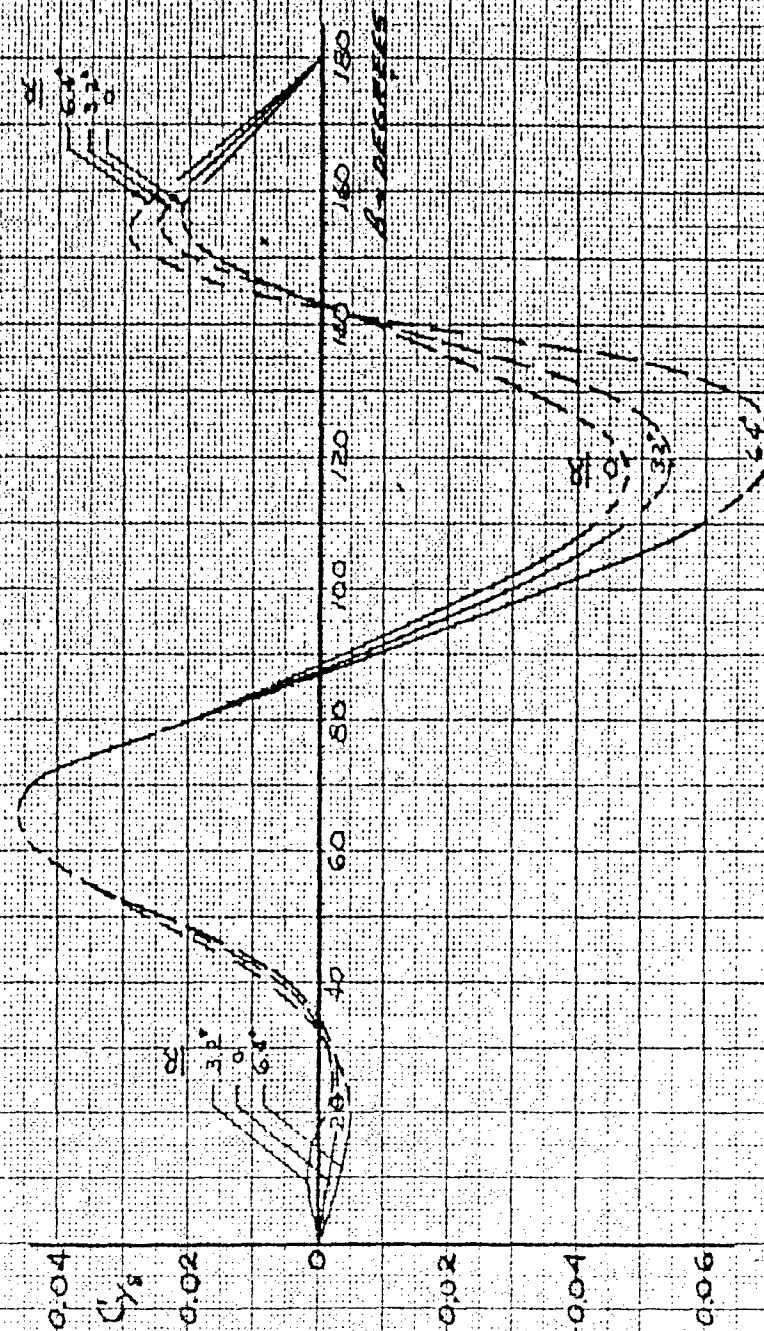


SECRET

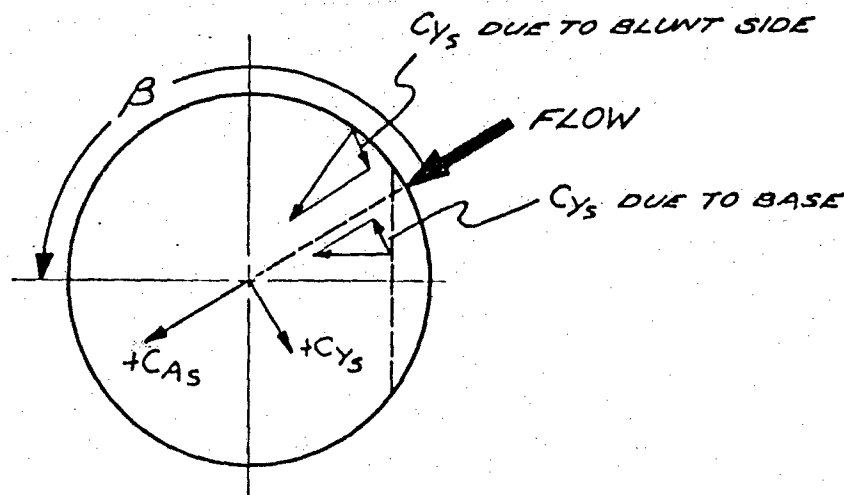
SECRET

FIGURE 2.4.9d

PYE WACKET F1X
 VARIATION OF SIDE FORCE COEFFICIENT WITH ANGLE OF SIDESLIP
 $SK=0.21$ POWER-OFF
 $M=1.0$



SECRET



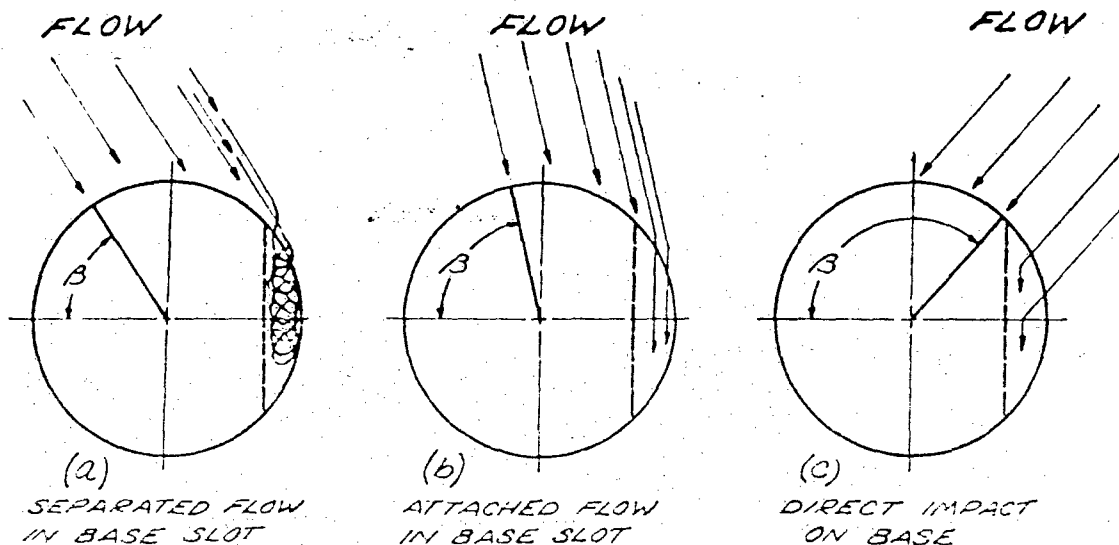
The data at Mach 1.0 shows that C_{Ys} is similar to the subsonic cases beyond a sideslip angle of 100° . However, the C_{Ys} is positive in the region of 40° to 90° . This difference between subsonic and supersonic C_{Ys} in the region of 40° to 90° is due to the effect of the blunt base. The high subsonic or low supersonic local flow expanding around the corner of the base causes extremely low base pressures. The result of these low pressures is a positive side force coefficient.

2.4.3.4 Yawing Moment Coefficient The power-off yawing moment coefficients are shown versus sideslip angle, with angle of attack as a parameter, for various Mach numbers in Figure 2.4.10. A positive C_{ns} indicates that the moment is tending to rotate the nose of the vehicle in a clockwise direction while a negative C_{ns} means that the moments are attempting to rotate it counterclockwise. The data shows that for all Mach numbers the missile can have either positive or negative yawing moment depending on the angle of sideslip. For the subsonic Mach numbers of 0.6, 0.8, and 0.9, C_{ns} is positive from β equal 0° to a β of approximately $+100^\circ$. From Mach 1.0, 1.2, 1.4, and 1.6, C_{ns} remains positive until a β of $+120^\circ$ to $+130^\circ$ is reached. It must be emphasized that the negative yawing moment at large sideslip angles tends to rotate the missile base into the wind. Hence, for launch at β of 180° , the base will tend to remain oriented into the wind, which is the desired flight attitude.

The graphs at the three Mach numbers of 0.6, 0.8, and 0.9 show abrupt increases in C_{ns} between β of 75° to 85° . These sudden increases are attributed to the aerodynamic effects of the blunt base. At angles

SECRET

of sideslip less than 90° , the air must flow around the corner formed by the base and the blunt side of the missile. This expansion around the corner makes the base act much like an airfoil. The general flow patterns are shown in the sketch below. At the minimum value of $C_{n\beta}$ prior to the sudden increase, the flow around the corner is completely separated. (See Sketch a). The pressures on the base slot are close to atmospheric, much like those on the top surface of a stalled wing. Further increase of the sideslip angle reduces the expansion angle of the flow. At a β of about 80° to 85° , the flow expands smoothly around the corner and very low pressures result in the base slot. (See Sketch b). These low pressures cause large positive peak yawing moment coefficients. For the peak $C_{n\beta}$ the pressures on the base are analogous to those on the leeward surface of a wing at high angle of attack just before stalling occurs. As the base becomes aligned with the flow, $\beta = 90^\circ$, the base pressure increases and the positive $C_{n\beta}$ decreases. Further evidence of the stall-like condition should be evident in the $C_{A\beta}$ and $C_{Y\beta}$ curves. However, the flow was very unstable in the pertinent β range and the curves were faired smoothly through scattered data points. Hence, the faired $C_{Y\beta}$ and $C_{A\beta}$ data do not show the stall. The stall was not evident in the data for Mach number larger than 0.9. Once the angle of sideslip has increased beyond a β of 90° , direct impact on the base results in extremely high base pressures (See Sketch c). The increasing pressures cause the yawing moment to become negative as β increases to 180 degrees. This holds true for both subsonic and supersonic flight.



SECRET

SECRET

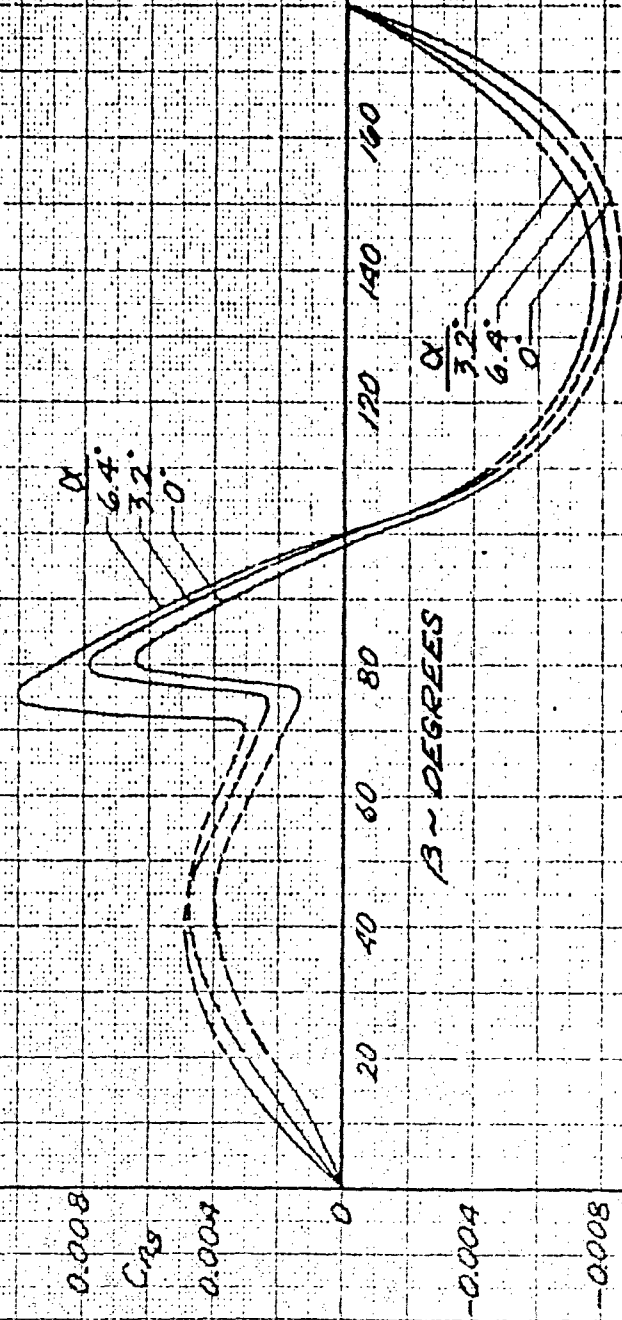
FIGURE 2.4.10a

PYE WACKET FTV

VARIATION OF YAWING MOMENT COEFFICIENT

WITH ANGLE OF SIDESLIP

$M = 0.6$ $C_G = 0.50$ $\beta = 0.21$ POWER-OFF



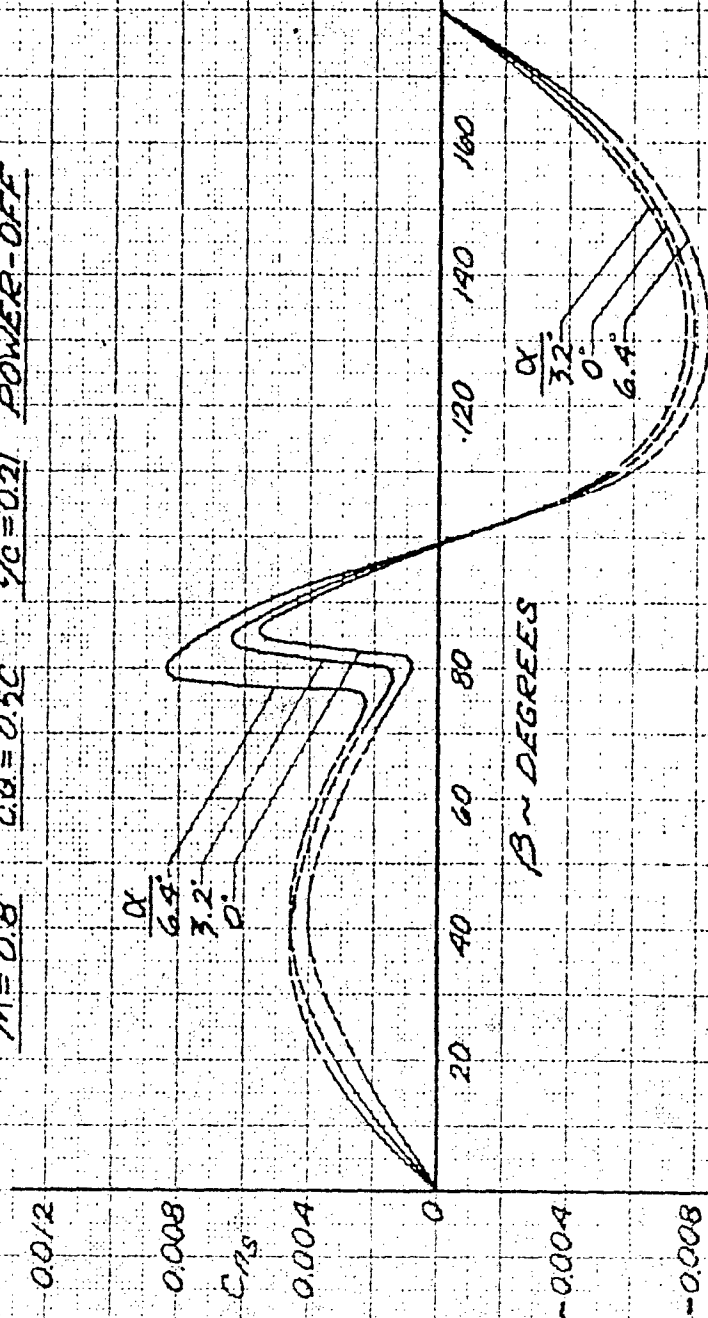
SECRET

SECRET

FIGURE 2.4.10 b
PYE WACKET FTV

VARIATION OF YAWING MOMENT COEFFICIENT
WITH ANGLE OF SIDESLIP

$M = 0.8$ $C_D = 0.5C$ $\gamma_C = 0.21$ POWER-OFF



SECRET

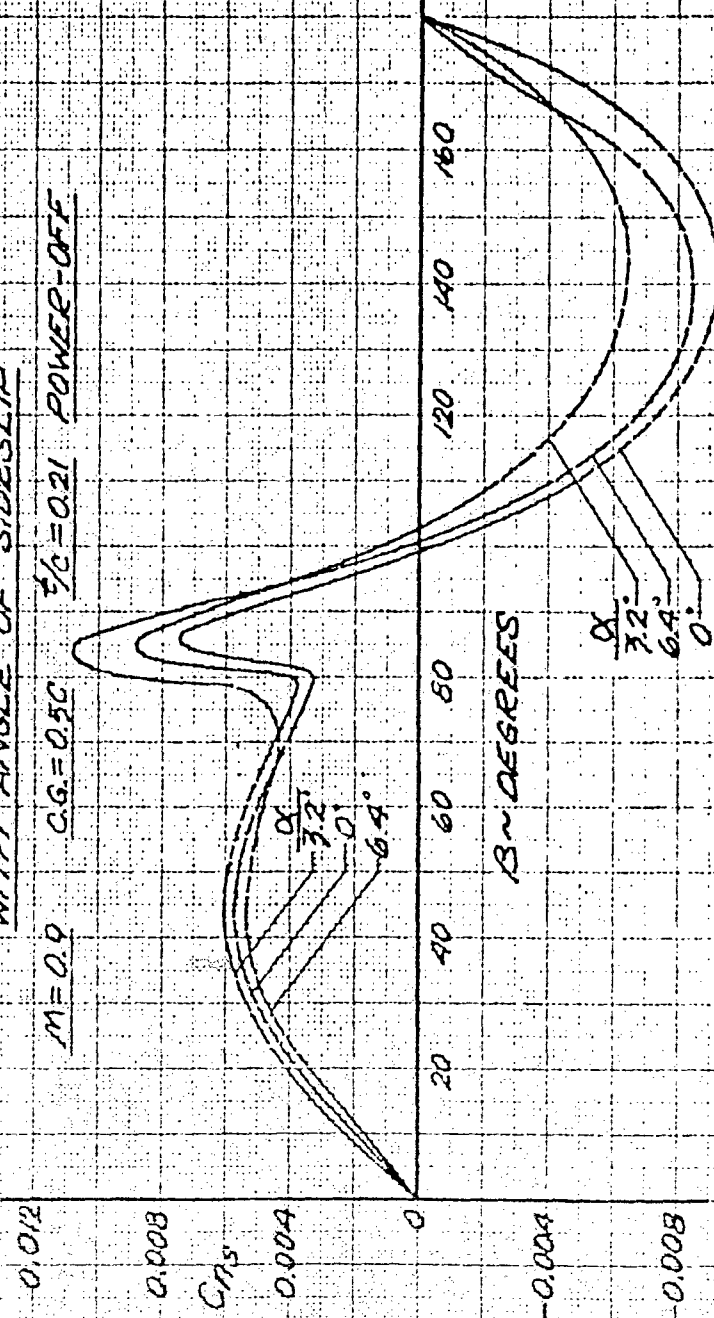
SECRET

FIGURE 2.4.105

PYE WACKET FTV

VARIATION OF YAWING MOMENT COEFFICIENT
WITH ANGLE OF SIDESLIP

$M=0.9$ $C.G.=0.50$ $\frac{1}{2}C=0.21$ POWER-OFF



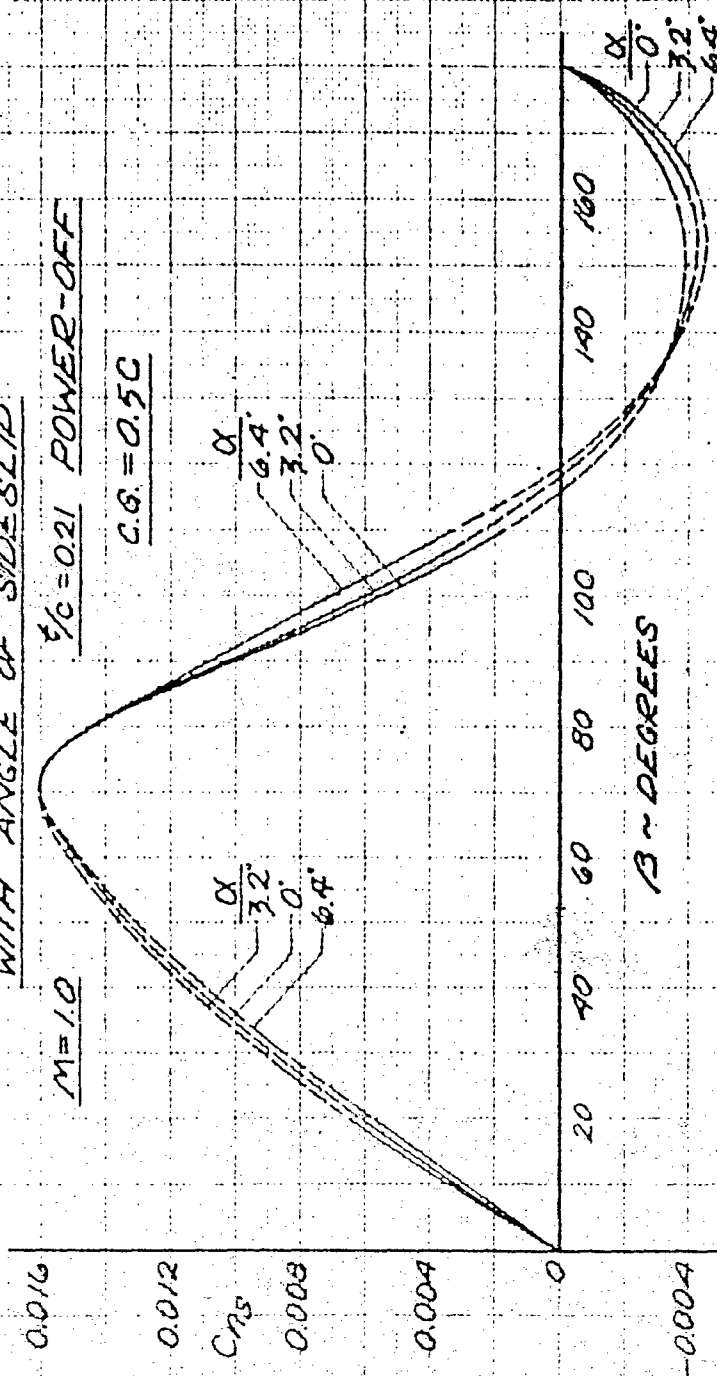
SECRET

SECRET

FIGURE 2.4.10 d

PYE WACKET FTV

VARIATION OF YAWING MOMENT COEFFICIENT
WITH ANGLE OF SIDESLIP



2.92

SECRET

SECRET

FIGURE 2.4.10c

PYE WACKET FTV

VARIATION OF YAWING MOMENT COEFFICIENT
WITH ANGLE OF SIDESLIP

$M=1.2$
 $\frac{1}{2}\rho=0.21$ POWER-OFF

$C.G.=0.5C$

$\alpha=0^\circ$

β - DEGREES

0.016
0.012
 $C_{Y\beta}$
0.008
0.004
0
-0.004

20 40 60 80 100 120 140 160 180

2.93

SECRET

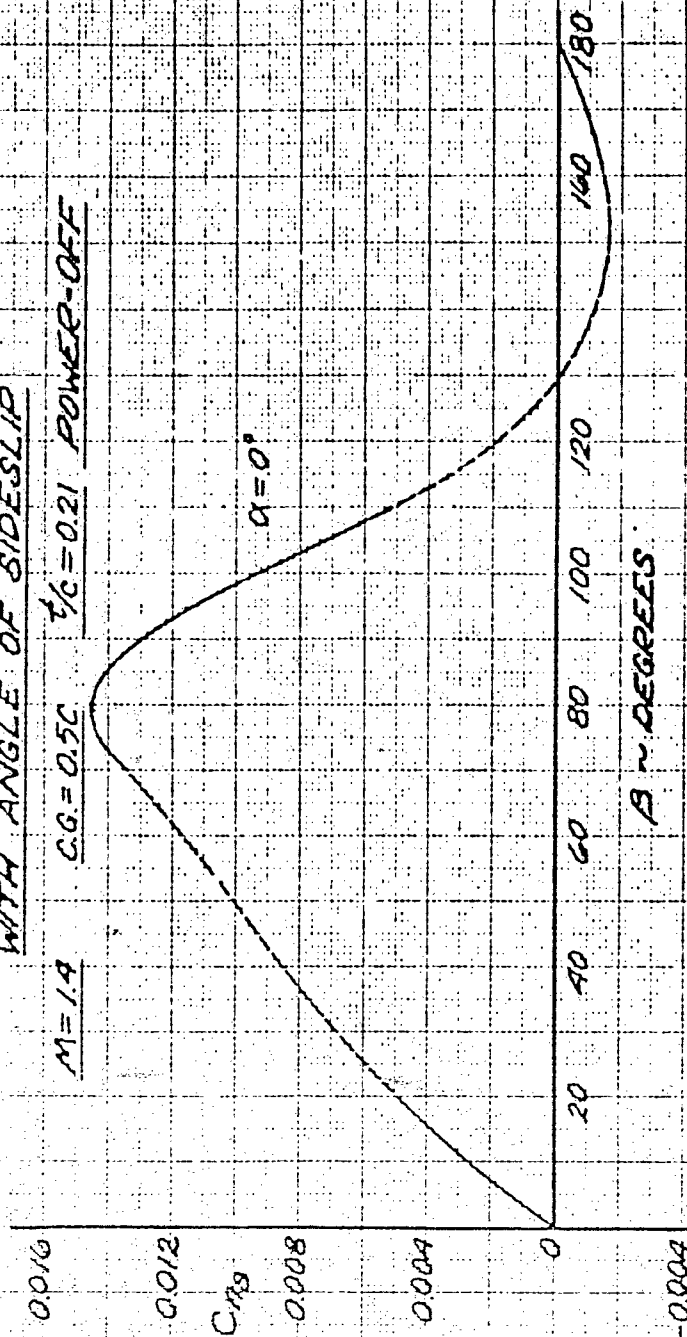
SECRET

FIGURE 2.4.10 f

PYE WACKET FTV

VARIATION OF YAWING MOMENT COEFFICIENT
WITH ANGLE OF SIDESLIP

$M=1.4$ $C.G.=0.5C$ $\frac{1}{2}C=0.21$ POWER-OFF



SECRET

SECRET

FIGURE 2.4.107

PYE WACKET FTV

VARIAION OF YAWING MOMENT COEFFICIENT

WITH ANGLE OF SIDESLIP

M=1.6

C.G.=0.5C

$\frac{1}{2}C=0.21$ POWER-OFF

0.016

0.012

$C_{Y\beta}$

0.008

0.004

0

-0.004

2.95

$\alpha=0^\circ$

β - DEGREES

20 40 60 80 100 120 140 160 180

SECRET

2.4.3.5 Rolling Moment Coefficient The variation of rolling moment coefficient with sideslip angle is shown in Figure 2.4.11. It is emphasized that the rolling moment is measured about the stability x_s axis. If the configuration were symmetrical, the center of pressure would lie on the x_s axis and no rolling moment could occur. At sideslip angles other than zero and 180 degrees, the PYE WACKET configuration is not symmetrical. The asymmetry with respect to the velocity vector results in a center of pressure shift off the x_s axis, and hence, a rolling moment is produced. However, the magnitude of the rolling moment is small in comparison with the pitching moment. The sensitivity of wind tunnel balances is low when such small moments are measured. This effect is observed in Figure 2.4.11 b as an erratic variation of the rolling moment with sideslip angle and angle of attack.

2.4.3.6 Center of Pressure Location The center of pressure is a theoretical point on the body where the total aerodynamic normal force is assumed to act. The center of pressure locations are presented in Figures 2.4.12 and 2.4.13 in terms of percent of body diameter aft of the leading edge.

Center of pressure locations as a function of Mach number are shown in Figure 2.4.12 for $\alpha = 0^\circ$ and 90° . The center of pressure locations were calculated using the ratio of the slopes of the pitching moment and normal force coefficients with angle of attack.

Figure 2.4.13 illustrates the variation of center of pressure for angles of sideslip between 0 and 100 degrees. The centers of pressure were computed for the planform by using the slopes of the pitching moment, rolling moment and normal force coefficients with respect to angle of attack. An example of the method of obtaining the planform center of pressure is as follows. The conditions are $\alpha = 0^\circ$, $\beta = 60^\circ$, $M = 0.6$, and a c.g. of 0.5 c.

$$\frac{x_s}{d} = \left| \frac{C_{m_{\alpha\beta}}}{C_{N_{\alpha}}} \right| = \left| \frac{0.0088}{0.0365} \right| 100 = 24.1\% d$$

$$\frac{y_s}{d} = \left| \frac{C_{l_{\alpha\beta}}}{C_{N_{\alpha}}} \right| = \left| \frac{-0.00076}{0.0365} \right| 100 = 2.08\% d$$

SECRET

FIGURE 2.4.11a

PYE WACKET FTV

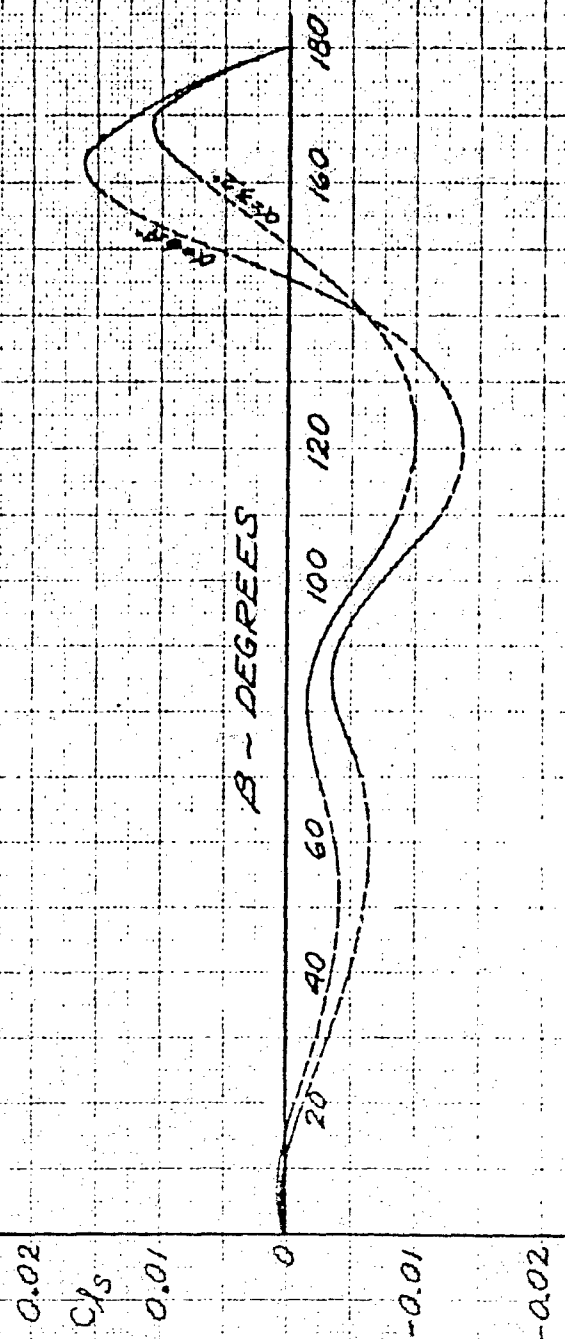
VARIATION OF ROLLING MOMENT COEFFICIENT
WITH ANGLE OF SIDESLIP

$\gamma_0 = 0.21$

POWER-OFF

C.G. = 0.5C

M = 0.6



SECRET

SECRET

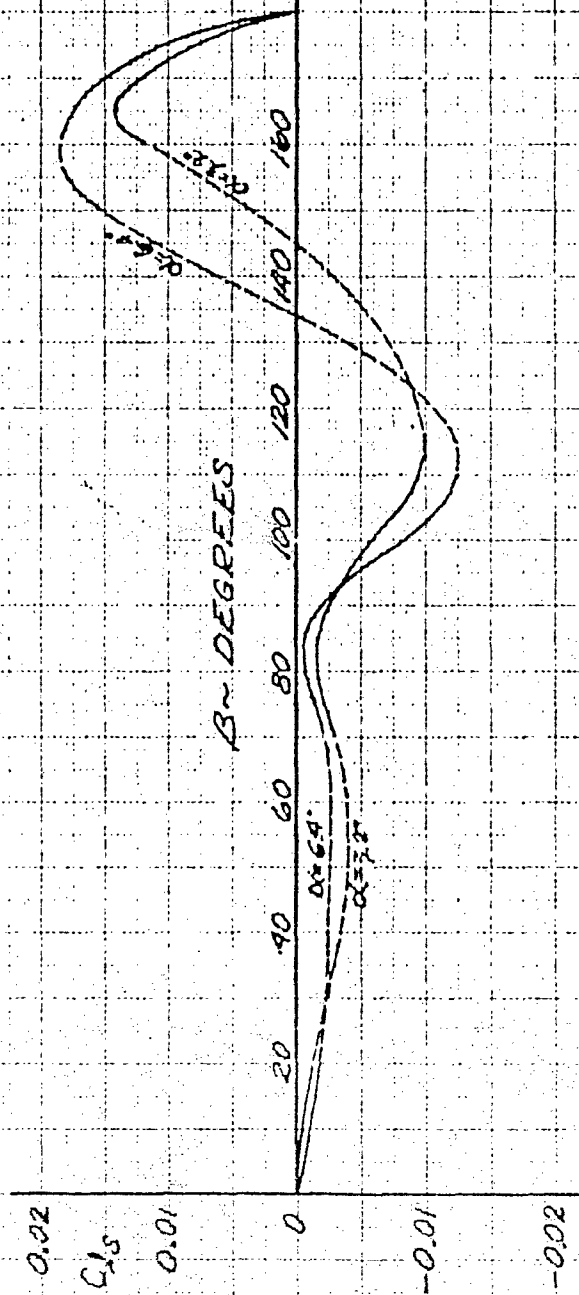
FIGURE 2.4.11b

PYE WACKET FTV

VARIATION OF ROLLING MOMENT COEFFICIENT
WITH ANGLE OF SIDESLIP

$\frac{t}{G} = 0.21$ POWER-OFF $CG = 0.50$

$M = 0.8$



2.98

SECRET

SECRET

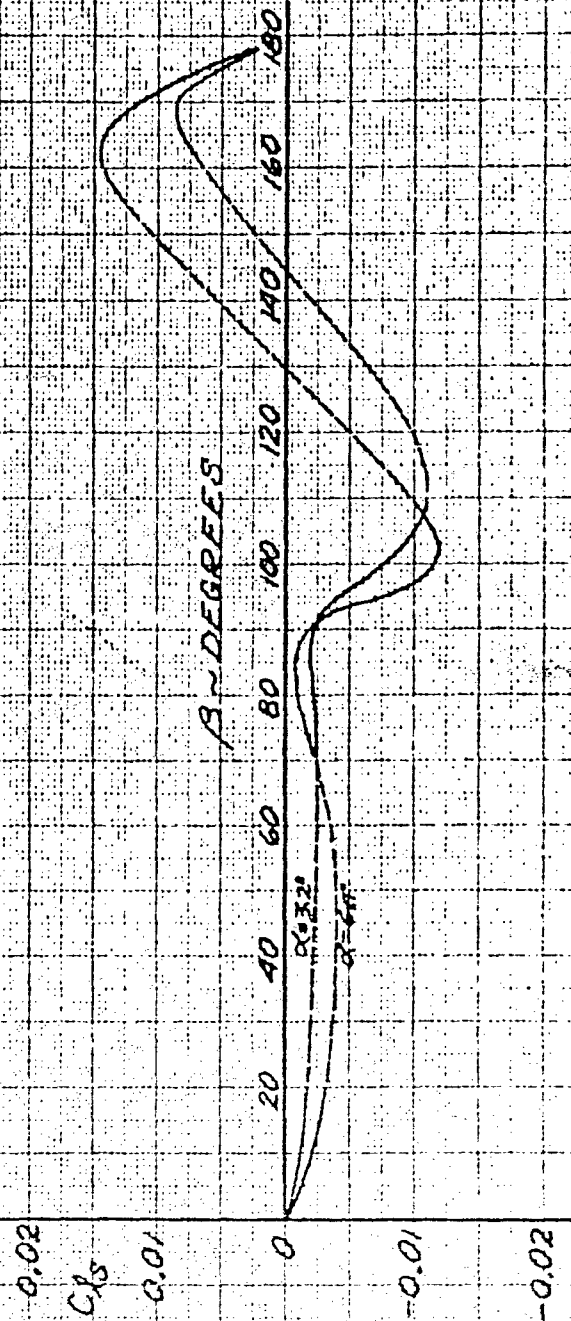
FIGURE 2.4.11c

PYE WACKET FTV

VARIATION OF ROLLING MOMENT COEFFICIENT
WITH ANGLE OF SIDESLIP

$\xi_0 = 0.21$ POWER-OFF $CG = 0.50$

$M = 0.9$



SECRET

SECRET

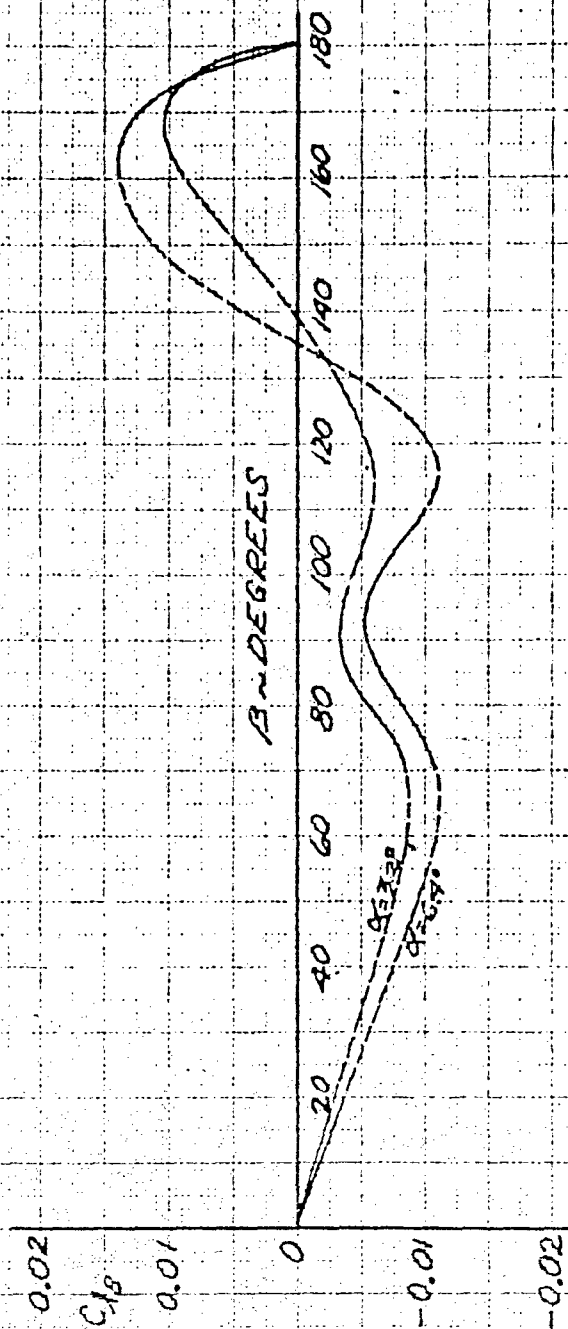
FIGURE 2.4.11B

PYE WACKET FTV

VARIATION OF ROLLING MOMENT COEFFICIENT
WITH ANGLE OF SIDESLIP

$\frac{1}{2}C = 0.21$ POWER-OFF $CG = 0.50$

$M = 10$



SECRET

SECRET

FIGURE 2.4.11c

PYE WACKET FTV

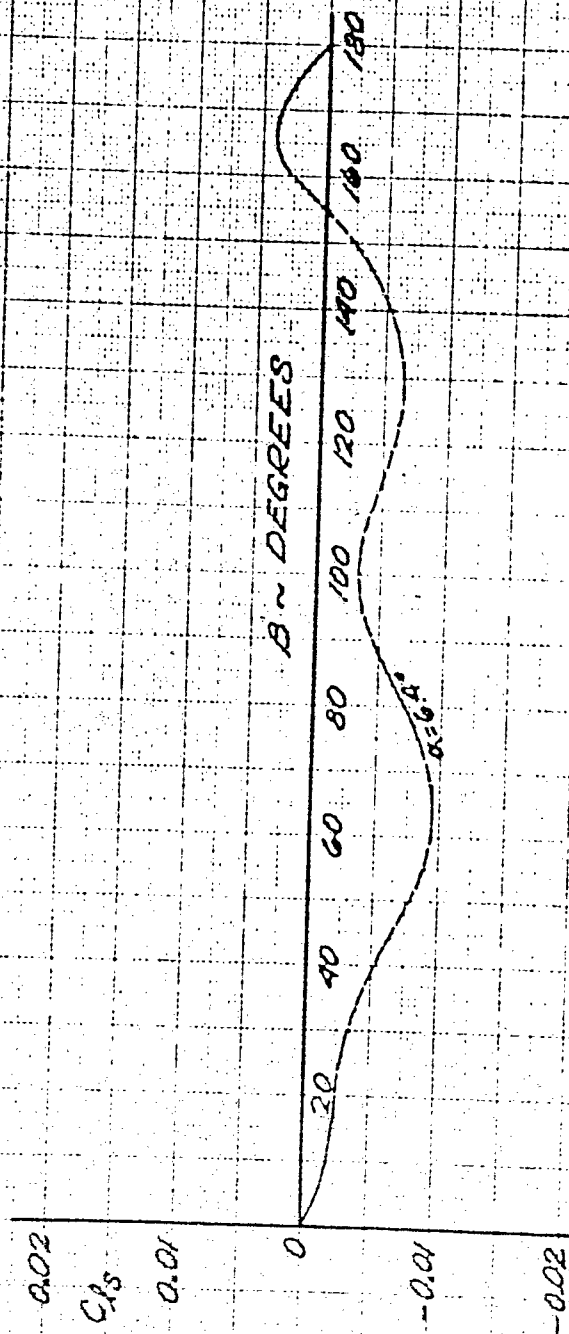
VARIATION OF ROLLING MOMENT COEFFICIENT
WITH ANGLE OF SIDESLIP

$t/c = 0.21$

POWER-OFF

$C.G. = 0.50$

$M = 1.2$



2.101

SECRET

SECRET

FIGURE 2.4.11F

PYE WACKET FTV

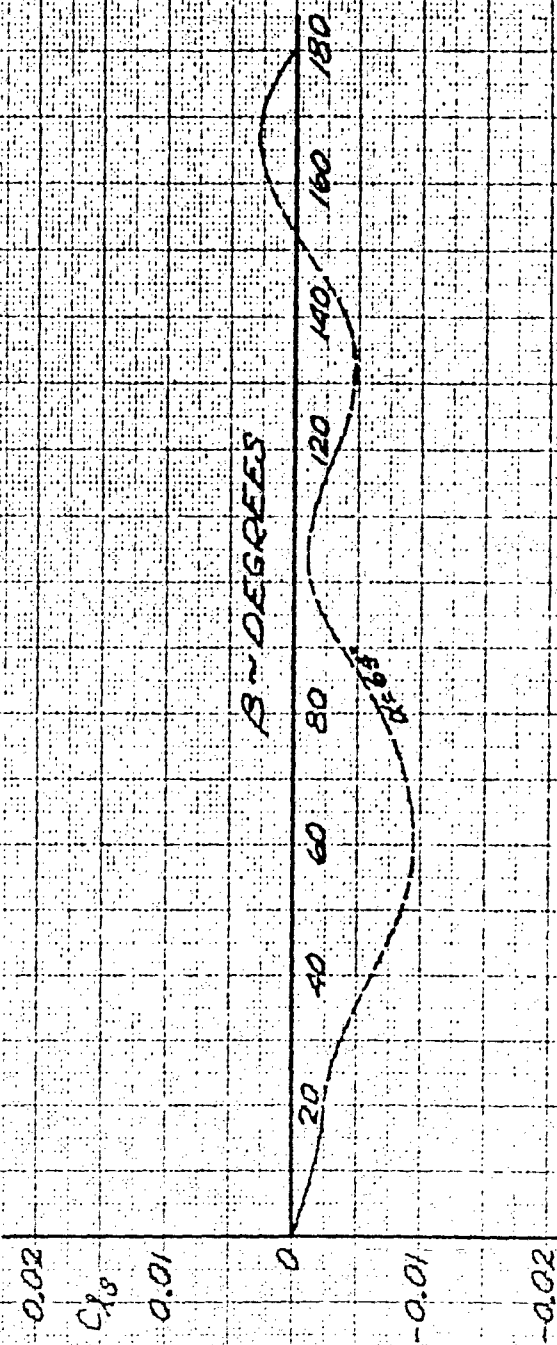
VARIATION OF ROLLING MOMENT COEFFICIENT
WITH ANGLE OF SIDESLIP

$\frac{t}{C} = 0.21$

POWER-OFF

$C_R = 0.50$

$M = 1.4$



2.102

SECRET

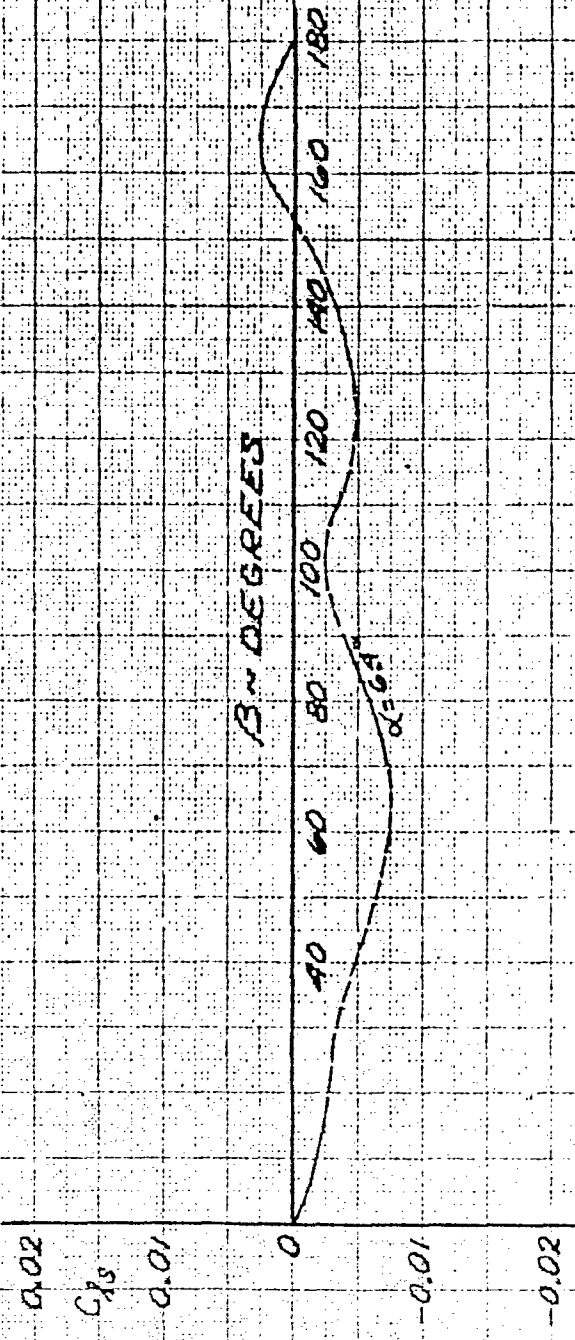
SECRET

FIGURE 24.119
PYE WACKET FTV

VARIAION OF ROLLING MOMENT COEFFICIENT
WITH ANGLE OF SIDESLIP

$\frac{1}{2}C = 0.21$ POWER-OFF $CQ = 0.50$

$M = 1.6$



2.103

SECRET

SECRET

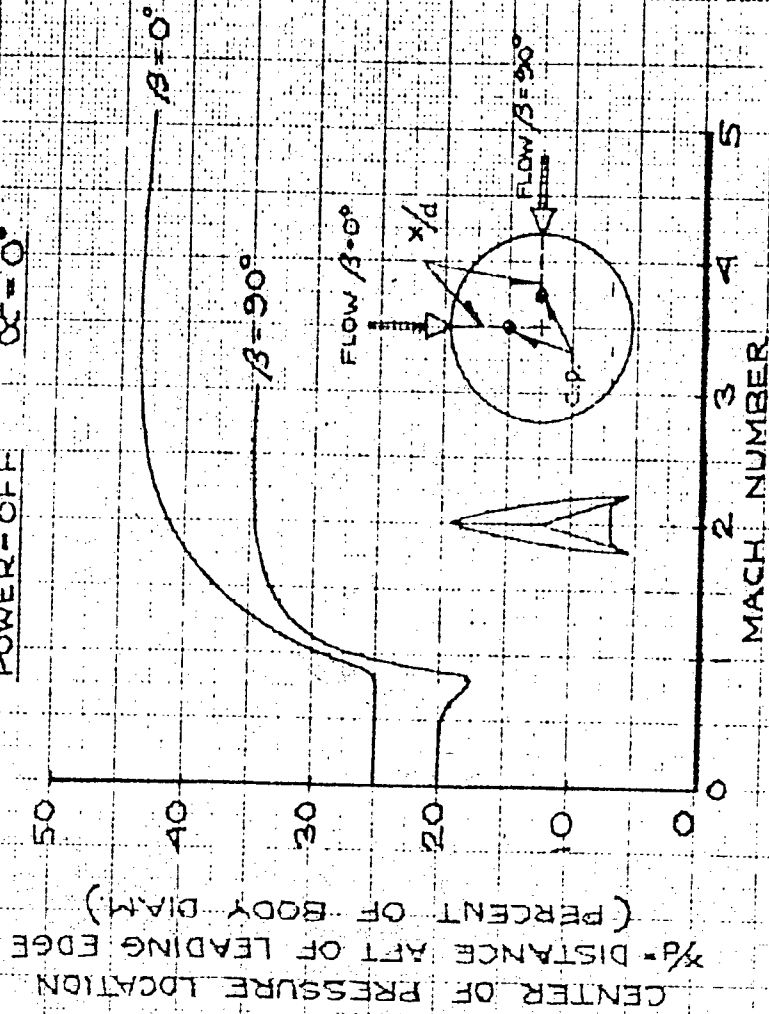
FIGURE 2.4.12

PYE WACKET FTV

CENTER OF PRESSURE LOCATION

VS MACH NUMBER

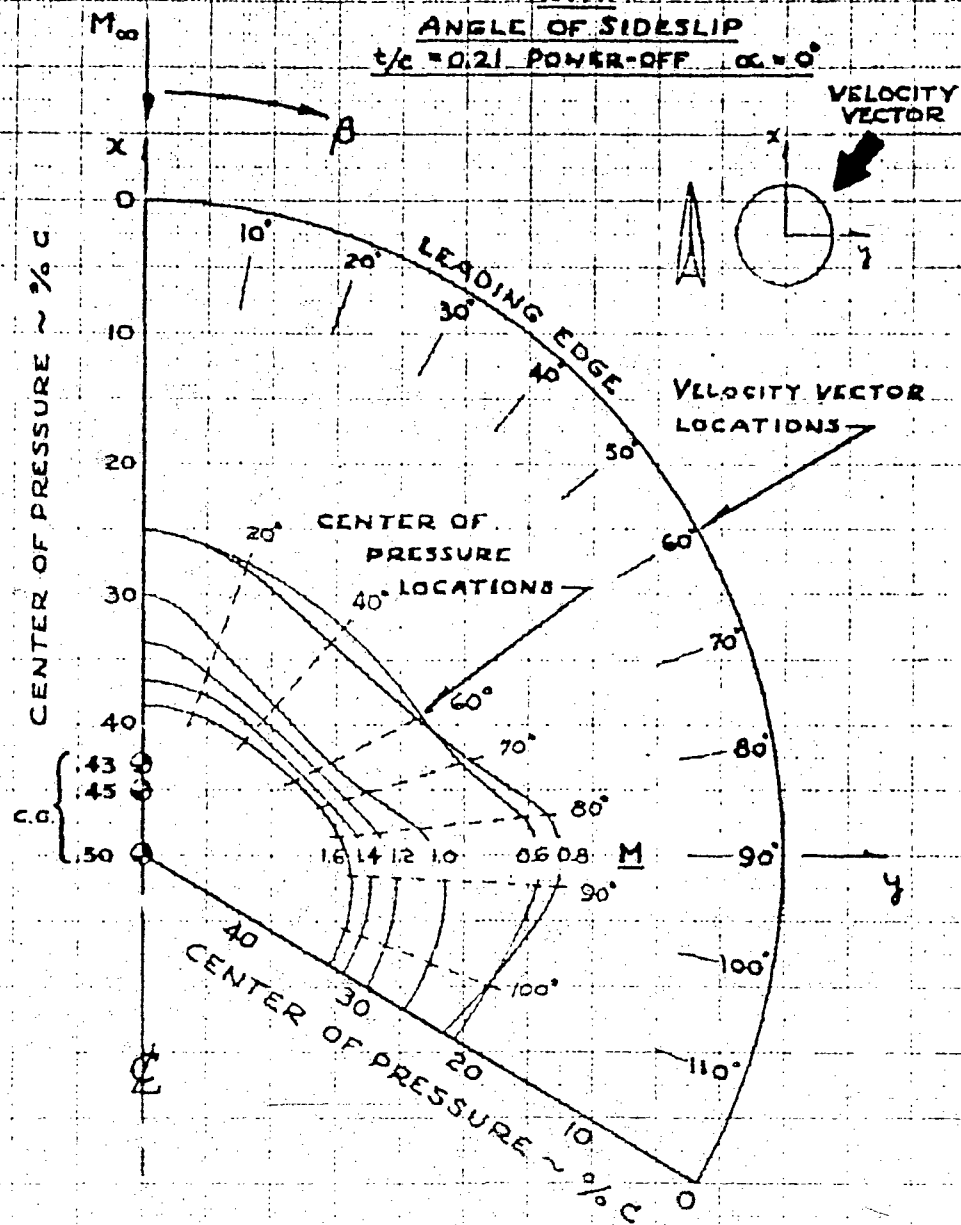
POWER-OFF $\alpha = 0^\circ$



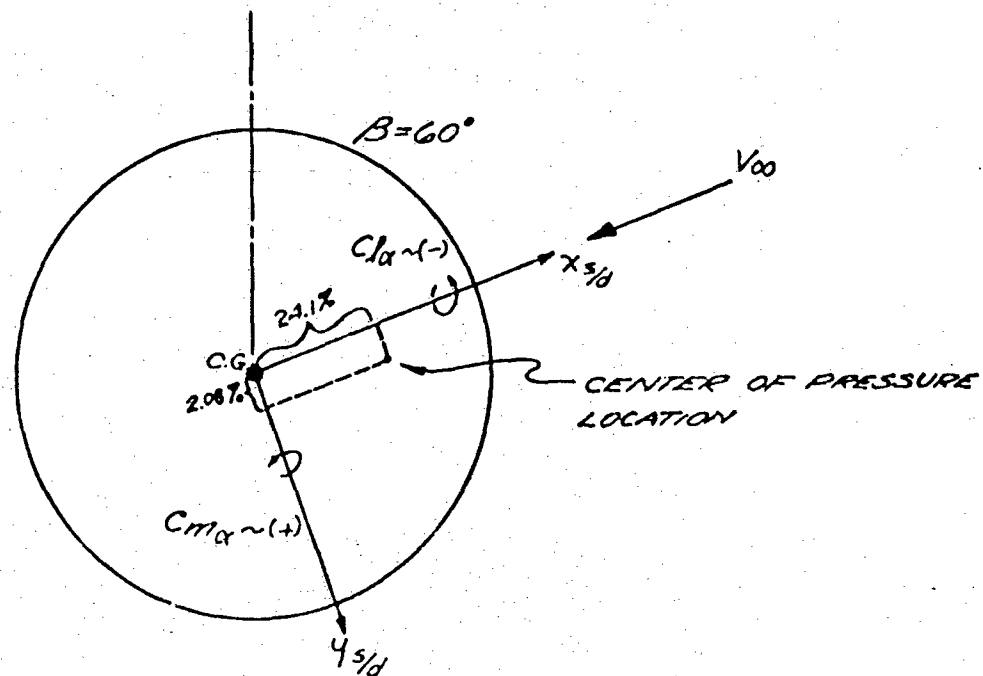
SECRET

SECRET

FIGURE 2.4.13
PYE WACKET FTV
VARIATION OF CENTER OF PRESSURE
WITH
ANGLE OF SIDESLIP
 $t/c = 0.21$ POWER-OFF $\alpha = 0^\circ$



SECRET



As illustrated in the sketch above, the absolute magnitude of the ratio of the moment and normal force was used in the calculation of the x_s and y_s center of pressure location. In order to arrive at the direction of the x_s and y_s C.P.'s, the signs are determined by the direction of rotation of the vehicle. Thus, the moment arm for a positive normal force and positive pitching moment, must lie between the center of gravity and the leading edge. As in the example shown above, a negative rolling moment will be produced by a positive normal force acting with a positive moment arm in the positive y_s direction.

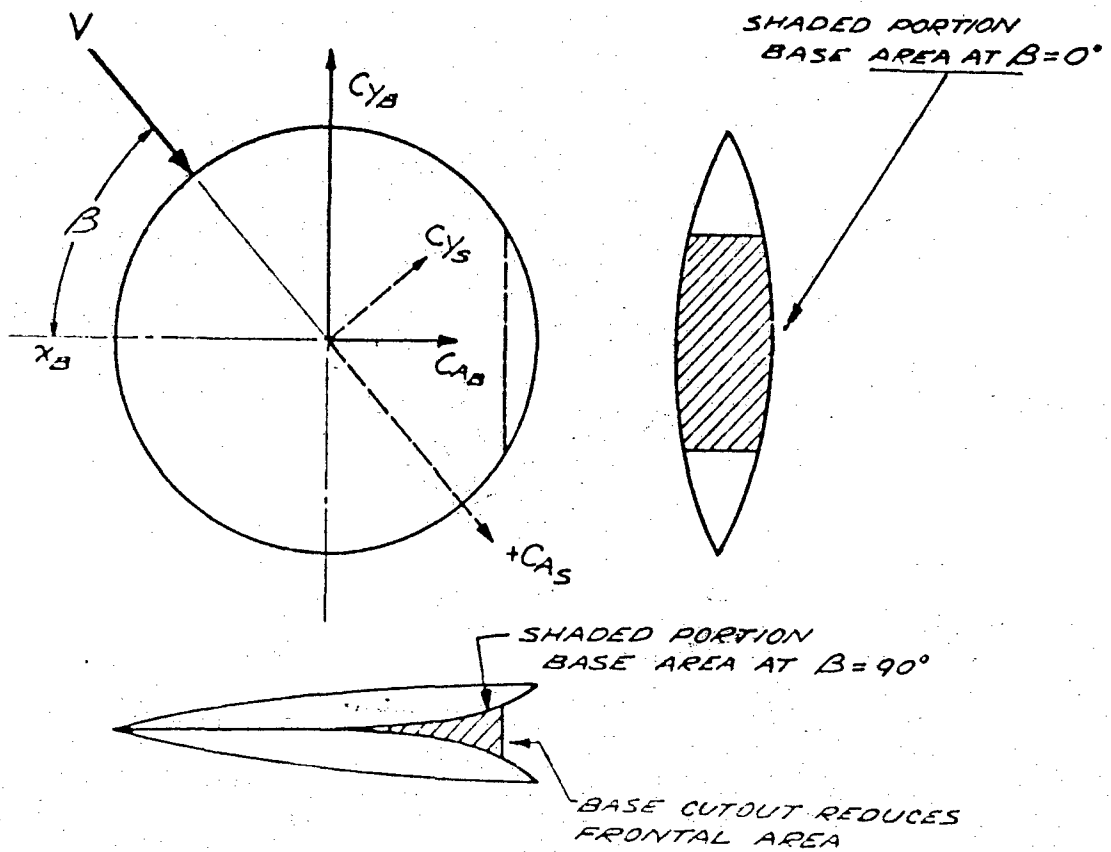
2.4.3.7 Axial Drag Coefficient The power-off axial drag coefficients are presented in Figures 2.4.14, 2.4.15 and 2.4.16. Figure 2.4.14 presents the axial drag coefficient, C_{AS} , for $\delta = 0^\circ$, 90° , and 180° for the entire Mach number range tested at $\alpha = 0^\circ$. Figure 2.4.15 presents a C_{AS} breakdown for $\delta = 0^\circ$ and $\alpha = 0^\circ$. The variation of C_{AS} as a function of sideslip angle with angle of attack as a parameter is shown for various Mach numbers in Figure 2.4.16.

SECRET

The relationship between C_A and C_Y for body and stability axis systems is shown below.

$$C_{A_S} = C_{A_B} \cos \beta - C_{Y_B} \sin \beta$$

$$C_{Y_S} = C_{A_B} \sin \beta + C_{Y_B} \cos \beta$$



2.107

SECRET

SECRET

A comparison of C_{A_s} values at $\alpha = 0^\circ$ (Figure 2.4.14), shows that the $\delta = 90^\circ$ drag is approximately 75% lower than the $\delta = 0^\circ$ drag at subsonic Mach numbers. As shown in the above sketch, the base and frontal areas are smaller for $\delta = 90^\circ$ than $\delta = 0^\circ$. Assuming that the base and surface pressure coefficients are the same for $\delta = 0^\circ$ and $\delta = 90^\circ$, the difference in drag can be partially explained on the basis of the difference in representative areas of the two positions.

The subsonic trend is reversed at supersonic speeds; i.e., the $\delta = 90^\circ$ drag is approximately 25% greater than the $\delta = 0^\circ$ drag. In the supersonic region, the bluntness of the $\delta = 90^\circ$ profile has a large influence on the drag. This influence is greater than the difference in base or frontal areas. Evidence of the drag increase due to bluntness can be seen in the schlieren pictures from the wind tunnel test. This picture, Figure 2.4.18 d, shows that the blunt section causes a very strong shock wave and hence high wave drag. As the missile is turned to sideslip angles greater than $\delta = 90^\circ$, the shock becomes normal to the base, and the drag increases at a rapid rate. The maximum drag is reached at $\delta = 180^\circ$, where the largest blunt area is presented to the flow.

The drag breakdown in Figure 2.4.15 separates the C_A at $\delta = 0^\circ$ and $\alpha = 0^\circ$ into base drag, skin friction drag, and wave plus after-body-drag components. The power-off base-drag component was computed from base pressures determined from wind tunnel tests of the pressure model. It must be noted that the blunt-base drag pertains only to the area of the "cutout" at the aft end of the missile as shown in the sketch.

$$C_{DB} = -C_{p_a} \frac{S_B}{S} \quad 2.4.9$$

where C_{p_a} = average base pressure coefficient over the base cutout,

S_B = projected area of cutout, and
 S = missile reference area.

For this case, main rockets off

$$\frac{S_B}{S} = \frac{41.0 \text{ in.}^2}{314.0 \text{ in.}^2} = 0.13, \text{ and} \quad 2.4.10$$

$$C_{DB} = -0.13 C_{p_a} \quad 2.4.11$$

The skin friction drag, prepared from reference 5.11, is presented for a full scale FTV configuration (diameter = 5 ft) at sea level. This corresponds to a Reynolds number range of 7×10^6 to 2×10^8 . By subtracting skin friction and blunt-base drag from the total FTV drag,

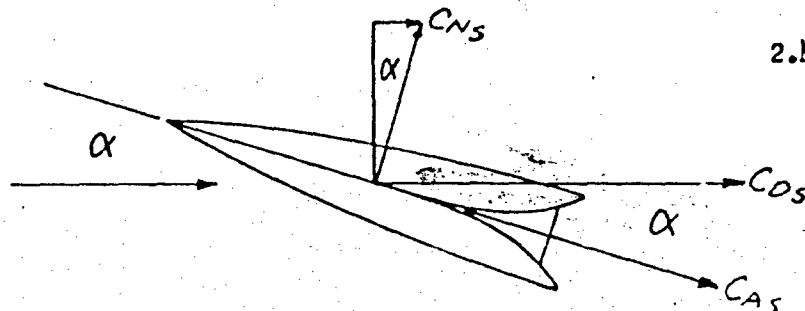
SECRET

the wave plus afterbody drag was obtained. It should be noted that afterbody drag is defined to be the drag on the blunt trailing edge not included in the base cutout. A drag breakdown was not computed for $\beta = 90^\circ$ because there was insufficient tunnel data to compute the effective base drag.

The variation of axial drag coefficient, C_{A_s} , as a function of sideslip angle for constant angle of attack, has the same general variation discussed for the β equal 0° , 90° and 180° cases at $\alpha = 0^\circ$. In the range of β from 0° to 20° , C_{A_s} is reasonably linear and varies by only a small value. For the sector where β varies from 70° to 110° , the C_{A_s} values are minimal at 90° . The test data, shown in solid lines, are available in the range of $\beta = 160^\circ$ to 180° at only Mach 0.6. The large values at 180° are due to the blunt base presented to the flow. The data shown in this range of sideslip angles for other Mach numbers were estimated. Since no data were obtained from tunnel testing in ranges of β from 20° to 70° , and 110° to 160° , the curves in this area were faired from the existing data. Hence, the graphs show only general trends in these regions.

Although the missile drag is presented for only $\alpha = 0^\circ$ in the form of C_{A_s} , the drag may be computed for angles of attack other than zero by the use of the following equations:

$$C_{D_s} = C_{A_s} \cos \alpha + C_{N_s} \sin \alpha$$



and if C_{D_s} at $\alpha = 0$ is defined as the zero lift drag ($C_{D_{0s}}$) then,

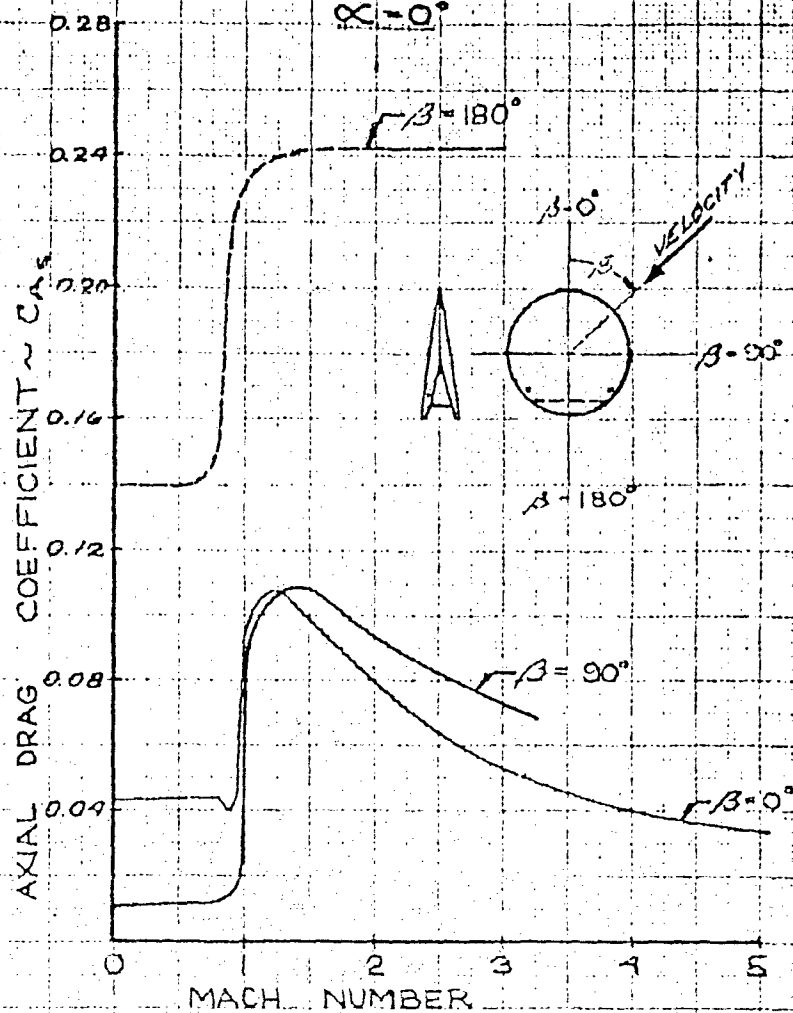
$$C_{D_{0s}} = C_{D_s}(\alpha=0) = C_{A_s}(\alpha=0) \quad 2.4.13$$

2.109

SECRET

SECRET

FIGURE 2.4.14
PYE WACKET FTV
AXIAL DRAG COEFFICIENT
VS. MACH NUMBER
MAIN ROCKETS OFF
CONTROL JETS OFF
 $\alpha = 0^\circ$



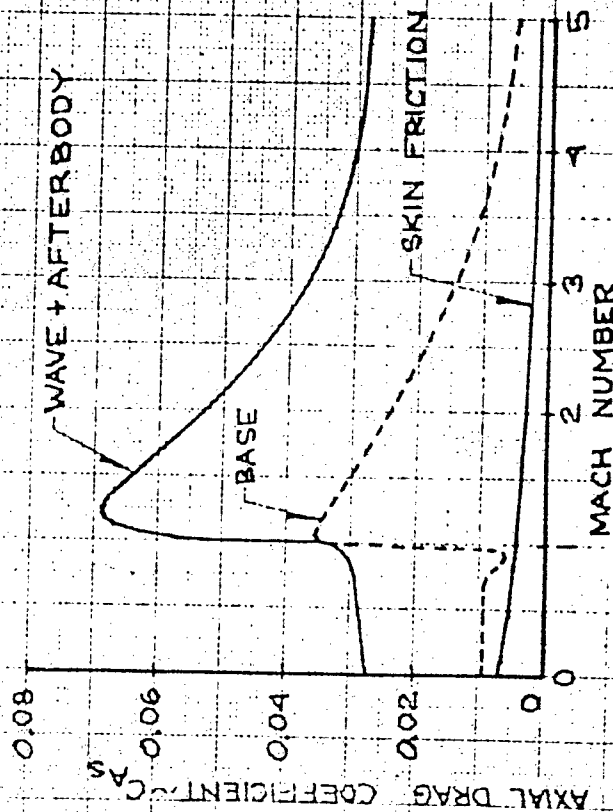
SECRET

SECRET

FIGURE 2.4.15

PYE WACKET FTV

AXIAL DRAG COEFFICIENT, $\beta=0$ VS. MACH NUMBER
WAVE, SKIN-FRICTION, AND BASE DRAG COMPONENTS
POWER-OFF $\alpha=0^\circ$ SEA LEVEL



SECRET

SECRET

FIGURE 2.4.16a

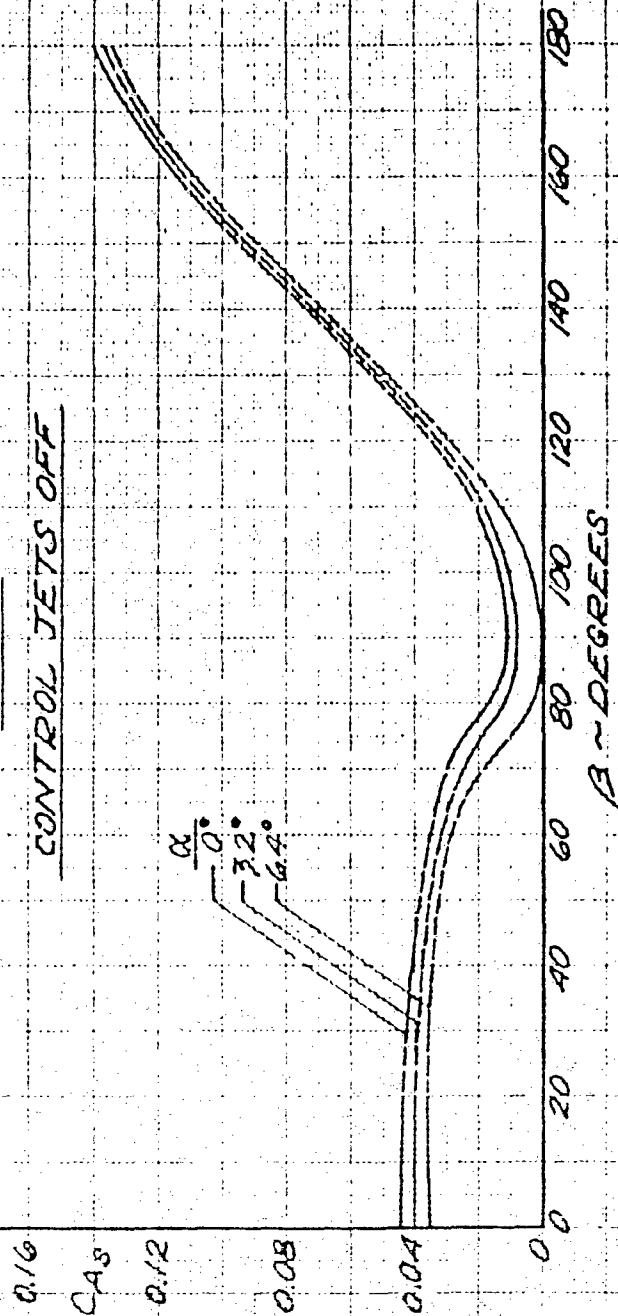
PYE WACKET FTV

VARIATION OF AXIAL DRAG COEFFICIENT
WITH ANGLE OF SIDESLIP

$C_{D0} = 0.21$ POWER-OFF

$M = 0.6$

CONTROL JETS OFF



SECRET

SECRET

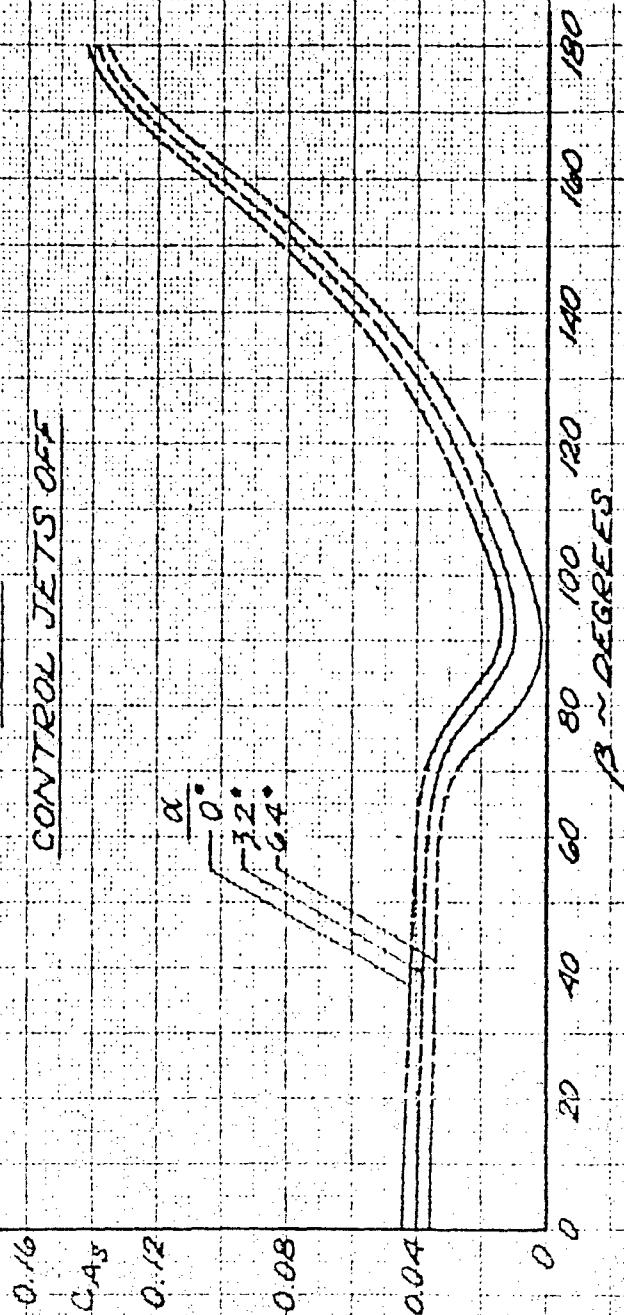
FIGURE 2.4.16b
PYE WACKET FTV

VARIATION OF AXIAL DRAG COEFFICIENT
WITH ANGLE OF SIDESLIP

$t/c = 0.21$ POWER-OFF

$M = 0.8$

CONTROL JETS OFF



SECRET

SECRET

FIGURE 2.4.16C

PYE WACKET FTV

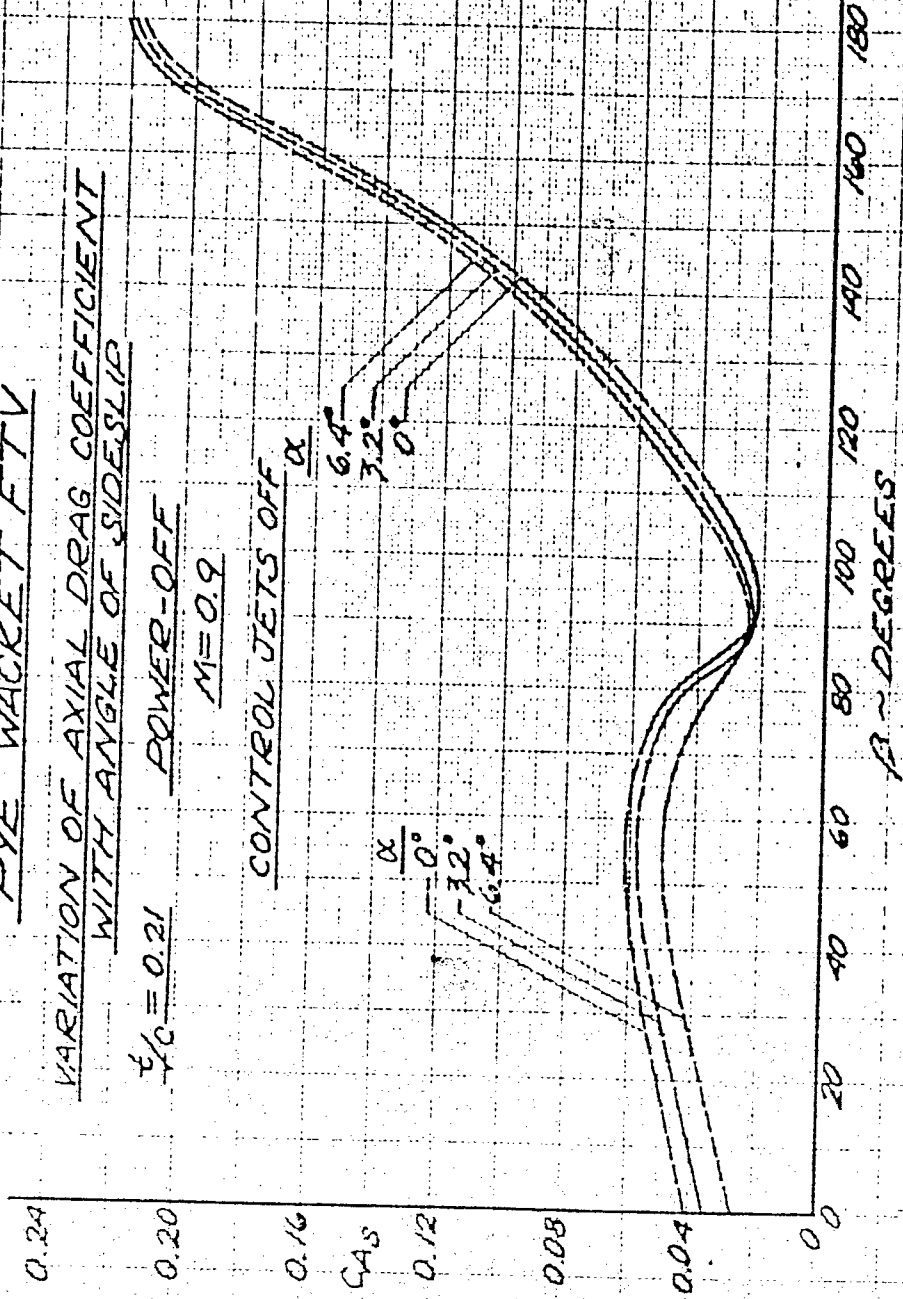
VARIATION OF AXIAL DRAG COEFFICIENT
WITH ANGLE OF SIDESLIP

$\frac{t}{c} = 0.21$

POWER-OFF

$M = 0.9$

CONTROL JETS OFF
 α



SECRET

SECRET

FIGURE 2.4.16d

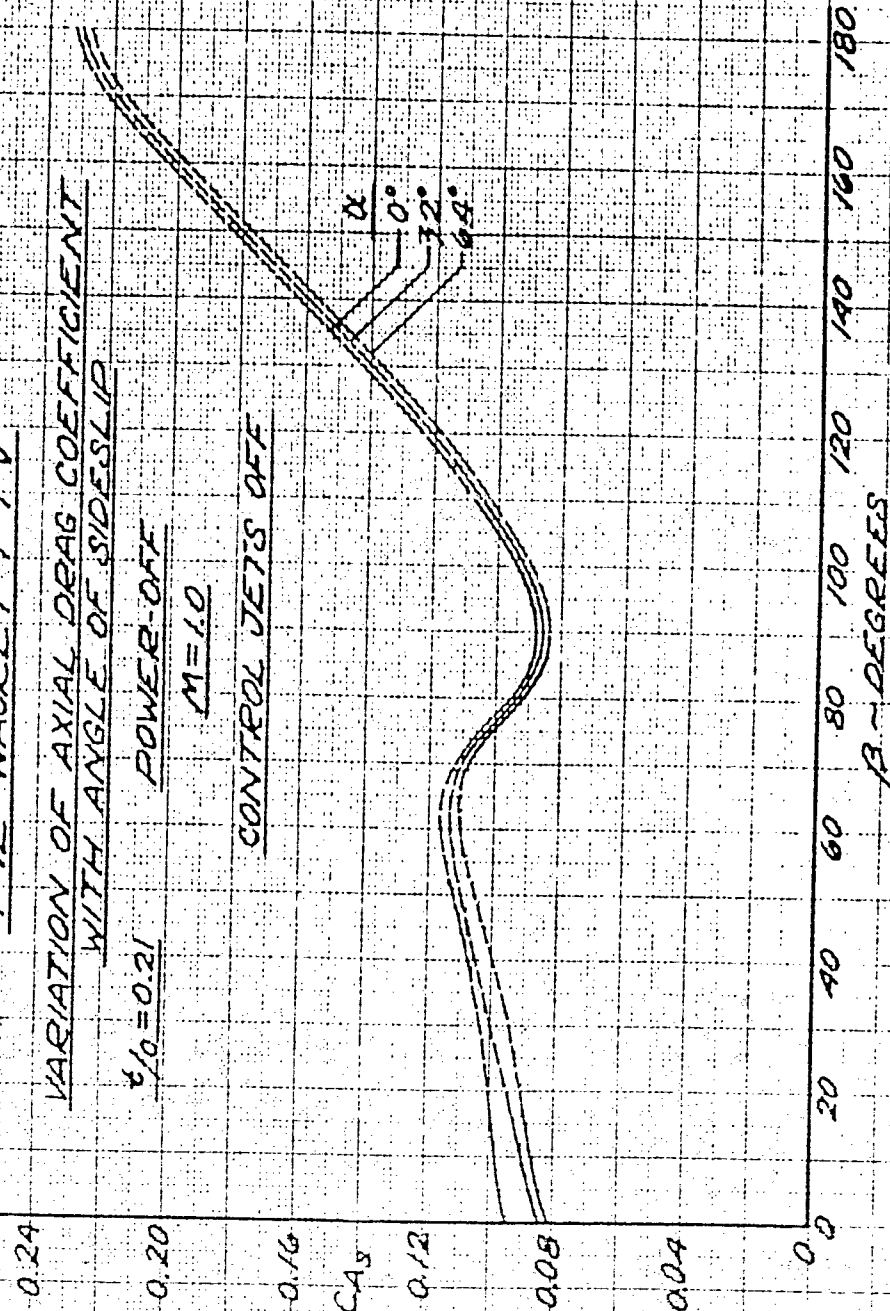
PYE WACKET FTV

VARIAION OF AXIAL DRAG COEFFICIENT
WITH ANGLE OF SIDESLIP

$\epsilon/\rho = 0.21$ POWER-OFF

$M=1.0$

CONTROL JETS OFF



SECRET

SECRET

FIGURE 2.4.16c

PYE WACKET FTV

VARIAION OF AXIAL DRAG COEFFICIENT
WITH ANGLE OF SIDESLIP

$t/c = 0.21$

POWER OFF

$M = 1.2$

CONTROL JETS OFF

α
 0°
 32°
 64°

β - DEGREES

0.24

0.20

0.16

C_{A9}

0.12

0.08

0.04

0

SECRET

2.116

180

160

140

120

100

80

60

40

20

0

SECRET

FIGURE 2.4.16 F

PYE WACKET FTV

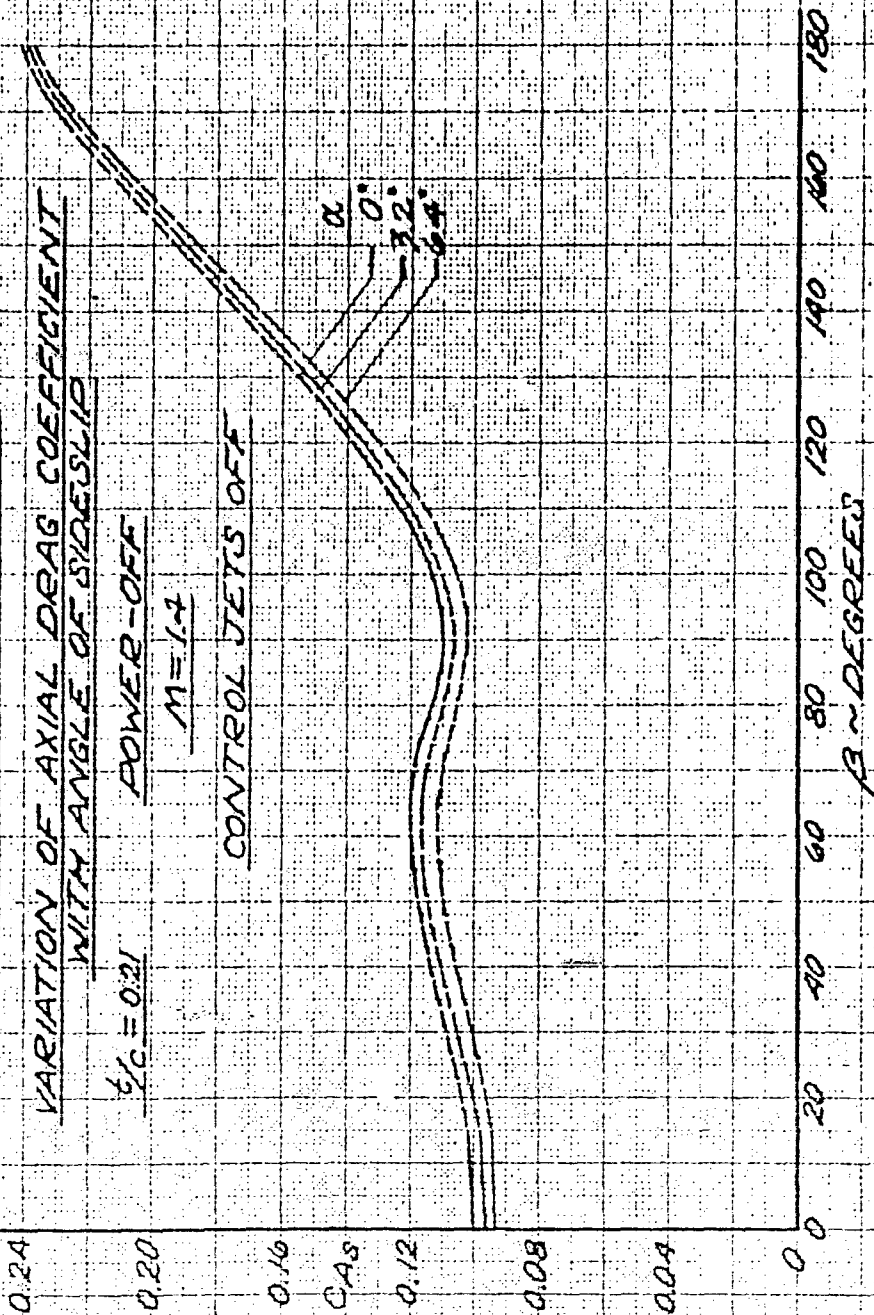
VARIATION OF AXIAL DRAG COEFFICIENT
WITH ANGLE OF SIDESLIP

$t/c = 0.21$

POWER-OFF

$M = 1.4$

CONTROL JETS OFF



2.117

SECRET

SECRET

FIGURE 2.4.16.3

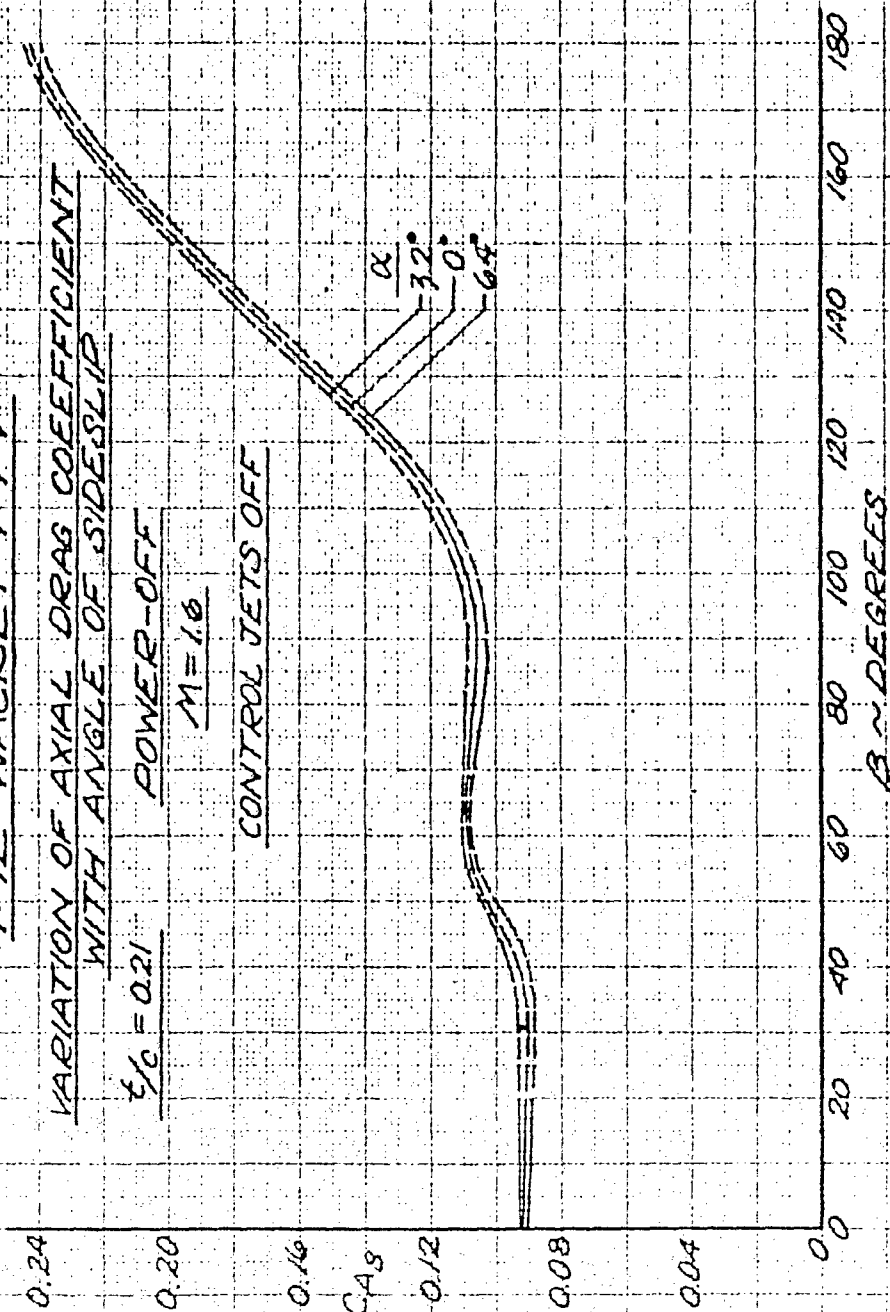
PYE WACKET FTV

VARIATION OF AXIAL DRAG COEFFICIENT
WITH ANGLE OF SIDESLIP

$\epsilon/c = 0.21$ POWER-OFF

$M = 1.0$

CONTROL JETS OFF



SECRET

SECRET

The drag induced with angle of attack is equal to:

$$C_{Di_s} = C_{D_s}(\alpha \neq 0) - C_{D_{0s}} \quad 2.4.14$$

or,

$$C_{Di_s} = C_{A_s} \cos \alpha - C_{N_s} \sin \alpha - C_{D_{0s}} \quad 2.4.15$$

Hence, either the induced drag or the total drag at angle of attack may be obtained from C_{A_s} and C_{N_s} data.

2.4.4 WIND TUNNEL PHOTOGRAPHS - JETS OFF Fluorescent-oil film and schlieren photographs of the PYE WACKET FTV wind tunnel models are shown in Figures 2.4.17 and 2.4.18. The photographs of the models represent a cross-section of the numerous pictures taken during the tests, and consequently do not include all Mach numbers, angles of attack, and angles of sideslip. The photographs presented in this Section were obtained from the Supersonic Von Karman Gas Dynamics Facility at A.E.D.C., Tullahoma, Tennessee. Schlieren photographs from the Transonic Propulsion Wind Tunnel were not included due to the lack of resolution. Fluorescent-oil film pictures were not made at the FWT transonic facility.

Examples of the fluorescent-oil film photographs may be seen in Figures 2.4.17. The test conditions were $M = 2.0$, $\beta = 0^\circ$, and $\alpha = 0^\circ$, 6° , and 12° . It is noted that the camera used to take the photographs was at a small angle to the planform of the model and, therefore, does not present a picture normal to the planform (see base of model in Figure 2.4.17a). Qualitatively, the fluorescent-oil pictures show the flow pattern on the windward side of the model. Fluorescent-oil film photographs with control jets on are illustrated in Section 2.4.7. Methods and applications of the fluorescent-oil film technique are given in Reference 5.12.

The schlieren photographs are presented in Figures 2.4.18 for control jets off. All pictures are for an angle of attack and angle of sideslip of zero degrees. The photographs shown were selected as representative of the profile and planform shock systems for forward, crosswind, and aft launch conditions (power-off). Extraneous shock waves are also apparent in all the pictures. These shocks are caused by the conical shaped bow shock wave emanating from the leading edge of the model which reflects off of the observation window, and/or

SECRET

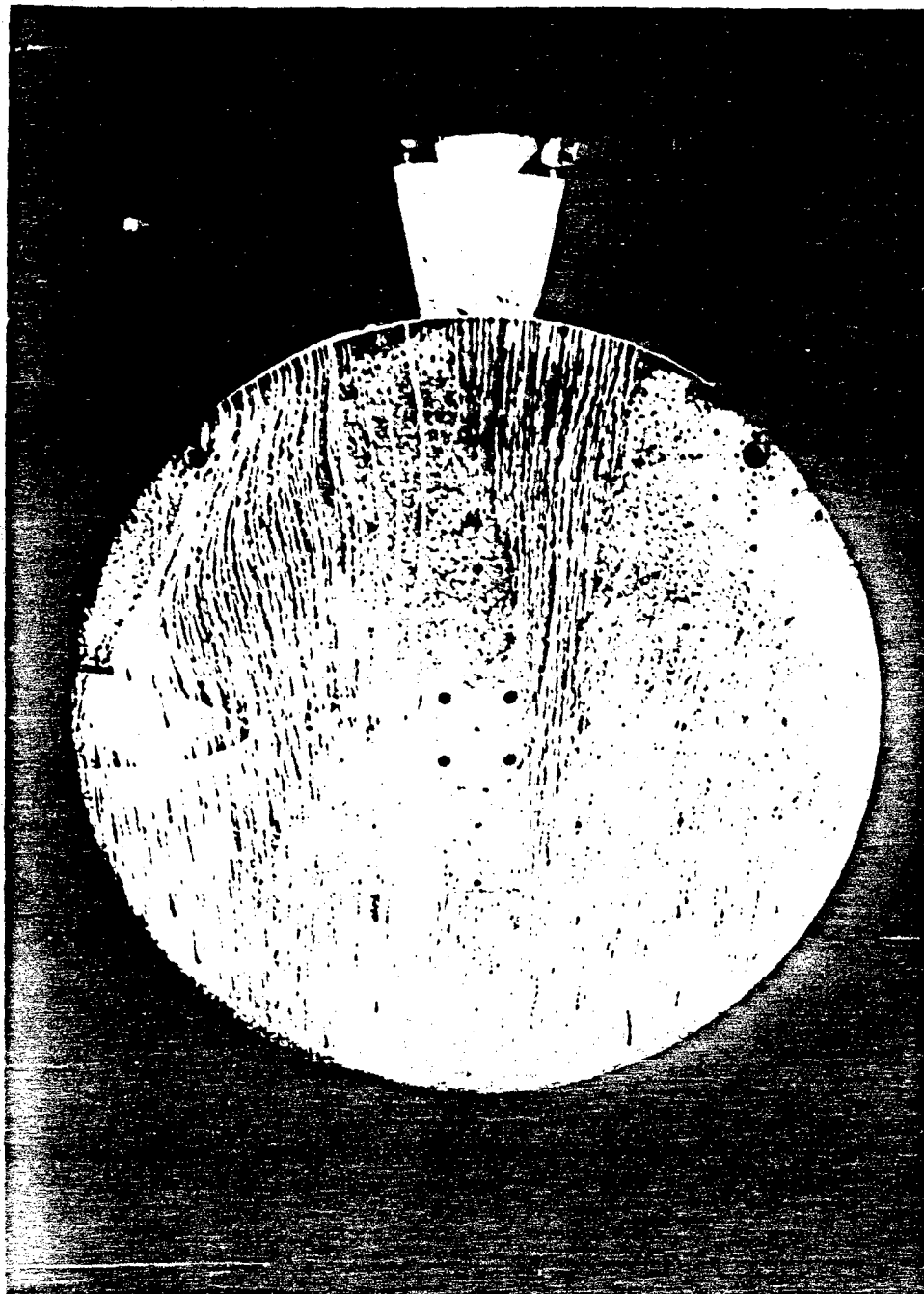


Figure 2.4.17 a Fluorescent-Oil Photograph of Windward Side
Jets Off, $M = 2.0$, $\alpha = 0^\circ$

2.120

SECRET

SECRET

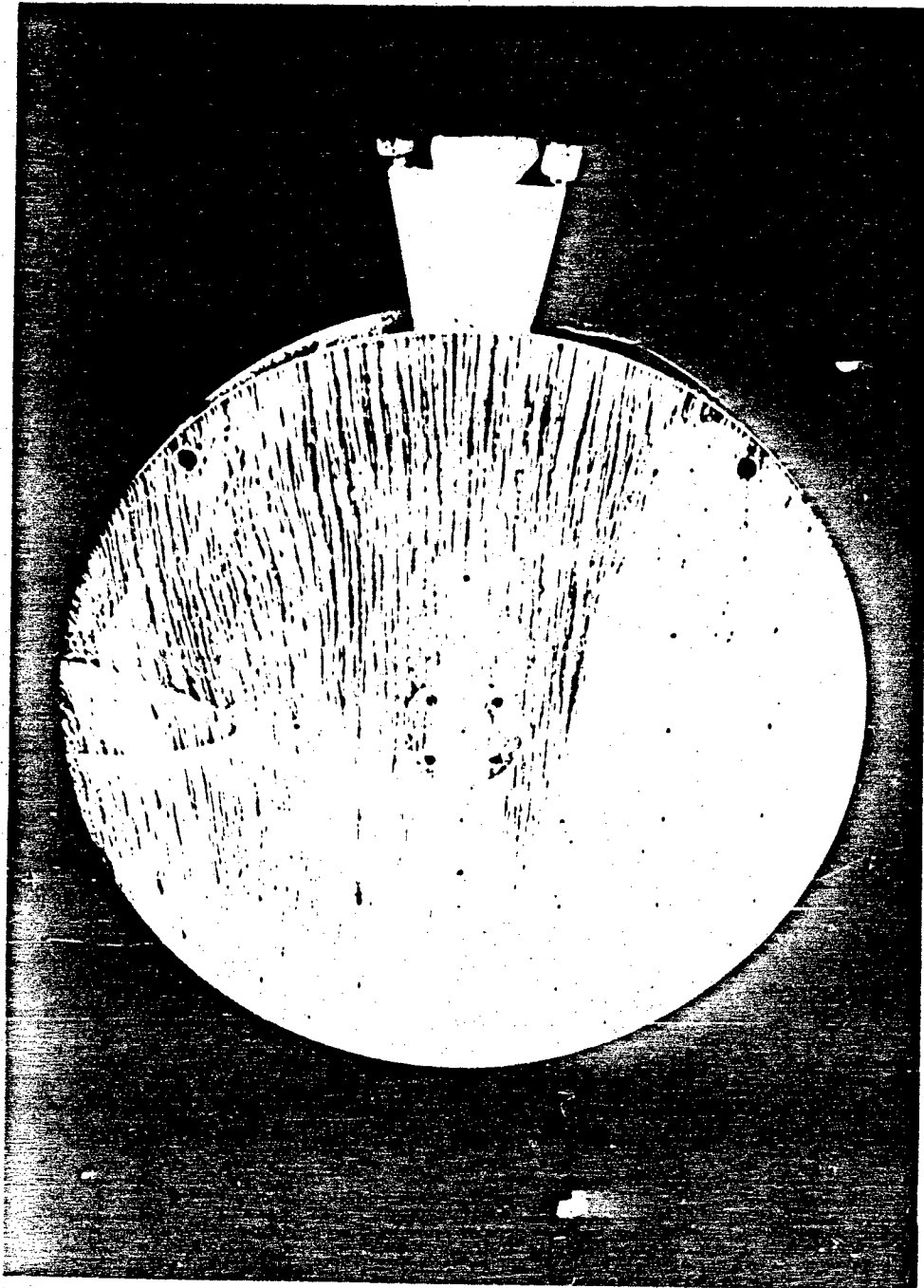


Figure 2.4.17 b Fluorescent-Oil Photograph of Windward Side
Jets Off, $M = 2.0$, $\alpha = 6^\circ$

SECRET

SECRET

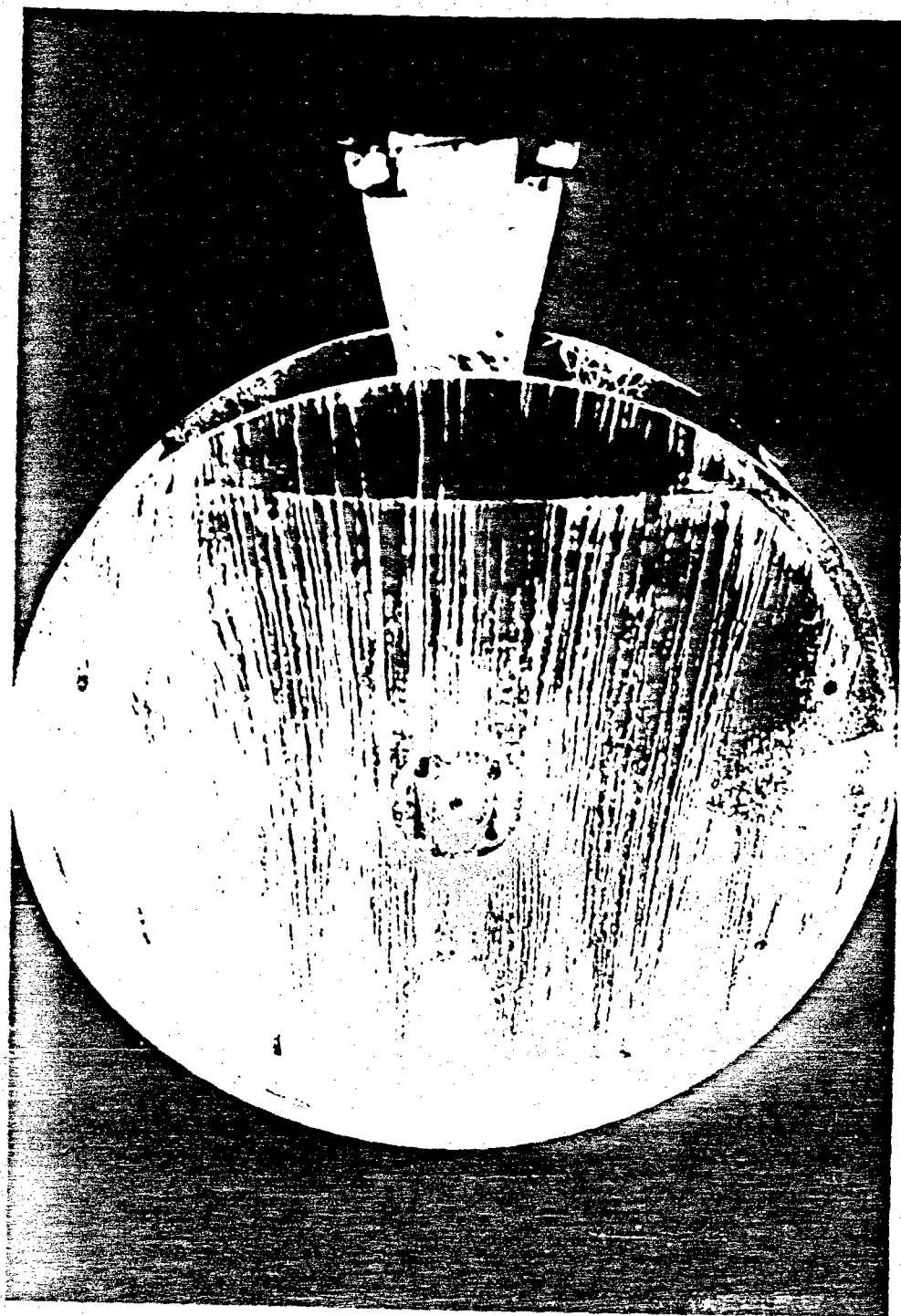


Figure 2.4.17 c Fluorescent-Oil Photograph of Windward Side
Jets Off, $M = 2.0$, $\alpha = 12^\circ$

2.122

SECRET

SECRET

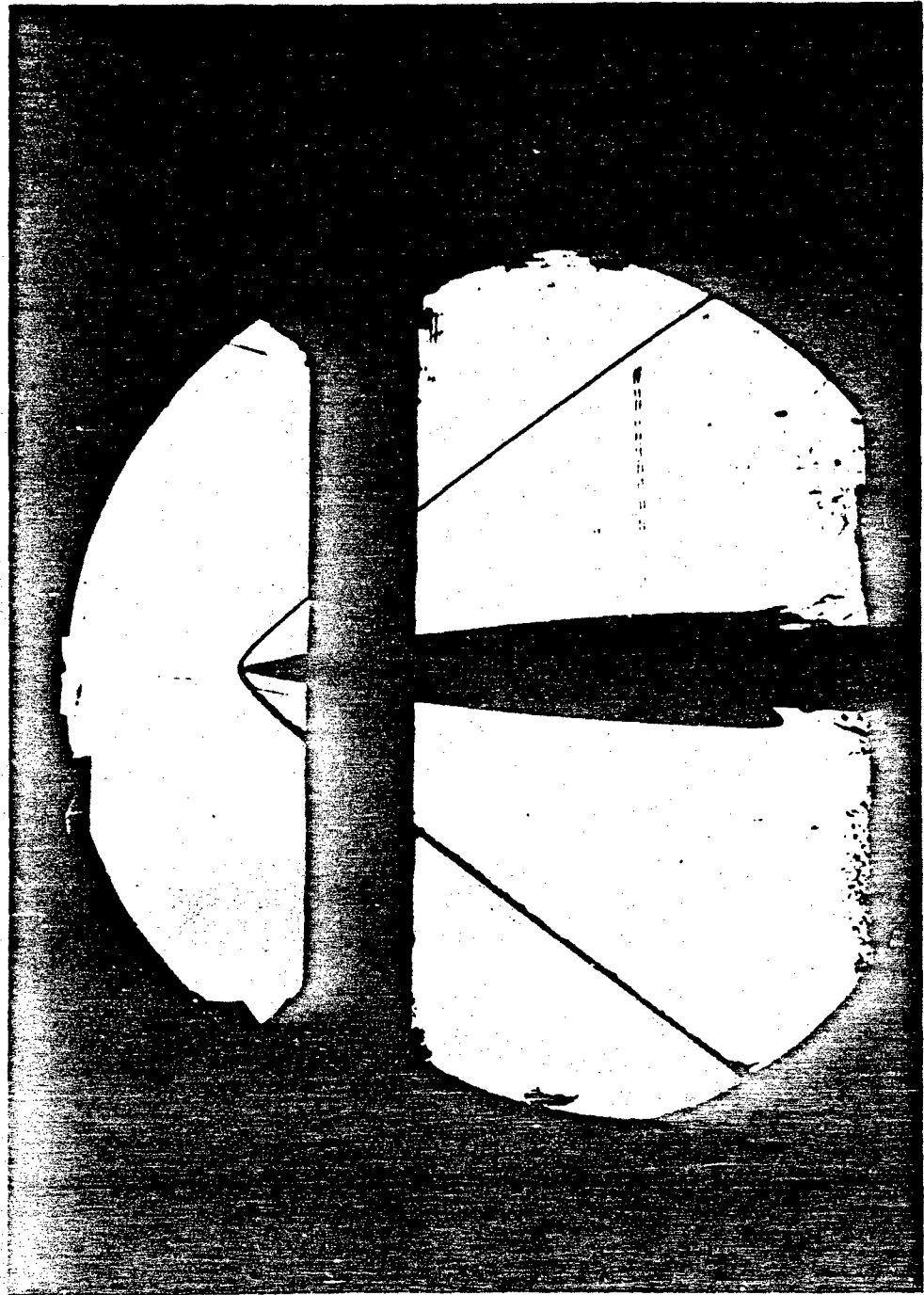


Figure 2.4.18 a Schlieren Photograph of Side View
Forward Launch, $M = 2.0$

2.123

SECRET

SECRET



Figure 2.4.18 b Schlieren Photograph of Plan View
Forward Launch, $M = 2.0$

2.124

SECRET

SECRET

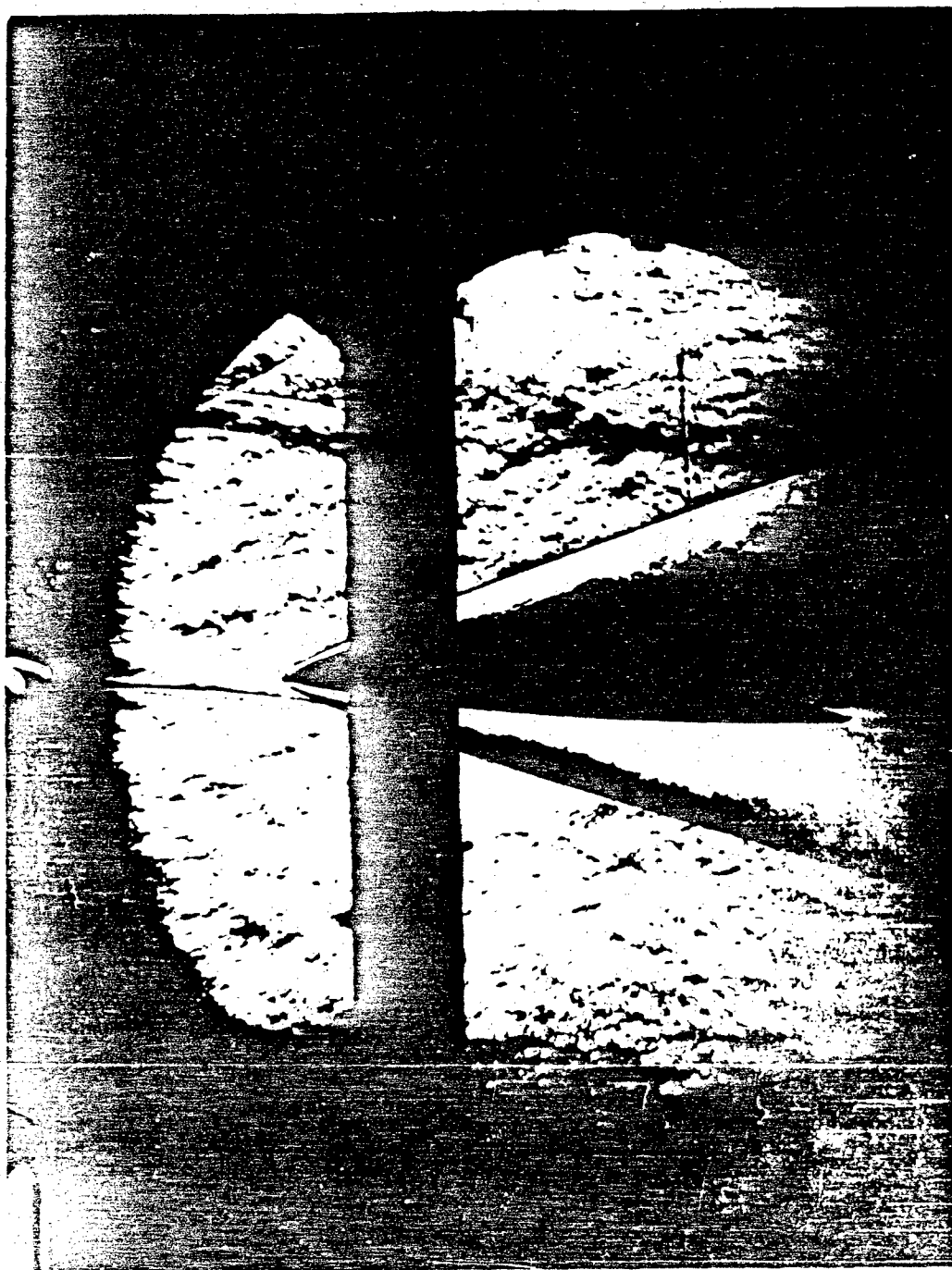


Figure 2.4.18c. Schlieren Photograph of Side View
Forward Launch, M=5.0.

2.125

SECRET

SECRET

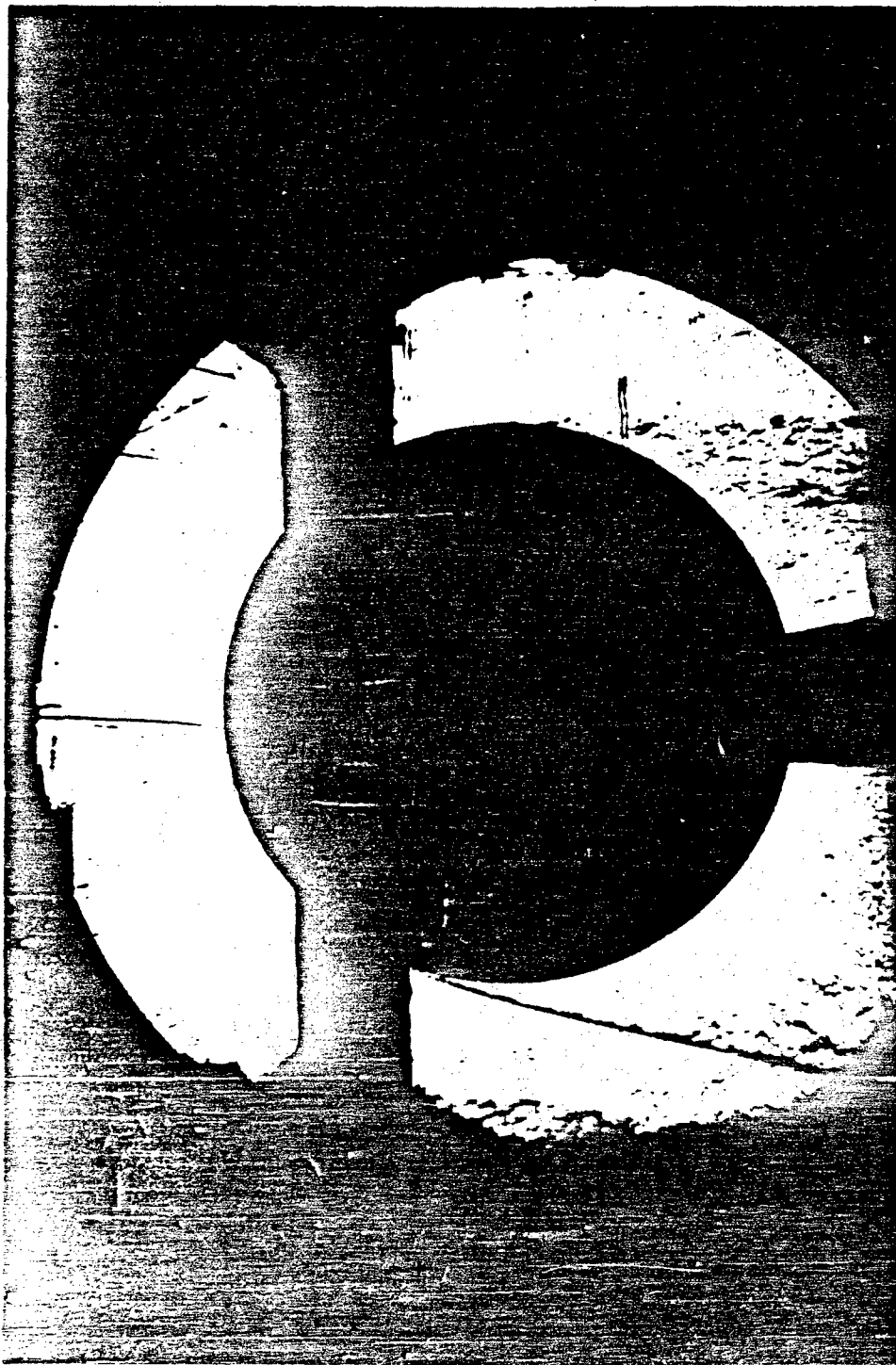


Figure 2.4.18d. Schlieren Photograph of Plan View
Forward Launch, $M=5.0$.

2.126

SECRET

SECRET



Figure 2.4.18 e Schlieren Photograph of Side View
Cross-Wind Launch, $M = 2.0$

2.127

SECRET

SECRET



Figure 2.4.18 f. Schlieren Photograph of Plan View
Cross-Wind Launch, $M = 2.0$

2.128

SECRET

SECRET



Figure 2.4.18 g Schlieren Photograph of Side View
Aft Launch, $M = 3.0$

2.129

SECRET

SECRET

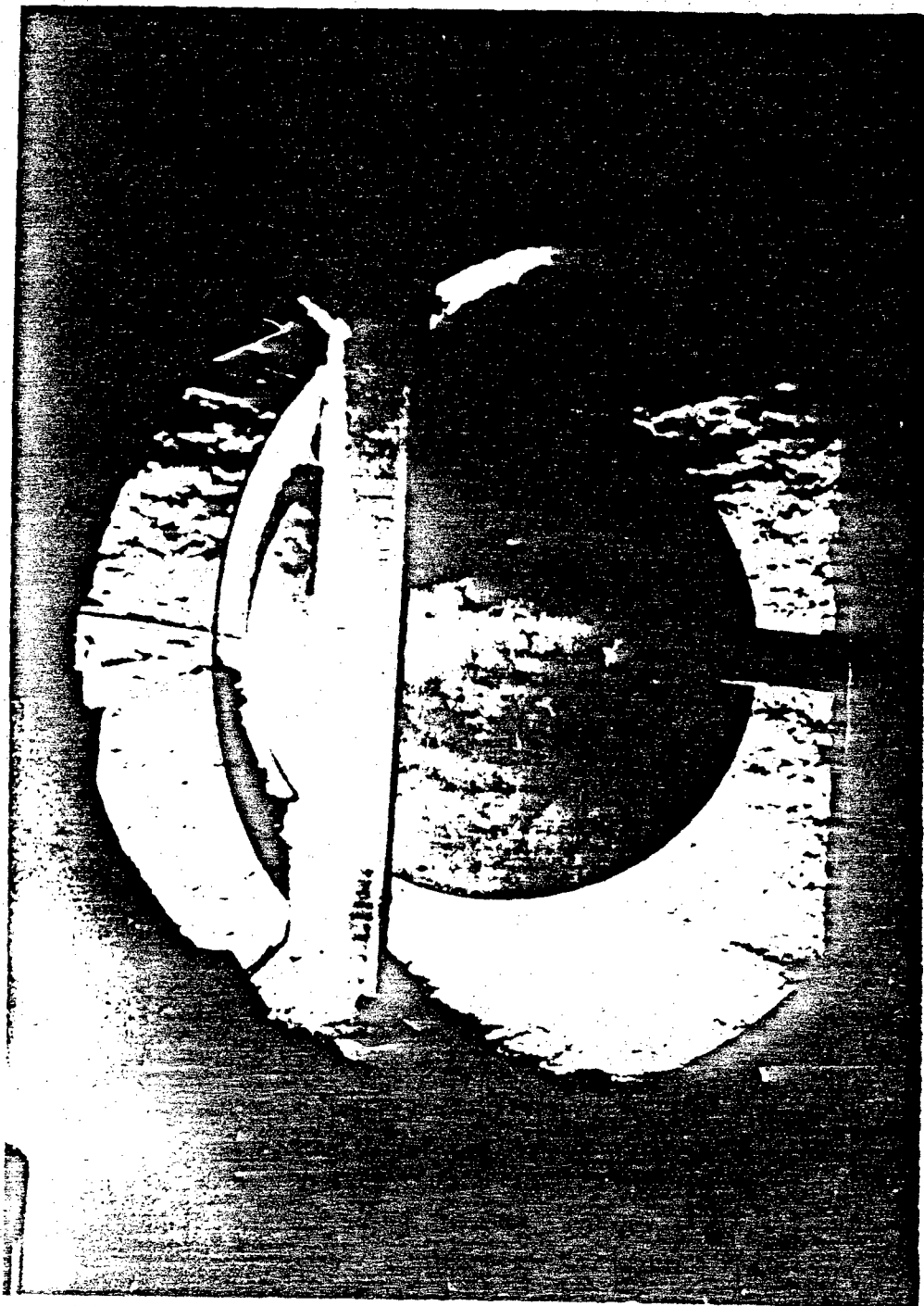


Figure 2.4.18 h Schlieren Photograph of Plan View
Aft Launch, $M = 3.0$

2.130

SECRET

imperfections in the window itself. The wide, vertical black strip appearing in the schlieren photographs is the frame of the observation window.

2.4.5 POWER-ON AERODYNAMIC CHARACTERISTICS The effect of main rocket motors and control jets on the aerodynamic coefficients of the PYE WACKET Feasibility Test Vehicle is discussed in this section. The power-on coefficients presented were estimated for use in computer studies to determine the flight characteristics of the PYE WACKET FTV. The effects of the main rocket motor were considered negligible for the coefficients of normal force, pitching moment and rolling moment for the low angle of attack range considered ($\alpha = 0^\circ$ to 4°) at sideslip angles up to 90° . The force and moment coefficients estimated for the power-on condition were: (1) axial drag, (2) side force, and (3) yawing moment. The estimated coefficients are presented only for sea level conditions since this will be the approximate launch altitude of the Feasibility Test Vehicle.

2.4.5.1 Axial Drag Coefficient The estimated axial-drag coefficient for power-on and power-off is presented in Figure 2.4.19 for zero angle of sideslip and angle of attack between $M = 0$ and $M = 5.0$. The axial-drag coefficient for main rockets on ($\beta = 0^\circ$ only) was estimated by reducing the main rocket-off, control jet-on, axial base-drag coefficients of Figure 2.4.20 by the ratio of the power-on base area to the power-off base area,

$$\frac{S_{BASE} (I/ON)}{S_{BASE} (I/OFF)} = 0.61$$

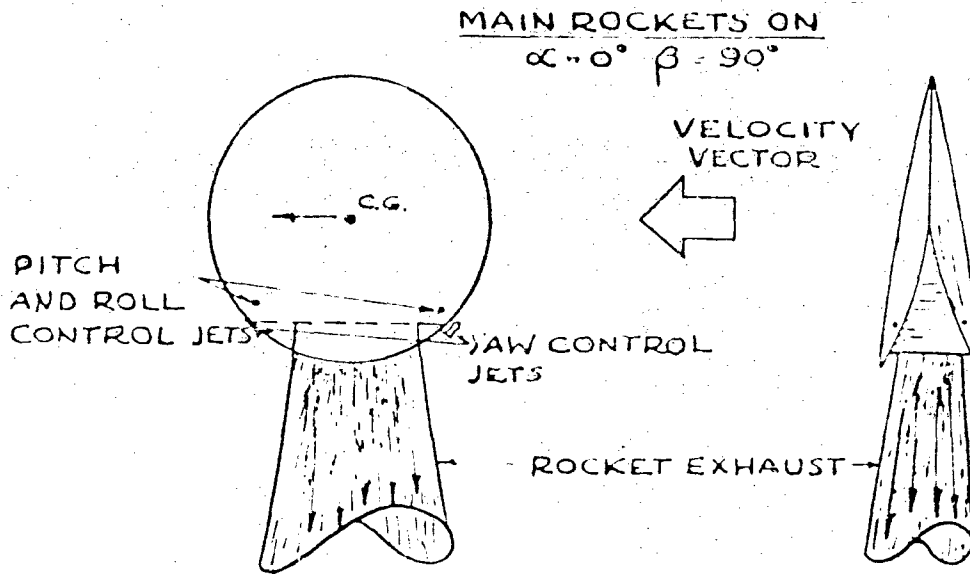
This factor amounts to approximately an eight to twelve percent reduction in total axial-drag coefficient for power-on flight. It is noted that the axial-drag coefficients are presented for both control jets and main motors operating since these conditions will prevail in the actual power-on flight phase of the FTV. As illustrated by the base drag coefficients of Figure 2.4.21, there is a marked increase in base drag due to operation of the control jets up to $M = 2.0$ with main rocket motor off. This increase in base drag is due to the pumping action in the wake of the jet causing entrainment of air from outside the jet, thus reducing the pressure behind the jet. This effect is substantiated in References 5.13 and 5.14 for pressures behind jets in subsonic and supersonic flow.

A drag breakdown for the axial-drag coefficients of Figure 2.4.19 is shown in Figures 2.4.20, 2.4.21, and 2.4.22. Figure 2.4.21 presents the base drag coefficient for main rockets off (control jets on and off), and Figure 2.4.20 presents C_{D_0} for main rocket on with control jets on for $\beta = 0^\circ$, $\alpha = 0^\circ$, as a function of Mach number up to $M = 5.0$.

SECRET

Again, as discussed previously, these curves present the 39 per cent reduction in base drag coefficient with main rockets on and control jets on due to the reduction in effective base area. The wave plus afterbody drag and skin-friction drag are shown in Figure 2.4.22. The total axial drag for a given power-on condition was obtained by adding the wave plus afterbody drag and skin-friction drag to the associated power-on base-drag component. The skin-friction drag coefficient was based on FTV Reynolds numbers at sea level (Reference 5.11).

The estimated axial drag coefficient at $\beta = 90^\circ$ for main rocket motors on is shown in Figure 2.4.23. The increase in C_{D_x} due to main motors on was estimated from assumed pressure distributions around the portion of the periphery affected when the main rockets are on. A sketch showing the power-on condition is illustrated below.



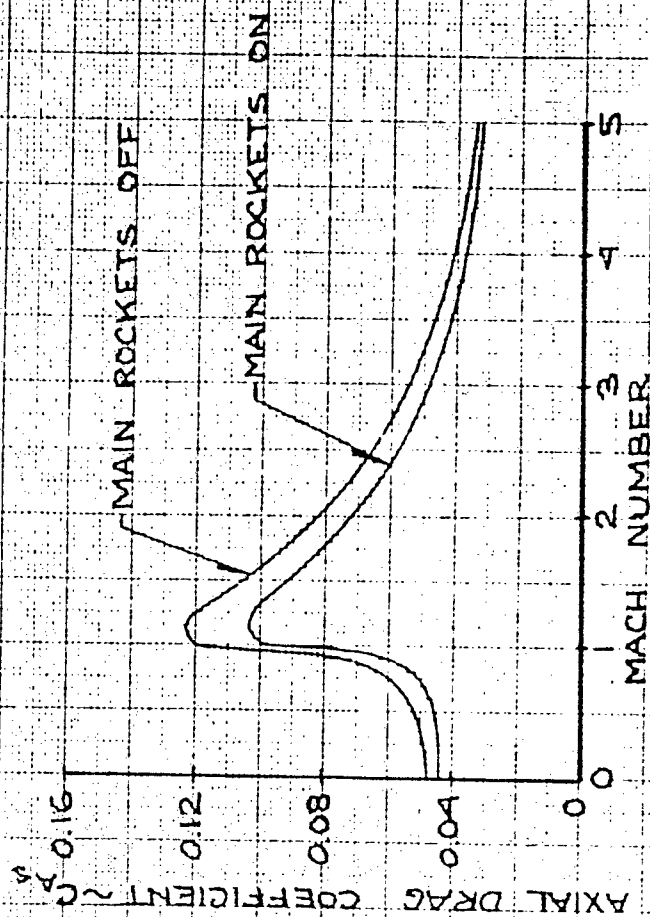
The pressure distributions for power-on were based largely on the correlation of pressures in front of and behind the reaction jets, Figure 2.4.39, and the data from References 5.13 and 5.14.

The axial-drag coefficient as a function of Mach number, from $M = 0$ to $M = 1.0$ with angle of sideslip as a parameter, is shown in Figure 2.4.24 for main rockets and control jets operating. These curves were derived from the power-on estimates of Figure 2.4.19, $\beta = 0^\circ$, and Figure 2.4.23, $\beta = 90^\circ$. As noted, the estimated axial-drag coefficient is presented for angles of sideslip from 0 to 90

SECRET

SECRET

FIGURE 2.4.19
PYE WACKET FTY
AXIAL DRAG COEFFICIENT, $\beta=0$ VS MACH NUMBER
COMPARISON FOR MAIN ROCKET ON AND OFF
CONTROL JETS ON
 $\alpha=0^\circ$



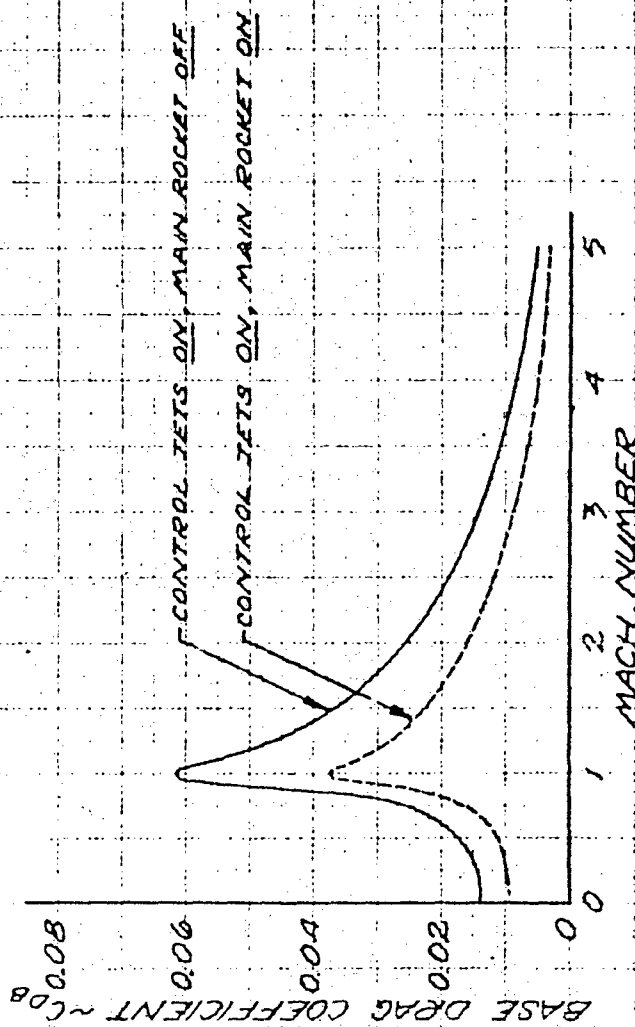
SECRET

SECRET

FIGURE 2.4.20
PYE WACKET FTV

COMPARISON OF POWER-ON AND POWER-OFF BASE DRAG

$\alpha = 0^\circ$ $\beta = 0^\circ$



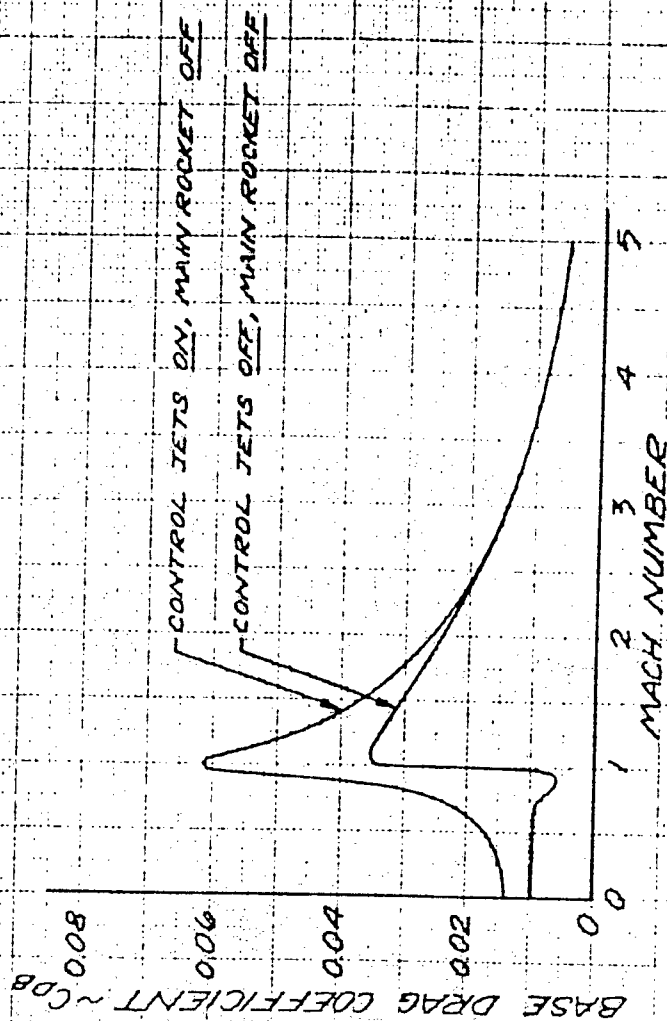
SECRET

SECRET

FIGURE 2.4.21
DYE WACKET FTV

COMPARISON OF CONTROL JET ON
AND CONTROL JET OFF BASE DRAG

$\alpha = 0^\circ$ $\beta = 0^\circ$



2.135

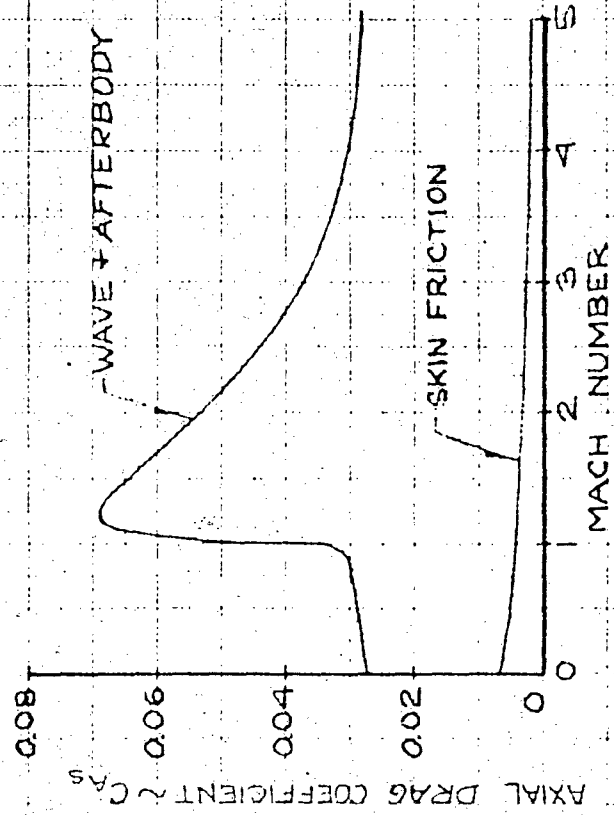
SECRET

SECRET

FIGURE 2.4.22
PYE WACKET FTV.

VARIATION OF COMPONENT AXIAL DRAG
WITH MACH NUMBER

$\alpha=0^\circ$ $\beta=0^\circ$ SEA LEVEL POWER-ON OR OFF



SECRET

SECRET

FIGURE 2.4.23

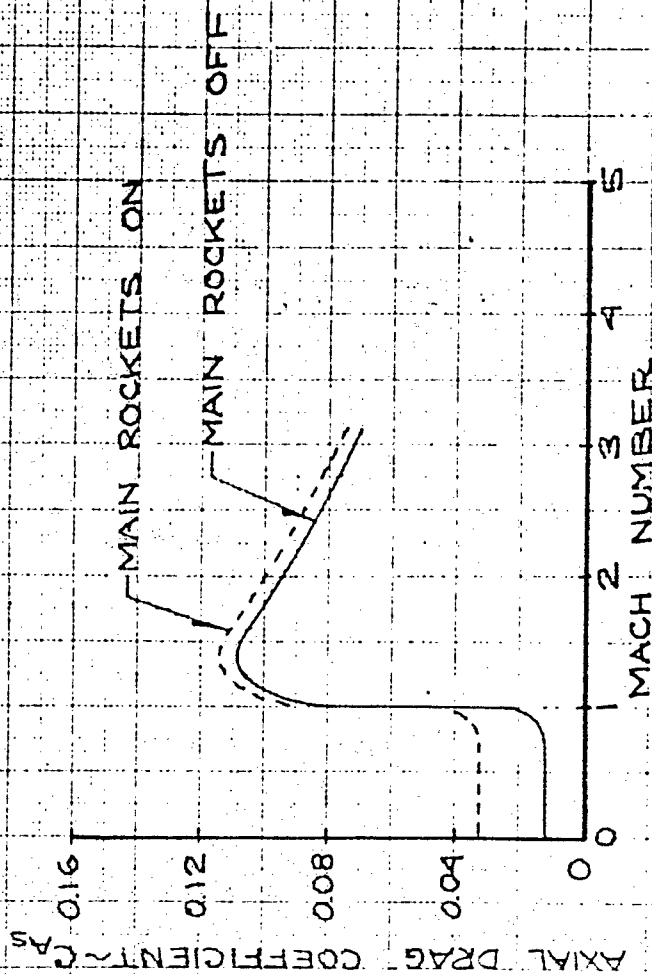
PYE WACKET FTV

AXIAL DRAG COEFFICIENT, $\beta = 90^\circ$ VS MACH NUMBER

COMPARISON FOR MAIN ROCKETS ON AND OFF

CONTROL JETS EITHER ON OR OFF

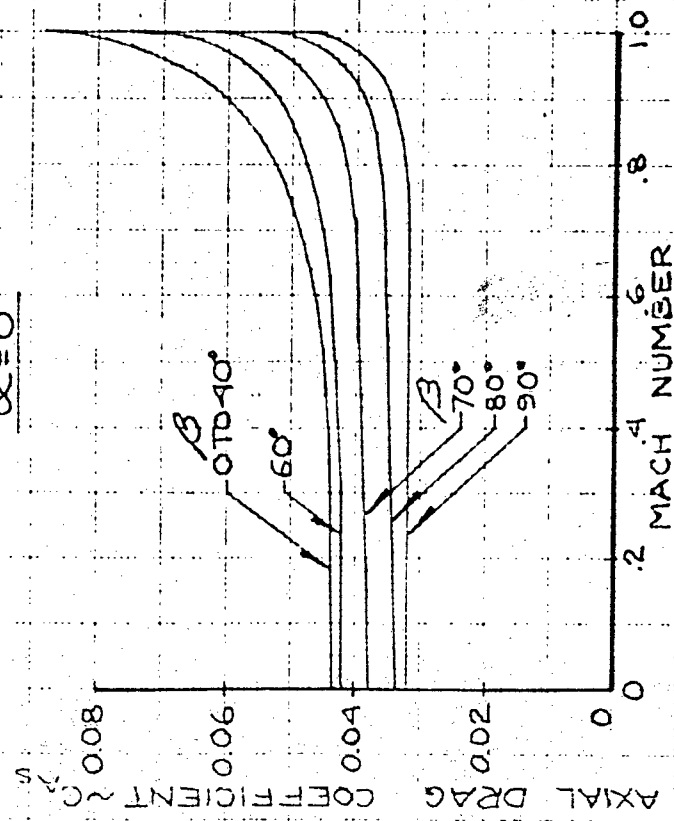
$\alpha = 0^\circ$



SECRET

SECRET

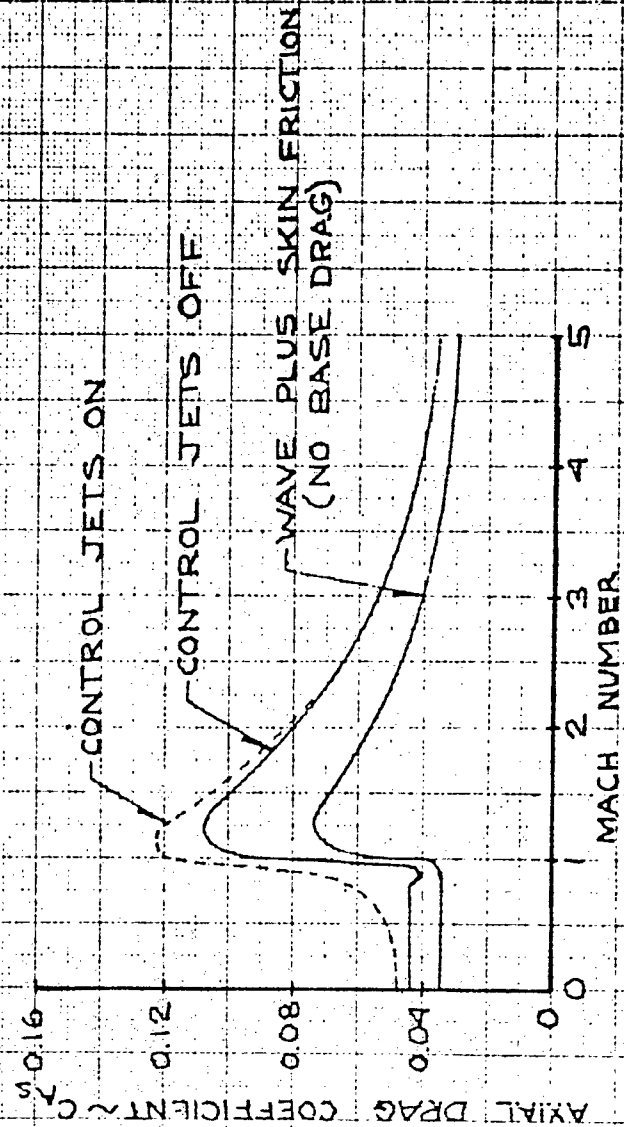
FIGURE 2.4.24
 PYE WACKET FTV
 AXIAL DRAG COEFFICIENT VS. MACH NUMBER
 COMPARISON FOR β , 0 TO 90 DEGREES
 MAIN ROCKETS ON
 CONTROL JETS ON
 $\alpha = 0^\circ$



SECRET

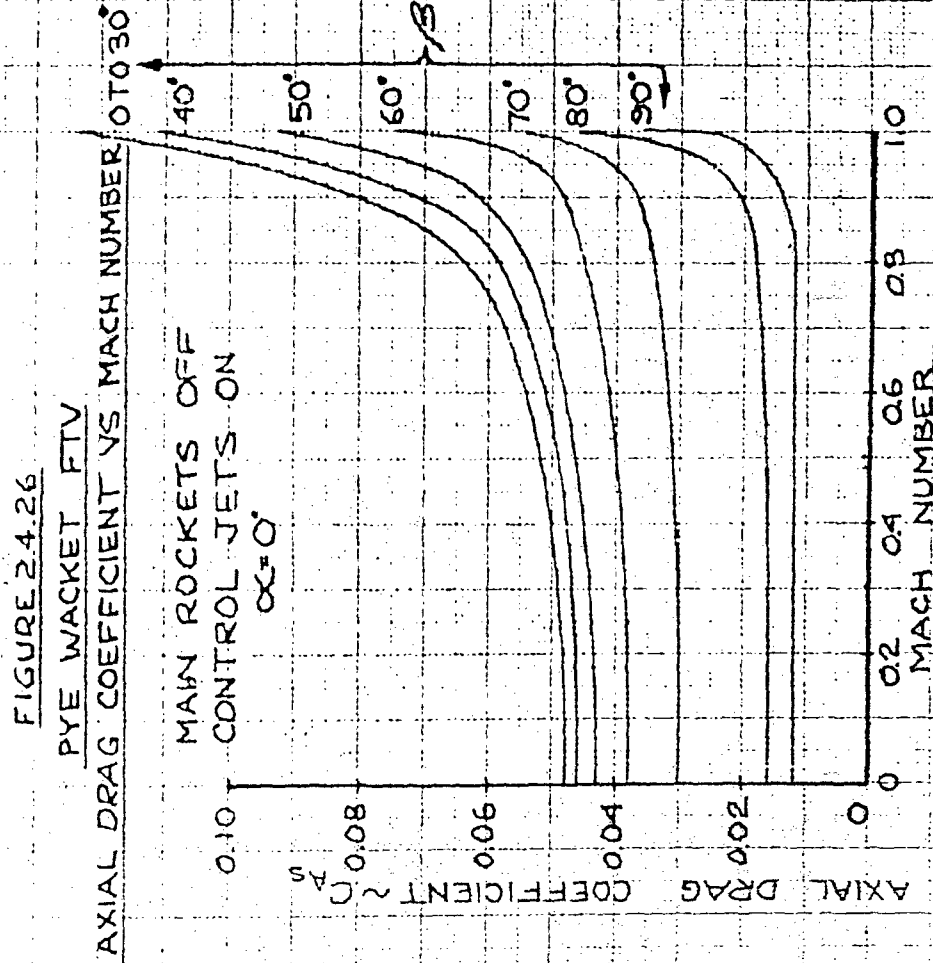
SECRET

FIGURE 2.4.25
PYE WACKET FTV
AXIAL DRAG COEFFICIENT, $\beta=0^\circ$ VS MACH NUMBER
COMPARISON FOR CONTROL JETS ON AND OFF
MAIN ROCKETS OFF
 $\alpha=0^\circ$



SECRET

SECRET



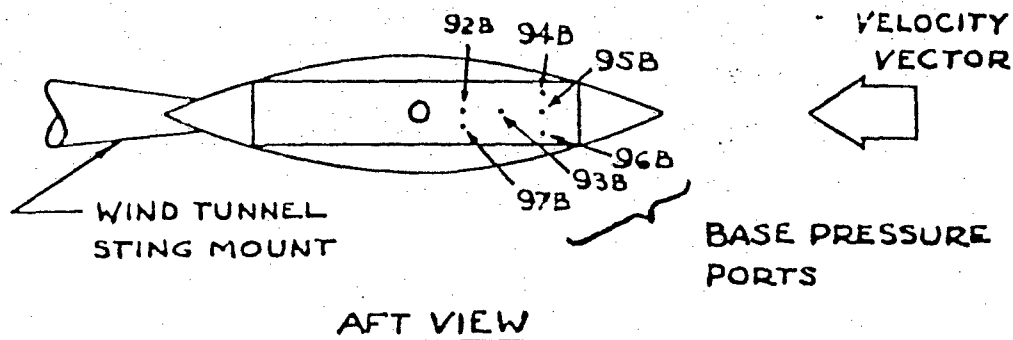
2.140

SECRET

SECRET

degrees for use in computations involving side-launch conditions. Aft launch estimations for main rockets on are not included because of the lack of experimental data. A discussion of some of the general aspects of rear launch conditions is presented in Section 2.7.1. The axial drag coefficient as a function of Mach number, for main rocket motors off and control jets on, is shown in Figures 2.4.25 and 2.4.26.

2.4.5.2 Side Force and Yawing Moment Coefficients The estimated side force and yawing moment coefficients for power-on are presented in Figures 2.4.27 and 2.4.28, respectively, with β as a parameter. The power-off wind tunnel side force and yawing moment data were used as a basis for determining the power-on coefficients. The power-off data was first modified by subtracting the estimated effects of the pressure distribution on the base. The base pressure data from the wind tunnel tests did not afford a complete distribution of pressure across the base, and consequently, estimations were made of the unknown pressure points on the base. A diagram is shown below with the pressure port locations indicated.



As shown in the sketch, pressures were obtained over approximately 30 percent of the base. This lack of complete data resulted in only an approximated base pressure distribution. In order to determine the pressure distribution in front of and behind the jets of the main rocket motor exhaust at $\beta = 90^\circ$, the pressure distribution was assumed to be the same as the pressure data in front of and behind the reaction jets as obtained from the pressure model wind tunnel test. These data are shown in Figure 2.4.39 as windward and leeward pressure coefficients for control jet chamber pressures of approximately 700 psia. A two-to-one trapezoidal pressure distribution on either side of the rocket exhaust extending to the edge of the base was assumed for the power-on estimations.

2.141

SECRET

SECRET

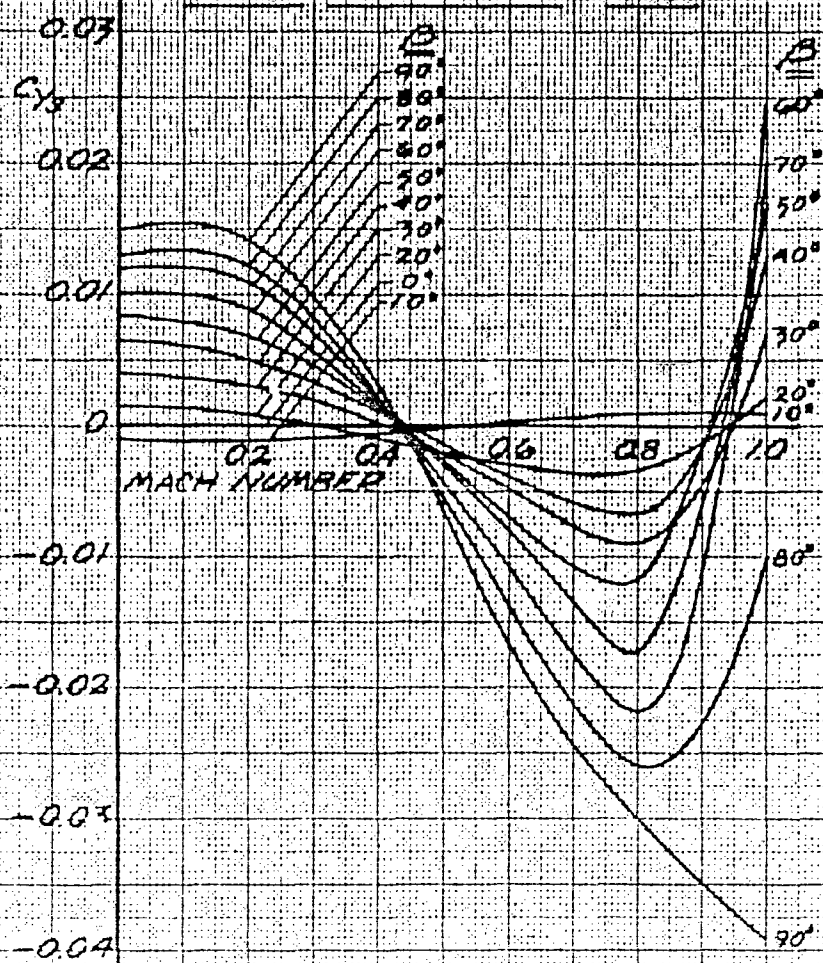
FIGURE 2.4.27
PYE WACKET FTV

ESTIMATED SIDE FORCE COEFFICIENT

VS

MACH NUMBER

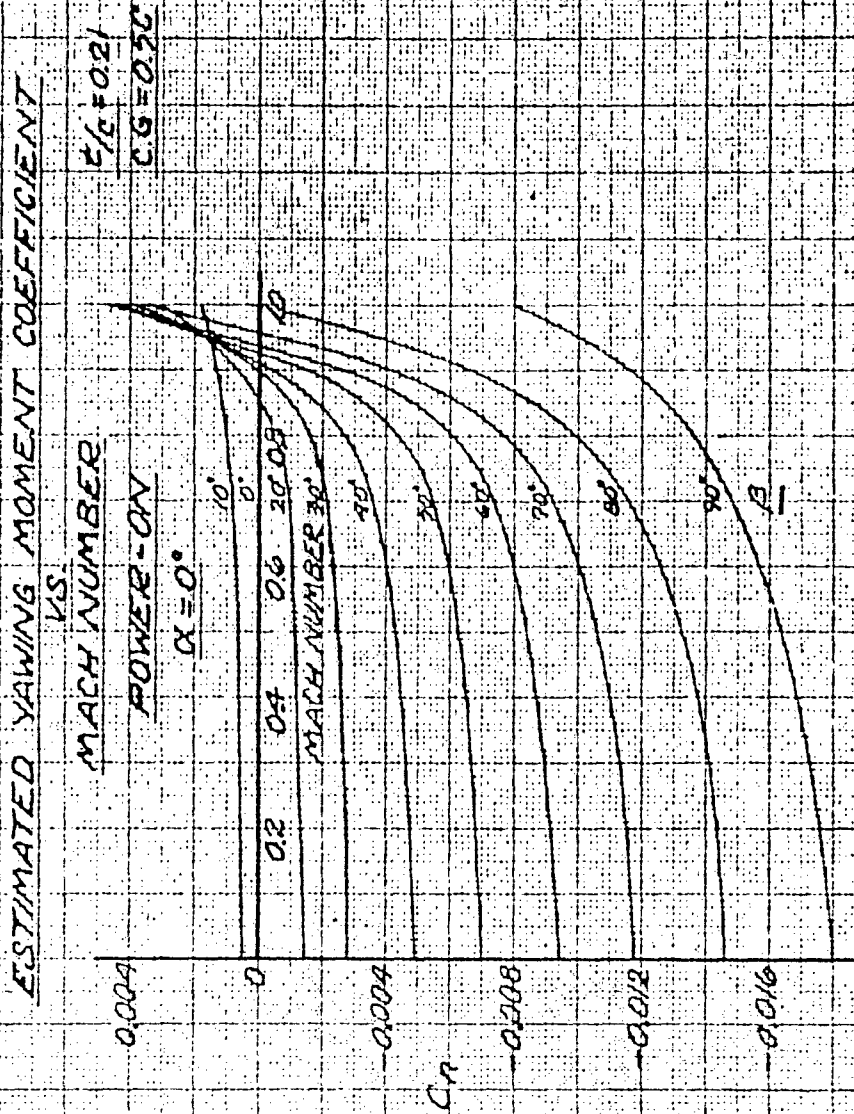
$\frac{1}{2}C = 0.21$ POWER-ON $\alpha = 0^\circ$



SECRET

SECRET

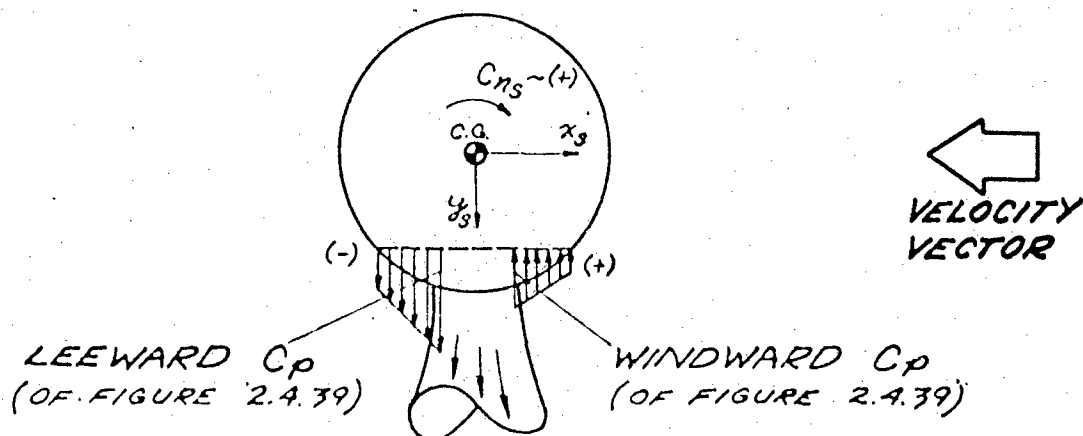
FIGURE 2.4.28
RYE WACKET FTV



SECRET

SECRET

A sketch of this assumed pressure distribution is shown below.



The assumed leeward and windward pressure distribution on either side of the rocket exhaust is highly destabilizing in the yaw plane with the maximum yawing moments occurring at the side launch condition of $\beta = 90^\circ$. An analysis of the required yaw control thrust for aerodynamic yawing moments and moments due to thrust misalignments may be found in Volume III, "Configuration and Autopilot/Control."

2.1.6 PRESSURE DISTRIBUTION

2.1.6.1 Control Jets Off The subsonic pressure distribution along any streamwise chord at zero sideslip angle is similar in shape to that of a two-dimensional airfoil with the same cross section. Figure 2.1.2 presents the longitudinal pressure distribution at $M = 0.6$, which is typical of subsonic Mach numbers, for different lateral positions. This curve shows the characteristic positive pressure coefficient near the leading edge. As would be expected from subsonic flow considerations, the longitudinal pressure distribution decreases non-linearly toward the rear of the vehicle. The lateral pressure distribution is nearly constant on the forward half of the missile, with larger variations toward the rear.

The supersonic longitudinal pressure distribution, as shown in Figure 2.1.30, is nearly linear as would be expected. Three-dimensional effects appear to be slight as evidenced by small differences in the

SECRET

SECRET

lateral pressure distribution. The peak pressure at the leading edge is a function of the local leading edge sweep angle. The variation of peak pressure around the leading edge periphery is approximately a cosine squared function of the local sweep angle, supporting the theoretical derivation presented in Section 2.2.1.

Figure 2.4.31 shows the effect of Mach number on the centerline pressure distribution. This plot clearly shows the transonic pressure coefficient rise. The peak leading edge pressure increases with Mach number to approximately $M = 1.3$ and then decreases with increasing Mach number. Also discernible is the characteristic linearization effect of supersonic Mach numbers.

The effect of angle of attack on the longitudinal centerline pressure distribution is shown in Figure 2.4.32. The local lift produced by a cross-section is proportional to the area between the curves of the windward and leeward sides. Since the pressure coefficient is more positive on the windward side, the direction of the lift is positive.

An unusual situation is apparent at a sideslip angle of 90 degrees. Because of the blunt base, the configuration is not aerodynamically symmetrical. Although the configuration appears entirely different to the free stream, the subsonic surface pressures are not too unlike the pressures for the forward launch position. This statement may be verified by noting that the subsonic normal forces of the two positions are essentially the same (see Figure 2.4.3). Supersonically, however, a noticeable reduction of normal force is apparent at $\beta = 90^\circ$. This normal force reduction can be attributed to the fact that portions of the blunt trailing edge are now effectively the leading edge. The blunt face induces local leading edge separation, resulting in a reduction of the normal force.

The effect of angle of attack on the lateral pressure distribution is shown in Figure 2.4.33 for the cross-wind launch position. Similar to the forward launch position, the normal force produced by the cross-section shown is positive. Another feature of the pressure distribution is apparent in Figure 2.4.33. The area between the windward and leeward curves, and hence, the normal force, is greater upstream than downstream. This trend is indicative of an upstream shift of the aerodynamic center of pressure with sideslip angle, Figure 2.4.13.

The most important aspect of the pressure distribution in the vicinity of 90 degrees of sideslip is its effect on the base slot. This slot behaves in the same manner as an airfoil. As the configuration is yawed from 110 to 70 degrees, the base can be considered to sweep an effective angle of attack from -20 to +20 degrees. At approximately

SECRET

SECRET

80 degrees yaw (effective base angle of attack of 10 degrees) the base stalls, resulting in a loss of lift on the base airfoil. The effect of this pressure in the base slot is predominantly felt in the yawing moment. The subsonic pressure coefficients recorded in the base slot are presented in Figure 2.4.34 as a function of sideslip angle. It should be emphasized that this phenomenon will occur only when the main rockets are not operating. In flight, the sideslip angle will not be in this vicinity after main motor burnout. However, this base pressure must be subtracted when estimating power-on yawing moments as explained in Section 2.4.5.2.

The 180 degree sideslip, or rear launch position, is analogous to blunt re-entry shapes and some of the same problems are encountered. Notable are the negative normal force and pitching moments observed for positive angles of attack in the high subsonic flow regime. A combination of pressure distribution studies and schlieren pictures are particularly useful in explaining the salient features of this phenomenon. However, no useable schlieren pictures were obtained subsonically; therefore, qualitative analysis of the flow field must be made from the pressure measurements and from the results of other investigations.

The concave base normal to the airstream induces local areas of high velocity as the flow expands around the edges. These induced velocities may exceed local sonic velocity and terminate in shock waves. These shock waves are apparent in schlierens obtained at supersonic velocities where the flow field behind the detached bow wave is essentially similar to subsonic flow. The shock waves produce an adverse pressure gradient which the boundary layer cannot support without separation. Because the airflow does not have the ability to complete the full expansion, the flow leaves the body at the leading edge and re-attaches to the body at some downstream point determined by the Mach number, Reynolds number, and angle of attack. As an aid to the flow visualization, the centerline pressure distribution is shown in Figure 2.4.35. Consider first the pressure distribution at zero angle of attack. As the airstream flows from the concave base to the surface of the vehicle, the large expansion around the lip of the base produces a very low pressure. This low pressure is in the vicinity of Station 20 in Figure 2.4.35. The local surface slope of the configuration is negative downstream of Station 20; consequently, the velocity of the airflow decreases. As the velocity decreases, the local pressure coefficients increase and reach positive values at the trailing edge.

Consider next the windward surface of the configuration at an angle of attack of 3 degrees. The pressure distribution trend is very similar to the zero angle of attack case. Notice, however, that the pressure

SECRET

SECRET

FIGURE 2.4.29

PYE WACKET FTV

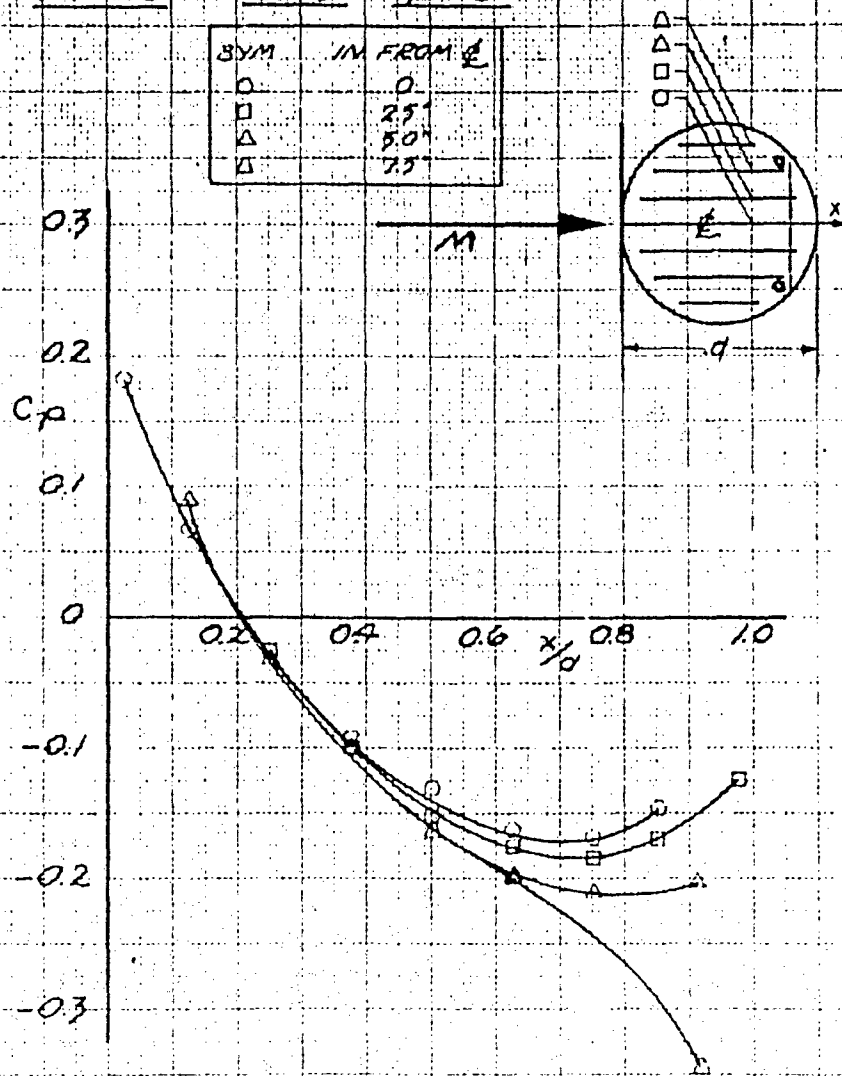
LONGITUDINAL PRESSURE DISTRIBUTION

$M=0.6$

$\alpha=0^\circ$

$\beta=0^\circ$

SYM	IN FROM ξ
O	0
□	2.5"
△	5.0"
▽	7.5"



2.147

SECRET

SECRET

FIGURE 2.4.30

PYE WACKET FTV

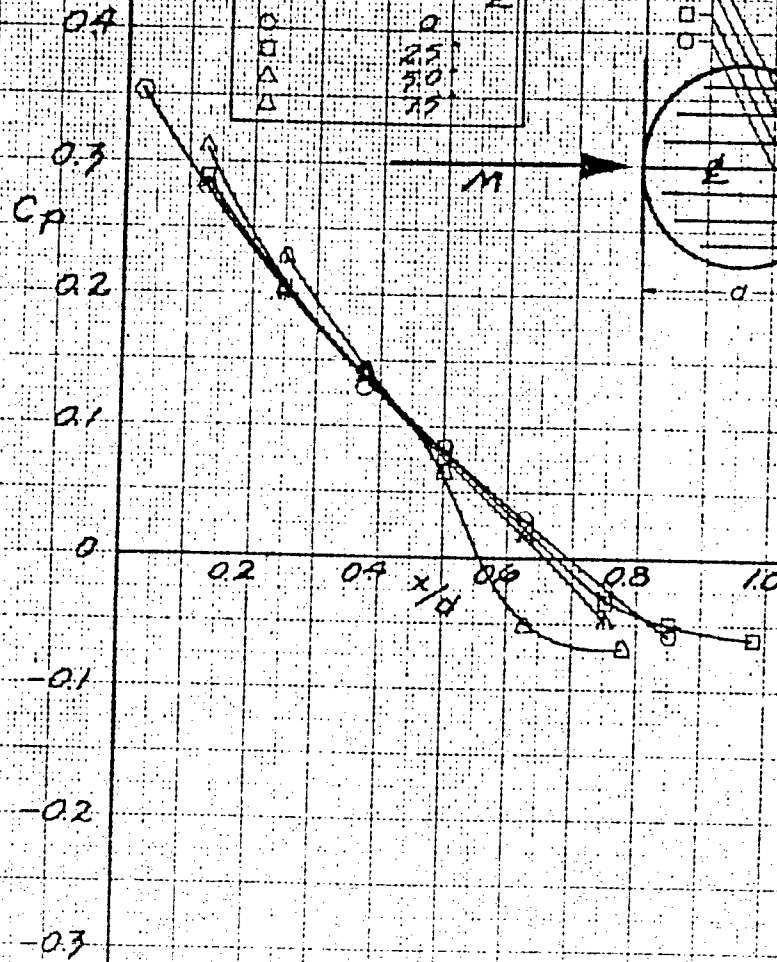
LONGITUDINAL PRESSURE DISTRIBUTION

$M=1.6$

$\alpha=0^\circ$

$\beta=0^\circ$

SYM.	IN FROM ξ
○	0
□	25
△	50
△	75



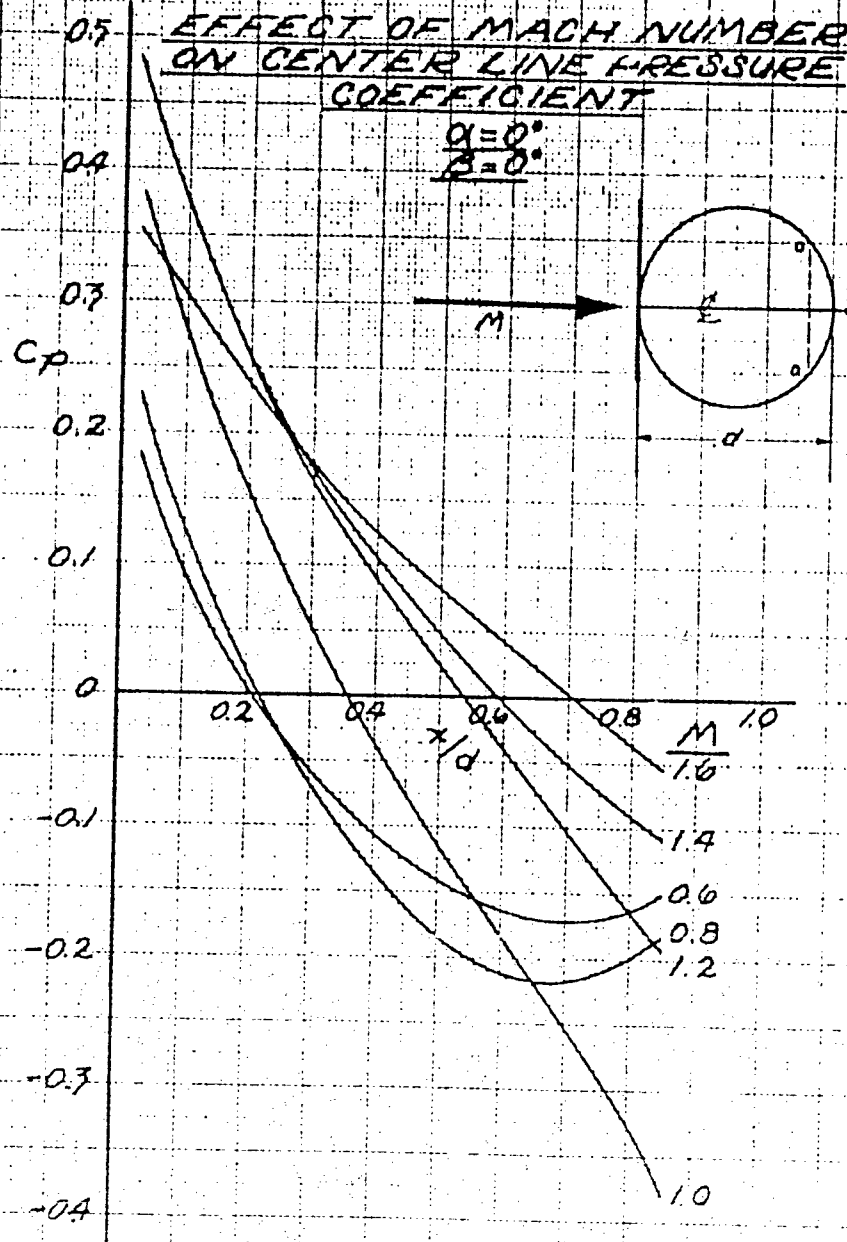
2.148

SECRET

SECRET

FIGURE 2.4.31

PYE WACKET FTV



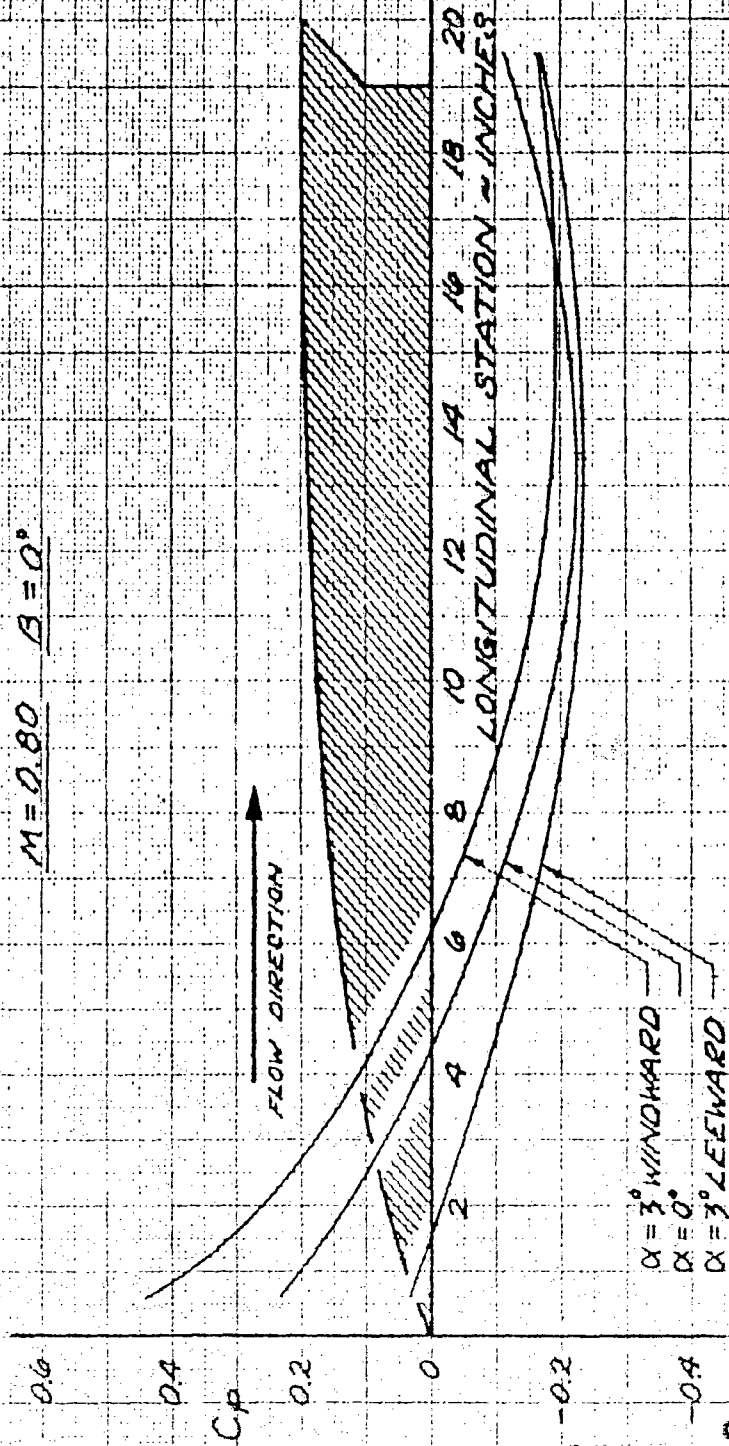
SECRET

SECRET

FIGURE 2.4.32
PYEWACKET.FTV

LONGITUDINAL PRESSURE DISTRIBUTION

$M = 0.80$ $\beta = 0^\circ$



SECRET

SECRET

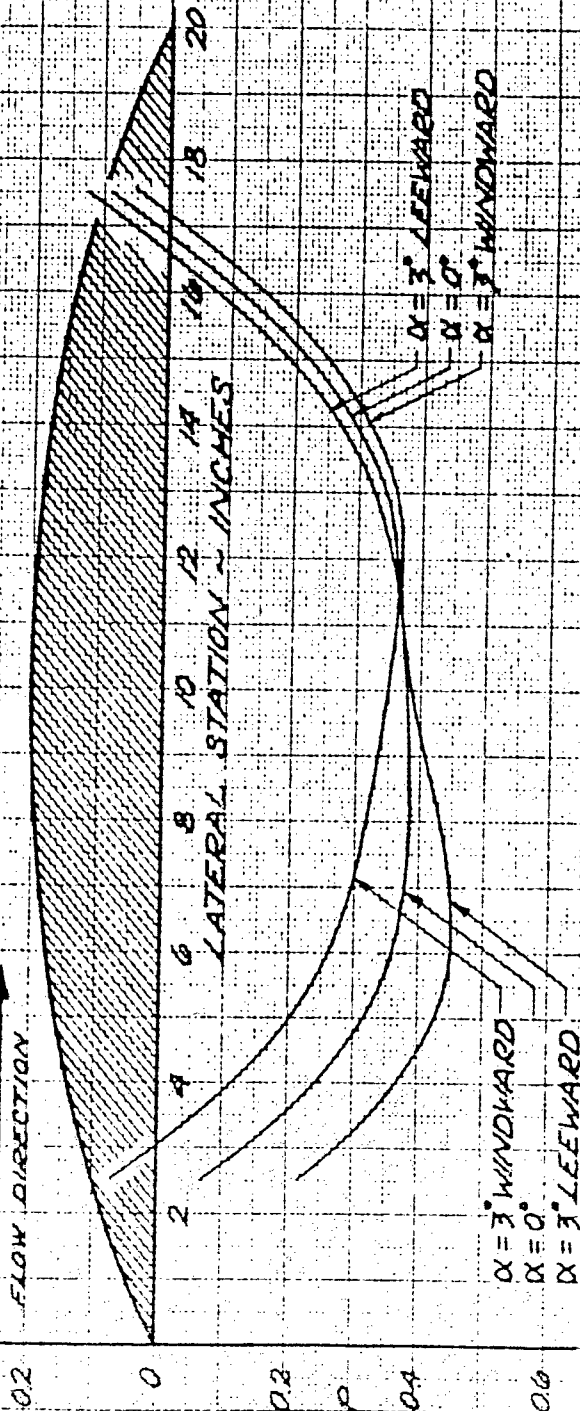
FIGURE 2.4.33

PYE WACKET FTV

LATERAL PRESSURE DISTRIBUTION

$M = 0.80$ $\beta = 90^\circ$

FLOW DIRECTION



2.151

SECRET

SECRET

FIGURE 2.4.34
PYE WACKET FTV

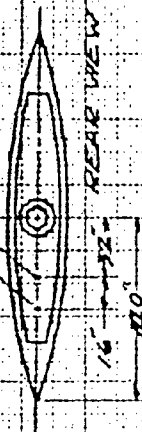
VARIATION OF BASE PRESSURE COEFFICIENT WITH SIDESLIP

ANGLE

$M=0.80$ $\alpha=0^\circ$

PRESSURE PORT 93

PRESSURE PORT 95



C_{PB}

2.52

120 140 160 180
 β - DEGREES

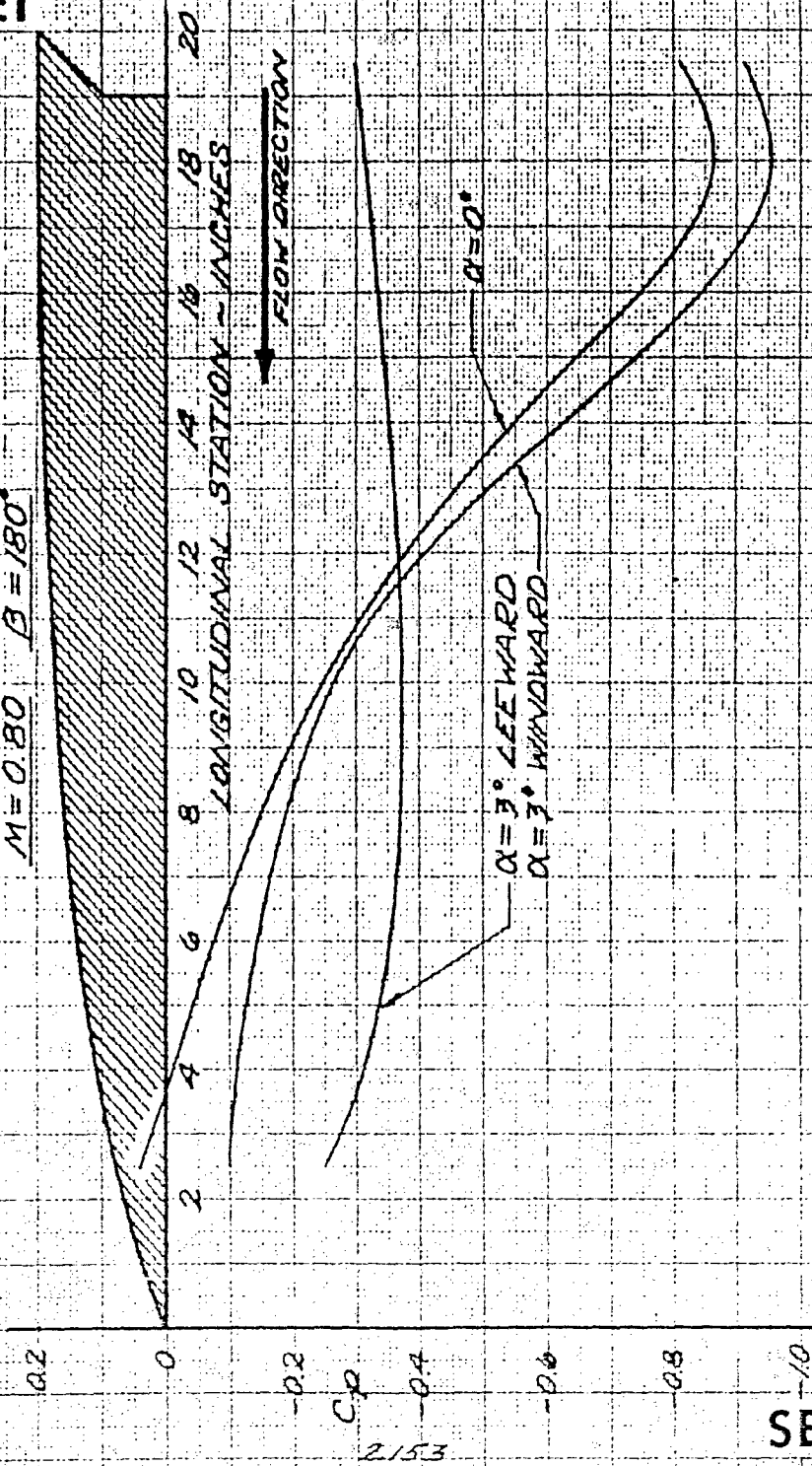
1.2
0.8
0.4
0
-0.4
-0.8

SECRET

SECRET

FIGURE 2.4.35
PYE WACKET FTV
LONGITUDINAL PRESSURE DISTRIBUTION

$M = 0.80$ $\beta = 180^\circ$



SECRET

SECRET

coefficients are more negative. This is caused by the fact that the flow must expand an additional 3 degrees around the base. The extra expansion produces a greater negative pressure at Station 20. The pressure coefficients then increase along the remainder of the configuration as in the zero angle of attack case.

The leeward side of the configuration produces a flow condition which is entirely different from the previous cases. The large adverse pressure gradient on the leeward side causes the flow to leave the surface of the vehicle. This can be observed by a pressure which is almost constant along the centerline. This flow separation is the cause of the unusual aerodynamic characteristics of the configuration in the rear launch position. The net area between the windward and leeward curves indicates that a negative normal force is produced for positive angles of attack. Also of importance is the force distribution along the centerline. The force upstream of the midchord is negative while the force downstream is positive. The combination of these forces produces a large negative, or restoring, pitching moment. It should be emphasized that the preceding discussion was concerned with the power-off case; the main rocket motor exhaust flow over the vehicle will alter the pressure distribution. A discussion of the probable flow structure with the main jet on is given in Section 2.7.1. Lack of experimental data precludes a quantitative analysis.

2.4.6.2 Control Jet On The method of control utilized by the PYE WACKET configuration is reaction jets. This choice was dictated primarily by considerations of omnidirectional launch, and secondarily by the superiority of reaction controls to aerodynamic controls at very high altitudes. However, when reaction jets are operated in the atmosphere, an interaction between the jet and the free stream occurs which can be very beneficial. This interaction is referred to as jet magnification and implies an induced pressure distribution on the body surrounding the jet. Because the jet induces both positive and negative pressure coefficients on the body, the sense of the induced force is dependant on the body geometry surrounding the jet. The magnitude of the force induced on the PYE WACKET configuration is presented in Volume III of this report; a qualitative analysis of the flow structure in the vicinity of the jet is presented in this volume.

A comprehensive study of the interaction of a reactive jet and the flow over a body has not been attempted until recent years. Previous research was confined to supersonic flow only. PYE WACKET reaction jets were tested in supersonic, transonic, and subsonic airstreams. The test was not specifically performed as a study of the local flow structure, so a detailed analysis cannot be made. However, with the aid of previous research, (Reference 5.14) and with experimental

SECRET

SECRET

evidence gained from the wind tunnel test, a good understanding of the flow structure was gained.

Subsonically, the only experimental results gained at the wind tunnel were the induced pressures surrounding the jets. Supersonically, however, both schlieren and fluorescent-oil pictures were taken. Figures 2.4.42a through 2.4.42f are selected examples of the schlieren pictures at zero sideslip angle. These pictures show that a detached normal shock wave forms around the jet. The high pressure behind this shock wave is transmitted upstream through the boundary layer and causes flow separation to occur. This effect can be seen in the schlieren pictures as an oblique shock wave ahead of and intersecting the normal shock. The pressure in this separated region is high, resulting in an interaction force which acts in the same direction as the force produced by the jet itself. Figures 2.4.41 a, b, and c are typical flow patterns taken with the fluorescent oil technique. The lines shown are actual streamlines very close to the body. The reverse flow is evident in front of the jet in the separated flow region.

Figures 2.4.36, 2.4.37, and 2.4.38 present the measured pressure coefficients in the vicinity of the reaction jet. The pressures were measured in three radial rings around the jet. Because the jet is very close to the trailing edge, only Ring 1 extended entirely around the jet. The measured pressures are shown for Mach numbers of 0.6, 1.6, and 3.0 and are representative of Mach numbers not shown.

Subsonically, the reaction jet induces a high pressure area upstream of the jet analogous to the stagnation region upstream of a solid body. This high pressure acts in the same direction as the jet thrust vector. However, this beneficial effect is overshadowed by the extremely low pressure induced on the leeward side of the jet. This pressure is lower than that expected behind a solid body and therefore suggests that a jet pumping effect is present. Figure 2.4.36c shows that the high pressure region extends upstream of Ring 3. Because the reaction jet is near the trailing edge, the low pressure is confined to a small area on the vehicle. The total force obtained by integrating the pressures in the subsonic region is positive. However, the location of the induced force is forward of the midchord, resulting in a pitching moment which is opposite in sign to that of the reaction control jets.

Supersonically, beneficial flow interference is achieved. The predominant feature of the induced pressure field is the large pressure upstream of the jet. The pumping effect on the leeward side of the jet is very small and therefore, only a small decrease in pressure is realized. The high pressure decreases rapidly upstream of Ring 3. The integration of the pressures results in a force acting in the

SECRET

FIGURE 24.36a

PYE WACKET FTV (180°)

PRESSURE COEFFICIENTS AROUND REACTION JETS

$\alpha = 0^\circ$ $\beta = 0^\circ$ $R = 100$

$M = 0.6$ RING 1

JET ON

JET OFF

(270°)

(90°)

DISTANCE FROM JET CENTER IN EXIT DIAMETERS	
1	0.72
2	2.20
3	3.60

C.P.

RATIO OF JET EXIT
DIAMETER TO MISSILE
DIAMETER = 0.03125

($\theta = 0^\circ$)

2.156

SECRET

SECRET

FIGURE 2.4.365

DYE WACKET FTV (180°)

PRESSURE COEFFICIENTS
AROUND REACTION JETS

$\alpha = 0^\circ$ $\beta = 0^\circ$ $P = 100$

$M = 0.8$ RING 2

RING

JET ON

JET OFF

(270°)

(90°)

C_p

DISTANCE FROM
JET CENTER IN
EXIT DIAMETERS

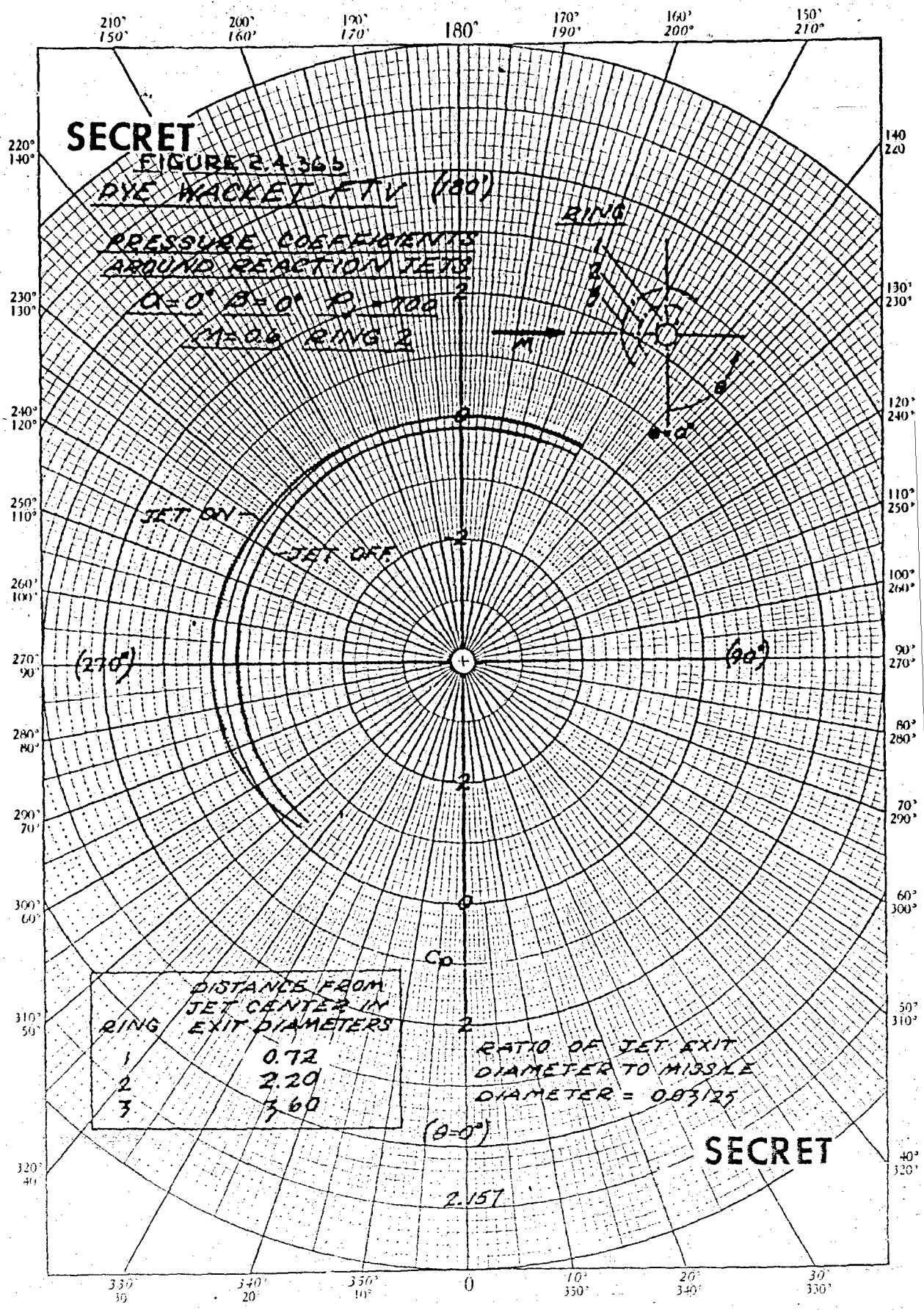
1	0.72
2	2.20
3	3.60

RATIO OF JET EXIT
DIAMETER TO MISSILE
DIAMETER = 0.03125

($\theta = 0^\circ$)

2.157

SECRET



SECRET

FIGURE 2.4.37A

PYE WACKET FTV (180°)

PRESSURE COEFFICIENTS
AROUND REACTION JETS

$\alpha = 0^\circ$ $\beta = 0^\circ$ $P_0 = 100$

$M = 1.6$ RING 1

RING

JET ON

JET OFF

(270°)

(90°)

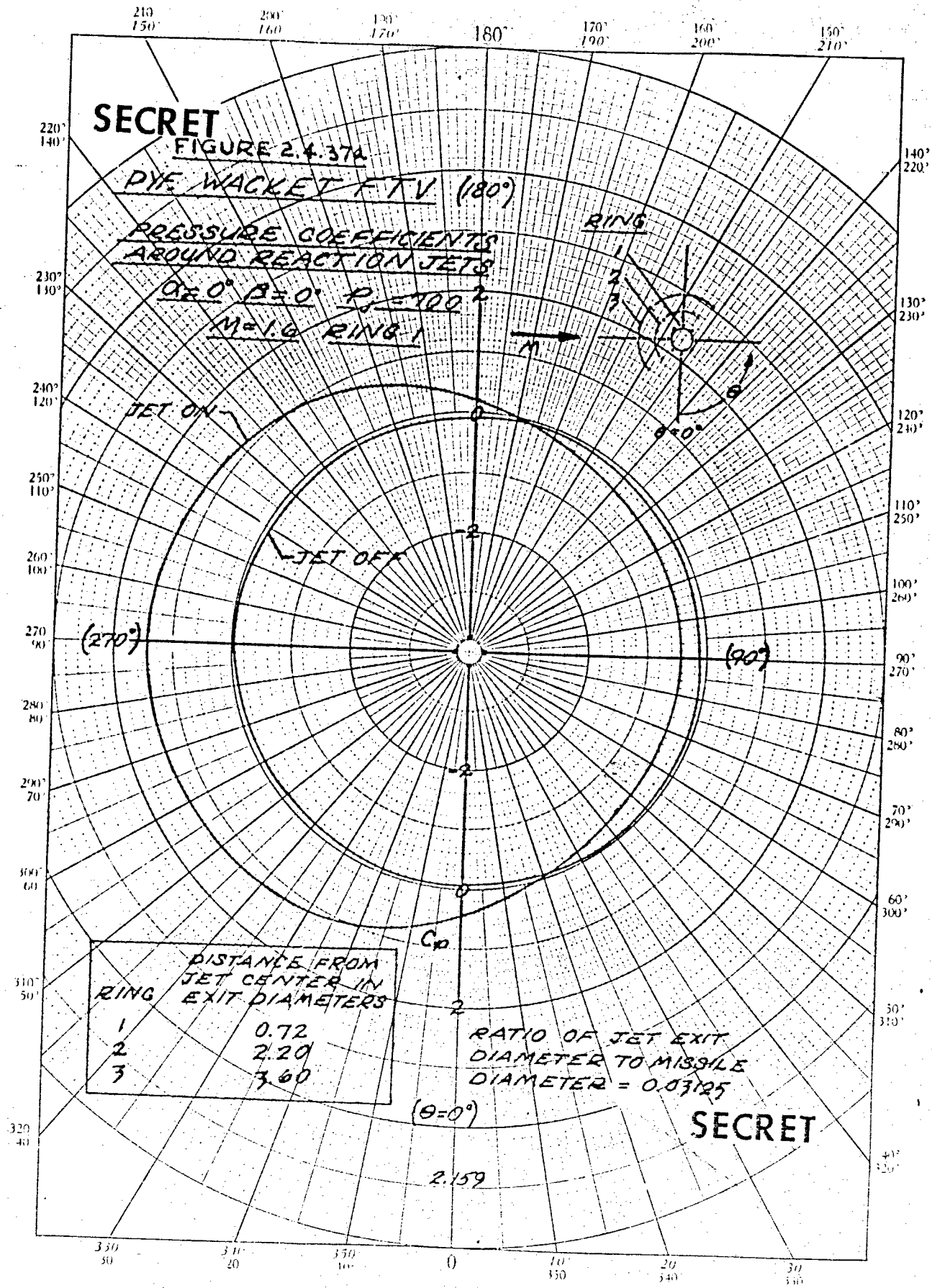
DISTANCE FROM JET CENTER IN RING EXIT DIAMETERS	
1	0.72
2	2.20
3	3.60

RATIO OF JET EXIT
DIAMETER TO MISSILE
DIAMETER = 0.0325

($\theta = 0^\circ$)

SECRET

2.159



SECRET

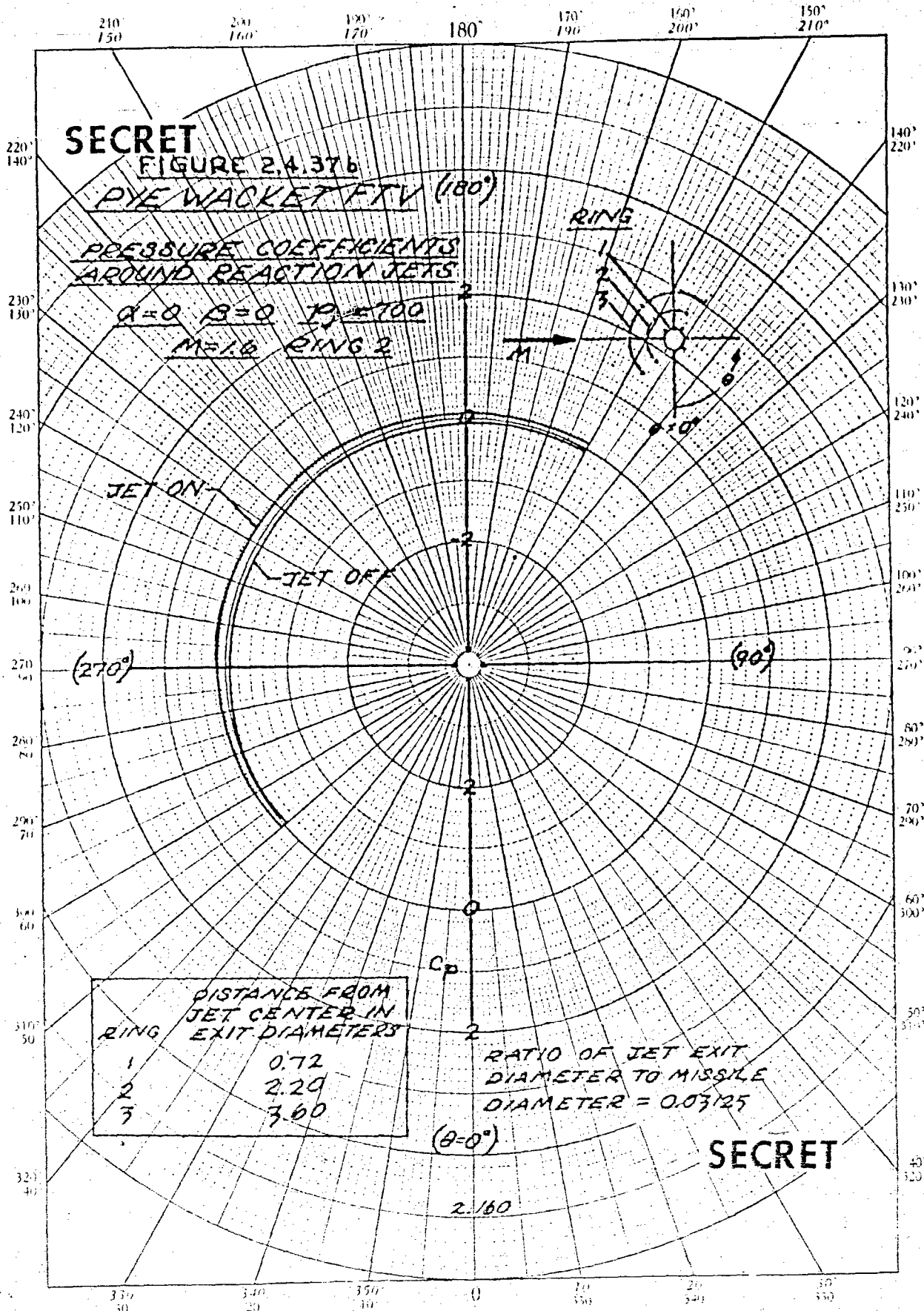
FIGURE 2.4.376

PYE WACKET FTV (180°)

PRESSURE COEFFICIENTS
AROUND REACTION JETS

$\alpha = 0$ $\beta = 0$ $P_1 = 100$

$M = 1.6$ RING 2



JET ON

JET OFF

(270°)

(90°)

DISTANCE FROM JET CENTER IN EXIT DIAMETERS	
RING	
1	0.72
2	2.20
3	3.60

RATIO OF JET EXIT
DIAMETER TO MISSILE
DIAMETER = 0.03125

($\theta = 0^\circ$)

2.160

SECRET

SECRET

FIGURE 2.4.37c

PVE WACKET FTV (180°)

PRESSURE COEFFICIENTS
AROUND REACTION JETS

$\alpha = 0^\circ$ $\beta = 0^\circ$ $P = 100$

$M = 1.6$ RING 3

RING

M

JET ON

JET OFF

(270°)

(90°)

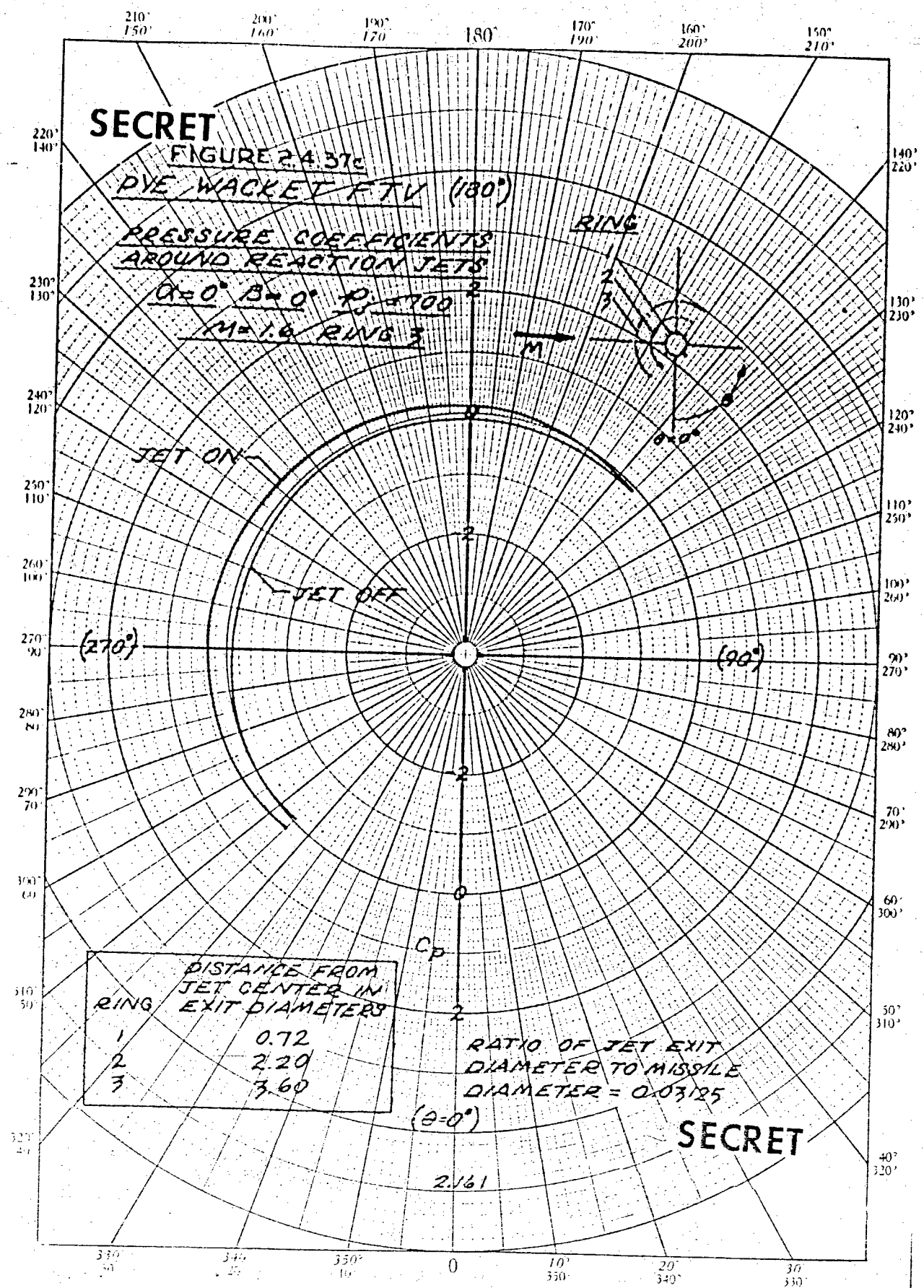
DISTANCE FROM JET CENTER IN EXIT DIAMETERS	
RING	
1	0.72
2	2.20
3	3.60

RATIO OF JET EXIT
DIAMETER TO MISSILE
DIAMETER = 0.03125

($\theta = 0^\circ$)

2.161

SECRET



SECRET

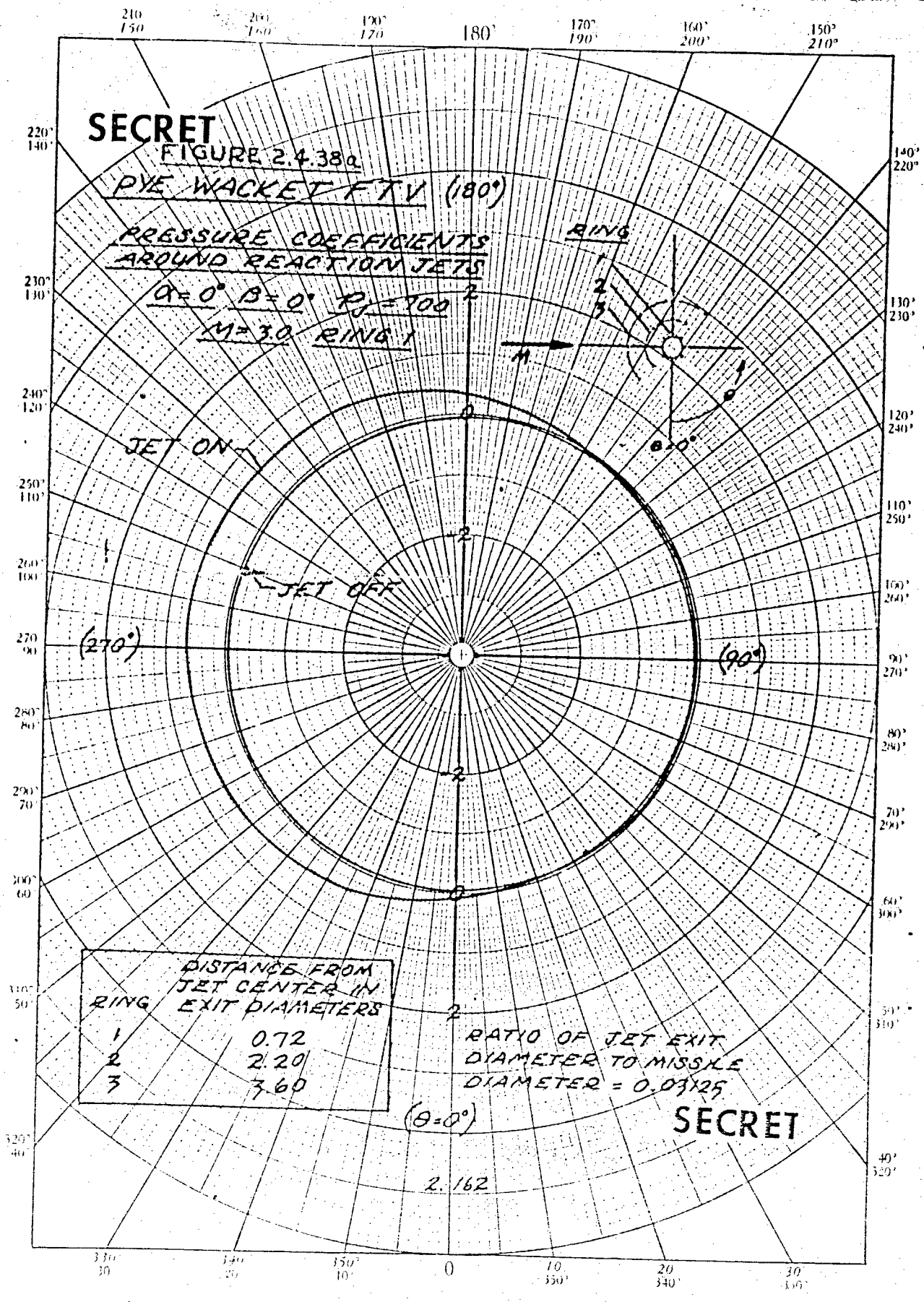
FIGURE 2.4.38a

PYE WACKET FTV (180°)

PRESSURE COEFFICIENTS
AROUND REACTION JETS

$\alpha = 0^\circ$ $\beta = 0^\circ$ $P_j = 100 \text{ lb}$

$M = 3.0$ RING 1



DISTANCE FROM JET CENTER IN EXIT DIAMETERS	
1	0.72
2	2.20
3	3.60

RATIO OF JET EXIT
DIAMETER TO MISSILE
DIAMETER = 0.03125

SECRET

2.162

SECRET

FIGURE 2.4.38b

PYE WACKET FTV (180°)

PRESSURE COEFFICIENTS
AROUND REACTION JETS

$\alpha = 0^\circ$ $\beta = 0^\circ$ $P_1 = 100$

$M = 3.0$ RING 2

RING

1
2
3

M

JET ON

JET OFF

(270°)

(90°)

C_p

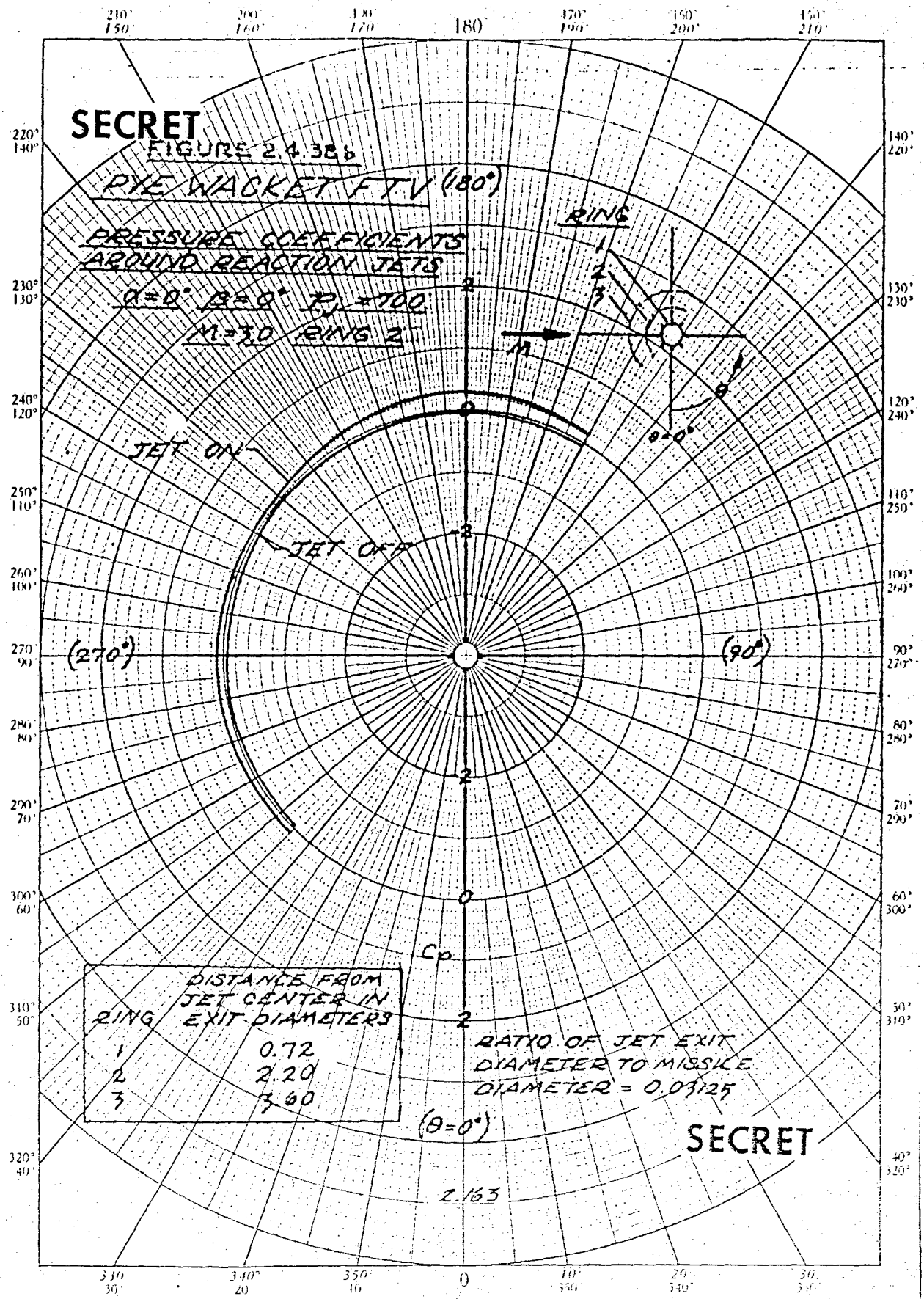
RING	DISTANCE FROM JET CENTER IN EXIT DIAMETERS
1	0.72
2	2.20
3	3.60

RATIO OF JET EXIT
DIAMETER TO MISSILE
DIAMETER = 0.03125

($\theta = 0^\circ$)

2.163

SECRET



SECRET

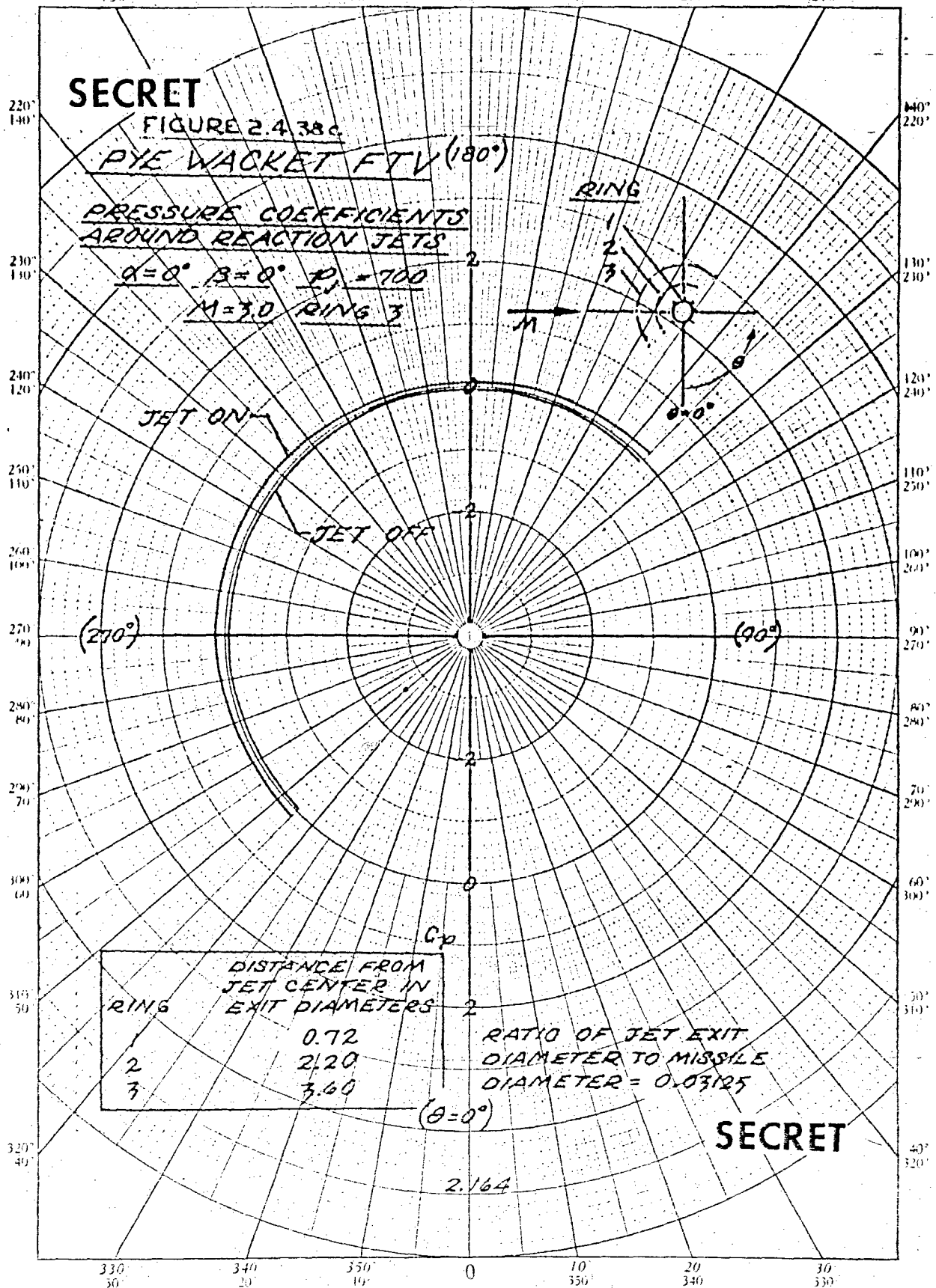
FIGURE 2.4.38c

PYE WACKET FTV (180°)

PRESSURE COEFFICIENTS
AROUND REACTION JETS

$\alpha = 0^\circ$ $\beta = 0^\circ$ $P_1 = 700$

$M = 3.0$ RING 3



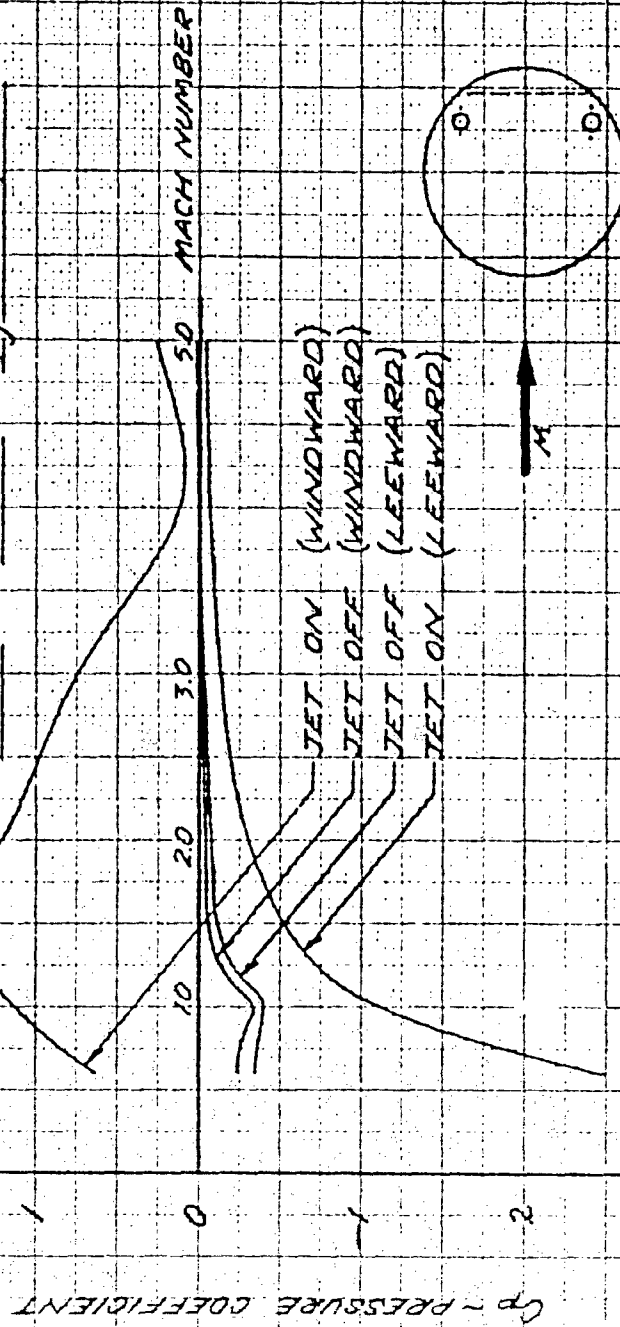
SECRET

FIGURE 2.4.39

PYE WACKET FTV

COMPARISON OF MAXIMUM AND MINIMUM PRESSURES ADJACENT TO REACTION JETS

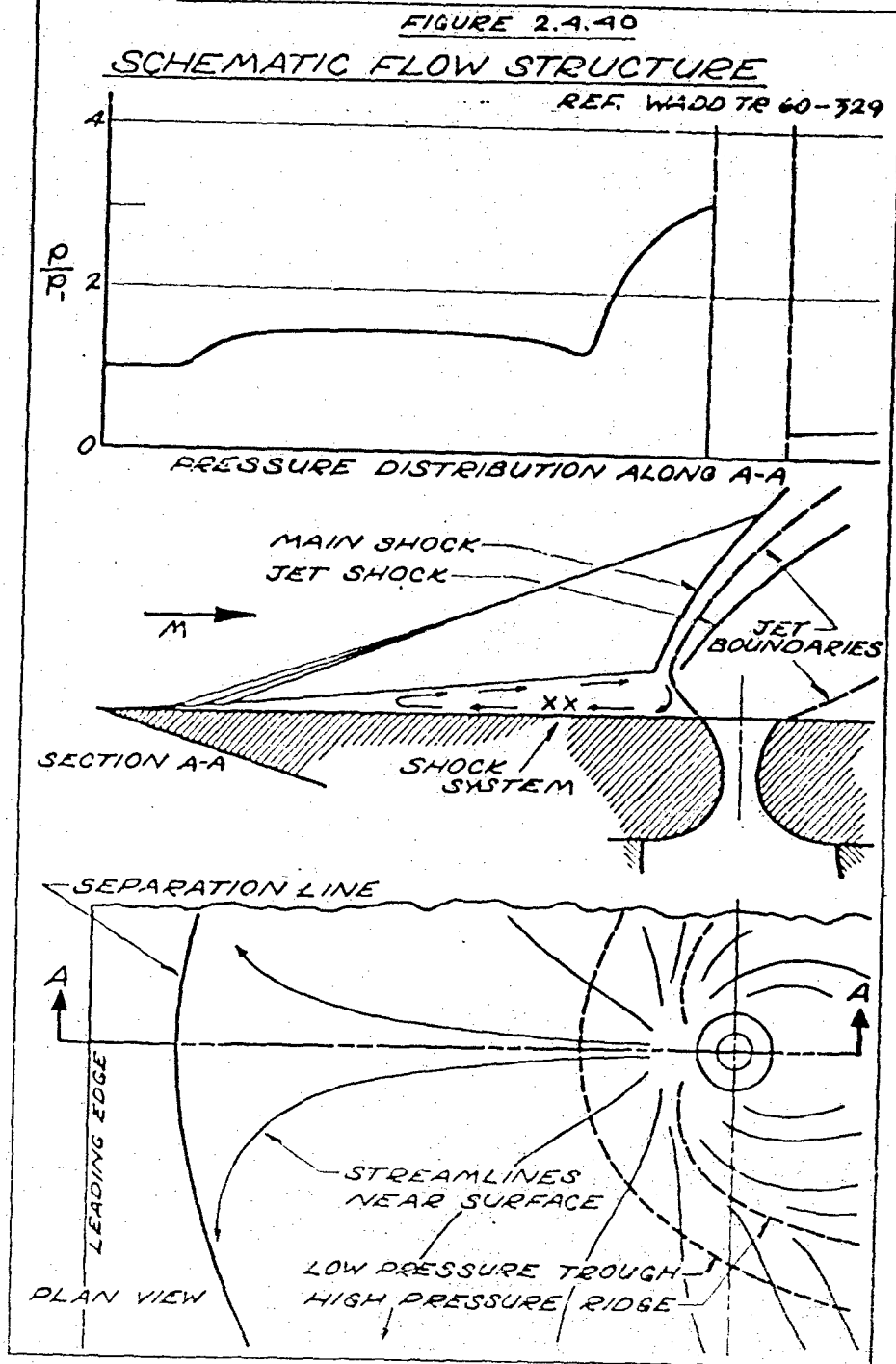
$\alpha = 0^\circ$ $\beta = 0^\circ$ $P_j = 700 \text{ p.s.i.a.}$



5912

SECRET

SECRET



same direction as the reaction jet thrust vector. This magnification factor is of the same order as the jet thrust itself in the low supersonic flow regime. In effect, the reaction jet thrust is doubled and the pitching moment magnification is beneficial in this velocity region.

Figure 2.4.39 presents the variation of the pressure immediately upstream and downstream of the reaction jet as a function of Mach number. This figure emphasizes the trends previously discussed. The difference between the curves shown for the windward and leeward pressures is indicative of the jet magnification factor. Subsonically the difference is negative and results in a reduced effective jet thrust. The maximum positive magnification factor is obtained in the transonic flow regime. The maximum magnification factor then decreases, but remains positive, with increasing Mach number.

Figure 2.4.40, showing the flow structure in the vicinity of a jet, was taken from Reference 5.11. Although the data obtained during the FYE WACKET test were not sufficiently complete for such a detailed sketch, all experimental measurements and observations were in excellent agreement with the figure.

2.4.7 WIND TUNNEL PHOTOGRAPHS - JETS ON: Fluorescent-oil film and schlieren photographs of the FYE WACKET FTV wind tunnel models, with control jets operating (one or both jets), are presented in Figures 2.4.41 and Figures 2.4.42. As discussed in Section 2.4.1 the photographs were obtained from the supersonic Von Karman Gas Dynamics Facility at A.E.D.C., Tullahoma, Tennessee. A complete description of the method of application of the fluorescent-oil film technique may be found in Reference 5.12. Basically, the method incorporates the use of a fluorescent petroleum base oil photographed under ultraviolet light.

The fluorescent-oil film photographs are presented in Figures 2.4.41 with either one or both reaction control jets operating at a measured chamber pressure of approximately 700 psia. All of the pictures were taken with the oil flow on the windward side of the model. A free-stream Mach number of 2.0 is common to the five photographs presented. Photographs at a higher Mach number were also obtained, but were not of the quality of the pictures shown here. The photographs of Figures 2.4.41 illustrate the large effect of the control jet exhaust on the flow field over the model. The shock wave in front of the control jets is evidenced by the dark area in front of and around the jets. Examination of the schlieren photograph of Figure 2.4.42a clearly indicates the relative position of the shock wave to be the same as that indicated in the photographs of Figures 2.4.41.

Schlieren photographs of the model in the forward, side, and

SECRET

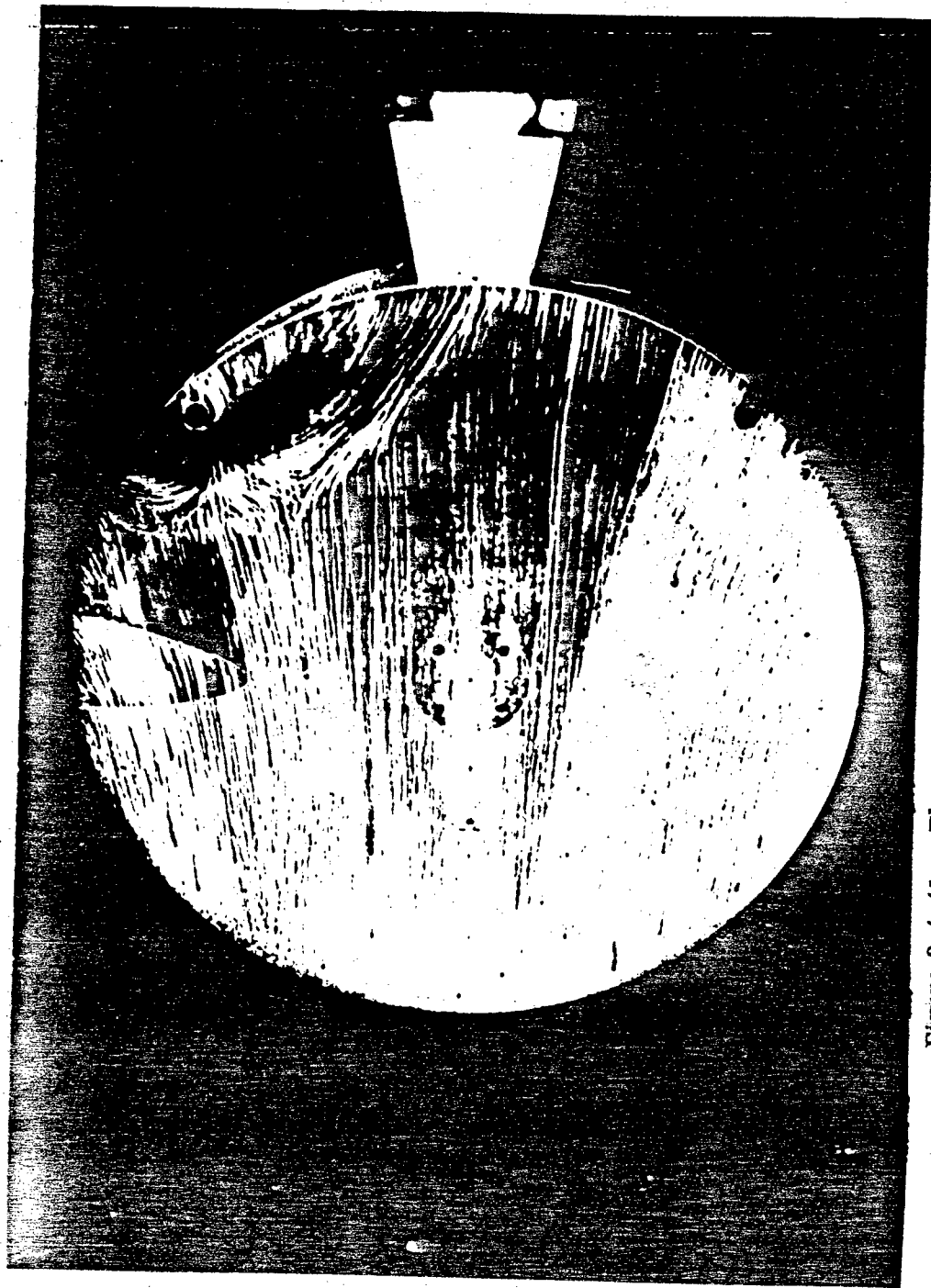


Figure 2.4.41 a Fluorescent-Oil Photograph of Windward Side
Right Jet On, $M = 2.0$, $\alpha = 6^\circ$

2.168

SECRET

SECRET

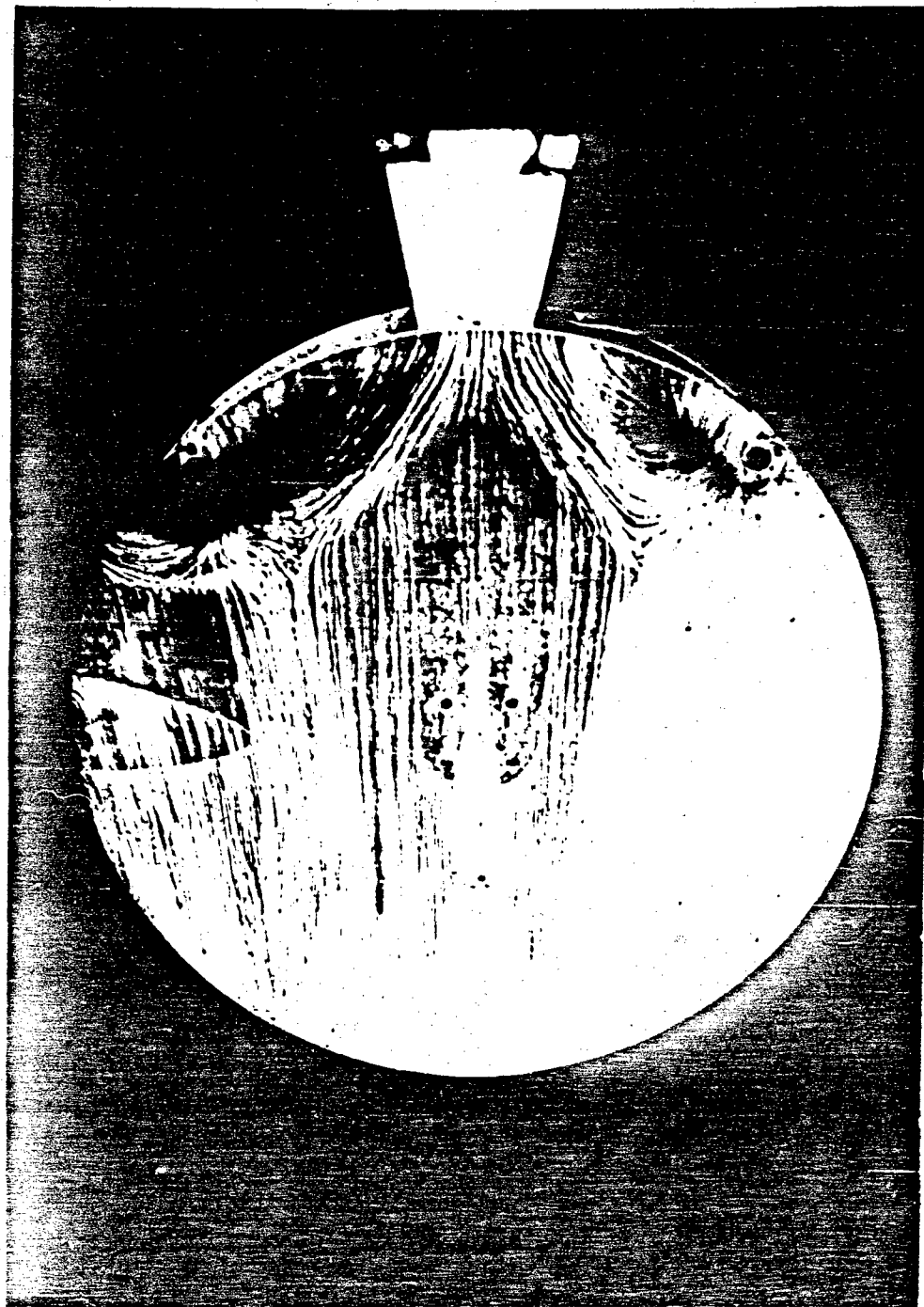


Figure 2.4.41 b Fluorescent-Oil Photograph of Windward Side
Jets On, $NI = 2.0$, $\alpha = 6^\circ$

SECRET

SECRET

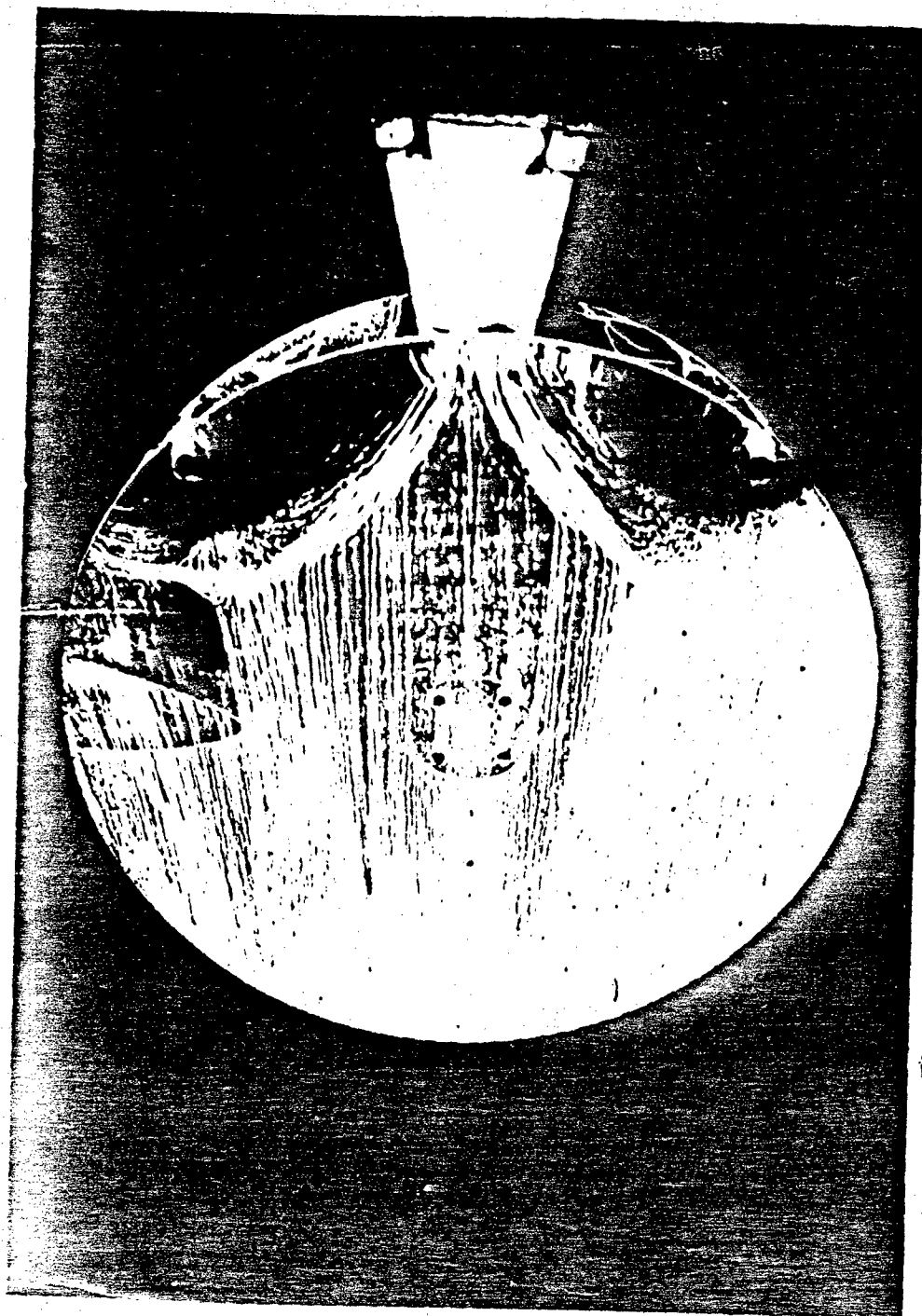


Figure 2.4.41 c Fluorescent-Oil Photograph of Windward Side
Jets On, $M = 2.0$, $\alpha = 12^\circ$

2.170

SECRET

SECRET

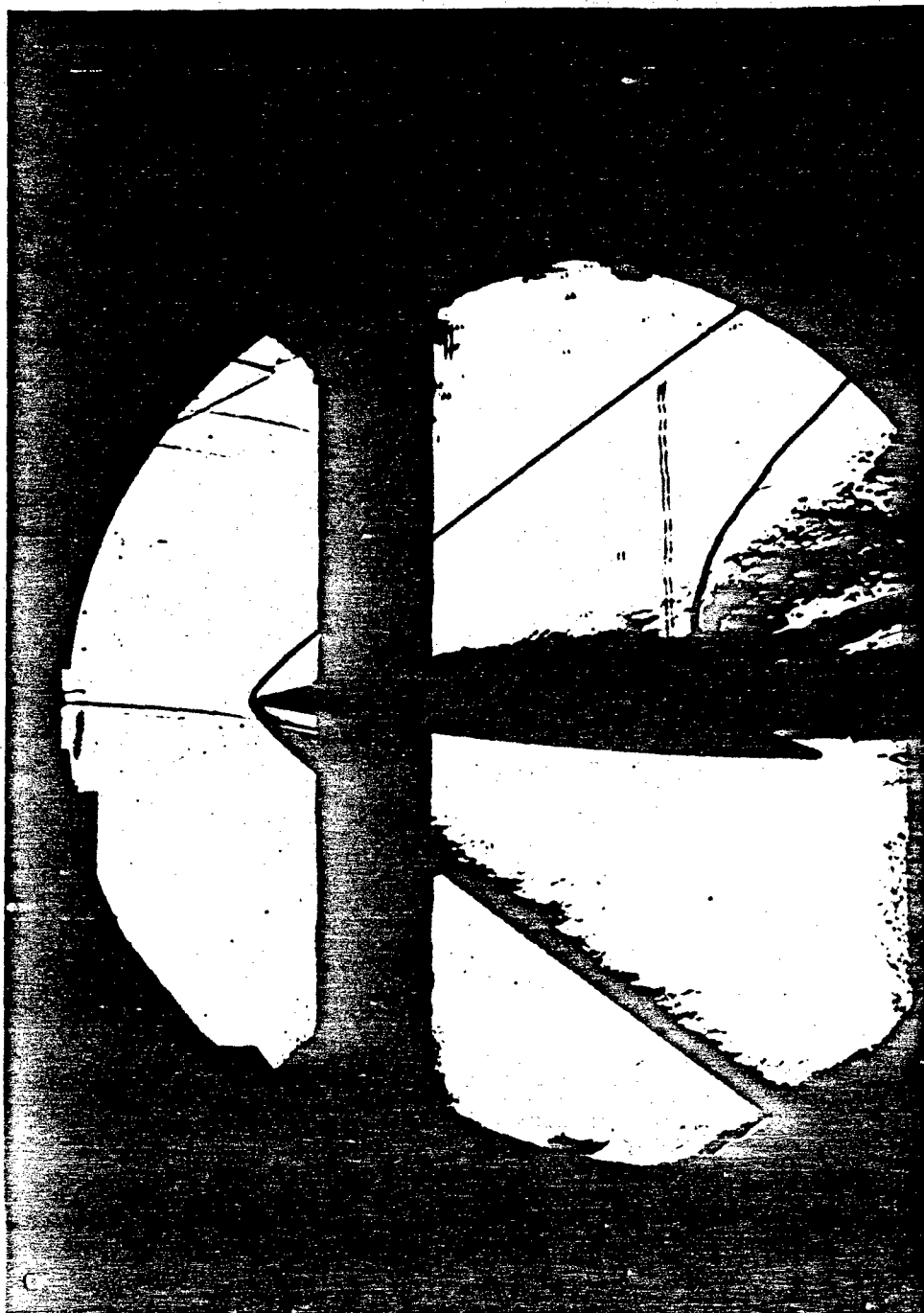


Figure 2.4.42 a Schlieren Photograph of Side View
Forward Launch, Left Jet On, $M = 2.0$

2.171

SECRET

SECRET

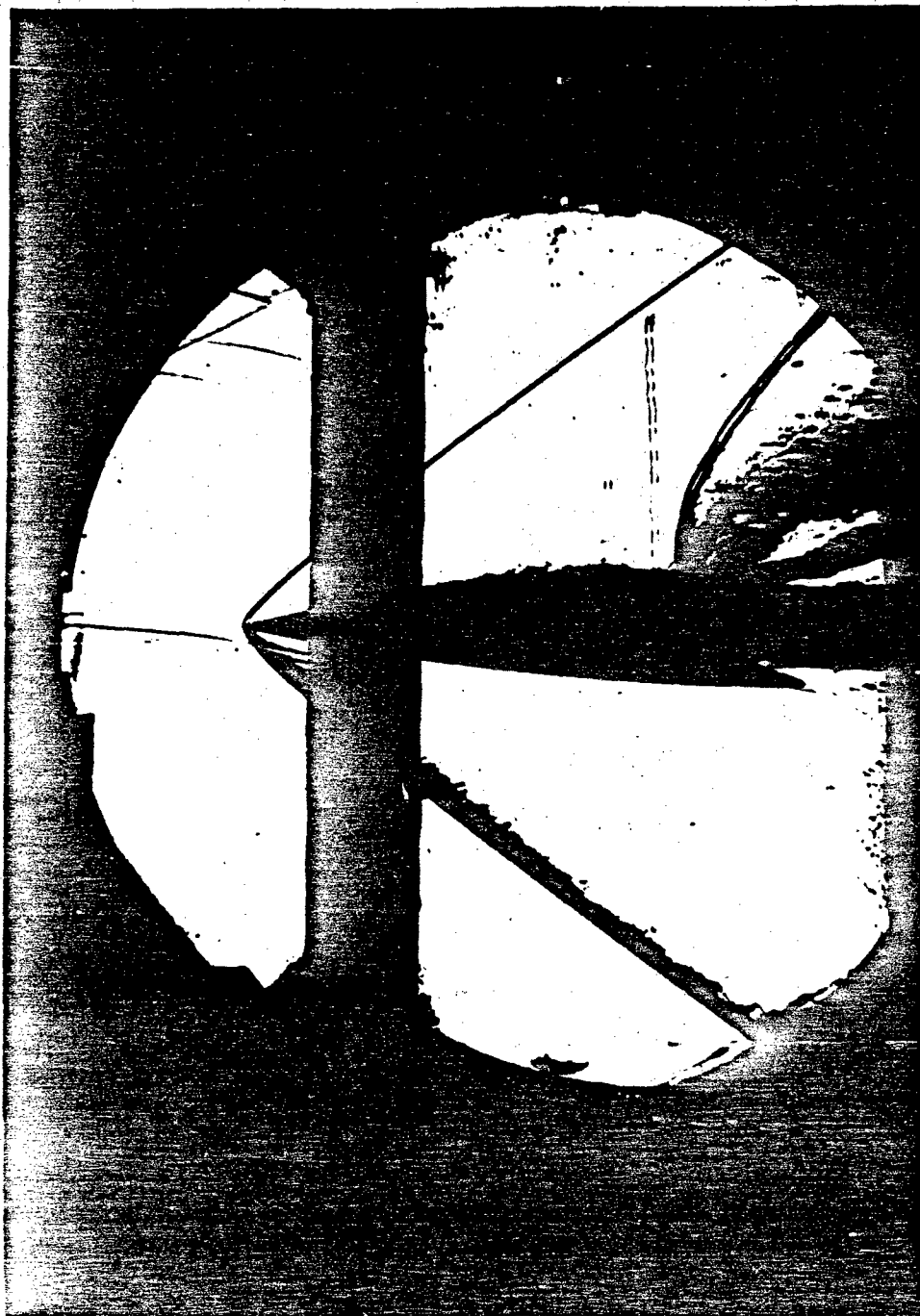


Figure 2.4.42 b Schlieren Photograph of Side View
Forward Launch, JetsOn, $M = 2.0$

2.172

SECRET

SECRET

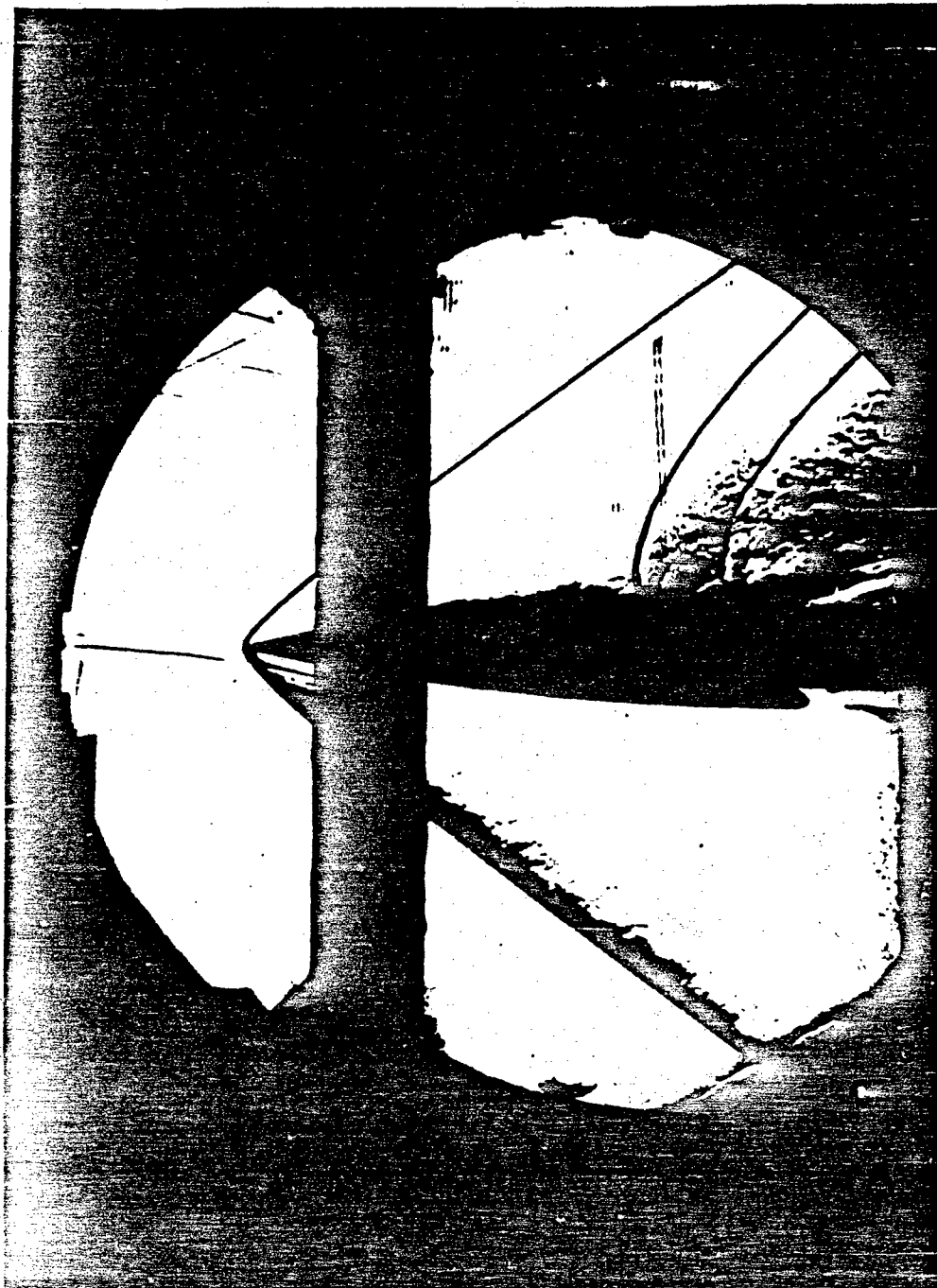


Figure 2.4.42 c Schlieren Photograph of Side View
Forward Launch, Jets On, $M = 2.0$, $\theta = 14^\circ$

2.173

SECRET

SECRET

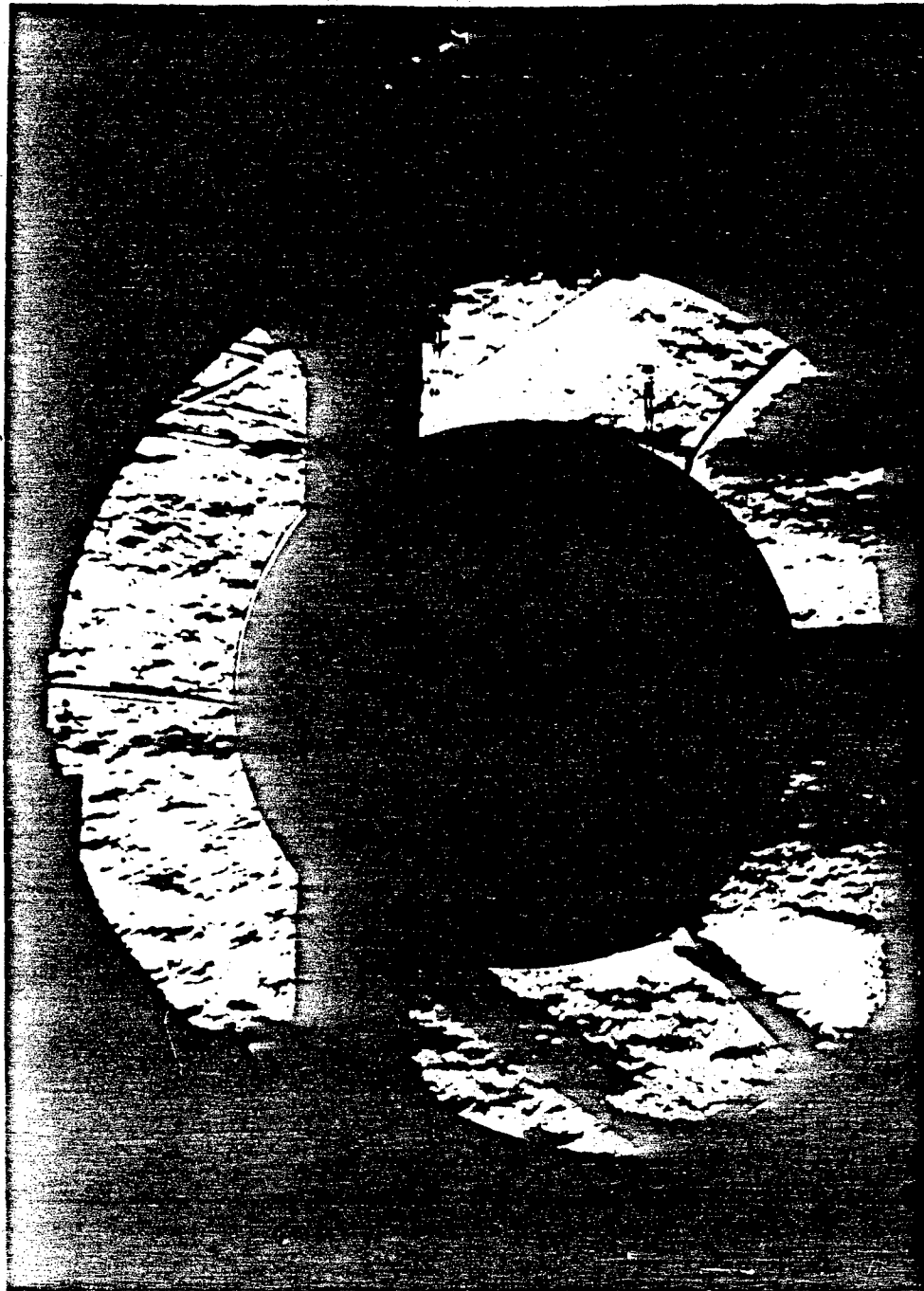


Figure 2.4.42 d Schlieren Photograph of Plan View
Forward Launch, Jets On, $M = 2.0$

2.171

SECRET

SECRET

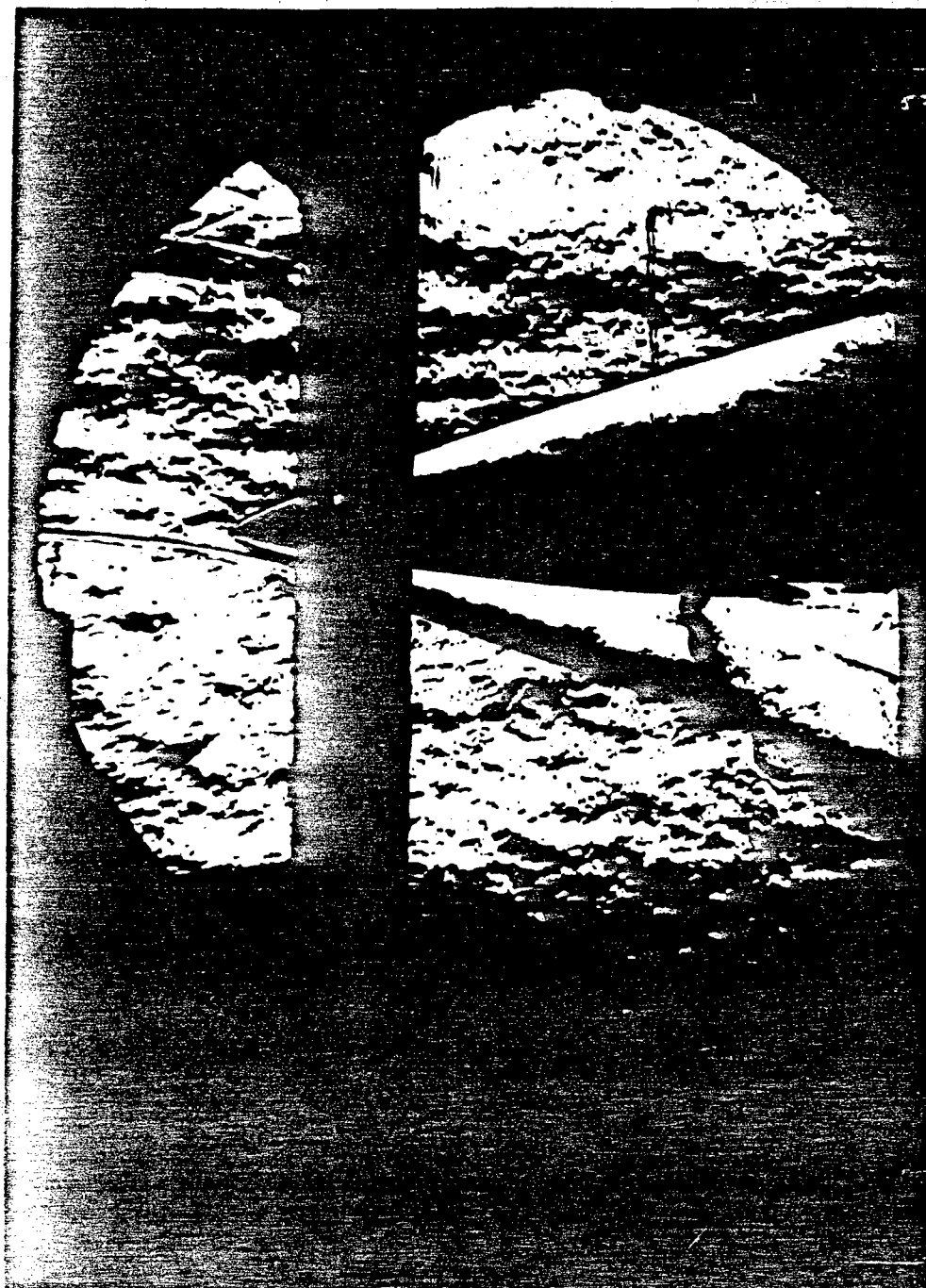


Figure 2.4.42 e Schlieren Photograph of Side View
Forward Launch, Jets On, $M = 5.0$

2.175

SECRET

SECRET

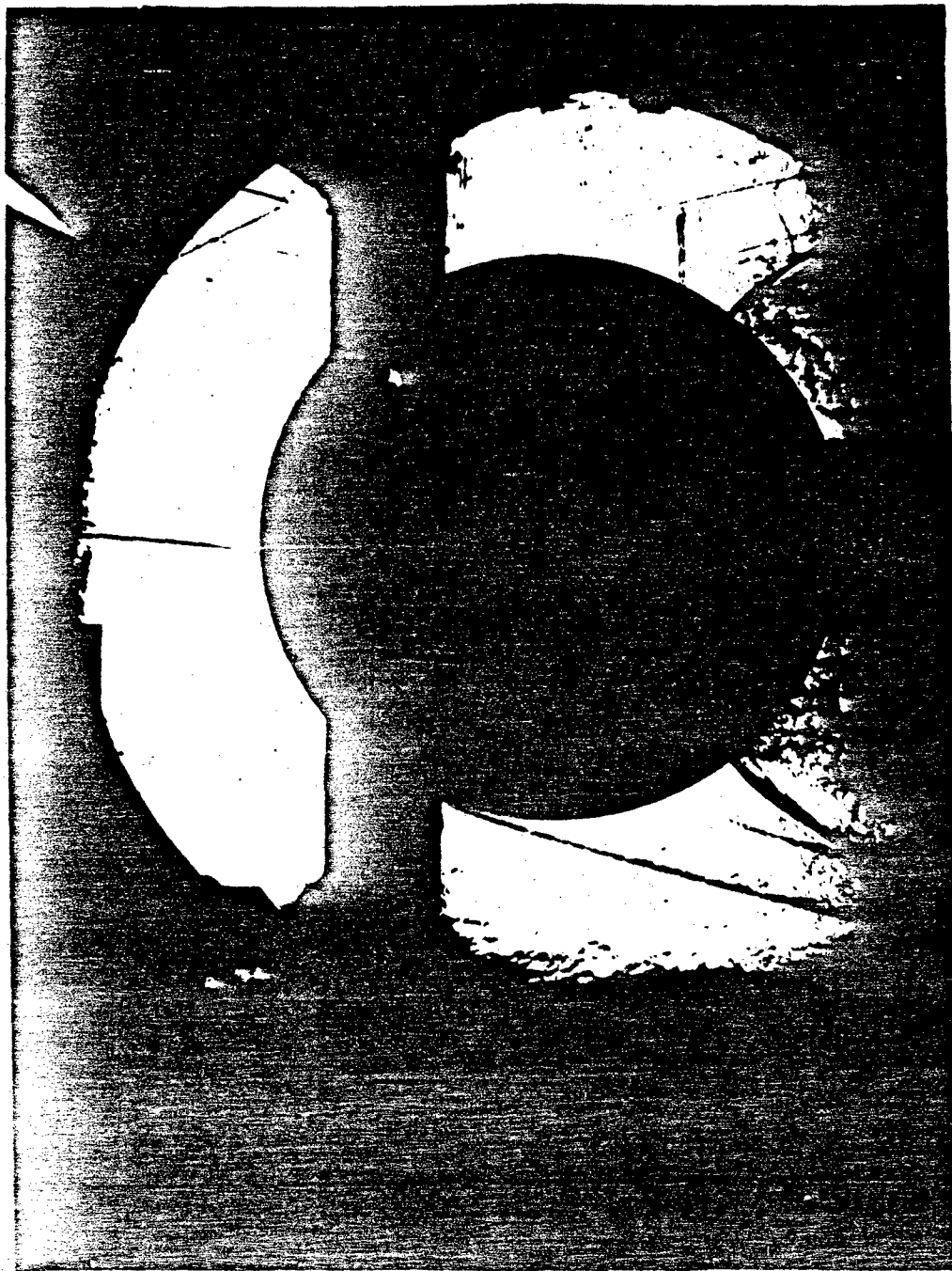


Figure 2.4.42 f Schlieren Photograph of Plan View
Forward Launch, Jets On, $M = 5.0$

2.176

SECRET

SECRET

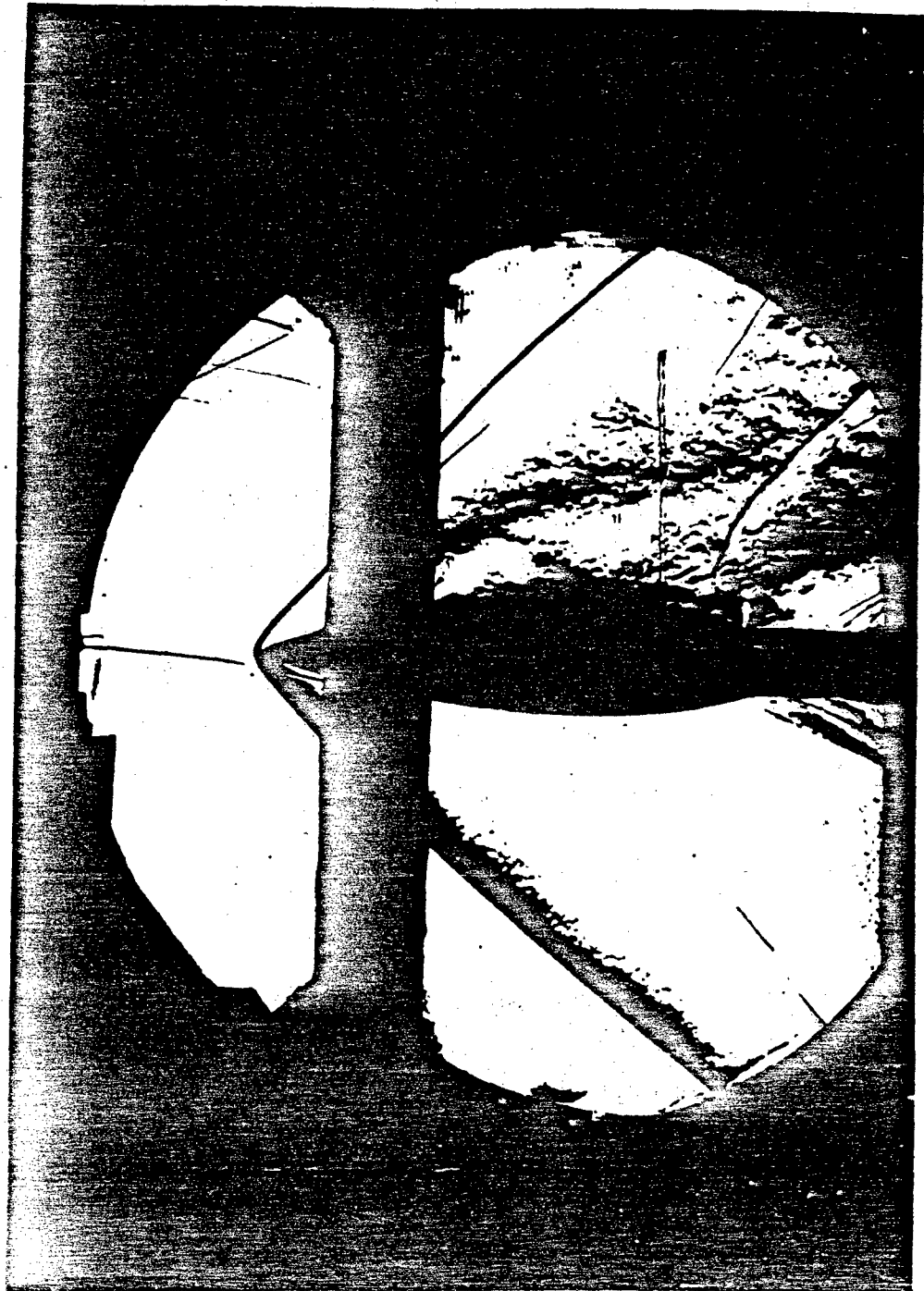


Figure 2.4.42 g Schlieren Photograph of Side View
Cross-Wind Launch, Jets On, $M = 2.0$

2.177

SECRET

SECRET



Figure 2.4.42 h Schlieren Photograph of Plan View
Cross-Wind Launch, Jets On, $M = 2.0$

2.179

SECRET

SECRET

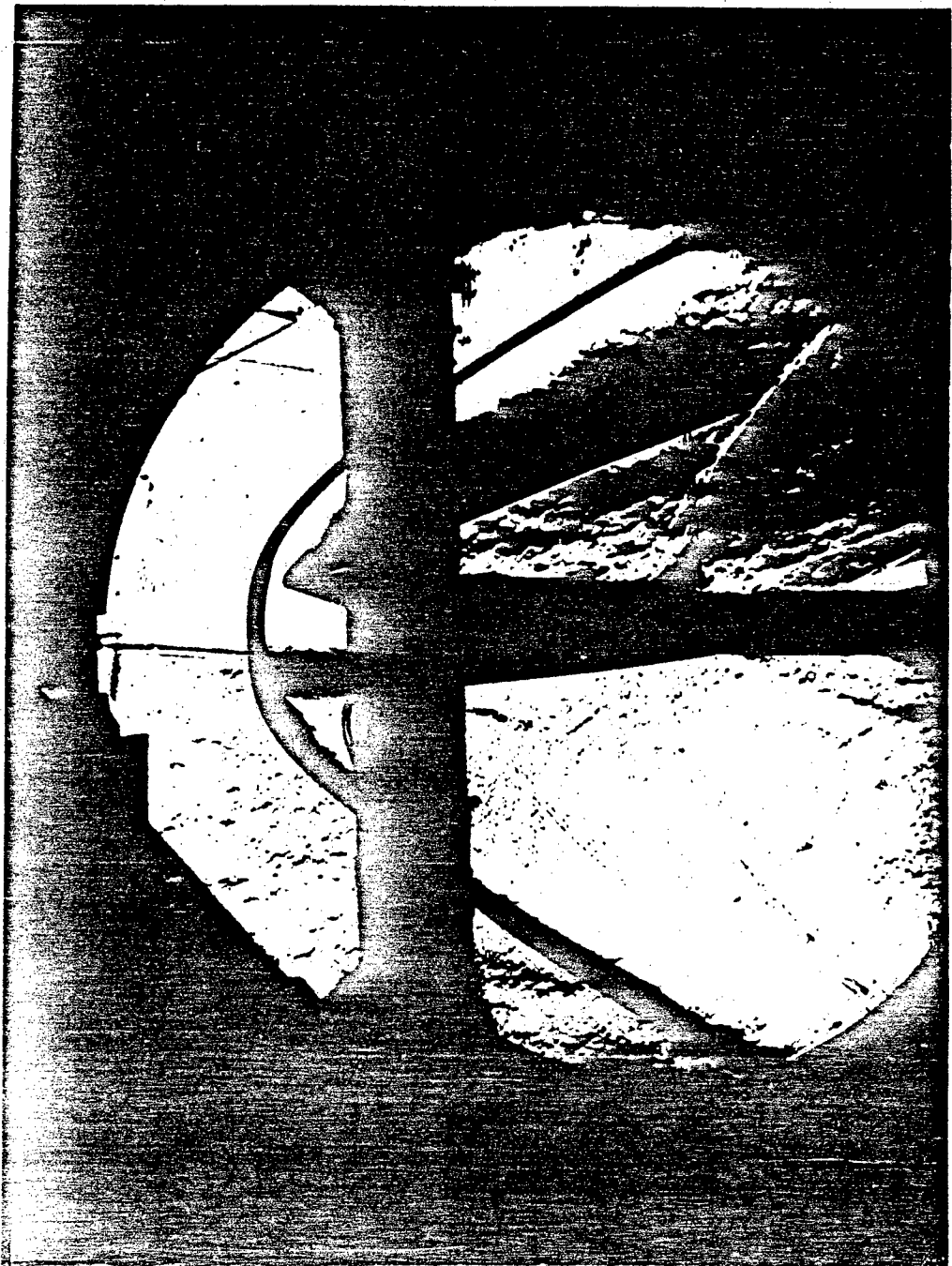


Figure 2.4.42 i Schlieren Photograph of Side View
Aft Launch, Jets On, $M = 3.0$

2.179

SECRET

SECRET

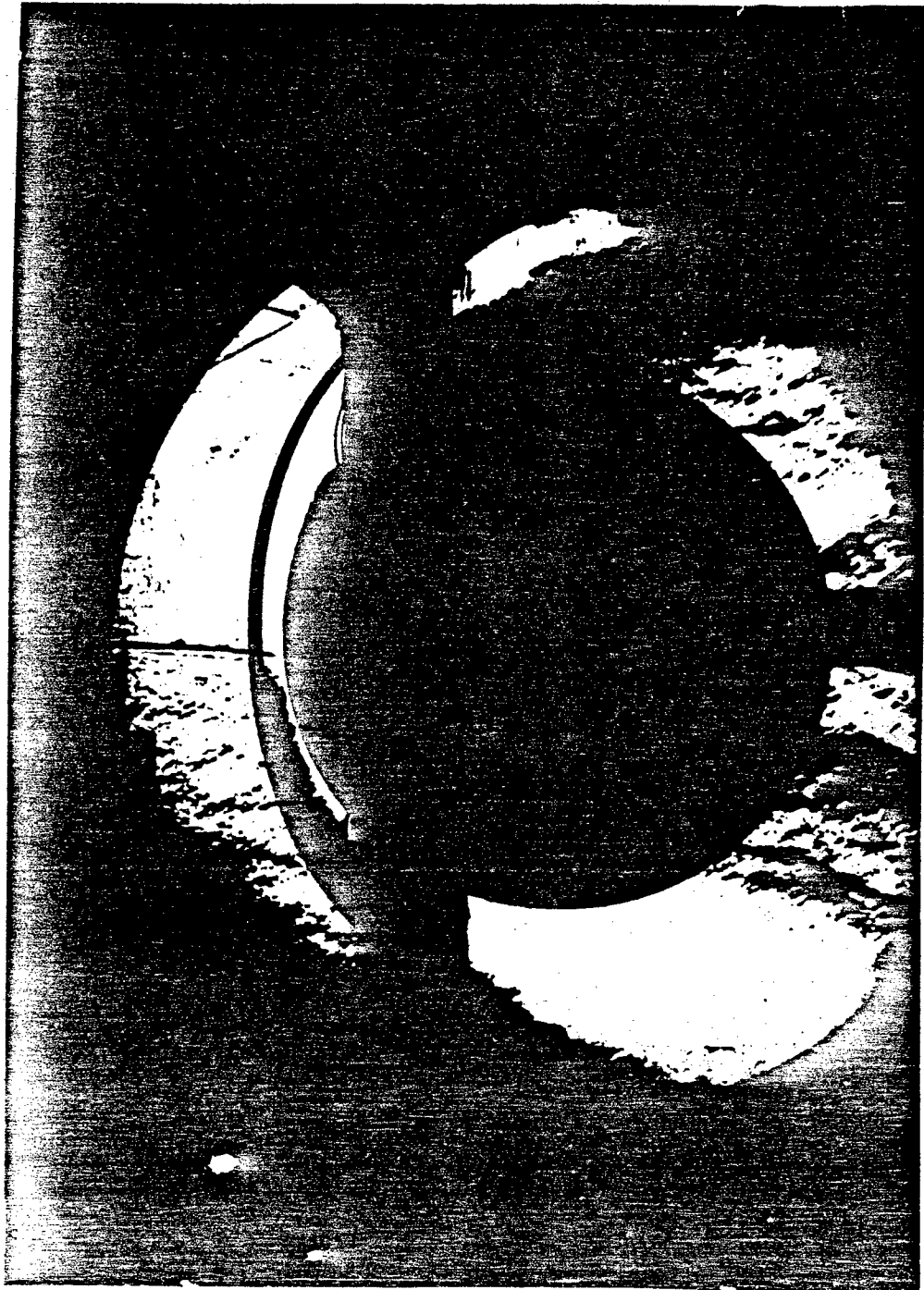


Figure 2.4.42 j Schlieren Photograph of Plan View
Aft Launch, Jets On, $M = 3.0$

2.180

SECRET

rear launch positions are presented in Figures 2.4.42. These photographs are of the profile and planform views of the shock system caused by the model and the exhaust of the reaction jets. Again, as stated in Section 2.4.4, extraneous shock waves are present in the photographs due to shock reflections from the observation window and/or from imperfections in the window. The photographs were taken at angles of attack and sideslip of zero degrees in all cases except Figure 2.4.42c. The sideslip angle of 14 degrees clearly shows the two shock waves emanating in front of the control jets. The planform view is shown in Figure 2.4.42d.

2.5 PERFORMANCE

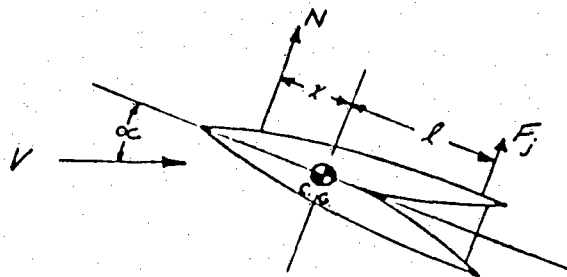
Sea level launchings present an extremely difficult environment for highly maneuverable missiles such as PYE WACKET. A major advantage of the PYE WACKET concept is its ability to maneuver at high altitudes where conventional missiles cannot. As a result of the high maneuverability, extremely high "g" loadings occur for moderate angles of attack in the dense, sea level air. Because of structural and available control limitations, a low missile angle of attack must be maintained. To emphasize the high maneuver capability of PYE WACKET at sea level, attention is drawn to Figure 2.5.1. This graph presents the normal acceleration in terms of "g's" as a function of Mach number. For an assumed launch weight of 425 pounds, the normal acceleration ranges from 0.6 g's per degree angle of attack at a Mach number of 0.6 to 10 g's per degree at a Mach number of 2.0. The assumed burnout weight of 285 pounds has a maneuver capability of 14.9 g's per degree at a Mach number of 2.0. Calculation of these values does not include the additional force produced by the reaction jets and associated magnification factors.

The angle of attack necessary to maintain level flight is shown in Figure 2.5.2 as a function of Mach number. At a launch Mach number of 0.6, a trim angle of attack of 1.3 degrees is required. The required angle drops down to 0.07 degrees for the empty weight condition at a Mach number of 2.0. As a result, the control system must be very sensitive to avoid high "g" loadings in the burnout Mach number range.

The maximum controllable angle of attack as a function of Mach number is shown in Figure 2.5.3 for the forward launch case. This curve is based on sea level conditions with a reaction jet thrust of 500 pounds each. Steady-state conditions were assumed with no jet magnification factors. The effect of jet magnification factors is presented in Volume III of this report. Figure 2.5.3 shows that a minimum controllable angle of attack of 2.1 degrees occurs at Mach 1.2 (equivalent to 8 to 12 g's). The controllable angle of attack increases rapidly as the

SECRET

Mach number is either increased or decreased. The increase at higher or lower Mach numbers is caused by different factors. A sketch of the force diagram is shown below:



Summation of moments gives the following equations:

$$Nx = F_j l \quad 2.51$$

$$C_{N\alpha} \propto q S x = F_j l \quad 2.52$$

$$\alpha = \frac{F_j l}{C_{N\alpha} q S x} \quad 2.53$$

The reaction jet force, F_j , is constant with Mach number as is the jet moment arm, l . Therefore, the control moment, $F_j l$, is also constant with Mach number. The two remaining parameters are: N , the normal force and x , the distance between the aerodynamic center of pressure and the center of gravity. These two variables determine the shape of the curve shown in Figure 2.5.3. In the low Mach number range the distance between the centers of pressure and gravity is large, but the normal force is low due to the low dynamic pressure, q . Therefore, a large angle of attack can be controlled. As the Mach number is increased above $M = 1.2$, the dynamic pressure increases rapidly. However, the aerodynamic center of pressure moves aft toward the center of gravity, resulting in a very small moment arm and hence, a large controllable angle of attack. In fact, at $M = 2.4$, the center of pressure and the center of gravity coincide (c.g. located at the 43% chord). Any angle of attack theoretically can be controlled at this Mach number. This rearward shift of center of pressure can be verified by referring to

2.182

SECRET

SECRET

FIGURE 2.5.1

PYE WACKET FTV

VARIATION OF MANEUVERABILITY WITH MACH NUMBER

SEA LEVEL

$\alpha = 0^\circ$

(REACTION JETS OFF)

PERCENT NORMAL G'S PER DEGREE ANGLE OF ATTACK

16
14
12
10
8
6
4
2
0

0 0.4 0.8 1.2 1.6 2.0 2.4

MACH NUMBER

W = 425 LB
W = 285 LB

2.183

SECRET

SECRET

FIGURE 2.5.2

PYE WACKET FTV

ANGLE OF ATTACK NECESSARY FOR LEVEL FLIGHT

SEA LEVEL

$\alpha = 0^\circ$

(REACTION JETS OFF)

TRIM ANGLE OF ATTACK

3.2
2.8
2.4
2.0
1.6
1.2
0.8
0.4
0

0 0.4 0.8 1.2 1.6 2.0 2.4

MACH NUMBER

$W = 425 \text{ LB}$

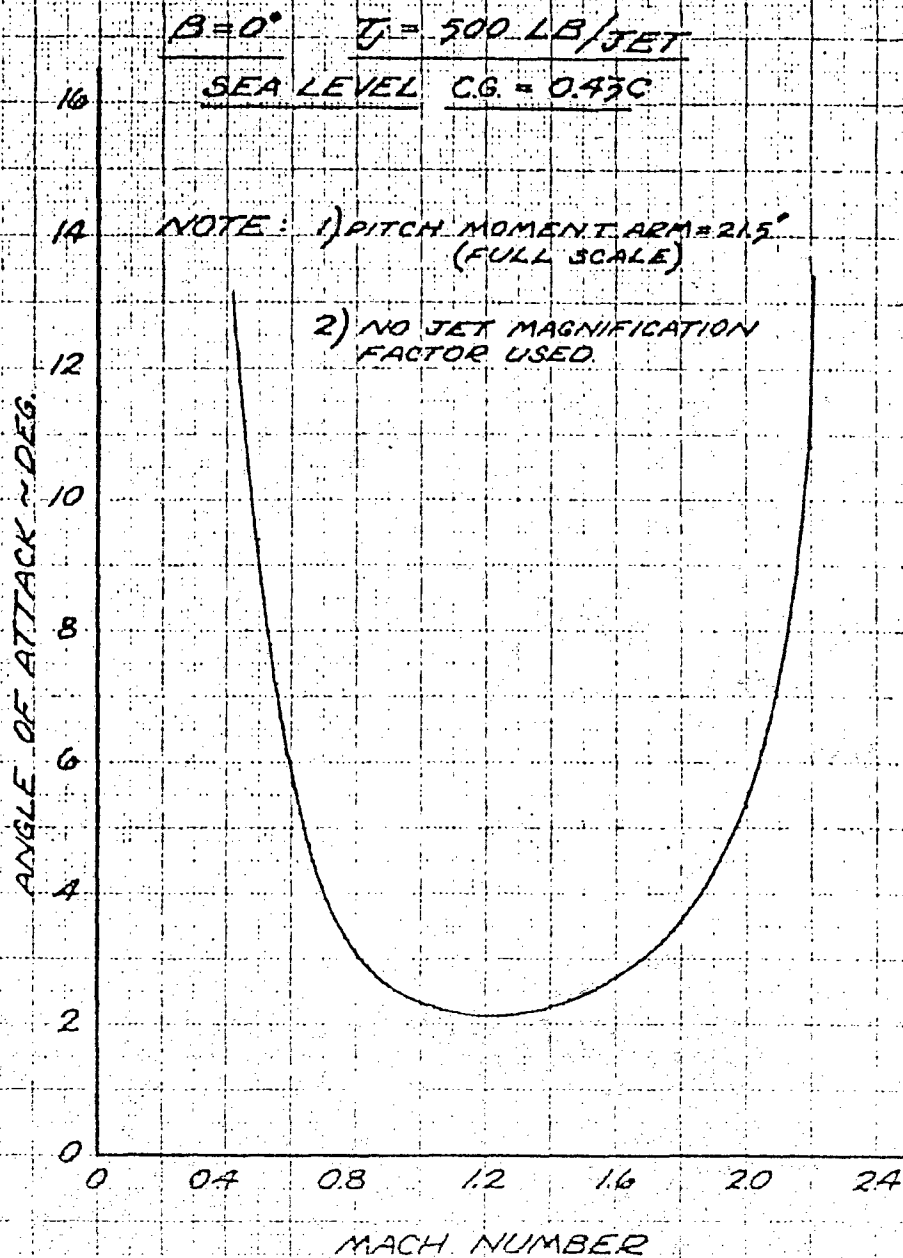
$W = 285 \text{ LB}$

2.184

SECRET

SECRET

FIGURE 2.5.3
PYE WACKET FTV
MAXIMUM CONTROLLABLE ANGLE OF ATTACK



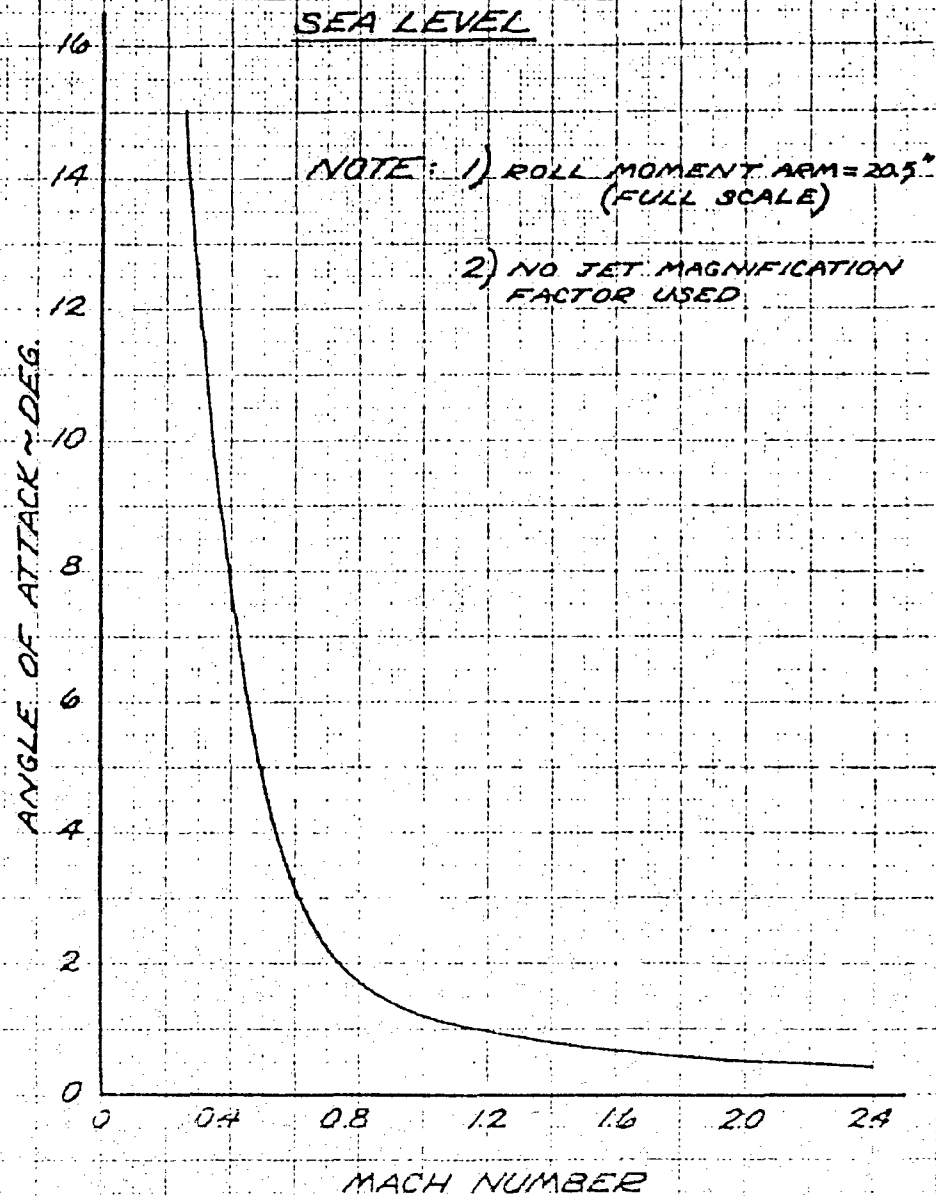
2.185

SECRET

SECRET

FIGURE 2.S.4
PYE WACKET FTV
MAXIMUM CONTROLLABLE ANGLE OF ATTACK

$\beta = 90^\circ$ $T_j = 500 \text{ LB/JET}$
SEA LEVEL



2.186

SECRET

SECRET

FIGURE 2.5.5
PYE WACKET FTV

MACH NUMBER TIME-HISTORY FOR FORWARD LAUNCH

$\alpha = 0^\circ$ $\beta = 0^\circ$

5 BURNOUT (147 SEC)

CONDITIONS

$h = 5.1$
 $W_0 = 425 \text{ lb}$
 $W_b = 285 \text{ lb}$
 $T = 13,500 \text{ lb}$

LAUNCH
MACH NO.

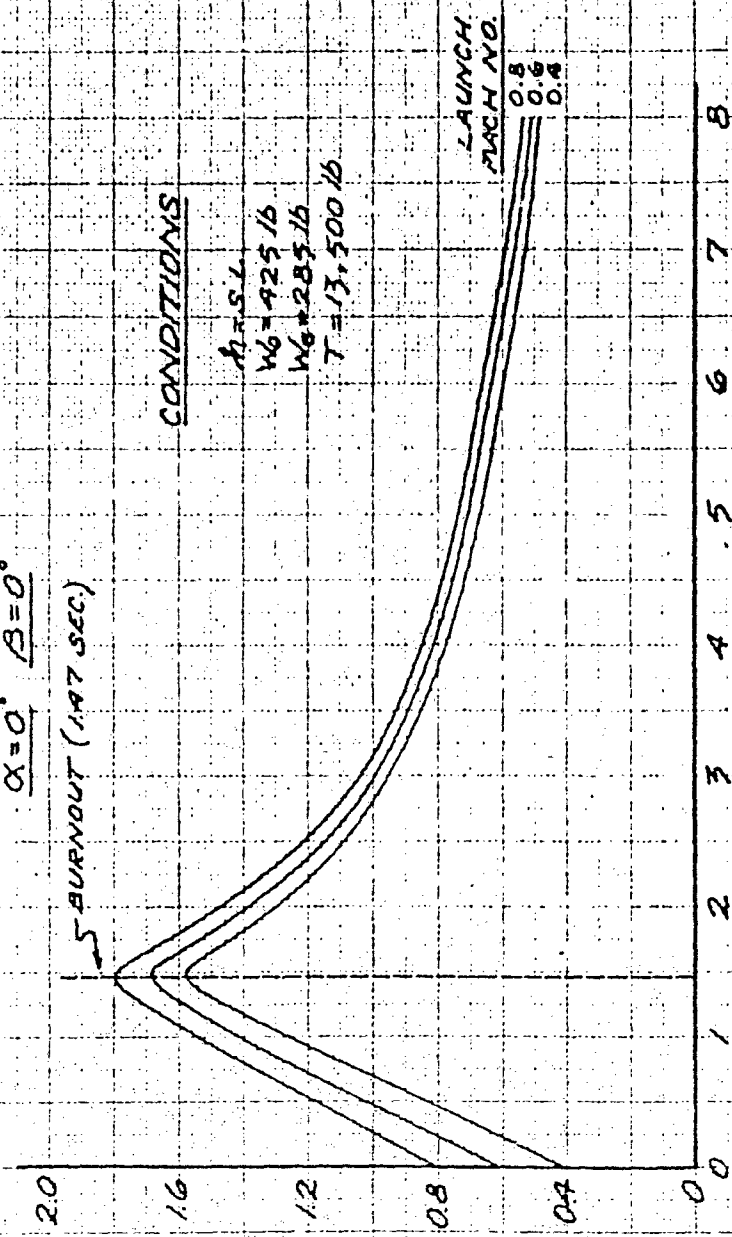
0.8
0.6
0.4

MACH NUMBER

TIME FROM LAUNCH ~ SEC.

SECRET

2.187



SECRET

Figure 2.4.12, Section 2.4.3.6.

Figure 2.5.4 is a similar curve for the cross-wind launch. A comparison of Figures 2.5.3 and 2.5.4 shows that the cross-wind launch will be more difficult than the forward launch. The maximum controllable angle of attack does not increase above $M = 1.2$ as did the forward launch because the center of pressure does not approach the center of gravity as closely. It should be noted that the center of gravity cannot be moved from the longitudinal centerline to alleviate the problem. However, it should be noted that this condition applies only to a sea level launch. The maximum controllable angle of attack is a direct function of air density so that an altitude launch will increase the maximum angle. Prototype launchings from an airplane will not encounter such rigid restrictions.

Mach number-time histories of the PYE WACKET FTV are presented in Figure 2.5.5 for the forward launch, $\beta = 0$, sea level flight condition. Three launch Mach number-time histories are shown at $M = 0.4$, 0.6 and 0.8 .

The equations used in the calculation of the Mach number-time histories throughout the power-on and coast phases are presented in Appendix 6.2. It is noted that the equations are closed-form equations utilizing linear approximations of the PYE WACKET FTV drag as a function of velocity. Comparisons with computer calculations using the standard iterative technique indicate very good agreement between the two methods. The maximum Mach numbers at the burnout time of 1.47 seconds are 1.58, 1.69 and 1.80 for the launch Mach numbers of 0.4, 0.6 and 0.8, respectively.

2.6 LAUNCH STUDIES

In order to substantiate the omnidirectional launch characteristics of the flight test vehicle, a controlled method of launch must be provided. The use of a rocket power sled is the most desirable from the standpoint of precise control, maximum data acquisition, and low cost. The scope of the Phase II task did not permit a detailed study of the launcher configuration; however, studies sufficient to outline a feasible launcher system compatible with the PYE WACKET FTV were conducted. Results of these studies, particularly aerodynamic aspects, are presented in the following sections.

2.6.1 SLED CONFIGURATION Figure 2.6.1 presents a side and end view of the Edwards Air Force Base High Speed Sled. The sled is approximately 22.5 feet long and 4 feet high. The distance between rails is 60.65 inches or approximately 5 feet. The vehicle has a pyramidal nose and has all protruding surfaces faired with oblique angles. It is an extremely low drag configuration. This sled, weighing 5300 lb at launch

SECRET

SECRET

and 3900 lb at burnout, utilizes a liquid rocket motor producing 50,000 lb of thrust for 4.5 seconds. An alternate configuration has four solid rocket motors producing a thrust of 44,000 lb for 2 seconds. This sled operates on a track 20,000 feet long including a 6000 foot braking area.

2.6.2 SUPPORT STRUCTURE The sled presented in the previous section provides the basic structure for a suitable launch system for the flight test vehicle. A suitable support structure must be designed to adapt the launch mechanism to the present sled.

A proposed sled structure for the forward launch case is presented in Figure 2.6.1. This arrangement mounts directly on top of the sled. This locates the flight test vehicle approximately 14 feet above the ground level and approximately 12 feet above the track. The structure consists primarily of two 4-1/2 inch thick walls which slope inward toward the sled longitudinal centerline. Approximately 8-1/2 feet above the top of the sled, the walls intersect a horizontal member, become parallel and end in a torque box structure. The walls consist of circular steel structural members with wedges for the leading and trailing edges. This arrangement is covered by thin aluminum sheet. On top of the torque box structure, two steel cylinders are attached which project horizontally and support the model forward of the torque box. A similar arrangement is proposed for the side launch structure and is illustrated in Figure 2.6.2. The only difference here is in the length and direction of the support stings. A preliminary estimate of the weight of the support structure indicated that the entire assembly, including the flight test vehicle, will weight approximately 1850 lbs.

2.6.3 ESTIMATED COMPOSITE SLED CHARACTERISTICS Estimates of the weight, thrust, and drag of the sled and support structure combination are contained in Figure 2.6.3. The drag coefficient data were estimated for incompressible flow using the available dimensions for the sled and support structure. Their variation with Mach number was estimated by applying the Prandtl-Glauert Rule. The reference area for the drag coefficients is the planform area of the flight-test vehicle. The weight and thrust variation were obtained from sled information and from the weight estimate for the support structure.

2.6.4 ESTIMATED SLED PERFORMANCE The acceleration, velocity and displacement-time histories were calculated from the data from Section 2.6.3. The results of the computations, performed for a 2000 foot altitude, are presented in Figure 2.6.4. In this diagram, acceleration, velocity, Mach number, and range of the sled are presented as a function of time from launch to rocket motor burnout. Also presented are the initial conditions for the launch. For one assumed launch Mach number,

SECRET

0.45, the pertinent sled conditions are; time = 2.25 seconds, range = 600 ft, and acceleration = 220 ft/sec^2 . No distinction was made in these computations between the forward and side launch cases. The accuracy of these estimates is taken to be $\pm 20\%$. The result due to a change in weight or drag of the vehicle, when the launch direction is changed, will be within the accuracy of the computation. The one important distinction between the two cases is the direction of the acceleration at the instant of launch relative to the vehicle axes. In the forward launch it is in a longitudinal direction and in the side launch, the acceleration is lateral.

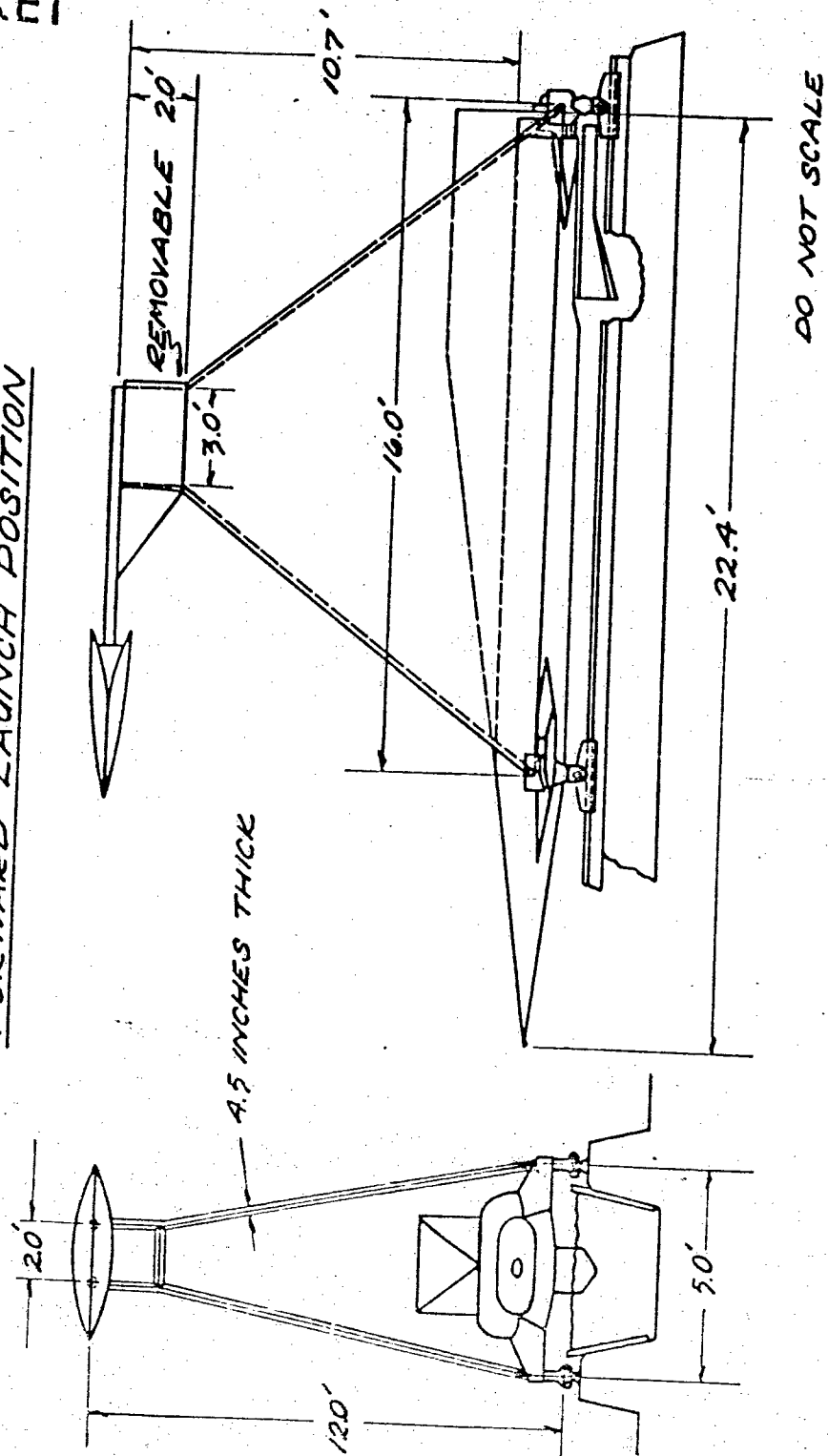
2.6.5 INTERFERENCE EFFECTS One major consideration for launching from a sled is the interference effects arising from the support structure and the proximity of the ground. For the latter condition, the ground presents a boundary which prevents the normal downward flow associated with the lifting capability of a vehicle in flight. Two actions take place as a result of this restriction. First, the lift curve slope of the wing or body is increased. This has been interpreted as an aspect ratio increase. In addition, the downwash behind the vehicle decreases. For incompressible flow, this effect has been estimated in Reference 5.15 by assuming an "image" wing and computing its interference on the wing in the proximity of the ground. The results of this determination are contained in Figure 2.6.5. The wing lift curve slope magnification due to the ground is presented as a function of height above the ground. As the lift curve slope ratio approaches one, the effect of the ground proximity goes to zero. For the configuration of Figure 2.6.1 the abscissa value is the order of five, indicating that the ground effect is less than one percent. This particular estimate is for incompressible flow. Data from Reference 5.16 were used to estimate the same information for compressible flow. Again, the effect is the order of one percent. Thus, the ground effect on the flight test vehicle is negligible.

Another interference effect of comparable importance is the flow angularities induced by the sled and support structure. Using the flow field data from Reference 5.17, and estimating the mean geometric chord for the sled, the longitudinal flow field in Figure 2.6.6 was prepared. Several assumptions were necessary in order to make this diagram. The first assumption was that the flow field over the sled is similar to that over a smooth wing section although the flow over a wing profile would be more conservative because the flow is essentially two-dimensional. The flow over the sled, because of its lower aspect ratio, would tend to be three-dimensional in nature. As a result, there would be a tendency to relieve the flow angularity over the edges. The conditions shown in Figure 2.6.6 would apply only at the center of the sled, and the angularities would be quickly reduced in the lateral regions of the sled. From this aspect, the condition assumed (two-dimensional) would be more critical. However, ground effect should have a major influence on the

SECRET

SECRET

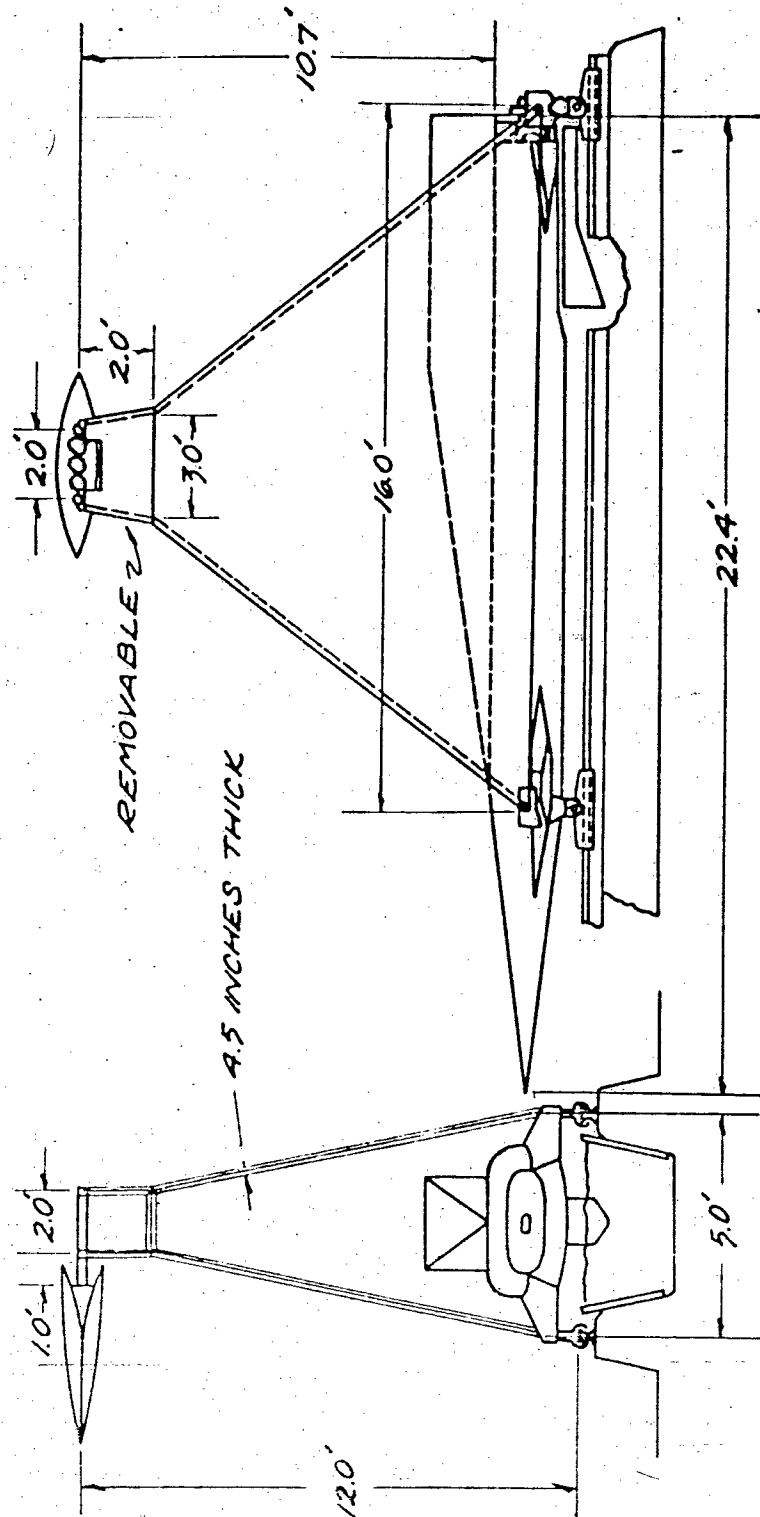
FIGURE 2.6.1
PYE WACKET FTV AND E.A.F.B. HIGH SPEED SLED
FORWARD LAUNCH POSITION



2.191

SECRET

FIGURE 2.6.2
PYE WACKET FTV AND E.A.F.B. HIGH SPEED SLED
SIDE LAUNCH POSITION

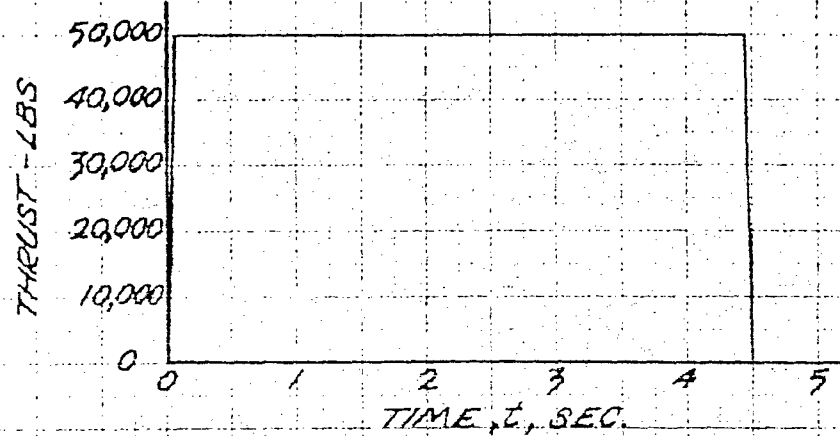
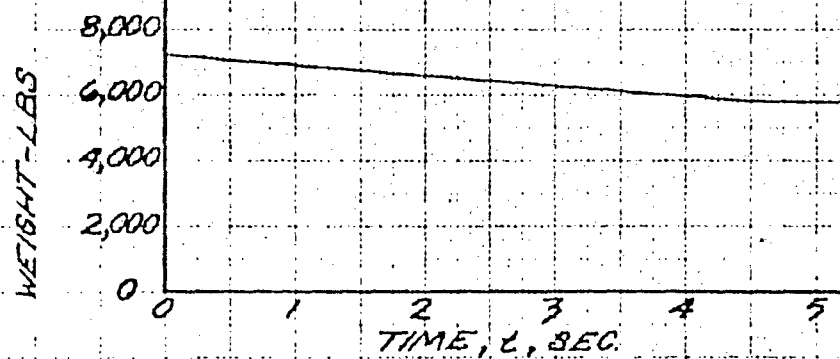
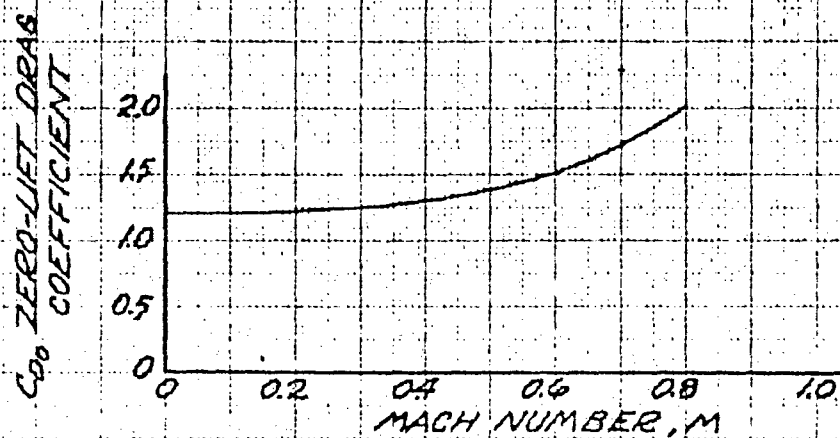


DO NOT SCALE

SECRET

FIGURE 2.6.3

ESTIMATED SLED CHARACTERISTICS



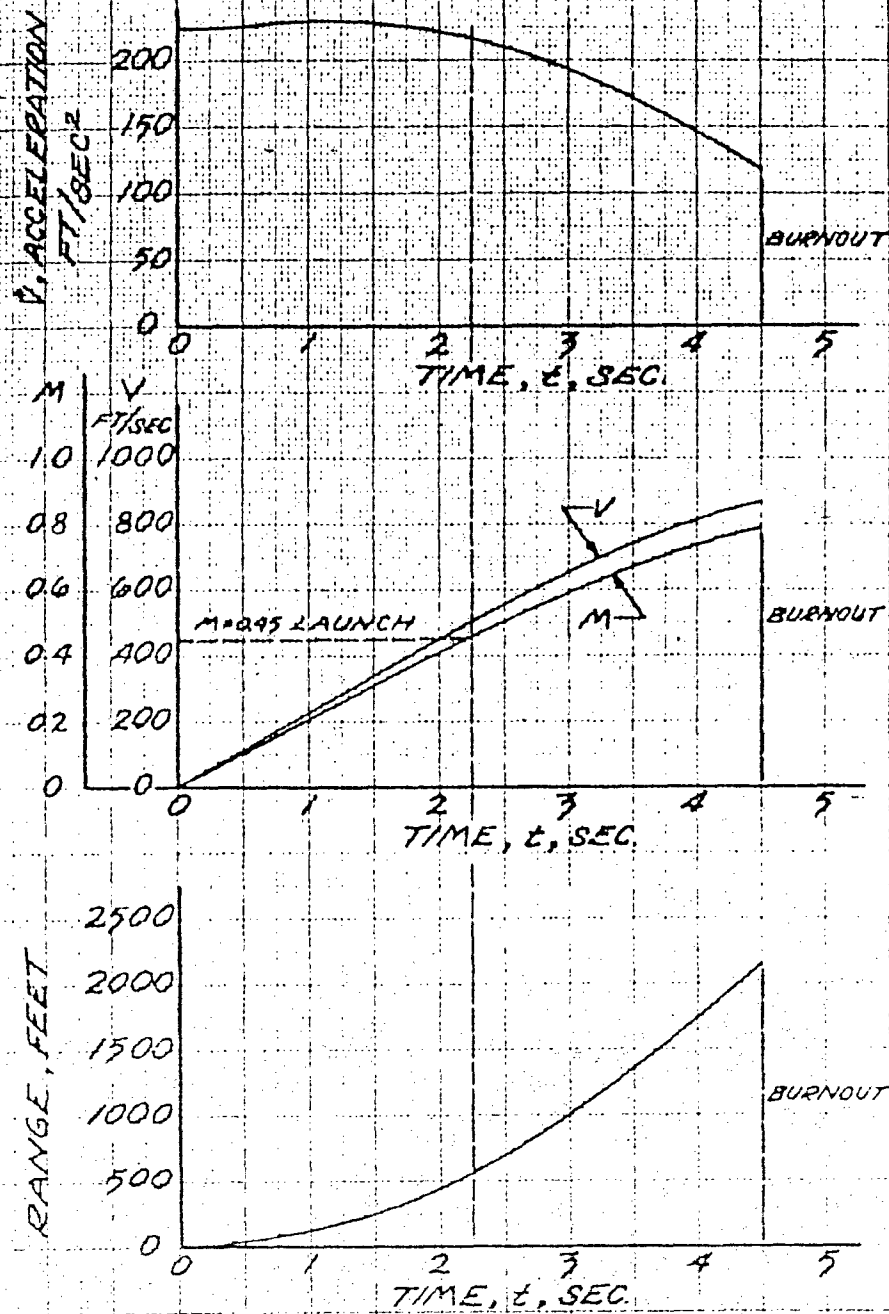
2.193

SECRET

SECRET

FIGURE 2.6.4

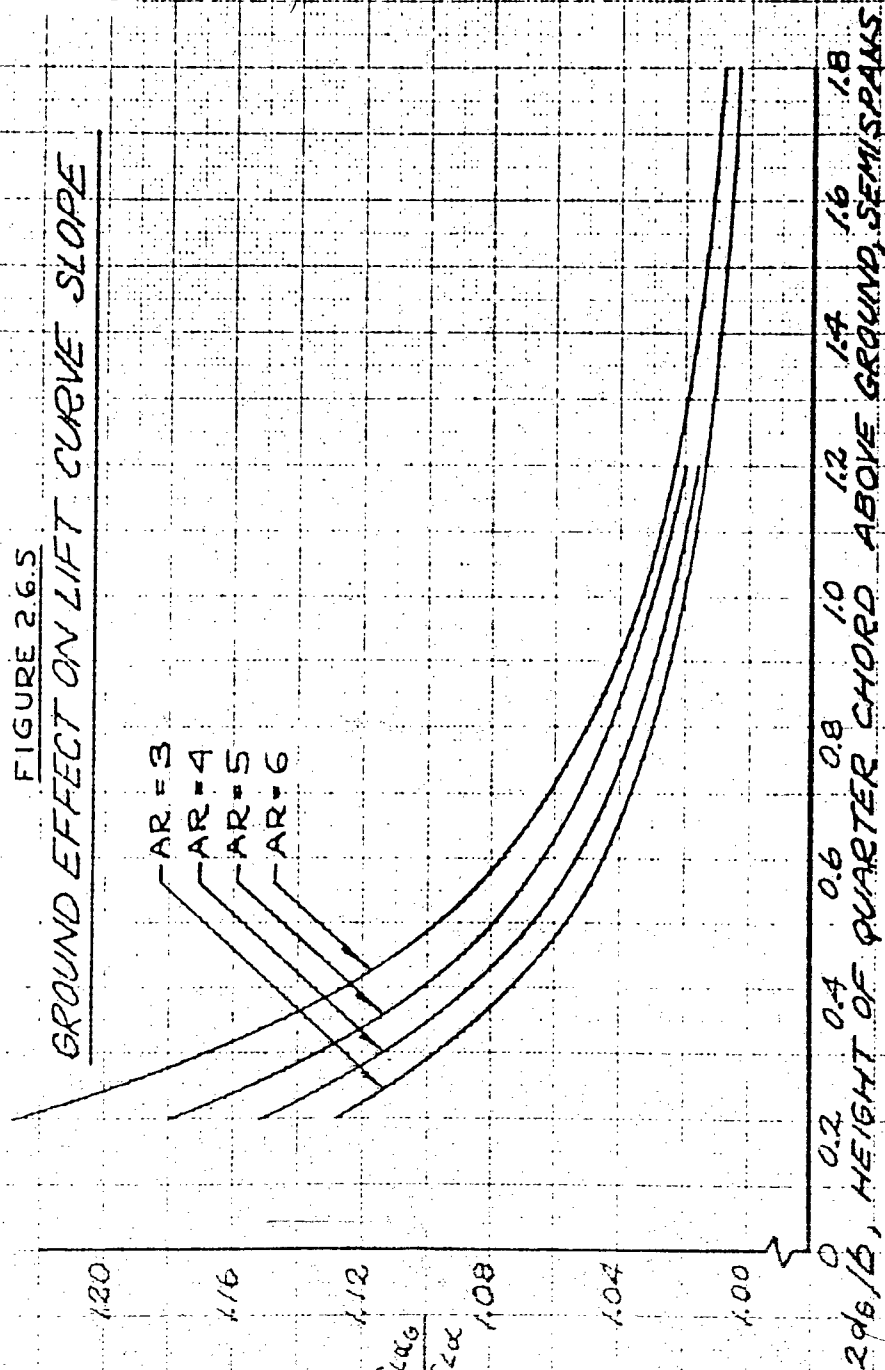
ESTIMATED SLED PERFORMANCE



2.174

SECRET

SECRET



2.195

SECRET

SECRET

FIGURE 2.6.6

LONGITUDINAL ANGULAR FLOW FIELD ABOUT AN AIRFOIL SECTION

$\alpha = -0.2^\circ$; $\beta = 0^\circ$
SUBSONIC FLOW

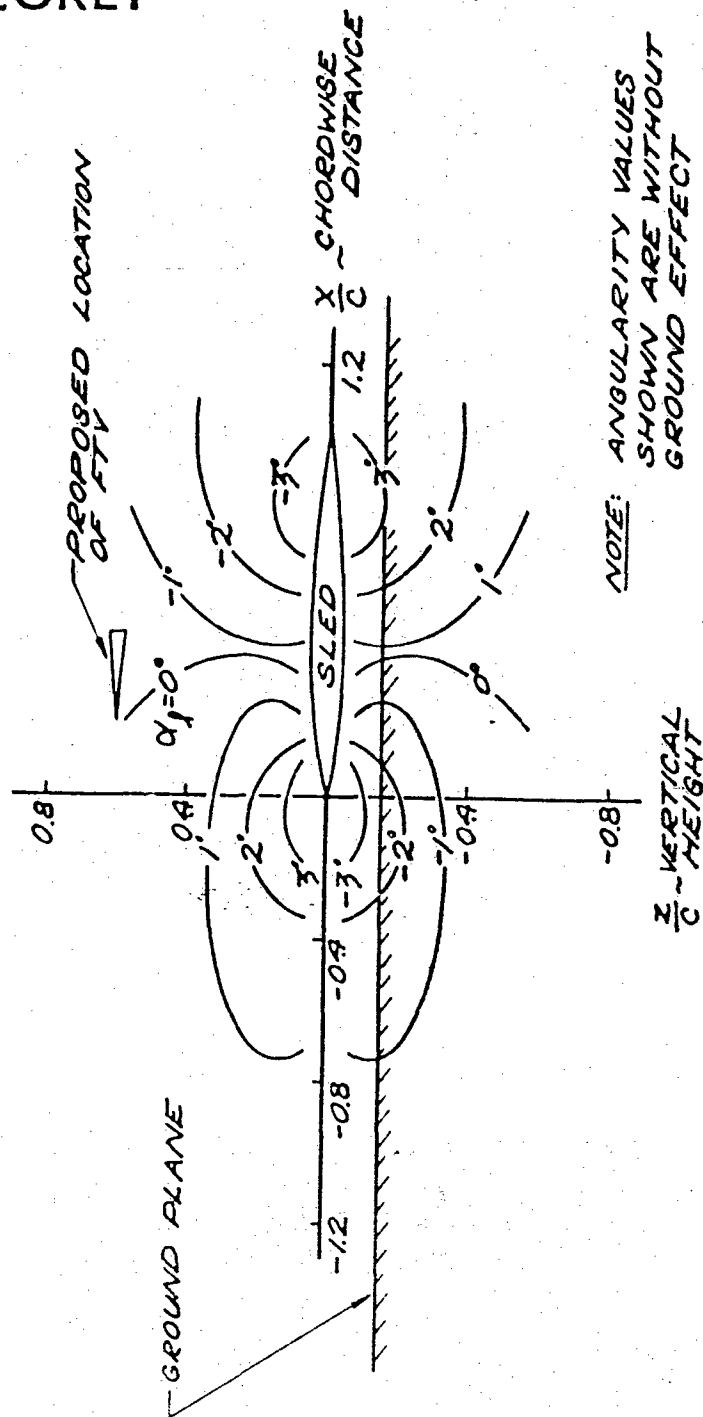
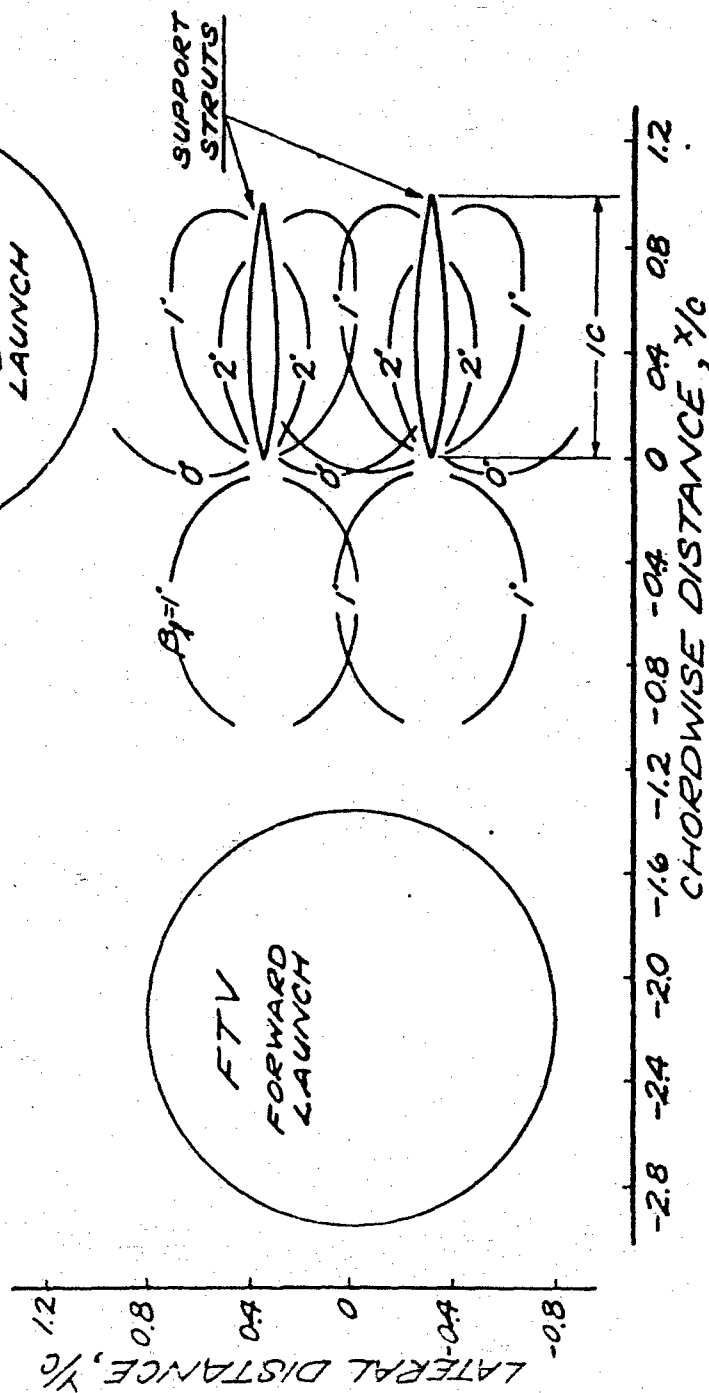


FIGURE 2.6.7

LATERAL ANGULAR FLOW FIELD IN THE VICINITY OF FTV

$\alpha = -0.2^\circ, \beta = 0^\circ$

SUBSONIC FLOW



SECRET

flow field about the sled. The data taken from Reference 5.17 is for a flow field not influenced by the ground boundary. Figure 2.6.6 shows the proximity of the ground plane to the sled. Using this data and extrapolating the results of Figure 2.6.5 indicates that the lift curve slope would be magnified by less than a factor of two. Here the assumption is made that the flow field is intimately associated with the lift curve slope. This factor may then be applied to the local angularities in Figure 2.6.6. On this basis, the position of the flight test vehicle may be expected to be in a range from 0 to -2 degrees angle of attack in the longitudinal plane.

Using the same reference, the lateral angularity fields were estimated for the support struts in the vicinity of the model. The same field is shown for the forward-and side-launch case. As indicated in Figure 2.6.7, no lateral angular flow fields are expected in either the forward or side launch case.

2.6.6 VIBRATION EFFECTS An additional source of disturbance during launch is the vibration which will be transmitted from the rails and rocket motor through the sled, the tower structure, and sting support to the flight test vehicle. This vibration will cause the sting support to deflect and introduce a disturbance at the time of launch. This means the vehicle will be subjected to an increment in angle of attack and in pitch angular velocity as an initial condition at launch. The magnitude of this disturbance is dependent on the fixity conditons of the sled and sting structure and on the elastic deformations of the structural components. No attempt has been made to determine the magnitude of these disturbances in this brief study of the launcher problem, however, careful attention will be given to this problem before the sled/launcher design is finalized.

2.7 PROBLEM AREAS

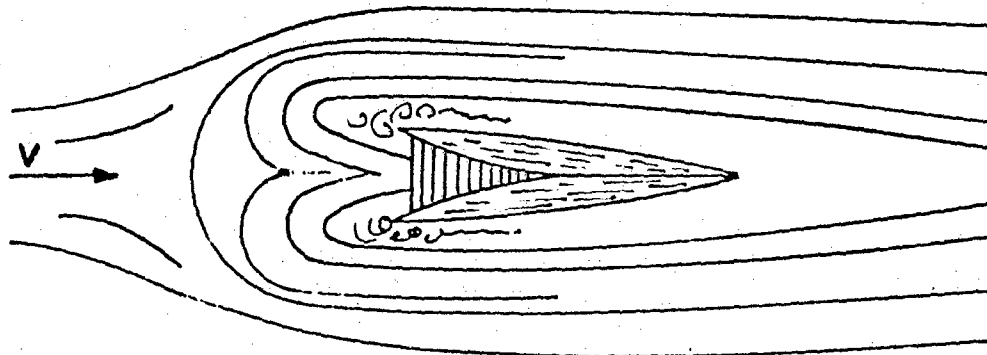
2.7.1 REAR LAUNCH, POWER ON The effect of the main rocket motor on the aerodynamic characteristics for sideslip angles between 0 and 180 degrees was estimated in Section 2.4.5. However, as pointed out in that section, only a very rough estimate could be made. The actual forces and moments induced on the body are a function of both the rocket motor characteristics and the body geometry as well as the actual flight condition. As was previously shown, the induced forces and moments can be larger than the body forces and moments themselves. Due to the large magnitude of these induced forces, a thorough examination of all aspects of the rocket motor interference should be made.

The effect of the rocket exhaust on the rear launch aerodynamic characteristics presents an entirely different problem which, due to

SECRET

SECRET

the flow complexity, has not previously been estimated. The following sketch shows the nature of the expected flow field.



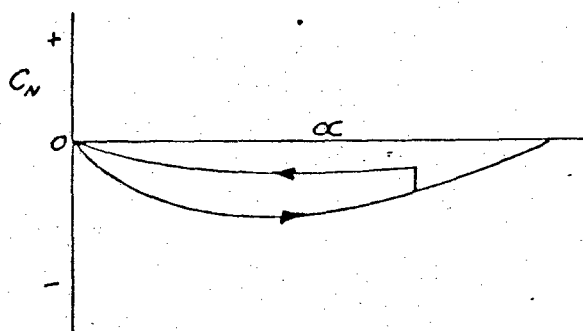
The rocket exhaust will flow back over the body altering the aerodynamic properties. Essentially, the missile will be flying in its own exhaust. The exhaust is expected to blanket the body with a layer of very low velocity gas, analogous to a very thick boundary layer. The thickness and velocity distribution of this layer is not known at this time. However, it is likely that no interference between the layer and the reaction jet will exist; i.e., the thrust produced by the reaction jet will be identical to that produced at zero velocity. It should be noted that although the relative velocity between the missile and the exhaust gas may be very low, it is still possible for forces and moments to exist on the missile. The exhaust flow over the missile would, in effect, create an entirely new airfoil as seen by the free stream flow. Differential pressures between the top and bottom of the new airfoil can be produced. These static pressures would be transmitted essentially unaltered through the exhaust flow field to the surfaces of the vehicle itself, thereby creating forces and moments. The flow separation apparent in the power-off case will definitely be altered. Since all the aerodynamic characteristics are a function of the degree of flow separation, it is apparent that entirely different aerodynamics will exist. Predictions of the interference cannot be made with any degree of confidence. Therefore, it is suggested that experimental evidence be gained before rear launch is attempted. This program should be carried out in a wind tunnel using actual rocket motors if possible, and if not, cold air simulation.

2.7.2 DYNAMIC CONSIDERATIONS An area which warrants investigation before high subsonic speed rear launch is attempted, is the possible

SECRET

SECRET

unsteady flow problem caused by the blunt base. This problem, however, is confined to the transonic flow regime, and is not expected to be serious for the contemplated FIV launch conditions. As reported in References 5.18, 5.19, 5.20, and as shown in Section 2.4.6.1, leading edge separation occurs for the rear launch position for transonic Mach numbers. At positive angles of attack, the upper surface is in a separated flow region. As the angle of attack is decreased, the separated flow reattaches and the opposite side separates. Reference 5.21 states that the angle at which reattachment occurs is lower than that where separation is induced. Therefore, depending on whether the angle of attack is increasing or decreasing, two different normal force values may exist for the same angle of attack. In effect, a hysteresis loop is formed in the normal force and consequently, the pitching moment curve. This effect is illustrated in the following sketch.



If the model oscillates with sufficient amplitude to enclose the hysteresis loop, it is apparent that the traverse of the loop creates an energy exchange by virtue of a nonconservative restoring force that can amplify the motion. Figure 2.7.1 is taken from Reference 5.22 and shows the qualitative Mach number range at which this motion occurred for various model shapes. The motion is a function of the model geometry as well as the free stream conditions.

Dynamic tests were not run during the PYE WACKET Phase II wind tunnel tests. However, a violent oscillation was encountered for the rear launch position. Because of the oscillations, data could not be obtained at zero angle of attack and 180 degrees of sideslip in a Mach number range $M = 0.75$ to 0.95 . An increase in angle of attack to three degrees eliminated the oscillation entirely. Changing the yaw angle from 180 degrees to 160 degrees lessened the severity of the oscillations, but did not in all cases eliminate it.



Although evidence indicates that such a problem may exist, it should

SECRET

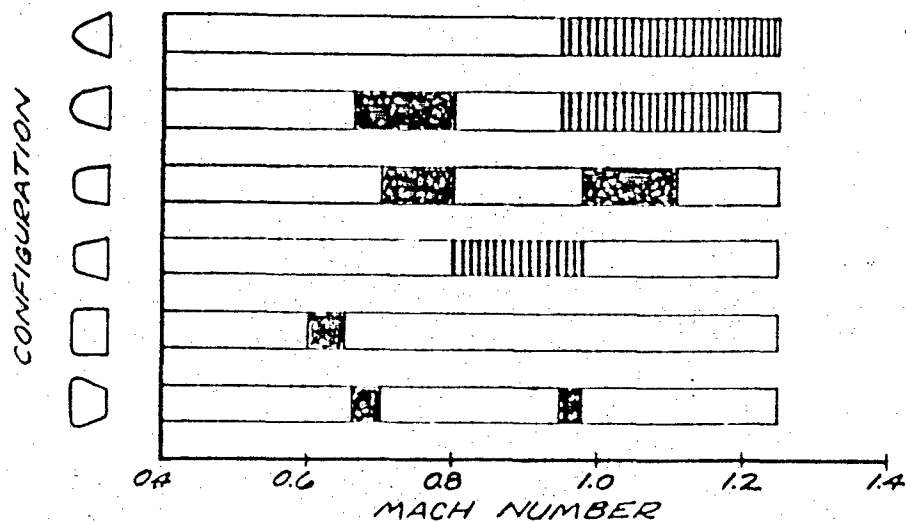
SECRET

FIGURE 2.7.1

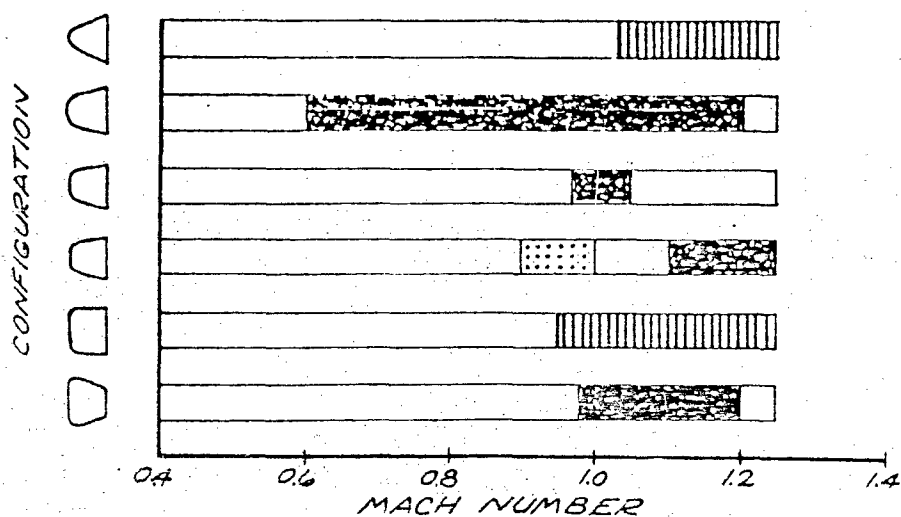
MACH NUMBER RANGE FOR MODEL
OSCILLATIONS AND MODEL BOUNCING

NONE  SLIGHT  MODERATE  STRONG 

REF. (NASA TM X-169)



MODEL OSCILLATING



MODEL BOUNCING

2.201

SECRET

be noted that all discussion so far was concerned with power-off conditions. The effect of the main rocket exhaust over the body is at this time unknown. It is possible that the power on effect might alleviate or even eliminate the problem, or that it could amplify the oscillating motion. It seems necessary, therefore, to more completely determine the extent of the problem if rear launches at transonic speeds are anticipated.

2.7.3 DAMPING DERIVATIVES To evaluate the dynamic flight characteristics of the PYE WACKET, it is necessary to know the longitudinal stability damping derivatives of the missile. These derivatives determine the time rate of decay of an oscillating motion of the missile caused by a flight disturbance. A disturbance from steady-state straight-line flight conditions induces variations in missile angle of attack. These changes in angle of attack give rise to damping moments which are the result of aerodynamic forces acting at some distance from the center of gravity. For the wing-like configuration of PYE WACKET, the longitudinal damping derivatives of major importance are $C_{m\dot{q}}$ and $C_{m\ddot{\alpha}}$.

The stability derivative $C_{m\dot{q}}$ is the change in pitching moment coefficient with varying pitch velocity. This derivative is important in longitudinal dynamics, since it is involved in the damping of the short-period pitching mode. The short period mode is of particular interest, because the period of oscillation of this mode becomes small near sonic velocity and the oscillation is therefore difficult to control. A negative value of $C_{m\dot{q}}$ increases the damping of this mode; consequently, high negative values of this derivative are desirable.

The stability damping derivative $C_{m\ddot{\alpha}}$ is the change in pitching moment coefficient with variation in rate of change of angle of attack. This rate of change of angle of attack results from a change in vertical sinking velocity (Z-axis) while the forward velocity (X-axis) remains constant. Like $C_{m\dot{q}}$, the derivative $C_{m\ddot{\alpha}}$ affects the damping of the short-period pitching mode. It is expected that $C_{m\ddot{\alpha}}$ and $C_{m\dot{q}}$ are of the same magnitude for a missile of the PYE WACKET configuration. Hence, both should be considered for design studies.

2.8 PROTOTYPE CONSIDERATIONS

The primary investigation of the Phase II study was directed toward the FTV configuration and its expected flight conditions. Emphasis was placed on the determination of aerodynamic characteristics for subsonic omnidirectional launch at sea level altitude. Although the prototype configuration differs slightly and the flight conditions differ greatly, data were obtained which are applicable to the 21 per cent thick prototype and its flight regime. Some data apply directly and some will have to be modified slightly for prototype applications.

SECRET

Application of current data is more difficult to apply to the 14 per cent thick prototype configuration. Good estimates may be made at supersonic speeds for the normal force, pitching moment, and drag for the forward launch. However, the aerodynamic characteristics at large sideslip angles cannot be predicted with the same degree of accuracy. The subsonic aerodynamic characteristics also cannot be entirely gained from present data. Flow separation, which is evident in many cases for the FTV configuration, is a strong function of model geometry. Therefore, the 14 per cent thick prototype configuration may have a different degree of separation rendering accurate aerodynamic predictions impossible.

The PYE WACKET concept displays its greatest effectiveness at high altitudes and velocities. The incorporation of reaction jet controls allows PYE WACKET to operate at altitudes where aerodynamic controls are ineffective. The Feasibility Test Vehicles, on the other hand, are to be tested under conditions which are most stringent. The proposed flights from a rocket sled encompass flight conditions near sea level with a maximum velocity in the vicinity of $M = 2.0$. It was pointed out that these flight conditions were dictated by the use of off-the-shelf components in the fabrication of the FTV vehicles. Although high Mach numbers cannot be reached with the proposed FTV rocket motors, the low altitude restriction imposes extremely high forces and moments on the missile. Using the very conservative assumption that the aerodynamic coefficients are constant with Mach number, the forces and moments become a direct function of the dynamic pressure. Figure 2.8.1 shows the variation of dynamic pressure with Mach number and altitude. Examination of this plot shows that a Mach number of 2 at sea level is equivalent to Mach numbers of 3.7, 7.5 and 15.4 at 30,000, 60,000, and 90,000 feet altitude, respectively.

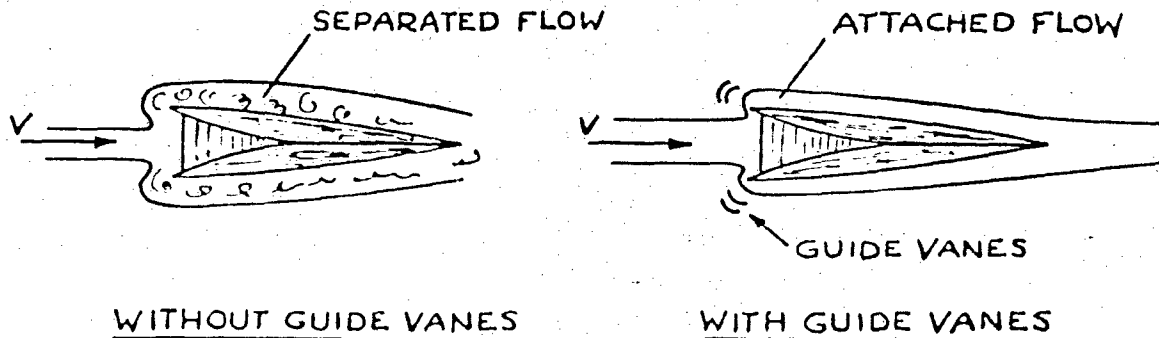
Figure 2.8.2 presents the launch Mach number range of Figure 2.8.1 expanded to a larger scale. From this plot, the severity of the launch conditions is clearly shown. A sea level launch at a Mach number of 0.6 produces forces and moments approximately equivalent to launching at Mach numbers of 1.1, 2.2, and 4.5 at 30,000, 60,000, and 90,000 feet altitude, respectively. It is evident from these plots that the anticipated launch conditions for the FTV configuration simulate much higher launch Mach numbers at altitudes where the PYE WACKET prototype is expected to be operational. In fact, the FTV launchings will impose higher forces and moments than the operational PYE WACKET will likely experience.

Rear launch from current bomber aircraft may prove to be a problem as pointed out in Section 2.7.2. The anticipated launch Mach number of 0.8 may be critical from a dynamic instability standpoint. Although proof of dynamic instability does not exist, indications are present. If it does prove to be a serious problem, at least two corrective methods may be employed. The effect of the main rocket exhaust on the

SECRET

SECRET

body aerodynamic characteristics could minimize or even eliminate the problem. If this can be proved, a power-on launching method may be devised similar to conventional air-to-air missiles. It may be recalled that a power-off launch was proposed in Phase I. If a power-on launch is not possible, another method of eliminating the dynamic problem shows promise. As pointed out in Section 2.7.2, the cause of the dynamic stability is asymmetric flow separation. If the flow remains attached, no serious problems should exist. A method of preventing flow separation can be accomplished by using guide vanes as illustrated in the following sketch.



Reference 5.23 shows that application of guide vanes greatly reduces the drag of a blunt body by reducing separation. As a point of interest, the guide vanes also reduce the base drag in forward flight. However, this drag reduction may be lost because of the induced drag of the vanes. The major advantage to be gained by the use of guide vanes on the PYE WACKET configuration should be elimination of the dynamic instability problem through prevention of flow separation in the rear launch attitude. The guide vanes could also eliminate the negative normal force and pitching moment that occurs at low angles of attack. An experimental investigation would have to be conducted to completely evaluate the effects of the guide vanes.

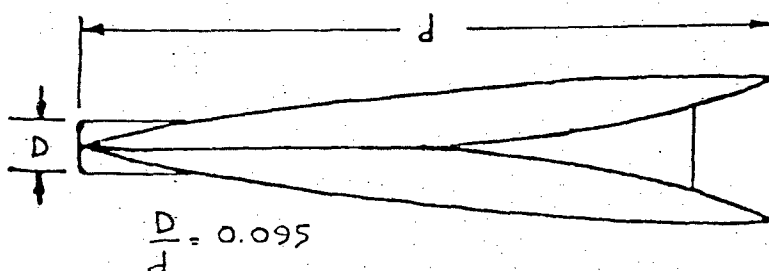
Launching from a supersonic bomber might cause the same dynamic instability since the missile must still pass through the transonic flow regime. However, the main rockets will be firing at this condition and may eliminate the problem. If this is not the case, a method such as the previously discussed guide vanes may be employed.

Launching from an aircraft presents a somewhat different condition than from a rocket sled. For the FTV sled launch, the missile will be mounted well above the sled to minimize the induced flow angularities from the sled. This will not be possible for an aircraft launch. The missile must fly through the induced flow field to clear the launch aircraft. This condition cannot be thoroughly investigated until the

SECRET

type of launching aircraft is selected. Reference may be made to a general description of the problem presented in the Phase I Feasibility Study, Reference 5.1.

Inherent in many of the possible prototype guidance systems is the necessity of adding a radome or IR seeker to the basic configuration. To assess the aerodynamic effect of such an alteration, a protuberance of the size and shape shown below was attached to a wind-tunnel model for tests at the two supersonic Mach numbers, 1.5 and 3.0.



The results of the test show that the normal force and pitch moment at zero sideslip angle are not significantly changed from the basic values shown previously. At $M = 1.5$, the seeker produces a small positive normal force at all angles of attack. The pitching moment contribution, however, is slightly negative at low angles of attack and positive at high angles of attack. At $M = 3.0$, the seeker produces no normal force and a very small negative pitching moment. The overall effect is an approximate five per cent reduction of the basic pitching moment.

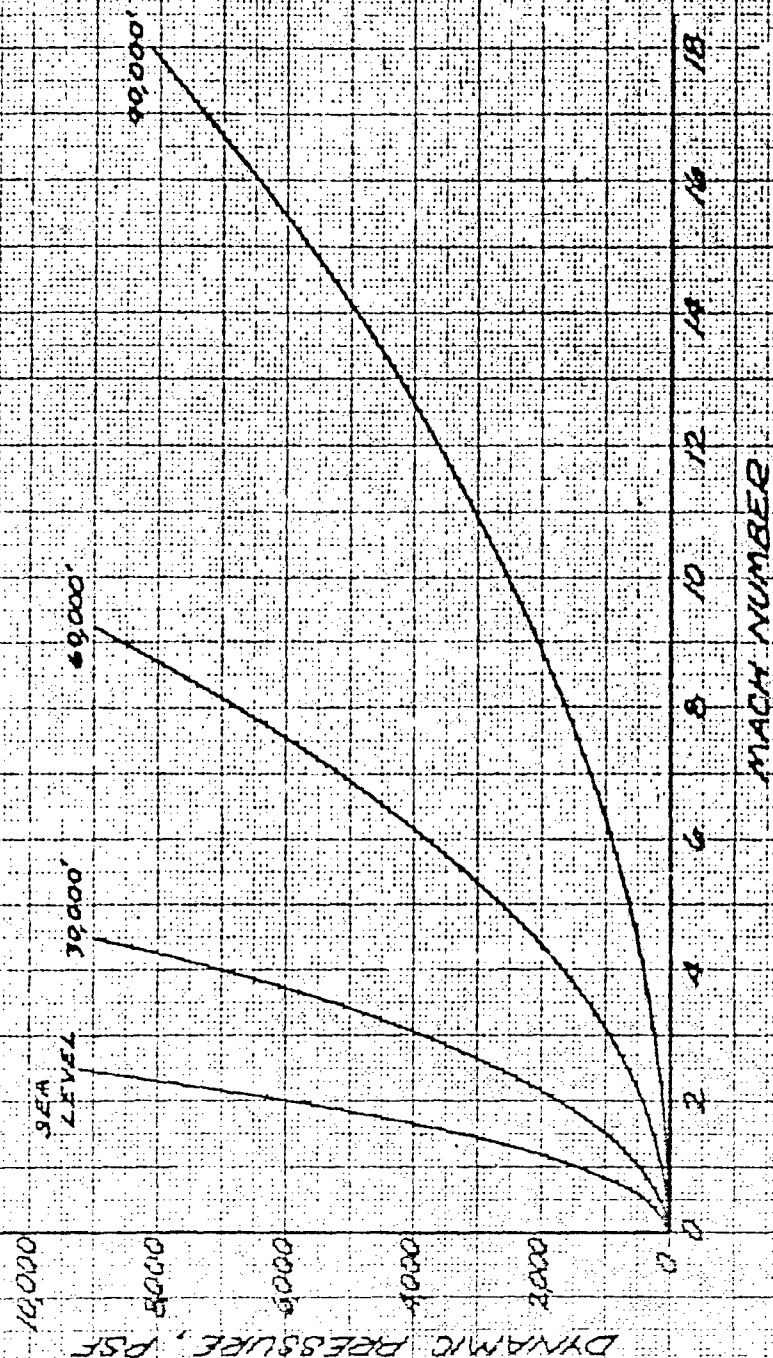
The effect of the seeker on the axial drag is more significant than that on the normal force and pitching moment. At zero sideslip angle, the seeker increases the axial drag by approximately five and ten per cent at Mach 1.5 and 3.0, respectively. This increase is approximately constant for angles of attack up to 15 degrees, the maximum tested.

The most predominant effect of the seeker on the aerodynamic characteristics occurs in the yawing moment. At $M = 1.5$, the basic yawing moment about the c.g. located at the midchord remains stabilizing, but is reduced by approximately one half at angles of sideslip up to 15 degrees. At $M = 3.0$, the configuration with the seeker is unstable about the midchord c.g. This instability is of the same order of magnitude as the stability of the configuration without the seeker. However, this destabilizing effect about the 0.5 C center-of-gravity location is not a significant problem because it is low in magnitude and because it is countered by the stabilizing effect resulting from the 0.43 C center-of-gravity location for the FTV.

SECRET

FIGURE 2.8.1

VARIAION OF DYNAMIC PRESSURE WITH MACH NUMBER



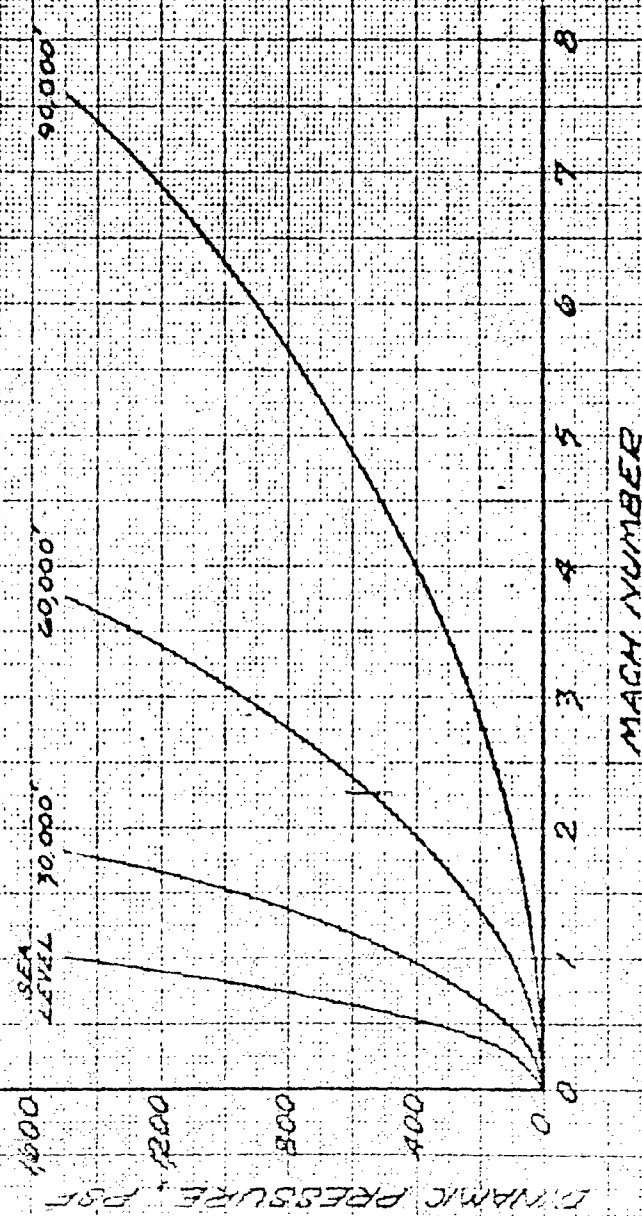
SECRET

902.2

SECRET

FIGURE 2.8.2

1
VARIATION OF DYNAMIC PRESSURE WITH MACH NUMBER



2022

SECRET

SECRET

Section 3.0
CONCLUSIONS

During the course of the FYE WACKET Phase II study, a large amount of data was obtained pertaining to omnidirectional launch. Data applicable to forward flight up to a Mach number of 5 were also obtained. Reaction jet magnification factors were determined for the same conditions. From these data, no major aerodynamic problems were apparent which would imperil a forward launch from a rocket sled. Assuming a clean separation of the missile from the sled, the critical Mach number from the standpoint of the control system is 1.2. At this Mach number, 2.1 degrees angle of attack can be controlled with 500 pound thrust reaction jets, assuming no jet magnification. However, the maximum positive jet magnification occurs at the same Mach number and may alleviate the critical area. Since no other problems are apparent, it can be concluded from an aerodynamic standpoint that forward launches from a rocket sled can be accomplished.

Cross-wind and rear launches are unique concepts and as a result, require a more extensive study program than is normally required. Although a comprehensive study program was completed in the Phase II project, a complete analysis of all aspects of the launching problems was not possible. A few unknowns, such as the exact effect of the main rocket motors on the aerodynamic characteristics and the stability damping derivatives, require additional analysis prior to cross-wind and aft rocket-sled launches to insure the greatest probability of success.

SECRET

SECRET

Section 4.0 RECOMMENDATIONS

All aspects related to a rocket sled launch could not be analyzed in this study phase. However, all critical areas were examined to the extent of available data. The following recommendations, therefore are based on the assumption that all foreseeable aspects of the rocket sled launch will be analyzed before a launch is scheduled.

1. Six-component force data should be obtained with the main rocket motor, and pitch and yaw reaction jets simulated. A fairly complicated wind tunnel model would be required in which interactions between the high pressure air lines and the force balance would be eliminated. The desired Mach number range is between 0 and 1. Primary emphasis would be placed on the rear and side launch model attitudes. If possible, this test should include transient effects caused by the pulsating reaction jets.
2. If the power-on yawing moment from the above test is found to be higher than expected, methods for reducing the moment may be investigated. As shown in Section 2.4.5.2, the power-on yawing moment is a function of the base geometry, i.e., the slot in the base. The base geometry can be altered to produce any desired yawing moment consistent with the varying conditions of flight.
3. A dynamic test should be conducted to determine the stability damping derivatives. Forward launch should be studied at Mach numbers up to 2. Only subsonic speeds need be tested for cross-wind and rear launch. Emphasis would be placed on the rear launch position to determine at what Mach number, if any, dynamic instability occurs.
4. If dynamic instability is apparent, methods such as guide vanes should be investigated to eliminate the problem.
5. The missile should be tested in the vicinity of a replica rocket sled to determine the extent of forces induced on the missile. These forces arise as a result of the rocket sled flow field and must be determined to define the initial launch conditions.

SECRET

SECRET

Section 5.0
BIBLIOGRAPHY

- 5.1 "PYE WACKET Lenticular Rocket Feasibility Study", AFGC-TR-60-25, May 1960, Secret.
- 5.2 Linnell, R. D., "Two Dimensional Airfoils in Hypersonic Flows," Journal of Aeronautical Sciences, Volume 16, No. 1 (January 1949) pp. 22-30.
- 5.3 Dorrance, W. H., "Two Dimensional Airfoils at Moderate Hypersonic Velocities," Journal of Aeronautical Sciences, Volume 19, No. 9 (September 1952) pp. 593-600.
- 5.4 Shapiro, A. H., "The Dynamics and Thermodynamics of Compressible Fluid Flow", The Ronald Press Company, New York, 1954.
- 5.5 Giese, D. J., Convair-Pomona TM 334-450, "PYE WACKET Wind Tunnel Test No. III - FWT Pre-Test Report", July 1960.
- 5.6 Giese, D. J., Convair-Pomona TM-334-454, "PYE WACKET Wind Tunnel Test No. IV, Pre-Test Report, Type A Wind Tunnel", July 1960.
- 5.7 Jones, R. D., and Featherstone, H. A., Convair-Pomona TM-334-451, "Estimated Omnidirectional Launch Aerodynamics for PYE WACKET FTV Configuration", July 1960.
- 5.8 Cleary, Joseph W., NASA TM X-370, "The Effects of Nose Bluntness on The Flow Separation and Longitudinal Characteristics of Ellipsoidal - Nosed Cylinder - Flare Models at Transonic Speeds", August 1960.
- 5.9 Polhamus, Edward C., NACA RM L 57F25, "Effect of Nose Shape on Subsonic Aerodynamic Characteristics of a Body of Revolution Having a Fineness Ratio of 10.94", August 1957.
- 5.10 "Aerodynamic Force Characteristics of Delta Wings at Supersonic Speeds," Jet Propulsion Laboratory, Pasadena, California, Report No. 20-82, September 1954.
- 5.11 Van Driest, E. D., NAA-AL-958, "Turbulent Boundary Layer for Compressible Fluids on an Insulated Flat Plate," North American Aviation, Inc., 15 September 1949.

SECRET

- 5.12 Loving, Donald L., and Katsoff, S., NASA MEMO 3-17-59L, "The Fluorescent-Oil Film Method and Other Techniques for Boundary Layer Flow Visualization", March 1959.
- 5.13 Dewey, Paul E., NACA TN 3442, "A Preliminary Investigation of Aerodynamic Characteristics of Small Inclined Air Outlets at Transonic Mach Numbers", May 1955.
- 5.14 Amick, James L., and Hays, Paul B. WADD TR 60-329, "Interaction Effects of Side Jets Issuing From Flat Plates and Cylinders Alined with a Supersonic Stream", The University of Michigan, June 1960.
- 5.15 Etkin, Bernard, "Dynamics of Flight," New York, N. Y., John Wiley and Sons Inc., 1959.
- 5.16 Wu, T. Y., Navord Report 6420, "Ground Interference on Bodies Moving Through a Compressible Fluid and Their Applications to Snort Sled Designs," U. S. Naval Ordnance Test Station, China Lake, California, July 1958.
- 5.17 Alford, William J., Jr., Silvers, H. Normal, and King, Thomas J., Jr., NACA RM L54J20, "Preliminary Low-Speed Wind Tunnel Investigation of Some Aspects of the Aerodynamic Problems Associated with Missiles Carried Externally in Positions Near Airplane Wings," December 1954.
- 5.18 Seiff, Alvin, and Whiting, Ellis, NASA TM X-377, "The Effect of the Bow Shock Wave on the Stability of Blunt-Nosed Slender Bodies", September 1960.
- 5.19 Fisher, Lewis R., and DiCamillo, Joseph R., NASA MEMO 1-21-59L, "Investigation of Several Blunt Bodies to Determine Transonic Aerodynamic Characteristics Including Effects of Spinning and of Extendible Afterbody Flaps and Some Measurements of Unsteady Base Pressures", January 1959.
- 5.20 Wiley, Harleth G., Kilgore, Robert A., and Hillje, Ernest R., NASA TM X-337 "Dynamic Directional Stability Characteristics for a Group of Blunt Reentry Bodies at Transonic Speeds", October 1960.
- 5.21 Cleary, Joseph W., NASA TM X-370, "The Effects of Nose Bluntness on the Flow Separation and Longitudinal Characteristics of Ellipsoidal-Nosed Cylinder - Flare Models at Transonic Speeds", August 1960.
- 5.22 Everhart, Philip E. and Lindsey, Walter F., NASA TM X-169, "Observations on the Flows Past Blunt Bodies at Transonic Speeds", June 1960.
- 5.23 Hoerner, Sigand F., "Fluid - Dynamic Drag," 1956.

SECRET

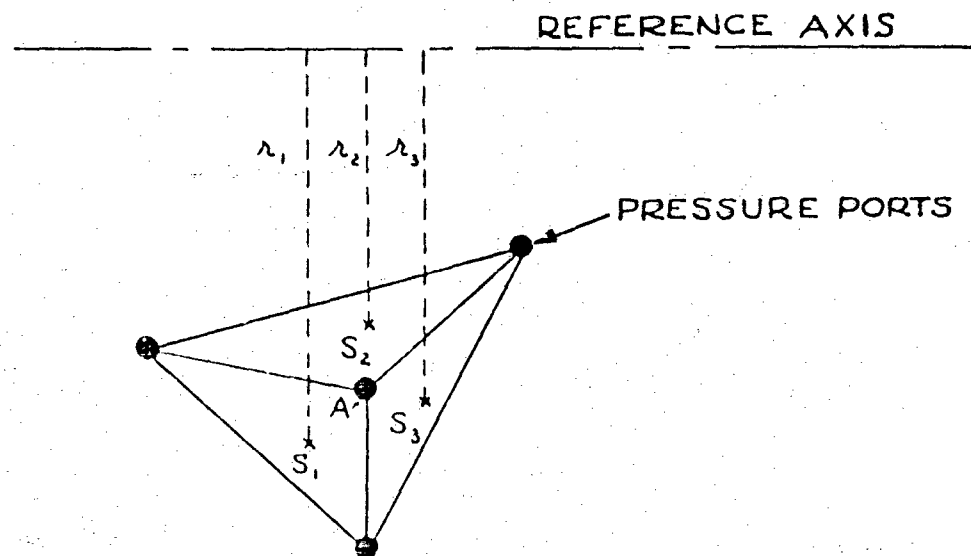
Section 6.0
APPENDIX

6.0 SURFACE PRESSURE INTEGRATION METHOD A numerical integration technique for use on digital computers was developed to obtain the aerodynamic force and moment coefficients acting on the missile as a result of the surface pressures. These surface pressures were obtained from wind tunnel tests. The basis for the method of integration concerns averaging the pressures over a given area and adding the incremental force and moments found from the average pressures. Although other techniques were considered, they were discarded because of the time and/or cost factors. The average pressure method was fairly easy to program on a digital computer, and lent itself well to the tunnel data handling systems.

In the calculation of the aerodynamic coefficients, it is necessary to obtain the average pressure acting over a given area. These area sections are determined by dividing the missile planform area, S , into triangular sectors with pressure ports at the three vertices of each area. The average pressure over each triangle is taken equal to one third of the sum of the three vertex pressures. It can be seen that the contribution of each measured pressure to the total force on the missile is equal to the pressure multiplied by one third of the area of the triangle. If a pressure port is at the vertex of a number of triangular areas, the total contribution of the pressure to the load is the pressure multiplied by one third of the sum of the areas of the adjacent triangles. In order to find the moments on the missile, the pressures are multiplied by one third of the sum of the products of the area of each triangle times its moment arm from the center of pressure for the area to a reference axis. For the example shown below, the following formulae apply to the pressure at the center port.

6.1

SECRET



RESULTING VALUES FROM PRESSURE PORT A

$$\Delta \text{ FORCE} = \frac{(\text{PRESSURE})_A (S_1 + S_2 + S_3)}{3}$$

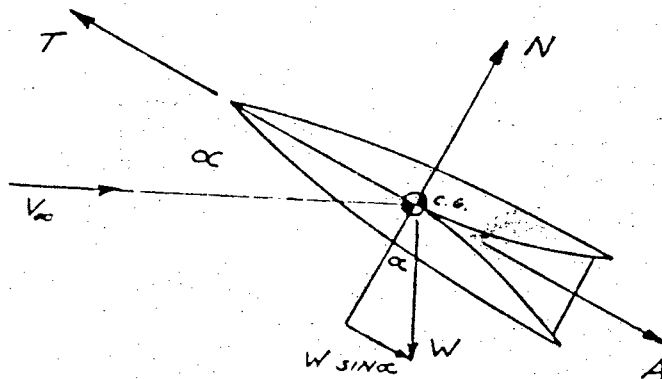
$$\Delta \text{ MOMENT} = \frac{(\text{PRESSURE})_A (S_1 \lambda_1 + S_2 \lambda_2 + S_3 \lambda_3)}{3}$$

WHERE: S = AREA OF TRIANGULAR SECTOR
 λ = MOMENT ARM FROM CENTER OF
 PRESSURE TO REFERENCE AXIS

SECRET

Summation of the incremental forces and moments obtained in the above manner for each pressure port yields the total values affecting the missile. The pressure multiplication factors are constants and were calculated for each pressure port. These constants were used in a digital computer for the numerical integration of the pressure data.

6.2 EQUATION FOR LEVEL FLIGHT TRAJECTORIES The derivation of the closed form equations of velocity as a function of time are presented in this section. The derivation of the equations are given for both the boost phase and coast phase of flight. A sketch of the forces acting on the missile is as follows:



Boost Phase

Summation of forces along the longitudinal axis are,

$$T - A - W \sin \alpha = \frac{W}{g} \dot{V} = \frac{W}{g} \frac{dV}{dt} \quad (6.2.1)$$

For level flight, at sea level conditions, the required angle of attack ranges from 3 degrees at $M = 0.4$ to less than 0.1 degree at $M = 2.0$ for $\theta = 0^\circ$, $W_0 = 125$ lbs (Figure 2.5.5). At launch Mach numbers of 0.4 and above, the average trim angle of attack will be in the neighborhood of 1 degree or less. Consequently, the deceleration term of $W \sin \alpha$ is neglected. Equation (1) then becomes,

$$T - A = \frac{W}{g} \frac{dV}{dt} \quad (6.2.2)$$

UNCLASSIFIED

where W = weight at any time, t ,

$$W = W_0 - \left(\frac{W_0 - W_e}{t_g} \right) t$$

W_0 = full weight, lb,

W_e = empty weight at end of boost, lb,

t_g = burning time, seconds, and

$$A = \frac{1}{2} \rho V^2 C_A S$$

$$\frac{A}{\rho S} = \frac{1}{2} V^2 C_A = aV + b = a(V_0 + V_g) + b$$

then axial drag in the linearized form becomes,

$$A = \rho S a (V_0 + V_g) + \rho S b$$

where a and b are the slope and intercept, respectively, of the function $A/\rho S$ versus velocity. Substituting the expressions for drag and weight into Equation (2) the equation becomes

$$T - [\rho S a (V_0 + V_g) + \rho S b] = \left[\frac{W_0}{g} - \left(\frac{W_0 - W_e}{g t_g} \right) t \right] \frac{dV}{dt}$$

(6.2.3)

Separating variables and integrating Equation (3), the total velocity is

$$V_0 + V_g = \frac{\frac{T}{\rho S} - b}{a} \left\{ 1 - \left(1 - \frac{a V_0}{\frac{T}{\rho S} - b} \right) \left[1 - \left(1 - \frac{W_e}{W_0} \right) \frac{t}{t_g} \right] \right\}^{\frac{\rho S g t_g a}{W_0 - W_e}}$$

6.4

UNCLASSIFIED

UNCLASSIFIED

Coast Phase

The expression for the velocity during the coast phase is obtained by Equation (2) with the thrust term equal to zero. The equation becomes,

$$-A = \frac{W}{g} \cdot \frac{dV}{dt} ; \text{ or } \frac{dV}{A} = - \frac{g dt}{W}$$

Substituting the linear expression for axial drag yields the form

$$\frac{dV}{\rho S a V + \rho S b} = - \frac{g dt}{W_c}$$

(6.2.4)

where t_c = time from turnout and

W_c = Weight at any time, t_c , or

$$W_c = W_{g/o} - (W_{R/g/o} - n \dot{W}_R t_c)$$

n = number of jets operating.

$\dot{W}_R = \frac{T_j}{S.I.}$ = rate of fuel consumption per control jet, lb/sec,

T_j = thrust per control jet - lb and

S.I. = Specific impulse - lb/lb/sec

Integrating Equation (4) and substituting initial conditions results in the velocity at any time during coast of

$$V = \left(V_{g/o} + \frac{b}{a} \right) e^{\frac{-\rho S a t_c}{W_{g/o} - (W_{R/g/o} - n \dot{W}_R t_c)}} \quad (6.2.5)$$

UNCLASSIFIED

UNCLASSIFIED

Since the weight of the reaction control jet fuel is small in relation to the burnout weight of the missile, a close approximation of the velocity may be obtained by averaging the weight (w_c) over the coast phase of flight. Equation (5) then becomes,

$$V = \left(V_{g,0} + \frac{b}{a} \right) e^{\frac{-\rho S a t}{W_{ave}}} \quad (6.2.e)$$

UNCLASSIFIED

INITIAL DISTRIBUTION

1	Wpns Sys Eval Gp	2	NASA, Space Task Gp
3	Hq USAF (AFDAF)	1	NASA - Ames Aeronautical Lab
3	Hq USAF (AFOOF)	3	NASA - Ames Aeronautical Lab
1	Hq USAF (AFETR)		Ames Rsch Cen, Lib
4	Hq USAF (AFDRT)	1	Arnold Engineering Dev Cen,
3	Hq USAF (AFORQ)		PWT
2	Hq USAF (AFCOA)	1	Arnold Engineering Dev Cen
1	AFSC (SCGS)		von Karman Facility
2	AFSC (SCI)	3	Convair Div
3	AFSC (SCR)	15	ASTIA (TIPCR)
1	DOD DFR & E,		AFGC
	Ofc of Asst Dir of Fuels,	1	ASO
	Materials and Ord	2	ASOW
2	Asst Sec of AF (Rsch & Dev)	6	ASOF
1	AU (Lib)	3	EGEH
1	AF Ofc of Scientific Rsch	2	PGTRI
1	SAC (DO)		
5	SAC (OA)		
5	SAC (FORQ)		
1	TAC (IOD)		
1	TAC (TMD)		
1	TAC (TIL)		
3	ADC (ADO)		
1	Ofc of Aerospace Rsch		
1	Inst of Air Wpns Rsch (Lib)		
1	PACAF (I FOOI -RQ)		
3	Ballistic Sys Div		
3	Space Sys Div		
1	USAFE (OA)		
1	USAFE (OTREQ)		
2	ASD (ASAT)		
4	ASD (ASL)		
1	ASD (ASO)		
7	ASD (ASZ)		
1	Dir, USAF Proj RAND		
1	Ofc of Ord Rsch		
2	Bu of Naval Wpns, P		
1	Bu of Naval Wpns, Conv Air		
	Wpns Sys Code RM-377		
1	Bu of Naval Wpns, OP-07		
1	Bu of Naval Wpns, OP-03		
1	Naval Air R & D Act Comd		

UNCLASSIFIED

<p>AD</p> <p>Convair/Pomona, Convair Division of General Dynamics Corporation, Pomona, California, PVE WACKET Feasibility Test Vehicle Study (Aerodynamics), UNCLASSIFIED TITLE, June 1961, 219 p. incl. illus. 53 refs. (AFSC Project 3811; ASD-TR-61-34 - Volume III) (Contract AF 08(635)-1168)</p> <p>SECRET NF report</p>	<p>UNCLASSIFIED</p> <p>1. Test vehicles 2. Hypersonic test vehicles 1. Det 4, Hq ASD II. Contract AF 08(635)-1168 III. Project 3811 IV. PVE WACKET</p>
<p>AD</p> <p>Convair/Pomona, Convair Division of General Dynamics Corporation, Pomona, California, PVE WACKET Feasibility Test Vehicle Study (Aerodynamics), UNCLASSIFIED TITLE, June 1961, 219 p. incl. illus. 53 refs. (AFSC Project 3811; ASD-TR-61-34 - Volume III) (Contract AF 08(635)-1168)</p> <p>SECRET NF report</p>	<p>UNCLASSIFIED</p> <p>1. Test vehicles 2. Hypersonic test vehicles 1. Det 4, Hq ASD II. Contract AF 08(635)-1168 III. Project 3811 IV. PVE WACKET</p>
<p>AD</p> <p>Convair/Pomona, Convair Division of General Dynamics Corporation, Pomona, California, PVE WACKET Feasibility Test Vehicle Study (Aerodynamics), UNCLASSIFIED TITLE, June 1961, 219 p. incl. illus. 53 refs. (AFSC Project 3811; ASD-TR-61-34 - Volume III) (Contract AF 08(635)-1168)</p> <p>SECRET NF report</p>	<p>UNCLASSIFIED</p> <p>1. Test vehicles 2. Hypersonic test vehicles 1. Det 4, Hq ASD II. Contract AF 08(635)-1168 III. Project 3811 IV. PVE WACKET</p>
<p>AD</p> <p>Convair/Pomona, Convair Division of General Dynamics Corporation, Pomona, California, PVE WACKET Feasibility Test Vehicle Study (Aerodynamics), UNCLASSIFIED TITLE, June 1961, 219 p. incl. illus. 53 refs. (AFSC Project 3811; ASD-TR-61-34 - Volume III) (Contract AF 08(635)-1168)</p> <p>SECRET NF report</p>	<p>UNCLASSIFIED</p> <p>1. Test vehicles 2. Hypersonic test vehicles 1. Det 4, Hq ASD II. Contract AF 08(635)-1168 III. Project 3811 IV. PVE WACKET</p>